EXPERIMENTAL AND NUMERICAL INVESTIGATION OF HEAT AND MASS TRANSFER DUE TO PULSE COMBUSTOR JET IMPINGEMENT

A Dissertation
Presented to
The Academic Faculty

By

Michael J. Psimas

In Partial Fulfillment
Of the Requirements for the Degree
Doctor of Philosophy in the
George W. Woodruff School of Mechanical Engineering

Georgia Institute of Technology

May, 2010

EXPERIMENTAL AND NUMERICAL INVESTIGATION OF HEAT AND MASS TRANSFER DUE TO PULSE COMBUSTOR JET IMPINGEMENT

Approved by:

Dr. Tim Patterson, Co-Advisor
School of Mechanical Engineering
Georgia Institute of Technology

Dr. Preet Singh
School of Materials Science and Engineering
Georgia Institute of Technology

Dr. Cyrus Aidun, Co-Advisor
School of Mechanical Engineering
Georgia Institute of Technology

Dr. William Wepfer
School of Mechanical Engineering
Georgia Institute of Technology

Dr. Sujit Banerjee
School of Chemical and Biomolecular Engineering
Georgia Institute of Technology

Date Approved: April 1, 2010

To My Wife and Parents

ACKNOWLEDGEMENTS

I would like to thank the many people who have helped me throughout my graduate study without whom this work would not have been possible. I would especially like to thank my co-advisors, Dr. Tim Patterson and Dr. Cyrus Aidun, for their support and guidance. Dr. Patterson's insight and practical perspective have been invaluable, as have his straightforward counsel and commentary. Always approachable, he has been a helpful and dependable advisor. I would like to thank Dr. Aidun for his patience, direction, and advice. His informative and detail-oriented approach to advisement has assisted tremendously with this process. I would also like to thank the committee members, Dr. Sujit Banerjee, Dr. Preet Singh, and Dr. William Wepfer, for their comments and suggestions which helped shape this dissertation. Finally, I am grateful to the Institute of Paper Science and Technology and the George W. Woodruff School of Mechanical Engineering for financial support during my graduate study.

TABLE OF CONTENTS

LIST OF TABLES

LIST OF FIGURES

LIST OF SYMBOLS

Letter Symbols

A	Area
c_p	Constant pressure specific heat
D	Diameter
E_{DRY}	Drying enhancement factor
E_{HF}	Heat flux enhancement factor
E_k	Turbulence kinetic energy
E_V	Velocity equivalency factor
h	Specific enthalpy
H	Nozzle to surface separation distance
I	Turbulence intensity
K	Permeability
k_m	Convective mass transfer coefficient
k_t	Convective heat transfer coefficient
L	Length
Le	Lewis number
m	Mass
M	Molar mass
Nu	Nusselt number
P	Pressure
Pr	Prandtl number

q''	Heat flux
r	Radial distance
R	Gas constant
R_{amp}	Velocity amplitude ratio
Re	Reynolds number
s	Liquid saturation
S_{ir}	Irreducible saturation
St	Strouhal number
T	Temperature
t	Time
u	Velocity in the x-direction
v	Velocity in the y-direction
W	Slot nozzle width
W_{NZ}	Nozzle to nozzle spacing
x	Distance in the x-direction
y	Distance in the y-direction
z	Distance in the z-direction

Greek Symbols

α	Thermal diffusivity
λ	Thermal conductivity
μ	Viscosity
ρ	Density

σ	Surface tension
σ_{RSD}	Relative standard deviation
τ	Dimensionless time
ϕ	Porosity or volume fraction
ψ	Relative humidity
ω	Oscillation frequency

Subscripts

a	Air
atm	Atmospheric
c	Capillary
cc	Combustion chamber
f	Final
g	Gas
i	Initial
l	Liquid
pk-pk	Peak to peak amplitude
ref	Reference value
s	Surface or solid
t	Turbulent
v	Vapor

SUMMARY

Porous media drying efficiency could be enhanced through incorporation of a pulse combustion driven impingement drying system. Under certain circumstances pulse combustors have been shown to improve both heat transfer and drying rate when compared to steady flow impingement. Despite this potential, there have been few investigations into the use of pulse combustor driven impingement jets for industrial drying applications. The research presented here utilized experimental and numerical techniques to study the heat transfer characteristics of these types of oscillating jets when impinging on solid surfaces and the heat and mass transfer when drying porous media. The numerical methods were extensively validated using laboratory heat flux and drying data, as well as correlations from literature. As a result, the numerical techniques and methods that were developed and employed in this work were found to be well suited for the current application. It was found that the pulsating flows yielded elevated heat and mass transfer compared to similar steady flow jets. However, the numerical simulations were used to analyze not just the heat flux or drying, but also the details of the fluid flow in the impingement zone that resulted in said heat and mass transport. It was found that the key mechanisms of the enhanced transfer were the vortices produced by the oscillating flow. The characteristics of these vortices such as the size, strength, location, duration, and temperature, determined the extent of the improvement. The effects of five parameters were studied: the velocity amplitude ratio, oscillation frequency, the time-averaged bulk fluid velocity at the tailpipe exit, the hydraulic diameter of the tailpipe, and the impingement surface velocity. Analysis of the resulting fluid flow revealed three

distinct flow types as characterized by the vortices in the impingement zone, each with unique heat transfer characteristics. These flow types were: a single strong vortex that dissipated before the start of the next oscillation cycle, a single persistent vortex that remained relatively strong at the end of the cycle, and a strong primary vortex coupled with a short-lived, weaker secondary vortex. It was found that the range over which each flow type was observed could be classified into distinct flow regimes. The secondary vortex and persistent vortex regimes were found to enhance heat transfer. Subsequently, transition criteria dividing these regimes were formed based on dimensionless parameters. The critical dimensionless parameters appeared to be the Strouhal number, a modified Strouhal number, the Reynolds number, the velocity amplitude ratio, and the H/D_h ratio. Further study would be required to determine if these parameters offer similar significance for other configurations.

CHAPTER 1

INTRODUCTION

The motivation for the research presented in this dissertation was provided by an Institute of Paper Science and Technology (IPST) project at the Georgia Institute of Technology directed at the application of Pulsed Air Drying (PAD) to commercial papermaking. The main objective of the IPST project was the development of pulse combustion drying technology for use on paper machines; of particular interest were machines which also employed standard multi-cylinder steam heated dryers. The current work focused on the heat transfer characteristics of oscillating jets when impinging on solid surfaces and the heat and mass transfer when drying porous media.

1.1 Pulsed Air Drying Project

Pulse combustor driven impingement drying, here referred to as Pulsed Air Drying (PAD), has the potential to offer energy and production advantages when compared to other drying processes. PAD can potentially provide increased drying rates and increased energy efficiency when compared to more traditional steady flow impingement dryers. Steady flow impingement drying yields higher drying rates than steam heated cylinder drying but requires considerably more energy than the dryer cylinders. Studies have shown the efficacy of PAD, but much of the underlying

phenomena are still not well understood (Wu and Mujumdar, 2006).

In modern papermaking, the dryer section is often the most expensive component of a paper machine in terms of both capital cost and operational cost due to the high energy requirements (Smook, 1992). Therefore, techniques and technologies that increase drying rates or offer improved energy efficiency are potentially valuable. In a modern paper machine the drying is performed by a series of cast iron cylinders approximately two meters in diameter. The sheet follows a serpentine path around these cylinders which are internally heated with steam. The latent heat of the condensing steam heats the cylinders and then the paper, evaporating the water in the sheet. The drying rate for this process is low; therefore, a large number of dryer cylinders, up to 100, are required. This leads to large space requirements and increased capital costs. Furthermore, the production capacity of the paper machine dryer section is greatly determined by the number of cylinders available. The paper must have minimum moisture content at the end of the dryer section, and there are limited methods available to increase the solids content of the sheet prior to the dryer section.

One possible avenue for increasing efficiency and decreasing dryer section size is an air impingement system (Kokko et al., 2003). Such systems are often employed in conjunction with a Yankee dryer for use in drying tissue grade products (Smook, 1992). In this configuration, the Yankee dryer uses a single large steam heated dryer cylinder approximately four meters in diameter. Simultaneously, heat is supplied by a surrounding convection air impingement hood. The convection heat transfer rate is in large part

controlled by the velocity of the impingement jets. This dual mode drying scheme significantly increases the drying rate. In order to further improve such a system, either the conductive or convective transfer modes can be enhanced. Possible improvement paths of the convective heat transfer portion include increasing the gas impingement velocity or temperature. However, the cost of increasing the velocity of the impingement jet increases with the cube of the velocity change, and increasing the temperature could damage the sheet. The Pulsed Air Drying (PAD) project, however, focuses on another avenue for improving convective drying: the use of pulsating impingement jets produced by pulse combustors.

Pulse combustors have been employed in various fields that require efficient heating or drying. Such applications include furnaces, heating units, power generation, and industrial gasifiers. In recent years, the papermaking industry has paid increased attention to the use of pulse combustors for impingement drying (Mujumdar, 2004). Pulse combustors are well suited for this task due to their superior heat and mass transfer rates when compared with their steady combustion counterparts. Additionally, pulse combustors typically have higher combustion efficiencies due, in part, to improved air-fuel mixing in the combustion chamber. This also reduces the excess air required for complete combustion which, in turn, increases thermal efficiency. Efficient mixing coupled with favorable flow characteristics also results in decreased production of thermal NO_x (Kudra and Mujumdar, 2002). Nevertheless, the heat transfer and drying enhancements provided by the pulsating combustion remain the most attractive qualities for industrial applications.

1.2 Research Objectives

The current work serves to further the development of pulse combustion technology for use at a commercial level. The research in this dissertation focused on the heat transfer characteristics of pulse combustor driven oscillating jets when impinging on a solid surface, as well as the heat and mass transfer when drying porous media. Of particular interest were the enhancements of heat and mass transport compared to similar steady flow jets. The approach that was employed was to analyze not just the heat flux or drying, but also the details of the fluid flow that resulted in said heat and mass transport. The research consisted of four main phases: an experimental study of heat and mass transfer from single and multiple pulse combustors, the development of numerical models and techniques used for the study of the impingement jets, validation of said methods using the experimental results and correlations from literature, and a numerical study of the relevant system parameters and their impact on heat and mass transport mechanisms.

Rather than attempting to use a single numerical model to study both the fluid flow above the sheet and the transport processes within the sheet, the problem was split into two separate domains. The commercial software FLUENT was used to investigate the fluid flow above the impingement surface. Conversely, the software program Matlab was employed to model the processes within the substrate. This model was coupled with the FLUENT simulations through the conditions at the interface boundary. More specifically, the heat transfer coefficients, jet temperatures, and pressure profiles that were predicted by FLUENT at the impingement surface were used to specify the drying

model's boundary conditions. This approach was employed because it was a time efficient yet effective method of studying the pertinent phenomena.

1.3 Dissertation Outline

Chapter 2 reviews research from published literature which is relevant to the current work. However, previous studies of the heat transfer and drying due to impingement from a pulse combustor are rather limited. Therefore, other types of flows are also discussed in order to supply the relevant background information and provide groundwork for analyzing more complex flows. Various types of pulsating impingement jets are discussed including those from pulse combustors. Additionally, work in the area of modeling the transport processes that occur when drying porous media is reviewed.

Chapter 3 presents the laboratory experiments investigating the heat flux from single and multiple impingement jet systems using both pulsating and steady flow jets. Chapter 4 presents the development of the model used in the numerical simulations of the fluid flow in the region above the impingement surface. The general modeling approach, governing equations, and solution procedures are presented. Additionally, the simulation domain and boundary conditions are discussed. The methods used in grid refinement and time discretization are demonstrated. Finally, the resulting grid size and time step independence is verified. Validation of the numerical model is discussed in Chapter 5. Similarly, Chapter 6 presents the results of the drying experiments that were conducted using various impingement drying configurations and substrates. The numerical model of

the substrate and drying processes in discussed in Chapter 7 and validated in Chapter 8.

Single impingement jets are studied first in order to more fully understand the underlying phenomena of pulsating impingement jet heat transfer. Chapter 9 presents the methods and results of the numerical study of the impact various system parameters have on heat transfer and fluid flow. The mechanisms of heat transfer enhancement and the manipulation of said mechanisms through alteration of system parameters were of primary interest in that chapter. Although guided by the experimental work in Chapter 3, the numerical study investigated ranges of parameters that were not easily obtained in the laboratory setting. In this chapter, the system parameters were studied individually in order to isolate the effects of each quantity.

Conversely, Chapter 10 discusses the combined effects of altering multiple system parameters. Rather than investigating the details of the heat transfer and its mechanisms, this chapter instead focuses on the overall trends and groupings of similar heat transfer mechanisms. The flow types observed in the numerical simulations are discussed and categorized. The distinct flow types that were encountered are grouped into flow regimes. Furthermore, criteria are proposed to describe the threshold values of input variables at which a change in flow regime occurred.

Chapter 11 presents the findings of a numerical study of multiple impingement jets. The effects of jet-to-jet interactions from both oscillating and steady flow jets were analyzed. Furthermore, the impact of phase difference of neighboring jets on said

interactions was investigated. Conclusions and a summary of the work are provided in Chapter 12.

1.4 Summary of Findings

Using an extensive validation process, the numerical methods that were developed and employed in this work were shown to produce accurate results. It was found that the key mechanisms of the enhanced transfer were the vortices produced by the oscillating flow. The size, strength, location, duration, and temperature of these vortices determined the extent of the improvement. High velocity amplitude ratios produced greater heat flux by producing larger and stronger vortices despite slightly lower vortex temperature. Impingement surface heat flux increased with mean tailpipe exit velocity as a result of increased vortex size, vortex strength, and energy input rate. Similarly, larger nozzles provided additional energy input which yielded greater heat flux. High impingement surface velocities led to decreased heat flux due to entrainment of cool ambient air which inhibited performance. Still, the ability of vortices produced by pulsating jets to disrupt the boundary layers that formed near the impingement surface drastically improved heat transfer enhancement when compared to steady flow jets. Thus, the work showed that pulsating impingement jets are well suited for drying substrates moving at a high speed. Jet-to-jet interactions in multiple nozzle systems were found to greatly affect heat transfer performance. The presence of multiple jets decreased the impingement angle of the main jet column, altered the bulk fluid flow, decreased the temperature in the inner region, and constrained the vortices in the region between the

jets, thereby reducing their size. These factors combined to inhibit heat transfer. However, much of this reduction in performance could be alleviated by employing jets that had a high phase difference.

Analysis of the fluid flow revealed three distinct flow types, as characterized by the vortex structures, each with unique heat transfer characteristics. These flow types were: a single strong vortex that greatly dissipated before the start of the next oscillation cycle, a single persistent vortex that remained relatively strong at the end of the cycle, and a strong primary vortex coupled with a short-lived, weaker secondary vortex. The secondary vortex and persistent vortex regimes were found to significantly enhance heat transfer. Furthermore, the effects of various operational parameters were also affected by the flow type. Transition criteria dividing these regimes were developed using dimensionless parameters. The critical dimensionless parameters appeared to be the Strouhal number, a modified Strouhal number, the Reynolds number, the velocity amplitude ratio, and the H/D_h ratio. Thus, the oscillatory, mean flow, and geometrical characteristics were all important factors. These factors were combined to form two dimensionless groups, Ψ_1 and Ψ_2. Critical values of these parameters described the observed transition from the secondary vortex and persistent vortex flow regimes to the transient vortex regime. Further study would be required to determine if these parameters offer similar significance for other configurations.

The work presented in this dissertation is the first comprehensive investigation linking specific flow structures from pulse combustor driven impingement jets with heat

transfer and drying performance. The work also is unique in the application of extensive experimental data to validate the modeling approach.

CHAPTER 2

BACKGROUND

This chapter reviews the literature relevant to the current work. However, the literature on heat transfer and drying due to impingement from a pulse combustor is rather limited. Steady impingement jets are discussed first. This supplies relevant background information and lays the groundwork for analyzing more complex flows. Pulse combustors are then discussed followed by heat transfer due to various types of pulsating impingement jets. Finally, work in the area of modeling the transport processes that occur when drying porous media is reviewed.

2.1 Steady Impingement Jets

This section discusses heat transfer due to steady impingement jets and gives background information on the basic flow structures, characteristics, and key parameters. This not only provides a basis for subsequent analysis, but also offers a point of comparison to highlight the unique features of pulsating impingement jets. The key characteristics of a steady impingement jet are shown in Figure 2.1; a similar description is provided by Incropera and DeWitt (2002).

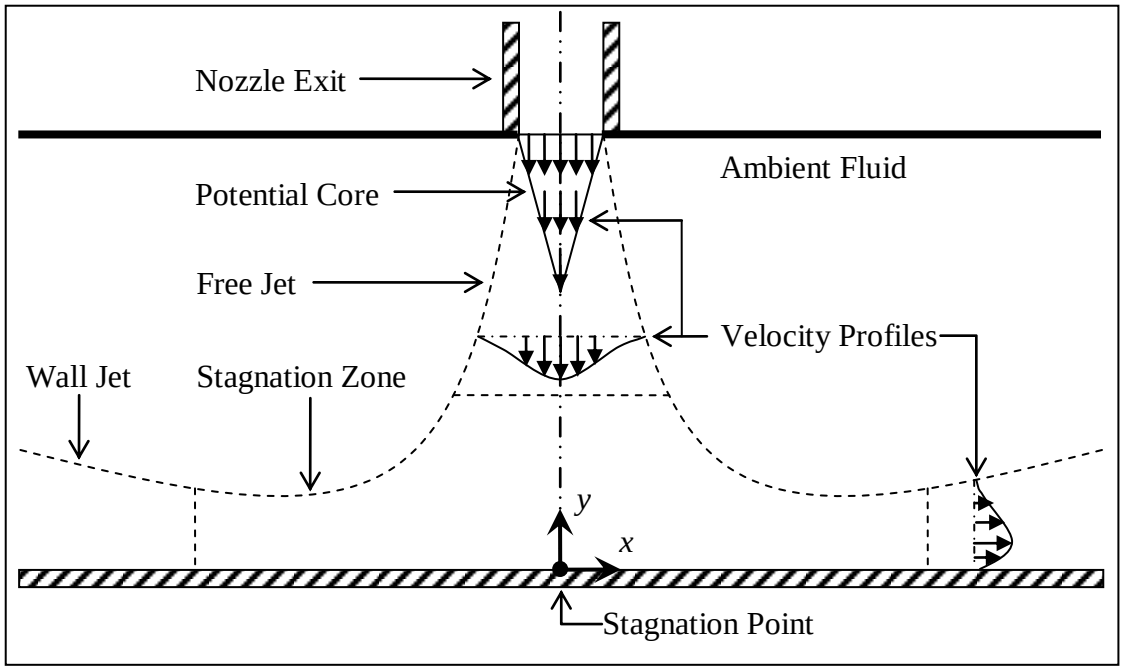

Figure 2.1: Components and characteristics of steady flow impingement jet.

The configuration shown in Figure 2.1 is typical of many single jet impingement scenarios: the jet discharges into a semi-quiescent ambient fluid. The four main regions on the jet are the potential core, free jet, stagnation zone, and wall jet. The potential core is the region within which the jet velocity remains equal to the uniform exit velocity. The free jet region is the portion of the flow over which the conditions are unaffected by the impingement surface. The jet is often turbulent and treated as having a uniform velocity profile at the nozzle exit. Farther away from the nozzle exit, however, the jet undergoes momentum exchange with the ambient fluid. The effects of this are twofold: the free jet broadens with decreasing y, and the potential core contracts. At some point downstream from the nozzle exit the jet velocity is less than the exit velocity and the potential core ceases to exist. The length of the potential core, which is the distance from the nozzle exit to the termination of the aforementioned uniform velocity profile, is typically 5 to 10

times the nozzle width. However, this length varies greatly with the flow characteristics and fluid properties at the nozzle exit as well as the nozzle geometric configuration. Farther downstream, the flow begins to be influenced by the impingement surface. In the stagnation zone the *y*-component of the fluid velocity approaches zero as *y* decreases due to the presence of the impingement target. Simultaneously, the fluid accelerates laterally; the direction that corresponds to the *x*-axis. The flow, which is now primarily parallel to the surface, continues to entrain zero-momentum ambient fluid. Thus, the flow becomes a decelerating wall jet.

The variation of the local Nusselt number with *x* typically follows one of two patterns: a maximum value at the stagnation point with monotonic decay as *x* increases, or a similar shape except for the addition of a secondary maximum located some distance away from the stagnation point. The critical factor that determines which profile is encountered is often the ratio of the nozzle to surface separation distance, *H*, to the hydraulic diameter of the nozzle, D_h. Lower values of H/D_h are more likely to produce the secondary local maximum. Examples of these profiles are given in Figure 2.2, along with a typical transitional value of the ratio H/D_h.

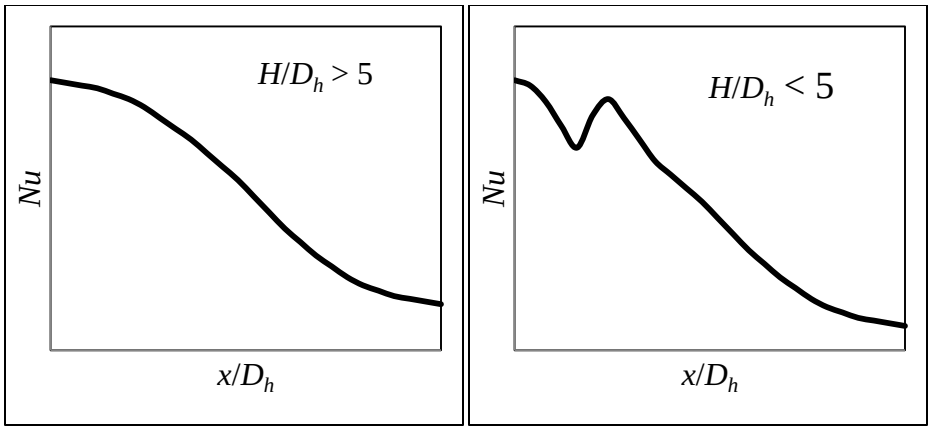

Figure 2.2: Representative local Nusselt number profiles for steady jet impingement.

The secondary local maximum in Figure 2.2 is attributable to a sharp rise in turbulence level. Most sources state that the transition from laminar flow in the stagnation region to a turbulent decelerating wall jet is primarily responsible for the increase in *Nu* (Martin, 1977; Popiel and Bogusiawski, 1986; Viskanta, 1993). However, an alternative explanation offered by some authors involves the role of Kelvin-Helmholtz instabilities. It is suggested that Kelvin-Helmholtz instability in shear layers between the impinging jet and ambient fluid produce coherent vortex rings. The rise in *Nu* is caused by intermittent impingement of these vortex rings onto the surface. Flow visualization and experimental measurement of surface heat transfer provide evidence of this phenomenon (Popiel and Trass, 1991; Meola et al., 1996; Angioletti et al., 2003).

Various other studies have also investigated the importance of turbulence and vortex structures to impingement jet heat transfer. Kataoka et al. (1987b) studied the heat transfer and turbulence characteristics of impinging water jets. Flow visualization was used to investigate the coherent vortex rings and large-scale eddies formed by these jets.

Well organized vortex rings were found within a distance of $4.5D_h$ of the nozzle exit, corresponding to the potential core length. However, beyond $4.5D_h$ the vortex rings deteriorated into less-organized structures. These large-scale eddies continued to decay farther downstream. The effect on heat transfer to the impingement surface was also studied. The heat transfer at the stagnation point was found to be greatest when $H/D_h = 6$. This ratio corresponded to two important features: the axial distance which produced the peak turbulence intensity of the large-scale eddies and the highest passing frequency of said eddies. It was found that the high passing frequency produced a so-called surface renewal effect. The boundary layers at the impingement surface were periodically broken up by the large-scale eddies. Since the boundary layers inhibit heat transfer, the sweeping behavior of the large-scale eddies partially accounted for the increase in *Nu*. The high turbulence level also helped elevate heat transfer.

2.2 Pulse Combustion Fundamentals

This section serves to present the basic description, operation, and characteristics of pulse combustors. The principle components of a pulse combustor and their functions are presented. The combustion cycle and associated flow characteristics are analyzed along with the criteria for establishing such phenomena. Finally, the principle advantage of pulse combustors, heat transfer enhancement, is discussed, and the difficulties in obtaining this enhancement are given.

Pulse combustion is an oscillatory process in which a fuel and an oxidizer

explosively react (combust) in a periodic manner. The intermittent nature of this process is due to the coupling of combustion-induced instability and corresponding resonant oscillations of the exhaust flow. In order to achieve self-sustaining pulsations, the combustion must spontaneously excite pressure (acoustic) oscillations that are in phase with the natural acoustic mode of the tailpipe. The three principal classes of combustor designs are the Rijke tube based on an open ended tube, the Schmidt-type based on the principles of the quarter-wave sound resonator, and the Helmholtz resonator (Zinn, 1996). The Helmholtz resonator is the subject of this work and is characterized by inlet valves for the air and fuel reactants, a combustion chamber that is the primary reaction site, and a single exhaust pipe through which the combustion products exit the system. The combustion chamber and exhaust pipe combination serves as an acoustic resonator (Zbicinski, 2002); therefore, the natural oscillation frequency is strongly determined by the geometry of the combustion chamber and the exhaust pipe. However, the air and fuel flow rates also influence this aspect of combustor behavior, albeit to a lesser degree (Kudra et al., 2003). The two types of inlet valves most often used are aerodynamic or mechanical. The former has no moving parts while the later utilizes flapper or rotary valves.

The typical combustion cycle of a Helmholtz type pulse combustor is given in Figure 2.3 (Dec et al., 1991). The fuel and air mixture in the combustion chamber combusts due to the chamber wall heat and remnant gases from the previous combustion cycle. This causes an increase in chamber pressure and a rapid acceleration of the gaseous combustion products. The pressure differential drives the hot gases through the

exhaust pipe and prevents further influx of reactants. Once a sufficient volume of exhaust gas exits the system, chamber pressure equalizes and the exhaust driving force is removed. However, the momentum of the tailpipe gases lead to additional discharge, resulting in a further reduction in combustion chamber pressure. This low pressure phase draws new reactants into the combustion chamber and can produce flow reversal of exhaust gas both in the tailpipe and in the area around the tailpipe exit (Thyageswaran, 2004). This flow reversal is an important feature as it has been shown to greatly affect heat transfer enhancement (Liewkongsataporn et al., 2006).

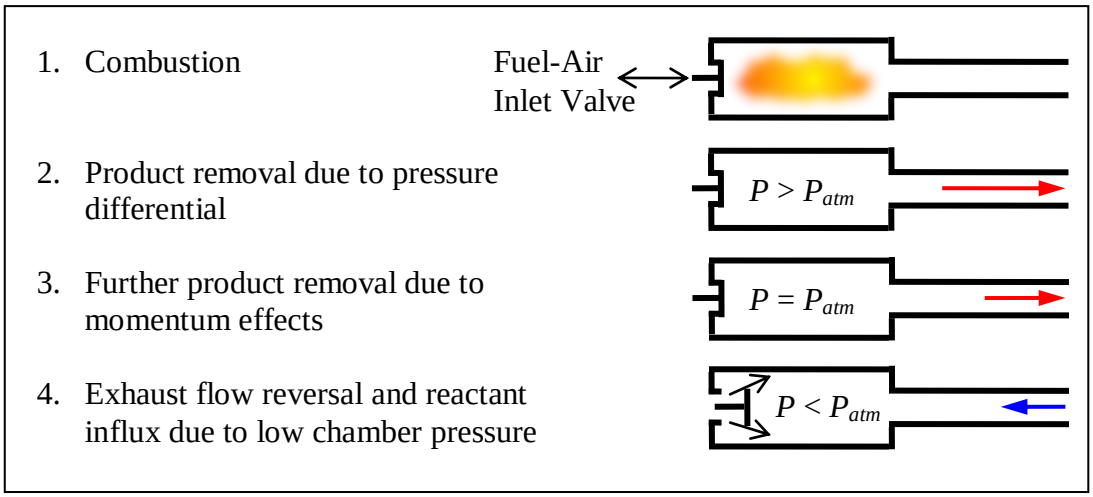

Figure 2.3: Combustion cycle of a Helmholtz type pulse combustor.

The relationship between combustion chamber pressure and exhaust exit velocity is shown in Figure 2.4. Naturally, the velocity oscillation has the same frequency as the driving pressure force. The phase of this oscillation, however, is shifted in time by one quarter of a cycle. This behavior is the expected outcome according to the momentum equation and has been verified experimentally by Dec et al. (1991).

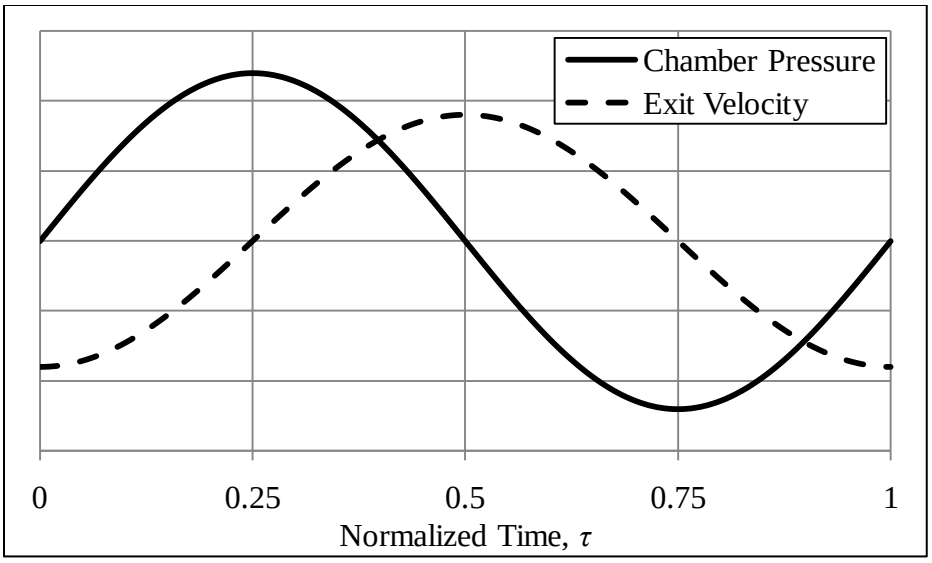

Figure 2.4: Relationship between chamber pressure and exhaust exit velocity.

In order to obtain the periodic behavior outlined in Figure 2.4 heat must be added to the system when $0 < \tau < 0.5$, which is the positive cycle of pressure oscillation (Zinn, 1996). This crucial phase relationship between the communication of heat and the vibration in the resonator is part of the Rayleigh criterion (Lord Rayleigh, 1945), and has been experimentally verified by many investigators (Reuter et al., 1986; Keller et al., 1989; Tang et al., 1995). Pressure variations in the combustor result in gas flow, and therefore cause heat release, volumetric expansion, and nozzle backpressure to fluctuate during the oscillations. In the absence of damping, self sustaining oscillations can occur if the product of the time varying parts of the backpressure and heat release, integrated over one oscillation cycle, is positive. Therefore, the criterion may be stated as

$$\oint \tilde{p}\tilde{q}_{\text{release}} dt > 0, \tag{2.1}$$

where $\tilde{p}$ is the time-varying backpressure and $\tilde{q}_{\text{release}}$ is the time-varying heat release. In essence, conditions are right for supplying energy to reinforce the oscillations if the fluctuating heat release is more in-phase than out-of-phase with the pressure vibration in the resonator. Keller et al. (1989) experimentally showed this relationship to be true for pulse combustors. In this study the amplitude of the heat release was found to be directly related to the pressure amplitude. The strongest oscillations occurred when the heat release and pressure pulsations were completely in-phase with each other, a condition that results in the highest heat release amplitude.

This heat release is supplied by the combustion of the air and fuel reactants. These reactants enter the combustion chamber when $0.5 < \tau < 1$, the negative portion of the pressure oscillation cycle. Therefore, in order to meet the Rayleigh criterion, the combustion reaction (heat release) must be postponed until $0 < \tau < 0.5$. This postponement is the result of three phenomena that occur between initial influx of reactants and final heat release (Keller et al., 1989). These phenomena are the mixing of reactant species with each other, the mixing of these reactants with remnant gases from the previous cycle, and the reaction (combustion) leading to heat release. The processes are bell-shaped functions of time, rather than discrete events, which can overlap. Subsequently, the peak of the heat release must occur during the positive cycle of the pressure oscillation for quasi-stable periodic operation. In general, the mixing of reactant species and combustion products accounts for most of the time delay.

As stated previously, the flow reversal of the tailpipe gases has been shown to greatly affect heat transfer enhancement. Higher levels of flow reversal have been shown to yield significantly higher heat transfer or drying rates (Liewkongsataporn et al., 2006). Thus, it is desirable to have large enough pressure oscillations in the combustion chamber to produce this reversal of the pulsating tailpipe flow. However, the flow parameters of a pulse combustor, such as oscillation frequency, pressure oscillation amplitude, heat release rate, and others, have a nonlinear dependence on each other (Dec and Keller, 1986).

2.3 Pulsating Impingement Jets

Heat transfer due to pulsating impingement jets has been relatively well studied. However, the subset of these studies that employed a pulse combustor to generate the pulsating flow is rather small. The flow characteristics produced by pulse combustors can differ greatly from those of other pulsating impingement jets. These other jets often had small velocity oscillation amplitudes, relatively low frequencies, and in some cases jets that pulsated intermittently rather than a continuously oscillating flow. Additionally, these jets failed to obtain flow reversal, an important factor in heat transfer enhancement. This section discusses both studies that did not have flow reversal and those that did. The studies that focused on impingement jets for which flow reversal was not present are reviewed first, followed by the few studies that did employ flow reversal.

2.3.1 Jets without Flow Reversal

In a numerical investigation, Mladin and Zumbrunnen (1995) showed that interactions between low-frequency and high-amplitude flow pulsations could actually reduce time-averaged Nusselt numbers by up to 16 %. Exhaust flow reversal was not employed in this study. Subsequent experimental work by Mladin and Zumbrunnen (1997) found that local Nusselt numbers (*Nu*) in the nozzle mid-plane increased by up to 12 % and increased by up to 80 % farther away from the centerline. This work utilized a single slot-type nozzle configuration with a rectangular cross section of 5×10^{-3} m by 50×10^{-3} m at the exit. A motor driven ball valve was utilized to produce pulsations in a compressor fed air supply line. As such, the minimum jet velocity was zero, and no reversal of the tailpipe flow was obtained. Additionally, the impingement surface was stationary, and no confinement hood was employed. A similar non-reversing-flow set up was later used by Mladin and Zumbrunnen (2000) to produce comparable experimental results.

Sailor et al. (1999) experimentally investigated an intermittent (rather than pulsating) jet in which a compressor-supplied-flow was cycled on and off with varying duty cycles using a mechanical valve. The apparatus that was used had an unconfined impingement area and a cylindrical nozzle with a diameter of 14×10^{-3} m. The use of the mechanical valve to produce intermittent flows resulted in a minimum velocity of zero rather than a negative value. Hence, flow reversal was not obtained. Heat transfer enhancements exceeding 50 % were obtained for a variety of operating conditions.

However, in this case the hot impingement surface was cooled by the jet rather than heated. Therefore, entrainment of ambient air, which was at a lower temperature than the surface, did not have the same adverse effects that would be encountered in the case of heating a cold surface. In such a case, increased entrainment due to pulsed conditions would decrease the jet temperature and thereby lower heat transfer. Keller et al. (1993) has shown that pulsating jets have significantly higher entrainment rates than steady jets.

Other numerical investigations have also predicted heat transfer enhancement. Poh et al. (2005) calculated Nusselt number enhancement of up to 17 % for water impingement jets with Re = 300, a frequency of 5 Hz, and a nozzle-to-surface spacing of 9 nozzle diameters. These conditions vary greatly from those of pulse combustors and no flow reversal was utilized. These simulations included a confined impingement zone and a circular jet cross section.

The study of pulsating jet arrays has received less attention than that of single impingement jets, despite the more likely use of arrays in industrial applications. Sheriff and Zumbrunnen (1999) used an orifice plate with nine air passages (nozzles) to investigate heat transfer from an array of pulsating jets. A supply line fed air to a motor-driven ball valve to supply oscillating flow to a common plenum. The flow then passed through the orifice plate which had a square array of 6×10^{-3} m diameter circular air passages. Air passage length was 12.7×10^{-3} m and adjacent orifice-to-orifice spacing was 36×10^{-3} m. This arrangement partially confined the flow due to the presence of the orifice plate. There was no observed flow reversal in these channels. The impingement jets were

used to cool a heated test specimen using a Reynolds number range of 2500 to 10000. These non-reversing jets failed to produce enhanced heat flux, even reducing *Nu* by as much as 18 % at the stagnation point compared to steady flows. However, heat transfer farther away from the stagnation point did not show a significant reduction, leading to more uniform cooling of the impingement surface.

A numerical study also investigated heat transfer due to multiple pulsating jets (Chaniotis et al., 2003). This work used a Lagrangian particle methodology, termed Smooth Particle Hydrodynamics (SPH), for the discretization of the governing equations. Pulsed and steady flows from single and dual slot jets were simulated using this method. The jets impinged on a constant heat flux plate, and cooling was compared using the maximum surface temperature. Confinement was employed; however, the maximum Reynolds number used was 533.3. These idealized jets had exit velocity profiles specified as a boundary condition. Parabolic velocity profiles were used in all cases and the centerline velocity was varied sinusoidally with time. The maximum oscillation amplitude was equal to the time-averaged centerline velocity, resulting in a minimum centerline velocity of zero. Thus, no conditions with flow reversal were investigated. The optimum operating conditions were found to be a minimum velocity of zero, a jet exit velocity frequency of 0.31831 Hz, and a resulting average Reynolds number of 133.33. Operating under such conditions, the dual slot pulsed jets produced an 11 % improvement in maximum temperature over comparable steady jets, and a 6 % improvement over a single steady jet with the same flow rate and total slot area.

2.3.2 Jets with Flow Reversal

Experimental and numerical work in the area of pulsating impingement jets with flow reversal is rather limited and has primarily focused on single nozzle systems. Work done at Sandia National Laboratories experimentally demonstrated the potential heat transfer advantages of pulsating jets compared to steady flow when impinging on a stationary surface (Keller et al., 1993). This is one of the few studies that did obtain flow reversal of the exhaust gases. In this study, the pulsating jet was created by a pulse combustor with a round cross section and tailpipe to combustion chamber volume ratio of approximately 1.0. Heat flux was calculated from the surface temperature history by assuming one dimensional heat flux in a semi-infinite solid. A limited number of cases were investigated; however, it was demonstrated that the pulse combustor produced heat transfer enhancement factors as high as 2.3. This enhancement factor was calculated as the ratio of the area averaged heat transfer coefficients for pulsed and steady flows. At the stagnation point (exhaust pipe centerline) the enhancement factor ranged from 1.8 to 2.3 depending on the nozzle to surface spacing. Farther away from the stagnation point the enhancement factors ranged from 1.5 to 2.3, again varying with the nozzle to surface spacing. Heat transfer coefficients were used to partially account for the differences in time averaged exhaust temperatures. This was done because the steady and pulsed flows that were used for the comparison had different temperatures. The pulsating flow had a maximum temperature of 1400 K, but it had a time averaged temperature of only 700 K at a distance 25×10^{-3} m downstream from the tailpipe exit due to entrainment from ambient air. In comparison, the steady flow had an exhaust temperature of 1200 K. A

more direct method of comparison between similar exhaust outflow conditions would be preferable. Additionally, a confinement hood, which is typically present in impingement paper drying and has been shown to produce greater enhancement (Liewkongsataporn et al., 2006), was not utilized in these experiments.

An important feature of this work was the observation of the fluid flow associated with the pulsating jet using schlieren photography and laser Mie scattering. The authors found that the pulsating jet produced key characteristic flow structures in the form of coherent toroidal vortices. These vortices formed around the free jet at the tailpipe exit. Three vortices of varying size were observed. The largest vortex was formed when the tailpipe exit velocity was positive, corresponding to outflow from the tailpipe. This primary vortex propagated away from the stagnation point and even moved downstream during the tailpipe flow reversal. This large, swirling structure led to entrainment of ambient air. Since the ambient temperature was much lower than the jet temperature at the tailpipe exit, the entrainment resulted in a rapid decrease in jet temperature along the axial distance from the tailpipe exit. The second vortex was formed during the later portion of the positive cycle of the exhaust velocity oscillation. This vortex was not only smaller than the primary vortex, but also behaved differently as the oscillation cycle progressed. Unlike the primary one, this secondary vortex did not propagate downstream. Due to the vortexes formation late in the positive cycle, the counter flow of the negative cycle led to this more stationary behavior. The negative portion of the velocity oscillation produced flow patterns at the tailpipe exit similar to a classical sink flow. The fluid entered the tailpipe omnidirectionally as opposed to the unidirectional flow of a free jet.

Finally, a tertiary vortex was observed at the end of the oscillation cycle, but was much weaker than the primary and secondary vortices. This work did not directly correlate the action of the individual vortices with there impact on the heat transfer to the surface.

Liewkongsataporn et al. (2006) experimentally found that paper drying rates produced by a single pulse combustor were higher than comparable steady flow by a factor of 2. This was for a confined case with a nozzle-to-surface distance equal to one nozzle diameter (H/D = 1). Removing the confinement reduced the drying enhancement to a factor of 1.5 for the same value of H/D. Pulsed drying enhancement was lower still for a confined case with H/D = 2. The samples that were tested were circular paper sheets made from bleached softwood pulp. The sheets had a diameter of 0.0762 m and an average basis weight of 0.275 kg/m^2. The pulse combustor used in these experiments had a tailpipe length of 0.2794 m, a tailpipe diameter of 0.0254 m, and a combustion chamber volume to tailpipe volume ratio of approximately 3.6. The drying enhancement was found to increase with increasing velocity amplitude ratio (R_{amp}), the ratio of the velocity oscillation amplitude (U_{amp}) to the mean velocity (U_{mean}). It was found that heat transfer was dependent on the magnitude of the flow reversal, which is directly related to R_{amp}. For this study the maximum value of R_{amp} was 2.6, indicating that flow reversal was achieved. However, the detailed processes that occurred within the sheet were not investigated. Detailed numerical studies were also conducted by Liewkongsataporn et al. (2008). Using a slot-type air jet and impingement confinement and flow reversal, heat transfer was calculated for numerous configurations. The impact of various system parameters was then analyzed and it was calculated that time-averaged surface heat

transfer increased with increasing velocity amplitude. Comparison with steady flow in this study also showed that the improvement in heat transfer was dependent on the velocity ratio of the flow reversal to the mean flow.

In an experimental investigation, Psimas et al. (2007) also found that higher levels of flow reversal produced greater heat flux enhancement. Pulsed flow conditions produced centerline heat flux twice that of steady flow using similar exhaust pipe diameters, combustion chamber geometries, time-averaged mean flow rates, and exhaust exit temperatures. Additionally, heat flux was measured at multiple locations in order to develop approximate heat flux profiles. From these results it was estimated that total heat transfer to a 0.08 m diameter circular section of the impingement surface was up to 59 % higher for the pulsed flow case.

In summary, an important finding is that higher levels of flow reversal tend to produce greater heat flux enhancement factors. The important factors linked to this flow reversal are the oscillation frequency and the ratio of the velocity amplitude to the mean value of the jet velocity. The mechanism responsible for the enhancement is likely the strong recirculating flow of the toroidal vortices. These large, swirling structures appear to be well-organized and an important feature of pulsating jets that obtain tailpipe flow reversal. Unfortunately, the majority of studies relating to pulsating impingement jets employed conditions that were different than those of interest to the current work. Thus far there have been no studies that focus on heat transfer or drying porous media due to impingement from multiple pulse combustor arrays with flow reversal.

2.4 Drying Porous Media

This section presents the relevant work associated with modeling the drying of porous media. This gives background information for the model described in Chapter 7. A porous medium is a complex system often consisting of a solid matrix permeated by a network of fluid filled voids. As a result, modeling the drying of this inherently multiphase system presents unique challenges.

In order to model the simultaneous heat and mass transfer that occurs in a porous medium, the relevant material characteristics must be considered. Simply adapting a diffusion theory model with a linear or nonlinear diffusivity parameter is insufficient for describing the complex transport processes in a porous medium. A common approach is to use conservation laws applied to small representative elements for which properties and characteristics are taken as the volume average. Huang (1979) used these macroscopic conservation laws and the principle of non-equilibrium irreversible thermodynamics to model moisture migration porous wall subjected to a temperature gradient. Combined with liquid and vapor equilibrium conditions, the aforementioned approach produced a set of basic equations for the simultaneous mass and heat transfer within the porous medium. A key finding of this work was that, in addition to diffusion, the capillary forces, which are greatly determined by the structure of the medium, were critical factors in the drying process.

Kaviany and Mittal (1986) employed a similar approach to investigate the drying

of a porous slab initially saturated with liquid. Volume averaged laws of conservation were combined with empirical constitutive relations to model the capillary driven liquid flow in the medium. It was found that the characteristic time, which was the time required for the surface to began to dry, was related to the ratio of the internal liquid transport conductance (Peclet number) to the external vapor transport conductance (Biot number). Additionally, the rate of mass transfer at the surface of the medium was found to strongly depend on the saturation of said surface. A surface saturation coefficient, which was a function of surface geometry and the free stream velocity, was defined. However, this coefficient was determined experimentally. These experiments employed convective heating of a bed of glass beads to determine the requisite empirical relationships. As such, this non-hygroscopic media involved no significant deformation and did not take into account issues faced when drying paper such as shrinkage and other dimensional changes.

Lu and Shen (2007) used a numerical model to predict paper drying due to multiple drying cylinders. A volume averaging approach was employed similar to the one described by Whitaker and Chou (1983). Conservation equations were applied to each of the liquid, vapor, and gaseous species. The primary modes of mass transport within the medium were convection and capillary action for the liquid phase and convection and diffusion for the gas and vapor. The simulation results were compared with data from the dryer section of a paper machine, and it was also shown that heat and mass transfer forecasts were in line with experimental results. Numerical predictions deviated only 4 % from the experimental values. Other specific aspects of the mass transport inside a paper

sheet, such as diffusion and characteristics of diffusivity parameters (Ramarao et al., 2003) and mechanical pressing (Nilsson and Stenström, 2001), have also been studied in detail. Additionally, Weineisen and Stenström (2005) modeled the effects of pore size distribution on through-air-drying of tissue using heat and mass transfer correlations for flow through cylindrical conduits and packed fiber beds.

Karlsson and Stenström (2005) developed a general, dynamic model describing the drying mechanisms of paper to predict temperature, moisture, and pressure profiles in the sheet. The main mode of heat transfer to the sheet was conduction from a heated cylinder. However, it was concluded that although assuming a saturated vapor phase is an excellent approximation for most applications, it may not be valid for drying methods in which hot air is forced through the sheet. In subsequent work, Karlsson and Stenström (2005) demonstrated good experimental agreement with the numerical findings, despite this saturated vapor phase approximation. A key feature of this model is that it included sheet shrinkage.

Materials for which shrinkage during drying is important require additional considerations compared to rigid materials. Katekawa and Silva (2006) provide an overview of these considerations and commonly used modeling techniques. One approach to including shrinkage affects is the domain adaptation method. This method accounts for deformation in the mathematical resolution of the problem, instead of the actual modeling stage. Empirical shrinkage models and phenomenological laws first require experimental drying tests. Hence, modeling can only occur after such

relationships are established. Therefore, this approach is more accurately a fitting or interpolation method rather than a predictive model.

A somewhat different approach was taken by Yang et al. (2001). This study used a simultaneous heat and moisture transfer model which was coupled with the principle of virtual work to account for shrinkage deformation during drying. Equations for the internal stress field were developed using the familiar strain-displacement and stress-strain relations. The principle of virtual work was used to supply an equilibrium equation. The resulting mathematical model showed reasonable agreement with experimental data for the prediction of moisture content, temperature, shape, and stress in a cylindrical potato sample.

Unfortunately, studies of porous media drying as a result of pulsating impingement jets are limited. Islam et al. (2003) used a liquid diffusion model to analyze drying due to intermittent parallel convective air flow. It was assumed that evaporation occurred only at the surface subjected to convective heat and mass transfer by the parallel air flow. Therefore, no phase change occurred within the drying material and internal vapor phase moisture transfer was negligible. The material was also modeled as having no voids or trapped air. The drying rate was assumed to be governed by conductive heat transfer and diffusion liquid moisture transfer within the solid. Despite these simplifications, the model showed good agreement with experimental results for drying of potato slabs due to steady and square wave intermittent air flows.

In summary, drying porous media involves simultaneous heat and mass transfer. Capillary effects are a critical driving force in the transport of the liquid species. The volume averaging approach has shown good agreement with experiment for non-hygroscopic materials and for paper products. Finally, shrinkage effects add complexity to the model and often require empirical fitting parameters.

CHAPTER 3

LABORATORY HEAT FLUX EXPERIMENTS

3.1 Introduction

Laboratory heat flux tests were conducted using pulsed and steady flow conditions for both single and multiple jet configurations. Aside from investigating the heat transfer characteristics and performance impact of pulse combustor impingement jets, these tests fulfilled three main needs. First, they were used to validate the results from the numerical simulations. Second, they aided in determining the limits of the two dimensional simplifications used in the modeling. This added validity to the modeling work and helped guide sample size selection for the drying tests. Third, heat flux tests provided a more detailed description of the heat transfer processes when compared to drying tests. This is because heat flux tests offered spatial and temporal resolutions that far exceeded those of the bulk drying tests. Additionally, these trials provided a point of reference for the drying experiments, allowing for comparisons with other heat flux studies.

3.2 Numerical Technique

3.2.1 Background and Motivation

The most common methods for determining convective heat flux are: 1) temperature difference measured over a given spatial distance with known thermal resistance, 2) temperature difference in a body with known thermal capacitance measured over time, 3) energy input or output directly measured, or 4) the temperature gradient in the fluid adjacent to the surface measured if the fluid properties are known. The last two of these categories were not actively pursued as they were deemed ill-suited to the demands of this project. A method involving the direct measurement of energy input or output does not have the response time needed for describing the phenomena of interest in this work. Obtaining heat flux by measuring the temperature gradient in the fluid adjacent to the surface is inadequate for high fluid velocities and large temperature gradients, which are both produced by pulse combustors.

Techniques utilizing a spatial temperature difference involve measuring the temperature close to the surface at two points separated by a thin material. Layered gages are the simplest form and rely on measuring the temperature on both sides of a thermal resistance layer. At steady state the difference in temperature readings is proportional to the flux into or out of the surface. In a transient system, however, an additional storage term exists which affects the gages ability to accurately measure the true heat flux. Although these gages are simple, they suffer from slow response times. Reducing the resistance layer thickness aids in lessening response time but also adds complexity to

practical sensor designs. Additionally, the thickness and thermal conductivity of the resistance layer, along with the operational temperature range, impact the sensitivity of these gauges.

The other category of heat flux measurement techniques involves recording temperature change with time and using an inverse mathematical scheme to calculate surface heat flux (Holmberg and Diller, 1995). One such gage is the slug calorimeter which measures the amount of energy absorbed by a small known mass as a function of time (Diller, 1993). This mass is embedded in the surface with surrounding insulation and is assumed to be of uniform temperature; therefore, only one temperature measurement is required. This assumption is only valid if the thermal resistance of the mass is extremely low. Even with low thermal resistances, however, the isothermal assumption can introduce significant error. Additionally, the inclusion of the mass adversely affects response time.

Alternatively, coaxial thermocouple type gages measure the transient temperature of a very thin connecting film. Under certain conditions, one can assume this film temperature is the same as the surface temperature. The surface temperature history can then be used to calculate heat flux at the surface (Sanderson and Sturtevant, 2002). One of the principal advantages of this method is that thermocouples can be relatively small, increasing positioning accuracy and reducing thermal mass. These gauges can also be positioned so that there is minimal disruption of the fluid flow field. Consequently, this was the method utilized for the current work.

3.2.2 Derivation

The physical basis for the derivation of the numerical technique is that a large block, initially at a uniform temperature, is instantaneously subjected to heating by the impingement jet. A schematic of this is provided in Figure 3.1.

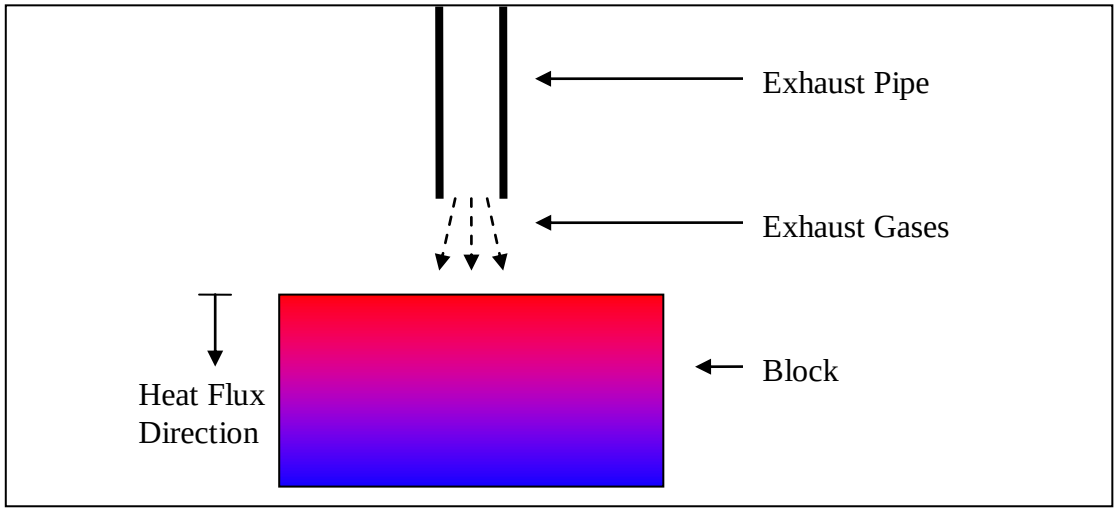

Figure 3.1: Schematic of the physical basis of the model.

In order to simplify the analysis, the block is modeled as a semi-infinite solid, as this case is well documented and allows analysis to be performed in only one dimension. This approach, as developed by Ahrens and Åström (1986) and Ahrens (1983), requires not only uniform initial block temperature, but also a thermal penetration depth that is less than the block thickness in the direction of heat flow. Additionally, a large area must be exposed to heating by the burner to reduce radial heat flow. Further consequences and limitations of the semi infinite approximation will be discussed later.

For a semi-infinite solid, the fundamental solution for a step change in the surface temperature of the block is (Ahrens, 1983)

$$U(x,t) = \frac{T(y,t) - T_{step}}{T_{initial} - T_{step}} = \frac{2}{\sqrt{\pi}} \int_0^{\xi} e^{-\frac{\xi^2}{2}} d\xi \tag{3.1}$$

where

$$\xi = y \sqrt{\frac{\rho_b c_p}{\lambda_b t}} . \tag{3.2}$$

In these equations $T_{initial}$ is the initial block temperature, T_{step} is the surface temperature of the block after the step change, and $T(y,t)$ is the temperature of a plane located a distance y from the surface at time t.

For a continuously varying surface temperature, Duhamel's theorem yields

$$T(x,t) - T_{initial} = \int_0^t [1 - U(y, t - t')] \frac{d(T_s - T_{initial})}{dt'} dt' , \tag{3.3}$$

where T_s is the time varying block surface temperature and $(t - t')$ represents a shift in time (Ahrens, 1983). Assuming constant thermal properties of the block, the surface heat flux, $q_s''(t)$, is simply

$$q_s''(t) = -\lambda_b \frac{dT}{dy}\Big|_{y=0} . \tag{3.4}$$

Combining equations (3.3) and (3.4) produces

$$q_s''(t) = -\lambda_b \frac{\partial}{\partial y}\left\{\int_0^t [1 - U(0, t-t')] \frac{d(T_s - T_{initial})}{dt'} dt' + T_{initial}\right\}$$

$$= -\lambda_b \frac{\partial}{\partial y}\left\{\int_0^t \frac{d(T_s - T_{initial})}{dt'} dt' - \int_0^t U(0, t-t') \frac{d(T_s - T_{initial})}{dt'} dt' + T_i\right\}$$

$$= -\lambda_b \frac{\partial}{\partial y}\left\{\int_0^t \frac{\partial}{\partial y} \frac{d(T_s - T_{initial})}{dt'} dt' - \int_0^t \left[\frac{\partial}{\partial y} U(0, t-t')\right] \frac{dT_s}{dt'} dt' + \frac{\partial T_{initial}}{\partial y}\right\} . \tag{3.5}$$

The first and last terms are equal to zero, leading to

$$q_s''(t) = \lambda_b \int_0^t \left[\frac{\partial}{\partial y} U(0, t-t')\right] \frac{dT_s}{dt'} dt' . \tag{3.6}$$

Using the fundamental solution given in equations 3.1 and 3.2 with x set to zero and $(t - t')$ substituted for t, equation 3.6 becomes

$$q_s''(t) = \lambda_b \int_0^t \left[\frac{\partial}{\partial y} \operatorname{erf}\left(y \sqrt{\frac{\rho_b c_p}{\lambda_b (t-t')}}\right)\right] \frac{dT_s}{dt'} dt'$$

$$= \lambda_b \int_0^t \sqrt{\frac{\rho_b c_p}{\pi \lambda_b (t-t')}} \frac{dT_s}{dt'} dt'$$

$$= \sqrt{\frac{\lambda_b \rho_b c_p}{\pi}} \int_0^t \sqrt{\frac{1}{(t-t')}} \frac{dT_s}{dt'} dt' . \quad (3.7)$$

At a given time, t_m, equation 3.7 may be discretized in the following manner for numerical implementation:

$$q_s''(t_m) \approx \sqrt{\frac{\lambda_b \rho_b c_p}{\pi}} \sum_{i=1}^{m-1} \left(\frac{dT_s}{dt'}\right)_i \int_{t_i}^{t_{i+1}} \frac{dt'}{\sqrt{(t-t')}} . \quad (3.8)$$

Equation 3.8 can be further simplified by means of the approximation

$$\left(\frac{dT_s}{dt'}\right)_i \approx \frac{(T_{s,i+1} - T_{s,i})}{\Delta t} , \quad (3.9)$$

which yields

$$q_s''(t_m) \approx \frac{1}{\Delta t} \sqrt{\frac{\lambda_b \rho_b c_p}{\pi}} \sum_{i=1}^{m-1} (T_{s,i+1} - T_{s,i}) \int_{t_i}^{t_{i+1}} \frac{dt'}{\sqrt{(t-t')}} \quad (3.10)$$

where Δt is the time step of the numerical method. The final equation for numerical implementation is

$$q_s''(t_m) \approx \frac{2}{\Delta t} \sqrt{\frac{\lambda_b \rho_b c_p}{\pi}} \sum_{i=1}^{m-1} (T_{s,i+1} - T_{s,i}) \left(\sqrt{t_m - t_i} - \sqrt{t_m - t_{i+1}}\right) . \quad (3.11)$$

This equation describes surface heat flux at each time step as a function of time, system parameters (λ_b, ρ_b, c_p, Δt), and surface temperatures. Thus, one needs only the temperature history of the surface to calculate heat flux for a given set of system parameters. The indices used in equation 3.11 are outlined in Figure 3.2.

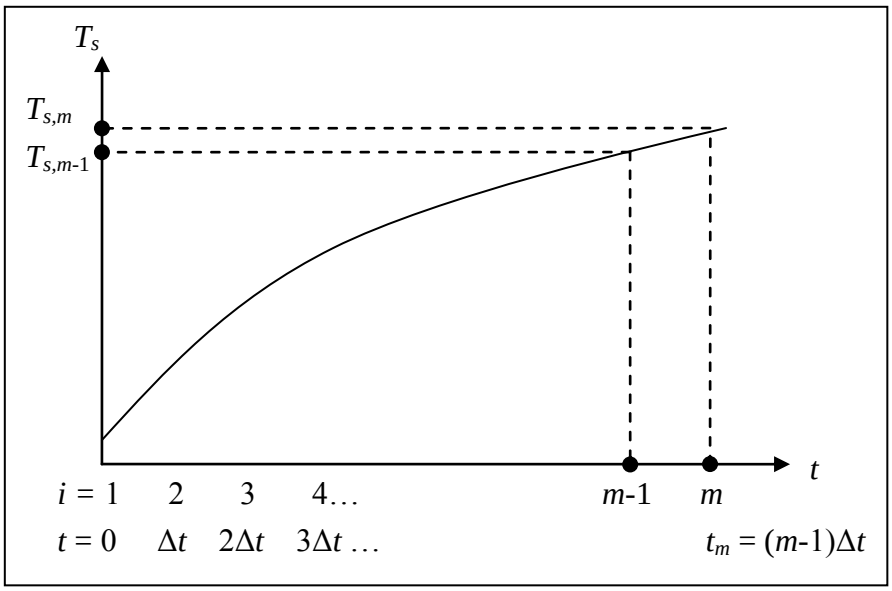

Figure 3.2: Overview of the indices used in the numerical model.

3.2.3 Performance

A constant heat flux test case was used to evaluate the model's performance as this case is well defined. The surface temperature behavior associated with constant surface heat flux is

$$T(0,t) - T_{initial} = 2q_o^{''}\sqrt{\frac{t}{\pi\lambda_b\rho_b c_p}}, \tag{3.12}$$

where $q_o^{''}$ is a prescribed constant heat flux (Ahrens and Åström, 1986). For model verification, the system parameters were assigned values based on typical real-world values of steel. These values are given in Table 3.1.

Table 3.1: Summary of values used in the assessment of the model's performance.

Parameter	Value
ρ_b	7.92×10^3 kg/m^3
c_p	456 J/kg·K
λ_b	55 W/m·K
$T_{initial}$	300 K
$q_o^{''}$	2.3×10^5 W/m^2
Δt	1.0×10^{-4} s

The system performance is summarized in Table 3.2 and an enlarged plot of the predicted and actual values is provided in Figure 3.3.

Table 3.2: Summary of system rise time.

Criterion	Time Steps
99 %	3
99.9 %	9
99.99 %	38

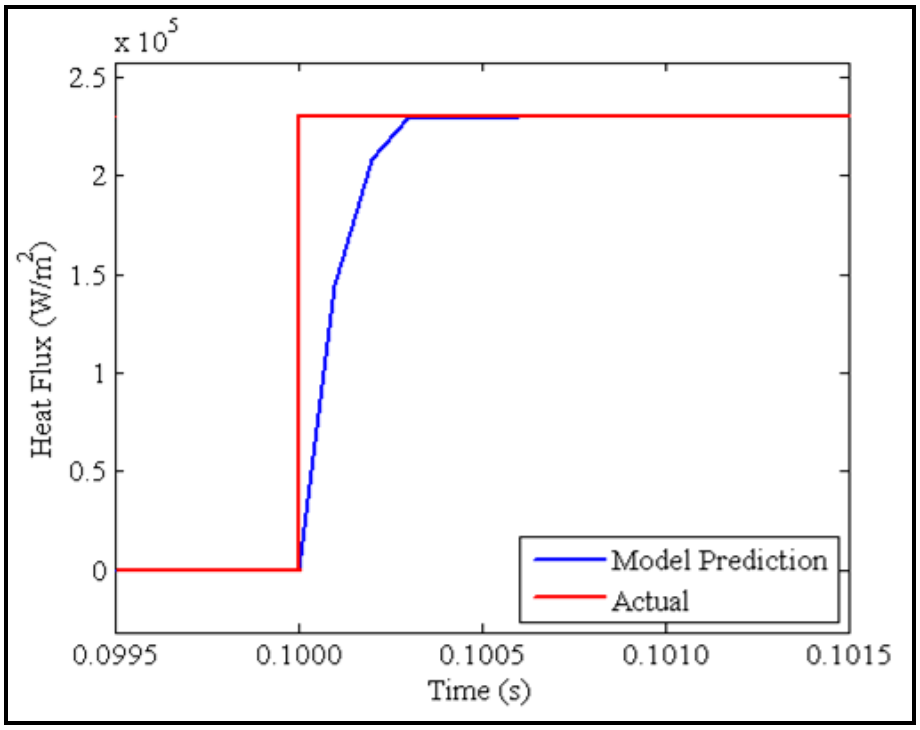

Figure 3.3: Comparison of predicted and theoretical values for step change in heat flux.

As Table 3.2 shows, the model computed heat flux to within 1% of the actual value in only 3 time steps. No overshoot was present and similar results were obtained for heat flux ranging from 1×10^{2} W to 1×10^{6} W and time step increments from 1.0×10^{-4} s to 1 s.

3.2.4 Implementation

Using the above described method to determine heat flux requires surface temperature to be accurately measured in a manner that does not violate the assumptions made during the derivation. Primary among these is the one dimensional heat flux approximation. Due to their small size, geometry, and low thermal mass, fast response

coaxial thermocouples are ideal for this application. One such thermocouple is the Medtherm TCS-061-J-4-CR-TGS2-B2CSR-BBT, which has a response time of 1×10^{-6} s and surface area for thermal measurement of less than 1×10^{-6} m^2. This is the exposed surface area of the instrument package, with the thermocouple junction being much smaller. The experimental apparatus consisted of three of these thermocouples embedded in a steel block such that their thermal measurement surfaces were coplanar with the heat transfer surface (i.e. the top of the block). The measurement surfaces were also collinear, with 2 cm spacing between them. A schematic of the experimental apparatus is given in Figure 3.4 with relevant block dimensions and thermocouple orientation

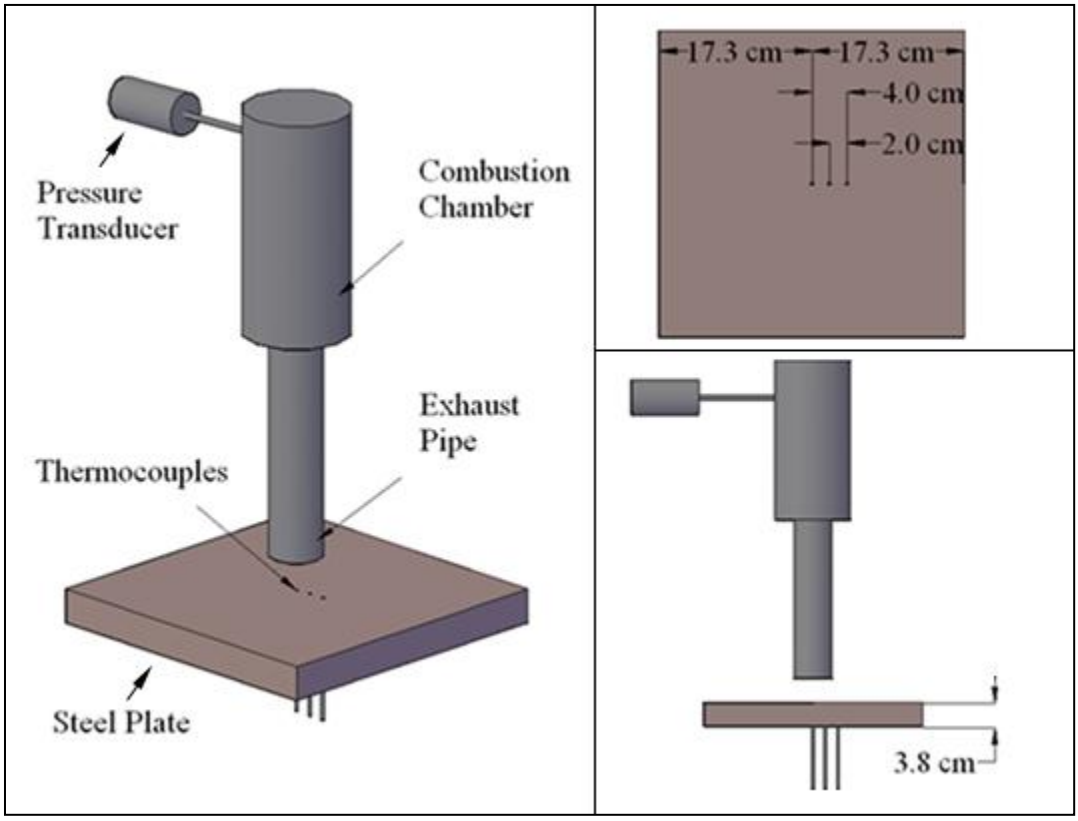

Figure 3.4: Schematic of heat flux plate used in experimental trials.

Steel was used as the block material because it has thermal properties similar to those of the thermocouples. The result is that virtually no temperature gradients existed in planes parallel to the heat transfer surface for the small neighborhood surrounding each thermocouple. This, in effect, eliminates radial heat flows and bolsters the one dimensional heat flux assumption. A similar effect could be obtained by using a thermal insulator for the block material; however, steel was chosen due to its advantageous surface properties (smoothness and flatness) and ease of thermocouple mounting. Three thermocouples were employed to aid in obtaining heat flux data as a function of radial distance from the exhaust pipe centerline axis during the stationary trials.

3.3 Stationary Surface Trials

The heat flux trials can be divided into two main groups: cases with a stationary impingement surface and cases involving a moving impingement surface. The stationary cases utilized a single round nozzle while the moving impingement surface cases employed either one or three slot-shaped nozzles. In all cases, however, a flame hood was placed around the exhaust pipe to add confinement for the hot exhaust gases.

3.3.1 Apparatus and Procedure

For the stationary impingement surface trials, thermal insulation was first placed on top of the heat flux plate. This combination was then positioned such that the thermocouple in the center of the plate was inline with the exhaust pipe center axis. The

insulation was removed approximately 1 s after data sampling was initiated. Thermocouple output and pressure transducer readings were recorded in μv and v, respectively, using an IOtech Personal DAQ-3000 data acquisition system. Sampling rates were between 4 and 10 kHz and data were collected for 5 s. Fuel (propane) and air volumetric flow rates were manually recorded before and after each trial. The plate was allowed to cool and equilibrate before subsequent trials were conducted. A diagram of the experimental setup for these trials is given in Figure 3.5. The spark plug shown in Figure 3.5 was used only to start the combustor, not to maintain combustion or to regulate the operational frequency.

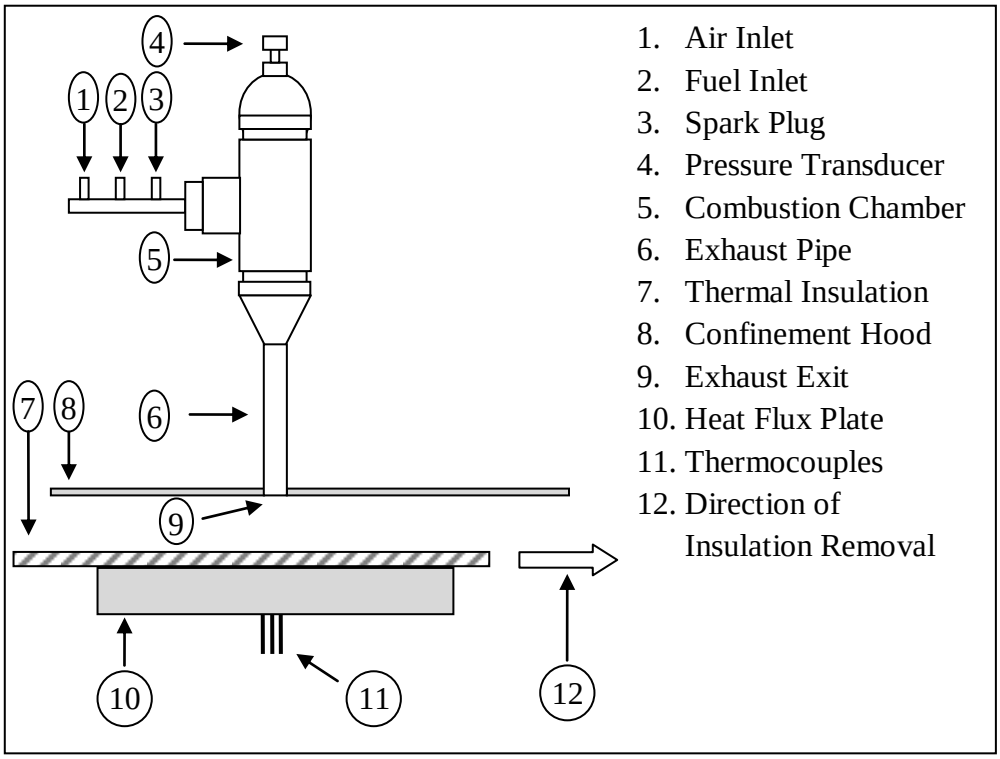

Figure 3.5: Diagram of experimental setup for stationary surface trials.

The combustor dimensions and geometrical arrangement used in the stationary impingement surface cases are given in Table 3.3. For consistency, the tailpipe region is defined as the portion with uniform cross section. The combustion chamber therefore includes any transitional pieces.

Table 3.3: Configuration employed in stationary impingement trials.

Parameter	Value
L_{cc}	0.305 m
D_{cc}	0.051 m
L	0.305 m
D_h	0.025 m
H	0.025 m
H/D_h	1
U_{surface}	0 m/s

Indicated air and fuel volumetric flow rates were corrected for pressure drop and specific gravity using

$$Q_{\text{actual}} = Q_{\text{indicated}} F_{SG} \sqrt{\frac{\Delta P + P_{atm}}{P_{atm}}}, \tag{3.13}$$

where Q_{actual} is the true volumetric flow rate and $Q_{\text{indicated}}$ is the measured value

(Omega, 2001). The pressure drop, ΔP, was also recorded for each trial. The specific gravity correction factor, F_{SG}, is 0.80 for the measurement of propane fuel flow on an air-calibrated gauge (Omega, 2001).

3.3.2 Sample Case

In the following section a sample case is discussed in detail. This provides an overview of the methods used in the data analysis as well as a demonstration of the typical values encountered during the stationary tests. Although not presented for the sake of brevity, similar analyses were performed for all trials.

3.3.2.1 Operational Conditions

The pertinent operational conditions for the sample case are given in Table 3.4. It should be noted that this is the only stationary trial in which the ratio H/D_h is 1.6. For all other stationary cases the ratio H/D_h is equal to 1, corresponding to the value given in Table 3.3.

Table 3.4: Operational conditions for sample case.

Parameter	Value
ΔP_{air}	3.10×10^{5} Pa
ΔP_{fuel}	2.76×10^{4} Pa
$\dot{\overline{m}}_{air}$	4.2×10^{-3} kg/s
$\dot{\overline{m}}_{fuel}$	2.8×10^{-4} kg/s
H	0.04 m
H/D_h	1.6
T_{exit}	900 K
Sampling Rate	1×10^{4} Hz

A portion of the pressure data for the sample case is given in Figure 3.6. The graph displays combustion chamber pressure as measured by the pressure transducer over a 0.05 s interval.

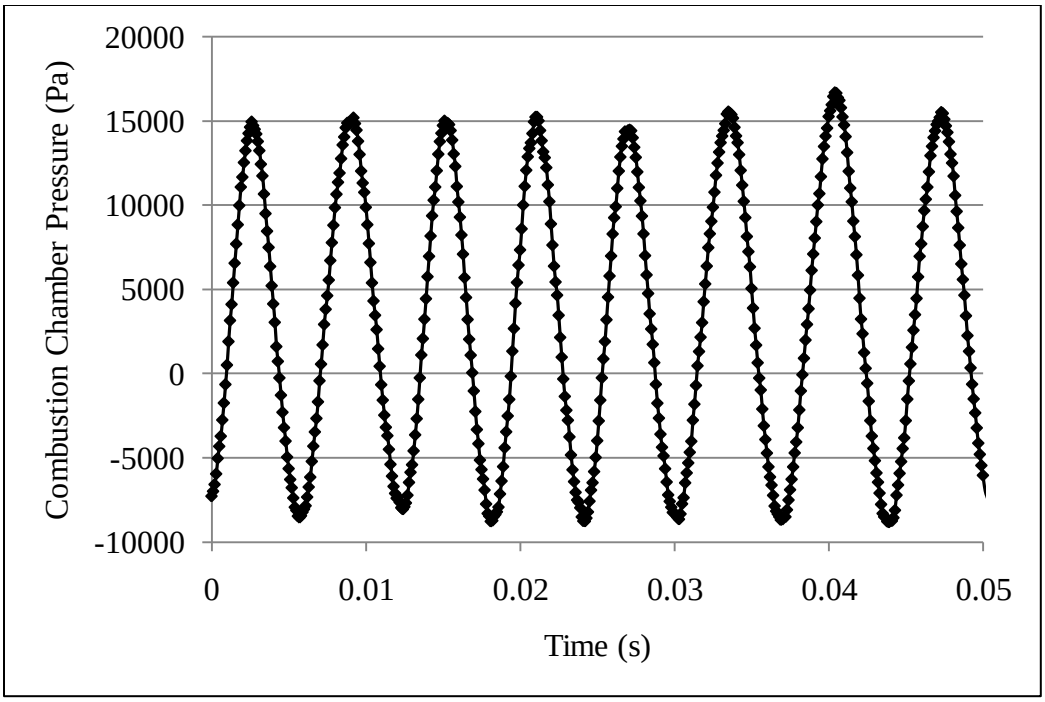

Figure 3.6: Portion of combustion chamber pressure data for sample case.

The pressure data was analyzed using a simple Matlab program. This program uses a fast Fourier transform to produce the single sided amplitude spectrum of the pressure signal. Figure 3.7 and Figure 3.8 display the amplitude spectrum of the combustion chamber pressure oscillations produced in the sample case. The primary frequency and corresponding period are obtained from this data. A summary of these results are presented in Table 3.5, along with the average combustion chamber pressure amplitude.

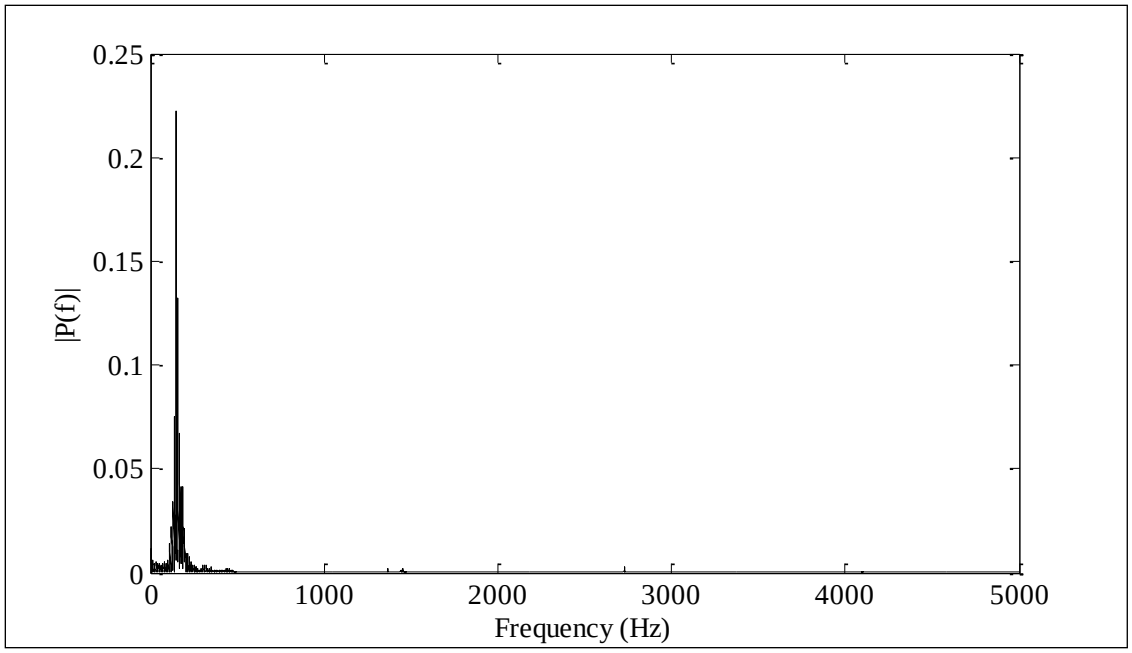

Figure 3.7: Single sided amplitude spectrum of pressure data for the sample case.

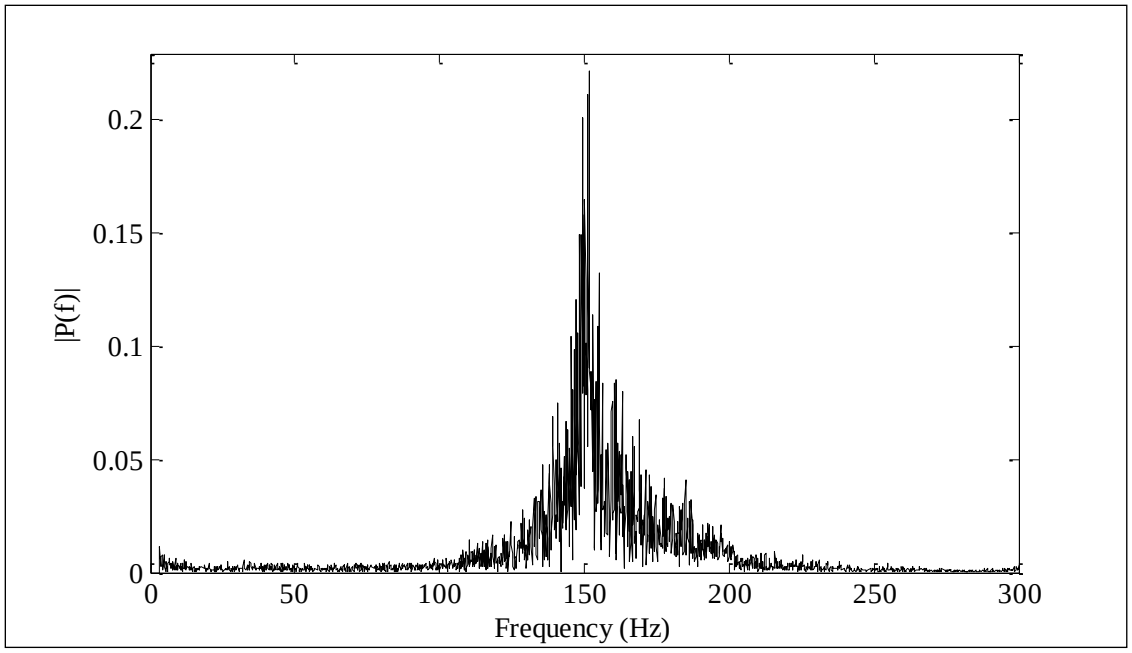

Figure 3.8: Portion of amplitude spectrum highlighting the primary frequency.

Table 3.5: Chamber pressure oscillation characteristics for the sample case.

Characteristic	Value
Major Frequency	151.67 Hz
Major Period	6.59×10^{-3} s
Average Amplitude	1.22×10^{4} Pa
Mean Pressure	3.10×10^{3} Pa

3.3.2.2 Temperature and Heat Flux

The temperature data for the sample case is shown in Figure 3.9 and Figure 3.10. In each figure data is presented for three different values of radial distance, r, from the exhaust pipe center axis. Figure 3.9 gives an overall view of the temperature trend while Figure 3.10 serves to highlight the severity of the signal noise. Figure 3.10 also shows the similarity in signal noise that occurs before and after insulation removal. This indicates that the noise was, in fact, a symptom of the experimental apparatus, rather than an indication of any trends in the data due to the velocity pulsations.

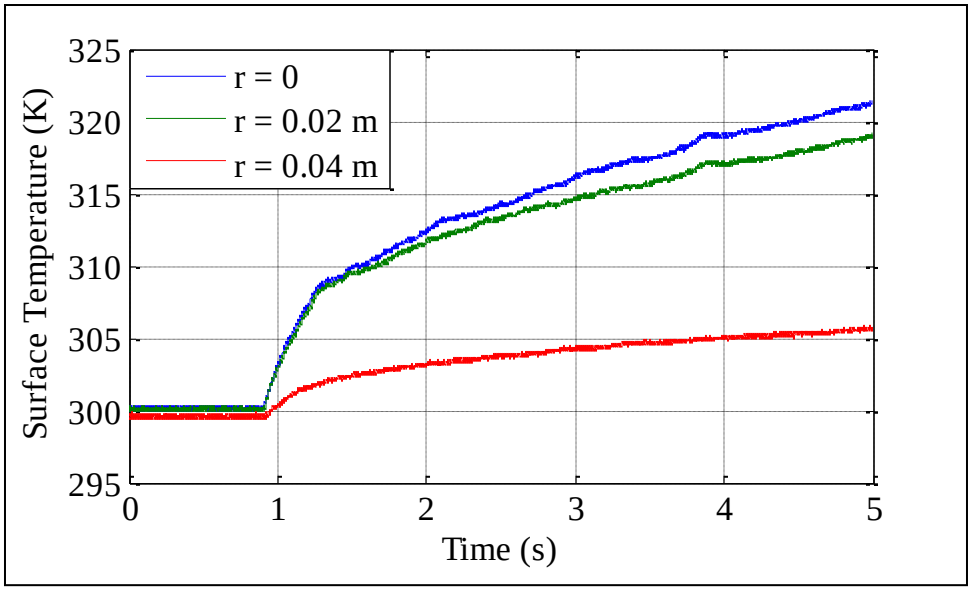

Figure 3.9: Temperature data for sample case at three different values of r.

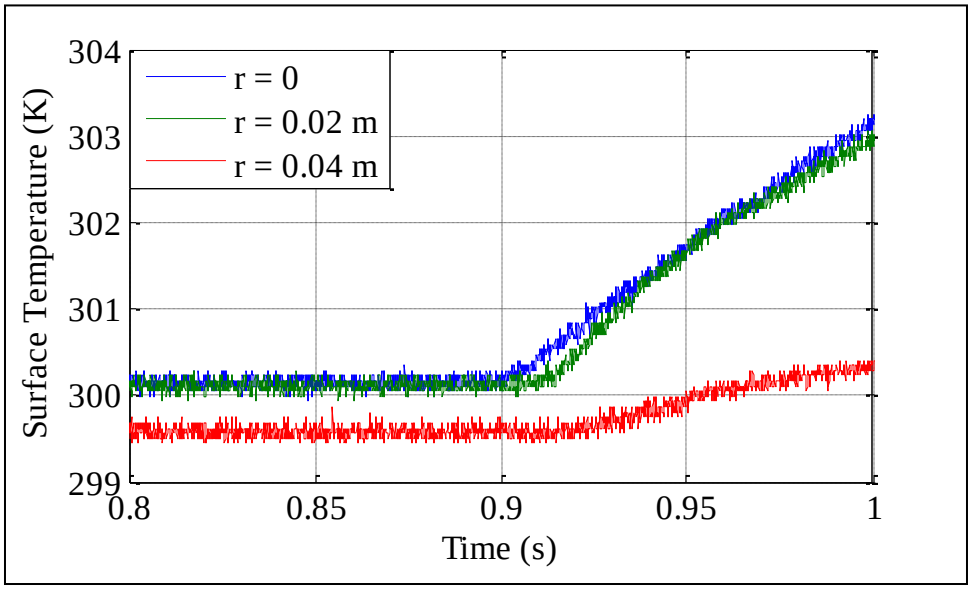

Figure 3.10: Portion of temperature data for sample case highlighting system noise.

The small temperature offset in the reading at r = 0.04 m is attributable to variations in thermocouple instrumentation. It is not expected to affect the heat flux results since heat flux was calculated from temperature variations over time at a single

location. A small temperature offset does not impact these calculations.

The same Matlab program used to obtain the single sided amplitude spectrum for the pressure data was used to analyze the frequency characteristics of the temperature data. Figure 3.11 shows the complete results for the sample case at r = 0. This plot demonstrates the significant impact of high frequency signal noise.

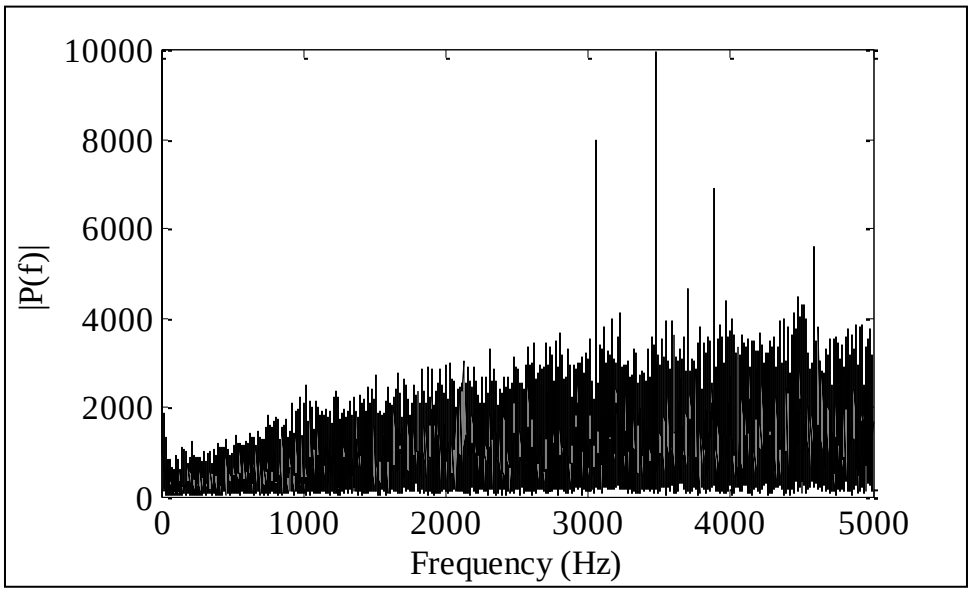

Figure 3.11: Amplitude spectrum showing high frequency noise in temperature data.

Figures 3.12, 3.13, and 3.14 show a portion of the amplitude spectrum highlighting the primary pulse frequency of 151.67 Hz for r = 0.00 m, r = 0.02 m, and r = 0.04 m, respectively. The effect is strongest at r = 0.02 m, somewhat diminished at r = 0.00 m, and barely perceptible at r = 0.04 m.

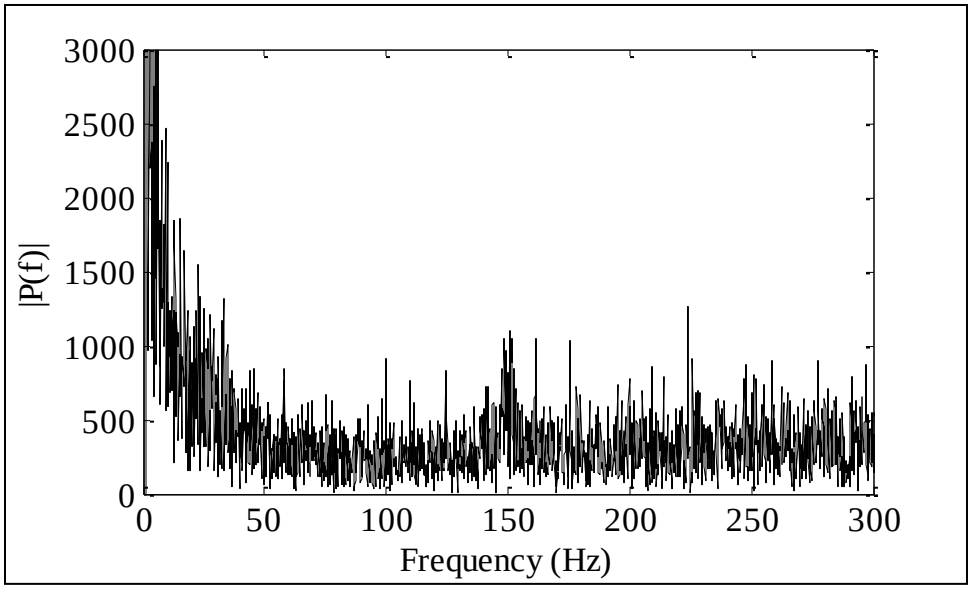

Figure 3.12: Portion of amplitude spectrum highlighting main frequency for r = 0.00 m.

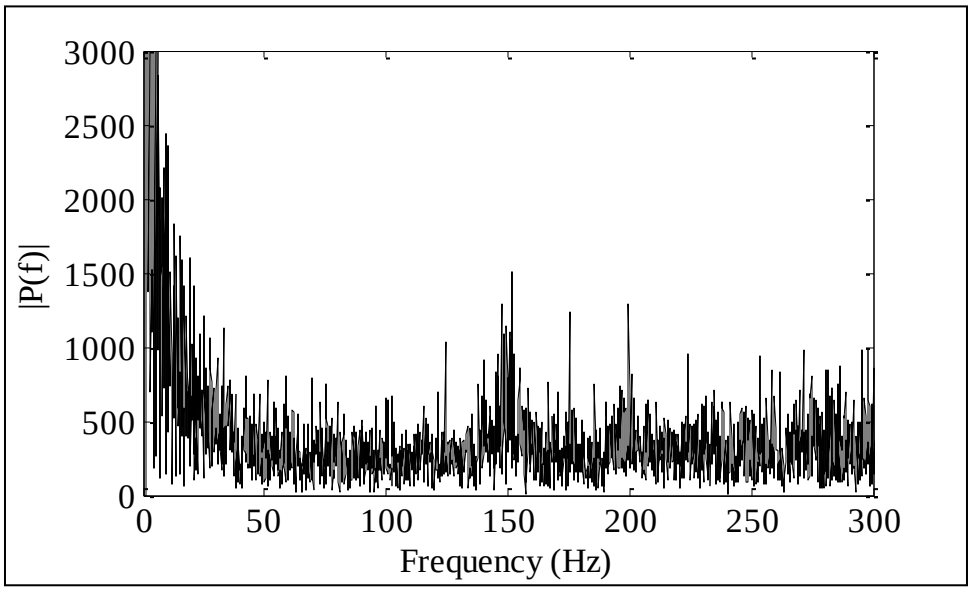

Figure 3.13: Portion of amplitude spectrum showing main frequency for r = 0.02 m.

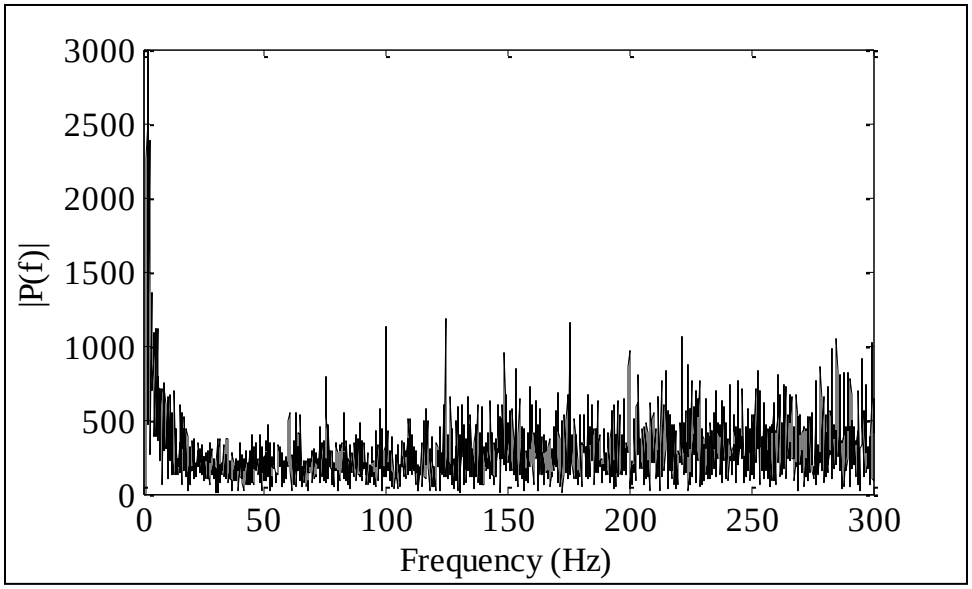

Figure 3.14: Portion of amplitude spectrum showing main frequency for r = 0.04 m.

In order to discern the pertinent trends from the data, a digital filter was employed in Matlab. More specifically, a linear, finite impulse response, low pass filter of order 100 was implemented with a windowing function design based on the Hamming window. The inverse numerical technique previously described was combined with this filtering method to calculate surface heat flux. The resulting heat flux is given in Figure 3.15.

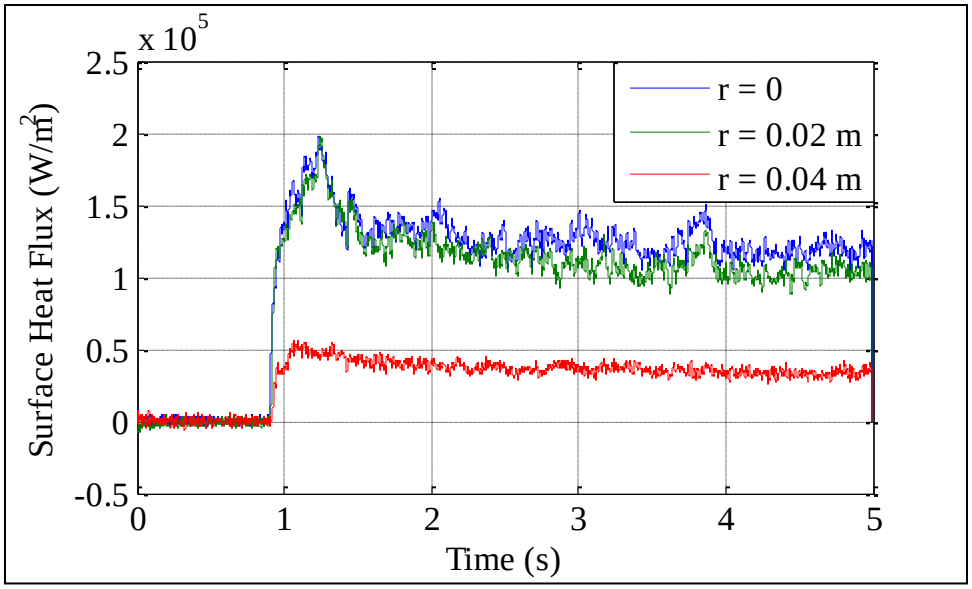

Figure 3.15: Calculated heat flux for sample case at three different values of r.

The large spike in heat flux after insulation removal is attributed to the temporary conditions produced by the shorter nozzle to surface gap due to the insulation thickness. Additionally, Figure 3.15 shows that the block is heated relatively uniformly in the range r = 0.00 m to r = 0.02 m, however, between r = 0.02 m and r = 0.04 m the heat transfer dropped significantly. These trends are presented quantitatively in Table 3.6.

Table 3.6: Summary of heat flux data for sample case.

r	q_s''
0	1.16×10^5 W/m^2
0.02 m	1.02×10^5 W/m^2
0.04 m	3.40×10^4 W/m^2

3.3.3 Results

Analyses similar to those presented in the sample case were performed for 13 additional stationary surface cases. The flow conditions and resulting surface heat flux at the stagnation point (r = 0.00 m) are summarized in Table 3.7. The velocity amplitude ratio, R_{amp}, was calculated using a simplified incompressible flow model developed by Ahrens (1979). Along with the data for each individual case, Table 3.7 provides the averages for trials conducted with similar exhaust outflow conditions. For example, cases HF1, HF2, and HF3 were steady flow cases with similar mean mass flow rates and exhaust pipe exit temperatures. The average value of $q_s^{''}|_{r=0}$ for this set of conditions was found to be 6.65×10^5 W/m^2. The results of similar calculations are also given for the group HF4-HF7 and the group HF9-HF11. These trials showed excellent repeatability with a maximum deviation from the average value of $q_s^{''}|_{r=0}$ of only 4.8 %, which occurred in case HF7.

Table 3.7: Summary of heat flux data for stationary surface cases.

Case	ω	R_{amp}	$\overline{\dot{m}}$	$\overline{T}_{exit}$	$q_s^{''}\|_{r=0}$
-	(Hz)	-	(kg/s)	(K)	(W/m^2)
HF1	-	-	4.5×10^{-3}	1327	6.62×10^{5}
HF2	-	-	4.5×10^{-3}	1327	6.84×10^{5}
HF3	-	-	4.5×10^{-3}	1327	6.50×10^{5}
Average	-	-	4.5×10^{-3}	1327	6.65×10^{5}
HF4	-	-	6.6×10^{-3}	1425	1.07×10^{6}
HF5	-	-	6.6×10^{-3}	1425	1.08×10^{6}
HF6	-	-	6.6×10^{-3}	1425	1.07×10^{6}
HF7	-	-	6.6×10^{-3}	1425	1.14×10^{6}
Average	-	-	6.6×10^{-3}	1425	1.09×10^{6}
HF9	-	-	6.6×10^{-3}	1150	5.90×10^{5}
HF10	-	-	6.6×10^{-3}	1150	5.87×10^{5}
HF11	-	-	6.6×10^{-3}	1133	5.91×10^{5}
Average	-	-	6.6×10^{-3}	1144	5.90×10^{5}
HF8	-	-	4.5×10^{-3}	922	3.17×10^{5}
HF12	152	3.37	4.5×10^{-3}	922	4.06×10^{5}
HF13	177	3.70	6.6×10^{-3}	1144	7.73×10^{5}

3.3.4 Discussion

The experiments HF8 and HF12, had similar time-averaged exhaust outflow conditions ($\dot{\overline{m}}$ and $\overline{T}_{exit}$), despite being steady flow and pulsed flow cases, respectively. This allows for a direct comparison to be made between steady and pulsed flow. In order to quantify the heat flux improvement produced by the pulsations, a heat flux enhancement factor, E_{HF} , was calculated for these trials. This dimensionless factor is the ratio of the heat flux in the pulsed flow case to that produced by the complimentary steady flow case. E_{HF} is 1.28 for cases HF8 and HF12, indicating a slight performance advantage for the pulsed flow. Similar comparisons can be made between the steady flow cases HF9-HF11 and the pulsed flow of HF13. The average value of E_{HF} for these cases is 1.31, indicating a similar improvement in heat transfer performance.

3.4 Moving Surface Trials

Moving impingement surface heat flux trials were conducted not only to study a different boundary condition, but also to provide a more detailed description of heat flux as a function of position. The nozzle configurations were also different in the moving surface trials when compared to the stationary cases. Single and triple slot-shaped nozzles were employed during these experiments instead of circular nozzles. Additionally, for each nozzle configuration, all experimental trials centered on only one time-averaged exhaust exit temperature, mass flow rate, and surface velocity. Given these parameters, the flow was either steady or pulsed. Since this was the only parameter that was altered, a

direct comparison could be made when investigating the impact of the pulsations.

3.4.1 Preliminary Work

In order to highlight the differences in performance between pulsed and steady flow, the pulse combustors must produce adequate pressure and velocity oscillations. This is because the velocity amplitude ratio (R_{amp}) appears to be a key predictor of heat flux enhancement (Liewkongsataporn et al., 2008). The combustion chamber and exhaust pipe combination acts as an acoustic resonator. Therefore, the pulse characteristics are principally determined by the geometry of these parts. Air and fuel flow rates also influence the oscillation frequency of the combustor, albeit to a lesser degree (Kudra et al., 2003). Given that mechanical valves were not employed, the principle method of altering R_{amp} remained the physical geometry of the combustor. However, since the detailed design and optimization of the burner was not the focus of this work, the process of finding a suitable burner design was limited to determining the ideal tailpipe length for the combustion chamber and exhaust pipe cross section used. As a result, the geometric configuration that was employed consisted of a rectangular slot exhaust pipe 80.3×10^{-3} m in depth and 6.4×10^{-3} m in width for a cross sectional area of 5.1×10^{-4} m^2. The results of these trials are presented in Table 3.8.

Table 3.8: Operational characteristics of 5 different tailpipe lengths.

Case	L	$\dot{\overline{m}}$	TA	ΔP_{pk-pk}	ω	T_{exit}	T_{cc}	$\overline{U}_{exit}$
-	(m)	(kg/s)	(%)	(Pa)	(Hz)	(K)	(K)	(m/s)
TL1	0.356	2.25×10^{-3}	1.15	2.41×10^{4}	95	422	1200	14.7
TL2	0.356	3.15×10^{-3}	1.16	3.10×10^{4}	100	478	1183	20.6
TL3	0.356	3.50×10^{-3}	1.06	3.18×10^{4}	115	644	1328	22.9
TL4	0.305	2.25×10^{-3}	1.15	2.28×10^{4}	100	467	1256	14.7
TL5	0.305	3.15×10^{-3}	1.16	3.03×10^{4}	110	550	1156	20.6
TL6	0.305	3.50×10^{-3}	1.08	3.24×10^{4}	130	628	1367	22.9
TL7	0.254	3.15×10^{-3}	1.16	2.83×10^{4}	115	550	1256	20.6
TL8	0.254	3.50×10^{-3}	1.07	3.17×10^{4}	120	561	1278	22.9
TL9	0.203	2.37×10^{-3}	1.09	1.79×10^{4}	145	628	1161	15.5
TL10	0.203	3.04×10^{-3}	1.12	2.55×10^{4}	120	578	1283	19.9
TL11	0.203	3.50×10^{-3}	1.07	2.83×10^{4}	125	622	1200	22.9
TL12	0.203	5.16×10^{-3}	1.19	3.38×10^{4}	160	817	1428	33.7
TL13	0.152	3.04×10^{-3}	1.12	1.79×10^{4}	150	683	1283	19.9
TL14	0.152	3.39×10^{-3}	1.04	2.48×10^{4}	135	678	1306	22.2
TL15	0.152	5.59×10^{-3}	1.30	3.52×10^{4}	165	933	1372	36.5

Various flow rates were tested for the five different tailpipe lengths given in Table 3.8. Although high peak to peak amplitude pressure pulsations are desirable, other factors such as exhaust exit temperature and combustion quality, as indicated by percent

theoretical air (TA) values close to 1, are also important. Therefore, the optimum combination of these factors was used to select the appropriate tailpipe length. Figure 3.16 is a plot of the percent theoretical air and exit temperature of the cases investigated, with the data labels indicating the case number. Case TL12 and case TL15 are not presented because the large amounts of excess air present in these cases were deemed unsuitable for the current work.

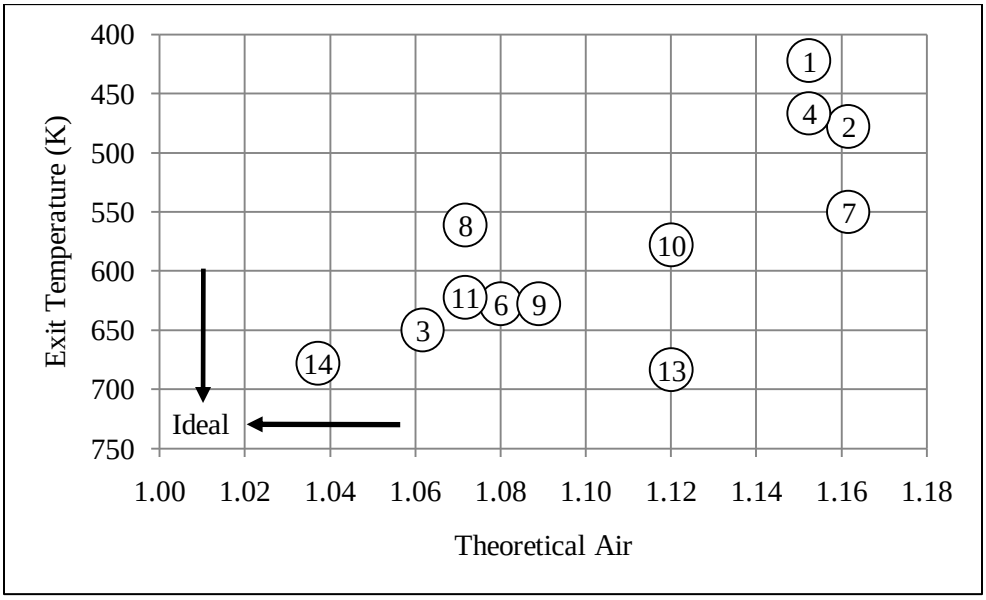

Figure 3.16: Results of pipe length trials. Data labels correspond to case number.

The ideal combination would have low excess air with relatively high exhaust temperature accompanied by large pressure pulsations. Although case TL14 appears to be a good candidate based on Figure 3.16, this case only produced peak to peak pressure pulsations of 2.48×10^4 Pa, the fifth lowest value of ΔP_{pk-pk}, thus making it a poor option. Case TL3, however, produced the second highest value of ΔP_{pk-pk}, 3.18×10^4 Pa, the second highest exhaust temperature, 644 K, and required the second lowest amount of

excess air, 6 %. As a result, the tailpipe length of 0.356 m which was used in Case TL3 was selected for subsequent trials. It should be noted that although the selected tailpipe is the longest one presented in Table 3.8, longer tailpipes were investigated but failed to ignite readily during the combustor start-up procedure.

3.4.2 Apparatus and Procedure

During the moving impingement surface trials, the heat flux plate was pulled through the impingement zone on a moveable sled such that it passed directly under the midpoint of the tailpipe. Two additional identical combustors were constructed and the three were positioned inline for the multiple nozzle experiments. Consequently, the thermocouples passed directly under all three combustors when being moved through the impingement zone. A pressure transducer measured oscillations in the combustion chamber, and thermocouples were used to measure the time-averaged combustion chamber temperature and tailpipe exit temperature. A diagram of the experimental configuration is given in Figure 3.17.

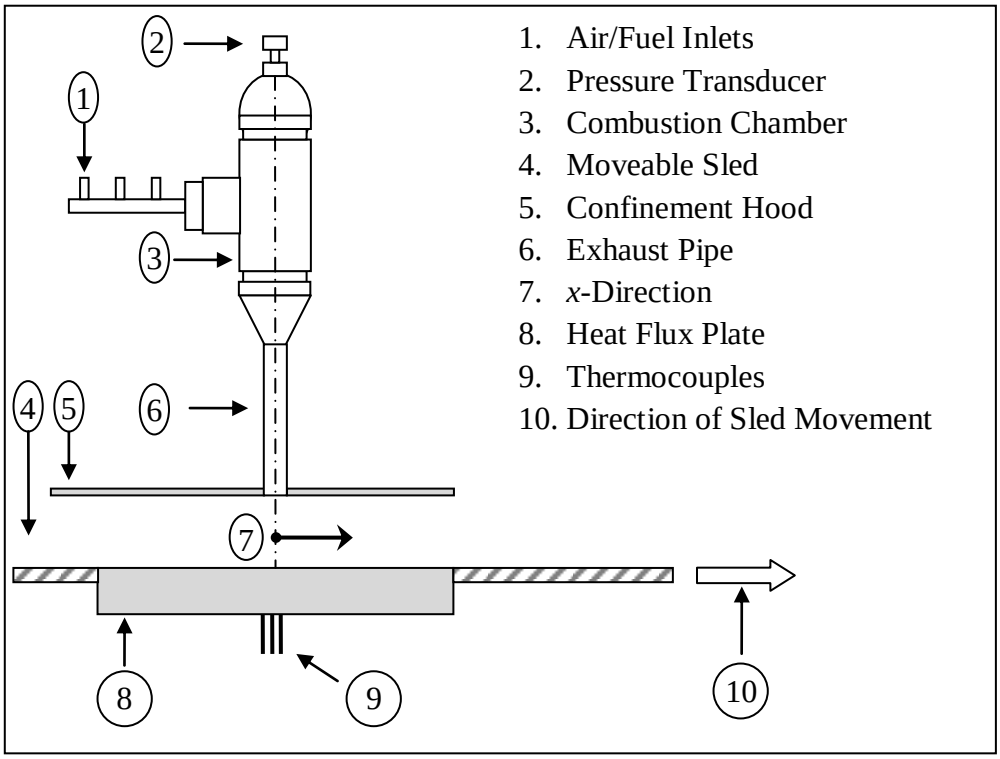

Figure 3.17: Experimental apparatus used in moving surface heat flux trials.

The sled was pulled through the impingement zone by a simple pulley system attached to a falling weight. The weight, mass of the sled, and friction between the sled and its rail system were adjusted so that a constant velocity was reached by the sled prior to entering the impingement zone. A linear position sensor was used to record the movement of the sled. Unfortunately, the switching mechanism employed in the data acquisition system had a small amount of electrical capacitance. This led to significant cross-talk between the channels monitoring the 0 to 3 V output of the position sensor and the microvolt signals from the thermocouples. This necessitated lowering the data sampling rate for the moving surface trials. Consequently a 200 Hz sampling rate was used for these cases with a 1024 oversample. The surface velocity and other operational parameters used throughout the moving surface trials are given in Table 3.9. The

hydraulic diameter, D_h, is calculated as twice the slot width.

Table 3.9: Configuration employed in moving surface trials.

Parameter	Value
L	0.356 m
D_h	0.0128 m
H	0.020 m
H/D_h	1.56
U_{surface}	0.6 m/s

In order to make comparisons between pulsed and steady flow, the same burners were used for both cases. The desired steady flow conditions were produced by heating the combustion chamber and tailpipe well beyond the normal operating temperature by manipulating the air and fuel flows. Once a suitably high temperature was reached, the fuel flow was stopped, and the air flow was heated by the residual heat of the chamber walls and tailpipe. As the burner cooled, the average air temperature slowly decreased. Once this temperature reached the desired value, the heat flux test was performed. Since this was a transient process, a separate analysis was performed comparing the rate change of the air temperature to the duration of a single test run and the time response characteristics of the temperature sensor. Given that the time duration of an individual test was approximately 3 s, it is not anticipated that the 1 °K/s drop in exhaust temperature was significant.

3.4.3 Single Nozzle Tests

3.4.3.1 Sample Case

This section presents the results from a sample moving surface trial with a single nozzle. Although analyses similar to those discussed for the stationary trials were performed, they are not discussed. Instead, this section focuses on the differences in methods and analyses. The sample case presented in this section has a case identification number HF27.

A plot of the combustion chamber pressure for the single nozzle sample case is given in Figure 3.18. This information was used to analyze the oscillation characteristics of the system. In contrast to the 200 Hz sampling rate used for the temperature and position data, the use of a separate acquisition system allowed pressure data to be recorded at 5×10^3 Hz.

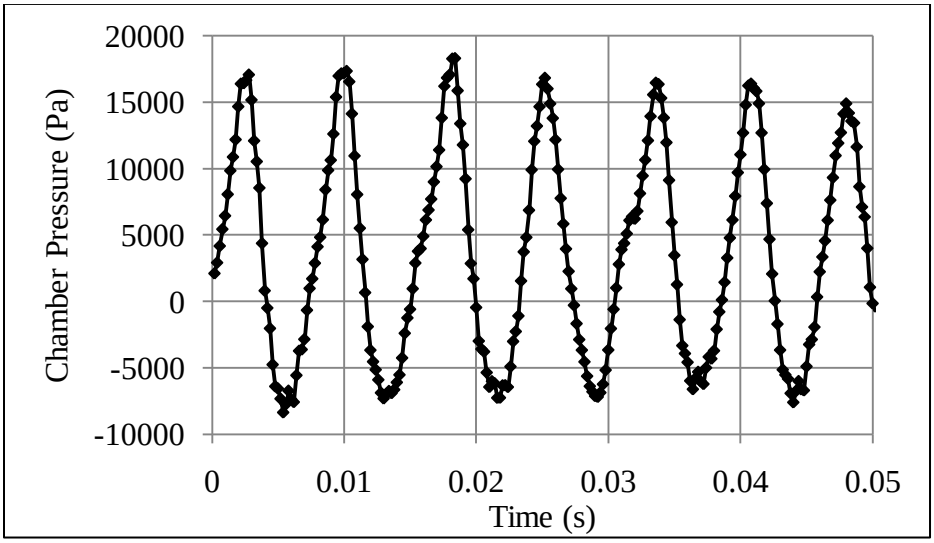

Figure 3.18: Combustion chamber pressure as a function of time for HF27.

The results obtained from spectral analysis of the pressure data are presented in Table 3.10, along with other operational conditions. As before, the velocity amplitude ratio was estimated using the simplified equation derived from incompressible approximation and acoustic resonator theory.

Table 3.10: Operational characteristics for case HF27.

Characteristic	Value
ω	135 Hz
Period	7.41×10^{-3} s
$\Delta P_{cc}/2$	1.25×10^{4} Pa
$\overline{P}_{cc}$	3.13×10^{3} Pa
$\overline{T}_{exit}$	674 K
$\dot{\overline{m}}$	3.7×10^{-3} kg/s
R_{amp}	3.43

The additional test equipment that was required for the moving surface cases led to additional electronic interference. Spectral analysis of the temperature data clearly shows a 60 Hz source of signal noise. This occurred during all tests regardless of the frequency of the pressure oscillations. In response to this additional noise source, a band stop filter was implemented during data analysis. The results of this can be seen in Figure 3.19, a plot of the single sided amplitude spectrum for the heat flux data with and without the band stop filter.

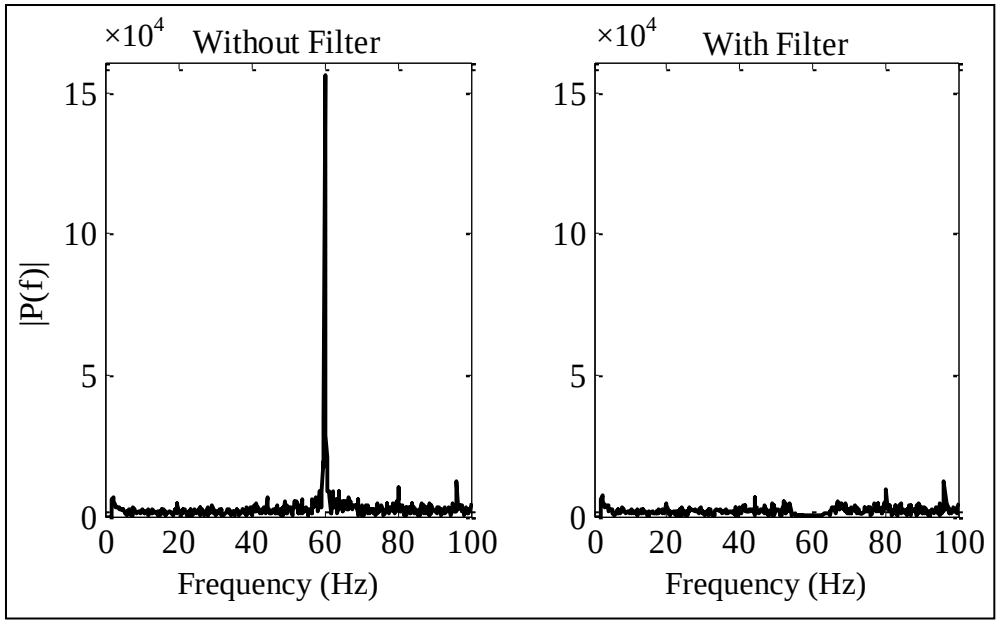

Figure 3.19: Effect of filter on amplitude spectrum of heat flux data for HF27.

The resultant heat flux is given in Figure 3.20. The line in this figure is a 3 point moving average that is presented only for visual clarity and was not used for analytic purposes.

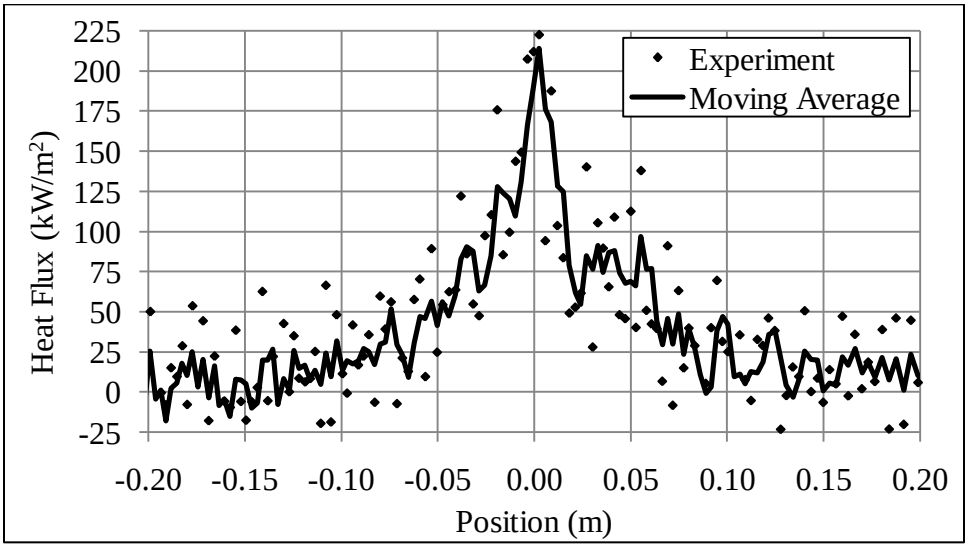

Figure 3.20: Heat flux versus position for HF27.

Three quantities were used to characterize the heat flux data for comparison between cases. Instead of using the maximum value to indicate the peak heat flux, the average heat flux within a 0.01 m band to either side of the nozzle centerline. This approach was employed for two main reasons. First, signal noise would produce artificially high values in some cases if only one data point was used. Therefore averaging over a range is a better indicator of actual performance. Second, the discrete, time-based sampling led to slight discrepancies between cases of the spatial location of the data points. In combination with the sharp slope of the heat flux profile, a single data point would not accurately describe heat transfer performance. Consequently, average heat flux for the ranges $|x| \leq 0.01$ m, $|x| \leq 0.03$ m, and $|x| \leq 0.128$ m were used to quantify heat flux profiles for comparison. These values were calculated using an area weighted average and a linear interpolation between data points. An enlarged view of the heat flux data for case H27, which highlights the ranges discussed, is given in Figure 3.21. The heat transfer characteristics are summarized in Table 3.11.

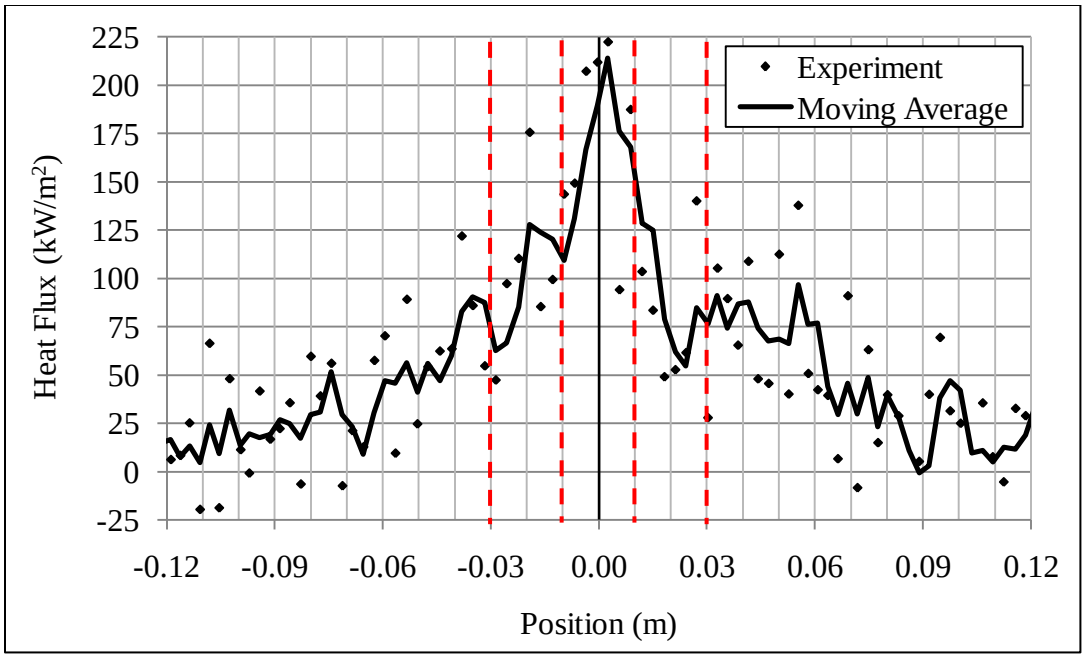

Figure 3.21: Portion of heat flux data for HF27 showing ranges used for comparison.

Table 3.11: Heat transfer performance for case HF27.

Range	$\overline{q}_s''$
-	(W/m^2)
$\|x\| \leq 0.010$ m	1.96×10^5
$\|x\| \leq 0.030$ m	1.27×10^5
$\|x\| \leq 0.128$ m	5.57×10^4

3.4.3.2 Results

The results of the single nozzle tests are given in Table 3.12 and Table 3.13 for

the steady flow and pulsed flow conditions, respectively. The results again show excellent repeatability with a maximum relative standard deviation of only 5.1 %.

Table 3.12: Summary of moving surface heat flux trials for steady flow conditions.

Case	$\dot{\overline{m}}$	$\overline{T}_{exit}$	$\overline{q}_s''\big\|_{\lvert x\rvert \le 0.010\ \text{m}}$	$\overline{q}_s''\big\|_{\lvert x\rvert \le 0.030\ \text{m}}$	$\overline{q}_s''\big\|_{\lvert x\rvert \le 0.128\ \text{m}}$
-	(kg/s)	(K)	(W/m^2)	(W/m^2)	(W/m^2)
HF14	3.6×10^{-3}	675	8.54×10^{4}	6.19×10^{4}	3.06×10^{4}
HF15	3.6×10^{-3}	675	8.91×10^{4}	5.87×10^{4}	2.75×10^{4}
HF16	3.6×10^{-3}	675	9.04×10^{4}	5.76×10^{4}	2.74×10^{4}
HF17	3.6×10^{-3}	675	8.94×10^{4}	5.87×10^{4}	2.80×10^{4}
HF18	3.6×10^{-3}	675	8.75×10^{4}	5.73×10^{4}	2.61×10^{4}
HF19	3.6×10^{-3}	675	8.87×10^{4}	5.97×10^{4}	2.90×10^{4}
HF20	3.6×10^{-3}	675	8.79×10^{4}	5.74×10^{4}	2.61×10^{4}
HF21	3.6×10^{-3}	675	9.30×10^{4}	5.60×10^{4}	2.58×10^{4}
HF22	3.6×10^{-3}	675	9.13×10^{4}	6.01×10^{4}	2.94×10^{4}
HF23	3.6×10^{-3}	675	9.56×10^{4}	5.70×10^{4}	2.68×10^{4}
HF24	3.6×10^{-3}	683	9.24×10^{4}	5.93×10^{4}	2.73×10^{4}
HF25	3.6×10^{-3}	683	8.88×10^{4}	5.86×10^{4}	2.66×10^{4}
HF26	3.6×10^{-3}	683	8.97×10^{4}	5.87×10^{4}	2.89×10^{4}
Average	3.6×10^{-3}	677	8.99×10^{4}	5.85×10^{4}	2.77×10^{4}
σ_{RSD}	0.0%	0.5%	2.8%	2.9%	5.1%

Table 3.13: Summary of moving surface heat flux trials for pulsed flow conditions.

Case	ω	R_{amp}	$\dot{\overline{m}}$	$\overline{T}_{exit}$	$\overline{q}_s''\big\vert_{\lvert x\rvert\leq 0.010\text{ m}}$	$\overline{q}_s''\big\vert_{\lvert x\rvert\leq 0.030\text{ m}}$	$\overline{q}_s''\big\vert_{\lvert x\rvert\leq 0.128\text{ m}}$
-	(Hz)	-	(kg/s)	(K)	(W/m^2)	(W/m^2)	(W/m^2)
HF27	135	3.43	3.7×10^{-3}	674	1.96×10^{5}	1.27×10^{5}	5.57×10^{4}
HF28	134	3.46	3.7×10^{-3}	672	1.92×10^{5}	1.29×10^{5}	5.70×10^{4}
HF29	134	3.45	3.7×10^{-3}	672	2.01×10^{5}	1.40×10^{5}	5.83×10^{4}
HF30	135	3.45	3.7×10^{-3}	675	2.11×10^{5}	1.31×10^{5}	5.73×10^{4}
HF32	137	3.46	3.4×10^{-3}	687	2.15×10^{5}	1.41×10^{5}	5.79×10^{4}
HF33	135	3.49	3.6×10^{-3}	681	1.97×10^{5}	1.39×10^{5}	5.75×10^{4}
HF34	136	3.49	3.6×10^{-3}	685	2.02×10^{5}	1.40×10^{5}	5.81×10^{4}
HF35	135	3.48	3.6×10^{-3}	676	2.05×10^{5}	1.33×10^{5}	5.64×10^{4}
HF36	135	3.46	3.7×10^{-3}	673	1.98×10^{5}	1.32×10^{5}	5.77×10^{4}
Avg.	135	3.46	3.6×10^{-3}	677	2.02×10^{5}	1.35×10^{5}	5.73×10^{4}
σ_{RSD}	0.6%	0.6%	2.6%	0.8%	3.5%	3.9%	1.4%

One additional method of analyzing the results is to study the data from all trials of a given flow condition, collectively. This more phenomenological approach of interpreting the data gives a clear view of the trends for each condition, even if only qualitatively. Figure 3.22 provides moving average trend lines of all the pulsed flow and steady flow data separated by flow type. The pulsed flow produced significantly higher peak values as well as a much broader heat flux curve.

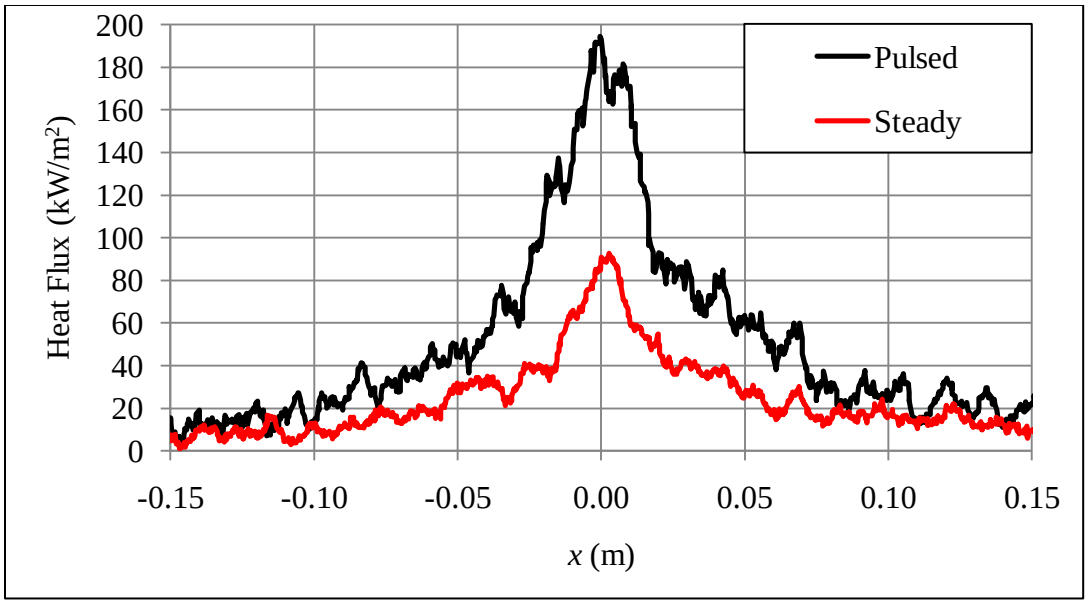

Figure 3.22: Heat flux trends for all single nozzle trials separated by flow type.

3.4.3.3 Discussion

In order to quantify the relative performance impact of the pulsed flow conditions, the heat flux enhancement factor was calculated for each range of interest. The results are given in Table 3.14, along with the average values used to calculate these ratios.

Table 3.14: Performance summary comparing single nozzle steady and pulsed flow.

	$\overline{q}_s''\big\vert_{\lvert x\rvert\le 0.010\text{ m}}$	$\overline{q}_s''\big\vert_{\lvert x\rvert\le 0.030\text{ m}}$	$\overline{q}_s''\big\vert_{\lvert x\rvert\le 0.128\text{ m}}$
Steady	8.99×10^4 W/m^2	5.85×10^4 W/m^2	2.77×10^4 W/m^2
Pulsed	20.2×10^4 W/m^2	13.5×10^4 W/m^2	5.73×10^4 W/m^2
E_{HF}	2.25	2.30	2.07

Perhaps the most significant and informative result given in Table 3.14 is the value of E_{HF} for the range $|x| \leq 0.128$ m which is 2.07. This quantity indicates the overall heat transfer impact of the pulsations and represents a substantial increase in performance. This was also a substantial increase in heat flux enhancement when compared to the stationary impingement surface tests and was a result of more optimal nozzle geometry, H/D_h spacing, and mean flow rate.

3.4.4 Three Nozzle Tests

The three nozzle tests were conducted using three combustors with similar design placed inline in the direction of sled movement. The distance between nozzle centerlines, W_{NZ} , was 0.15 m. A diagram of the experimental setup is provided in Figure 3.23. The same mass flow rate used in the single nozzle tests, 3.6×10^{-3} kg/s, was used for each combustor in the multiple nozzle trials.

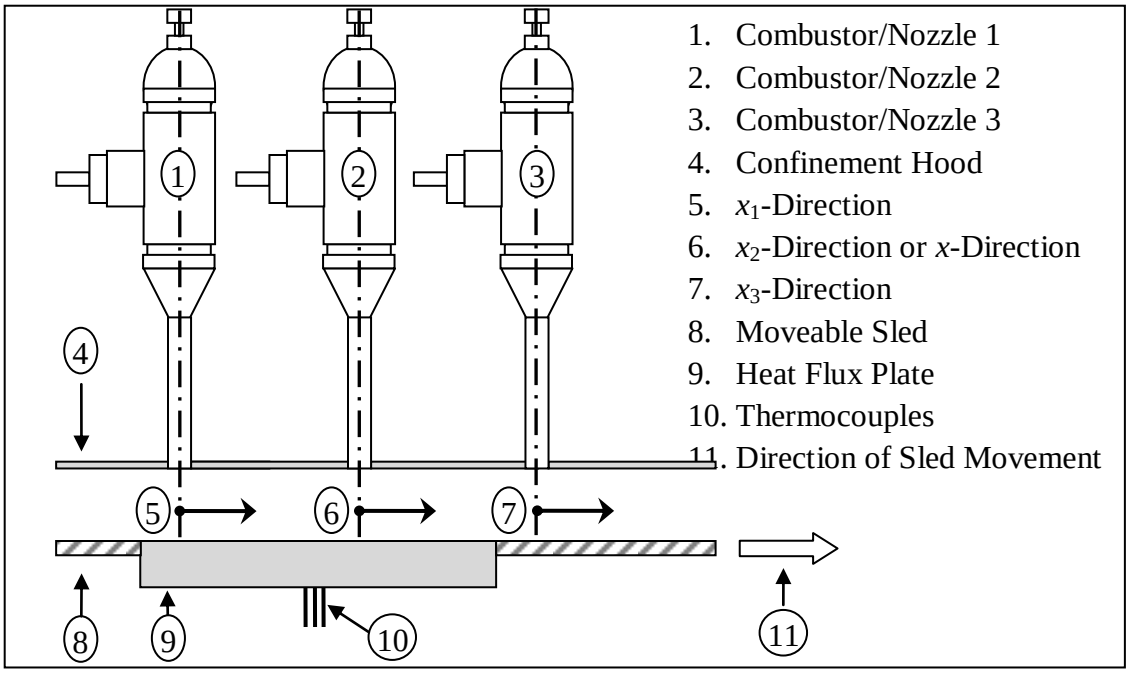

Figure 3.23: Experimental apparatus used in multiple nozzle heat flux tests.

3.4.4.1 Sample Case

The operational characteristics of case HF37, a steady flow case, are given in Table 3.15. The same exhaust outflow conditions were used for each of the three nozzles in the trial. The heat flux produced by this three nozzle system is shown in Figure 3.24.

Table 3.15: Operational characteristics for case HF37.

Characteristic	Value
$\overline{T}_{exit}$	1005 K
$\dot{\overline{m}}$	3.6×10^{-3} kg/s
U_{surface}	0.6 m/s

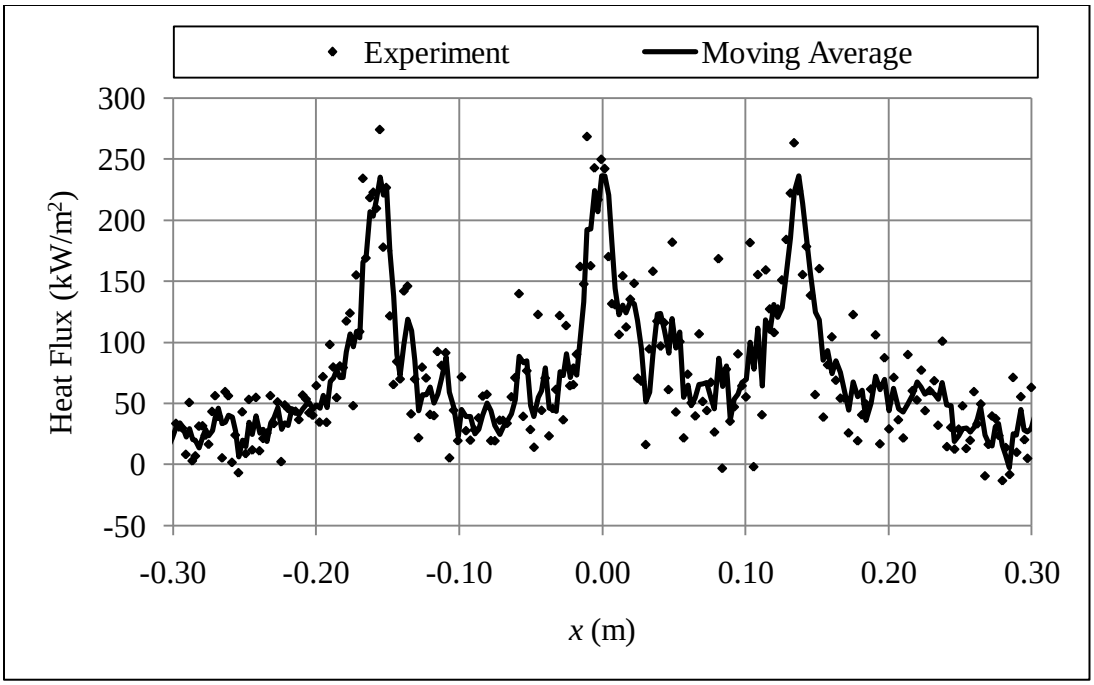

Figure 3.24: Heat flux versus position for HF37.

Criteria similar to those used in the single nozzle cases were used to describe the heat flux resulting from multiple impingement jets. However, for these cases the average heat flux was calculated for the regions surrounding each individual nozzle. These regions were $|x_n| \leq 0.01$ m and $|x_n| \leq 0.03$ m where n refers to the coordinate system associated with each nozzle. Additionally, the average heat flux for the entire region $|x| \leq 0.30$ m was calculated as a means to quantify the heat transfer performance in the entire impingement zone. The results for these calculations for case HF37 are given in Table 3.16.

Table 3.16: Performance characteristics of case HF37.

		Nozzle			Avg.	σ_{RSD}
		1	2	3		
$\overline{q}_s^{''}\big\vert_{\lvert x_n\rvert \le 0.010\text{ m}}$	(10^5 W/m^2)	2.26	2.32	2.09	2.22	4.5%
$\overline{q}_s^{''}\big\vert_{\lvert x_n\rvert \le 0.030\text{ m}}$	(10^5 W/m^2)	1.35	1.48	1.38	1.41	3.9%
$\overline{q}_s^{''}\big\vert_{\lvert x_n\rvert \le 0.3\text{ m}}$	(10^5 W/m^2)	-	0.72	-	-	-

The three combustors had a 4.5 % relative standard deviation in $\overline{q}_s^{''}\big\vert_{\lvert x_n\rvert \le 0.010\text{ m}}$ despite having similar exhaust outflow conditions. The relative standard deviation of $\overline{q}_s^{''}\big\vert_{\lvert x_n\rvert \le 0.030\text{ m}}$ for the combustors was slightly lower at 3.9 %.

3.4.4.2 Results

The flow conditions for the multiple nozzle cases are given in Table 3.17. The experiments demonstrated high repeatability. R_{amp} had the maximum relative standard deviation of 4.2 %.

Table 3.17: Flow conditions employed in multiple nozzle trials.

Case	ω (Hz)	R_{amp}	$\dot{\overline{m}}$ (g/s)	$\overline{T}_{exit}$ (K)
HF37	-	-	3.6	1005
HF38	-	-	3.6	1005
HF39	-	-	3.6	1005
HF40	-	-	3.7	1005
HF41	-	-	3.6	1005
HF42	-	-	3.7	1005
HF43	157	3.57	3.6	1004
HF44	156	3.58	3.6	1000
HF45	156	3.59	3.6	1001
HF46	156	3.60	3.7	1005
HF47	155	3.93	3.7	1004
HF48	155	3.62	3.7	1007
HF49	154	3.64	3.6	1005
HF50	156	3.59	3.6	1004
HF51	153	3.66	3.6	1004
HF52	155	3.62	3.6	1004
HF53	156	3.91	3.6	1004
HF54	154	3.95	3.6	1002
HF55	153	3.98	3.7	1003
Avg.	155	3.71	3.6	1004
σ_{RSD}	0.8%	4.2%	1.3%	0.2%

Analyzing the results of the three nozzle trials is slightly more complex than doing so for the single nozzle cases. This is due to the fact that there were performance deviations not only between trials, but also between combustors. Table 3.18 gives the peak heat flux values for the steady flow cases as quantified by $\overline{q}_s''\big|_{|x_n|\leq 0.010\text{ m}}$ and the associated deviations. For example, HF37 had an average $\overline{q}_s''\big|_{|x_n|\leq 0.010\text{ m}}$ value of 2.22×10^5 W/m^2 with a relative standard deviation between nozzles of 4.5 %. Conversely, Nozzle 1 produced an average value of 2.33×10^5 W/m^2 for $\overline{q}_s''\big|_{|x_n|\leq 0.010\text{ m}}$ with a relative standard deviation between trials of 3.5 %.

Table 3.18: Steady flow heat flux results for ±0.010 m region around each nozzle.

-		$\overline{q}_s''\big\|_{\lvert x_n\rvert\leq 0.010\text{ m}}$ (10^5 W/m^2)			For a Given Case	
		Nozzle 1	Nozzle 2	Nozzle 3	Avg.	σ_{RSD}
HF37		2.26	2.32	2.09	2.22	4.5%
HF38		2.48	2.37	2.48	2.44	2.2%
HF39		2.26	2.36	2.37	2.33	2.2%
HF40		2.30	2.30	2.24	2.28	1.2%
HF41		2.38	2.39	2.25	2.34	2.6%
HF42		2.32	2.57	2.26	2.38	5.6%
For a Given	Avg.	2.33	2.38	2.28	2.33	1.8 %
Nozzle	σ_{RSD}	3.3%	3.7%	5.3%	3.0%	-

On average, each combustor yielded a $\overline{q}_s^{''}\big|_{|x_n|\leq 0.010\text{ m}}$ value of 2.33×10^5 W/m^2 with a 1.8 % deviation between combustor averages and a 3.0 % deviation between trial averages. The relative standard deviation for $\overline{q}_s^{''}\big|_{|x_n|\leq 0.010\text{ m}}$ across all of the steady flow cases was only 4.6 %. Similar analyses were performed for these cases using $\overline{q}_s^{''}\big|_{|x_n|\leq 0.030\text{ m}}$. These results are provided in Table 3.19. The average value of $\overline{q}_s^{''}\big|_{|x_n|\leq 0.030\text{ m}}$ for all cases and combustors was 2.33×10^5 W/m^2 with a relative standard deviation of 8.2 %. Although this deviation is larger than that calculated for the region $|x_n| \leq 0.01$ m, it still represents minimal dispersion.

Table 3.19: Steady flow heat flux results for ±0.030 m region around each nozzle.

-		$\overline{q}_s^{''}\big\|_{\lvert x_n\rvert\leq 0.030\text{ m}}$ (10^5 W/m^2)			For a Given Case	
		Nozzle 1	Nozzle 2	Nozzle 3	Avg.	σ_{RSD}
HF37		1.35	1.48	1.38	1.41	3.9%
HF38		1.62	1.62	1.62	1.62	0.2%
HF39		1.59	1.58	1.53	1.56	1.6%
HF40		1.54	1.62	1.42	1.53	5.6%
HF41		1.53	1.69	1.47	1.56	6.0%
HF42		1.79	1.89	1.59	1.76	7.1%
For a Given	Avg.	1.57	1.65	1.50	1.57	3.8 %
Nozzle	σ_{RSD}	8.3%	7.6%	5.7%	6.6%	-

The average heat flux over the entire impingement zone defined by $|x| \leq 0.03$ m is given in Table 3.20. The relative standard deviation of this quantity for the steady flow trials was 7.6 %, again showing excellent repeatability.

Table 3.20: Steady flow heat flux results for ±0.30 m region around center nozzle.

Case	$\overline{q}_s''\big\|_{\lvert x_1\rvert \leq 0.30\ \text{m}}$
HF37	7.22×10^4 W/m^2
HF38	9.11×10^4 W/m^2
HF39	8.87×10^4 W/m^2
HF40	8.59×10^4 W/m^2
HF41	8.67×10^4 W/m^2
HF42	9.16×10^4 W/m^2
Average	8.60×10^4 W/m^2
σ_{RSD}	7.6%

The pulsed flow cases, however, showed much more variation between combustors. The performance characteristics of these trials are provided in Table 3.21. The center combustor consistently produced higher heat flux than the other two. Although lower than the center nozzle, the heat flux values produced by the two outer nozzles were comparable to each other. This result was expected rather than the consistent values produced by the steady flow cases, since no ventilation was used between jets. Thus, jet-to-jet interactions were different for the centrally located

combustor than they were for the outermost burners. Still, the results do show good agreement between cases, with a maximum σ_{RSD} of 7.8 %.

Table 3.21: Pulsed flow heat flux results for various regions around each nozzle.

Case	$\overline{q}_s''\big\|_{\lvert x_n\rvert \le 0.010\text{ m}}$ (10^5 W/m^2)			$\overline{q}_s''\big\|_{\lvert x_n\rvert \le 0.030\text{ m}}$ (10^5 W/m^2)			$\overline{q}_s''\big\|_{\lvert x_1\rvert \le 0.30\text{ m}}$
-	n=1	n=2	n=3	n=1	n=2	n=3	(10^5 W/m^2)
HF43	5.41	5.69	5.46	3.42	4.21	3.64	2.21
HF44	5.12	5.56	4.46	3.03	4.44	3.43	2.21
HF45	5.26	5.72	4.97	3.40	4.36	3.69	2.14
HF46	5.27	6.11	5.39	3.46	4.39	3.45	2.15
HF47	4.74	5.44	5.27	2.89	4.04	3.69	2.17
HF48	4.99	5.40	5.05	3.49	4.03	3.62	2.15
HF49	4.75	5.21	4.77	3.12	3.88	3.22	1.92
HF50	5.02	5.07	4.72	3.23	3.67	3.04	1.84
HF51	4.88	5.71	5.02	3.36	4.02	3.33	1.95
HF52	4.95	4.84	4.94	3.18	3.73	2.91	1.90
HF53	4.58	5.81	4.98	2.93	4.26	3.20	1.95
HF54	4.54	5.61	4.84	3.48	3.66	3.12	1.97
HF55	4.56	5.45	4.59	3.40	3.97	3.04	1.96
Avg.	4.93	5.51	4.96	3.26	4.05	3.34	2.04
σ_{RSD}	5.6%	5.8%	5.7%	6.3%	6.4%	7.8%	6.2%

On average, $\overline{q}_s'' \big|_{|x_n| \leq 0.010 \text{ m}}$ for nozzle 2 was 11 % and 10% higher than it was for nozzles 1 and 3, respectively. Similarly, $\overline{q}_s'' \big|_{|x_n| \leq 0.030 \text{ m}}$ for nozzle 2 was 19 % and 18% higher than it was for nozzles 1 and 3, respectively.

The combined results from all multiple nozzle heat flux experiments are shown in Figure 3.25, separated by flow type. This plot uses a moving average to qualitatively show the trends associated with the pulsed and steady flows. The two profiles have similar shapes with one exception. The pulsed flow showed a pronounced increase in heat flux in the region $x \leq 0.015$ m.

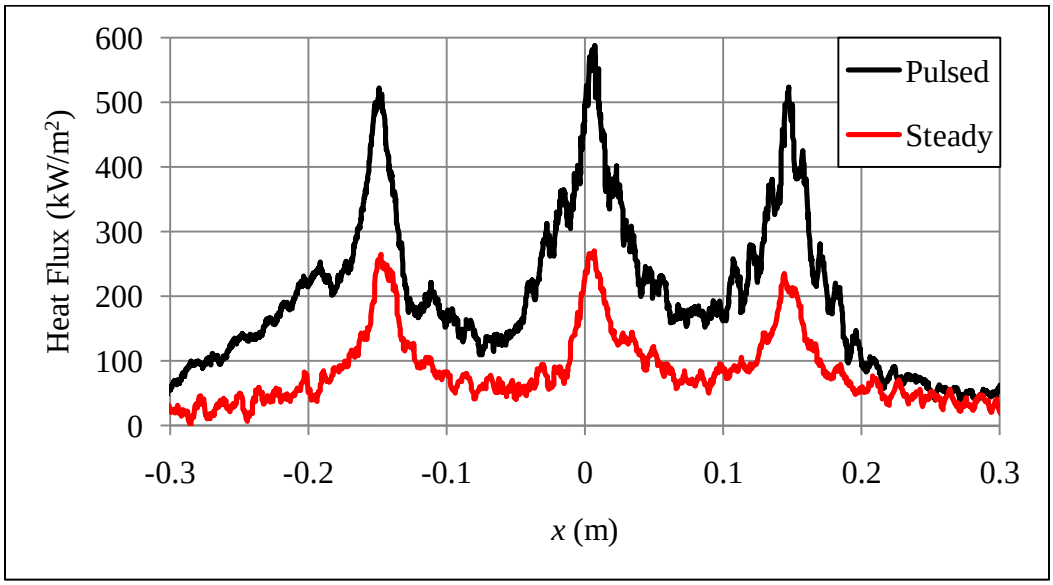

Figure 3.25: Heat flux trends for all multiple nozzle trials separated by flow type.

3.4.4.3 Discussion

The average heat flux enhancement factors for each region are given in Table

3.22. The values associated with each nozzle are also given. The heat flux enhancement was greatest for the center nozzle, with E_{HF} values of 2.31 and 2.46 for the regions $|x| \leq$ 0.01 m and $|x| \leq 0.01$ m, respectively.

Table 3.22: Performance summary comparing multiple nozzle steady and pulsed flow.

Region	E_{HF}			Average E_{HF}
	Nozzle 1	Nozzle 2	Nozzle 3	
$\|x_n\| \leq 0.01$ m	2.11	2.31	2.17	2.20
$\|x_n\| \leq 0.03$ m	2.08	2.46	2.23	2.26

Over the entire impingement zone, $|x_n| \leq 0.3$ m, E_{HF} was found to be 2.37. As with previous cases, this shows a dramatic increase in heat transfer. It should be noted, however, that this value is not directly comparable to the result obtained for the single nozzle case since they have different regions of interest.

3.5 Verification of Experimental Method

3.5.1 Approach

In order to verify the results obtained using the above method, a separate experimental procedure was devised and implemented. This method was intended only to corroborate the average heat flux values, not the transient effects. In this approach an object of known mass, geometry, and thermal properties was heated for a specified period

of time. The object was then removed from the impingement jet, insulated, and allowed to reach an equilibrium temperature. The amount of thermal energy imparted to the object may then be calculated by

$$E = mc_p \Delta T_{\text{avg}} \,, \tag{3.14}$$

where E is the energy absorbed by the object, m is the mass, c_p is the specific heat, and ΔT_{avg} is the change in average temperature of the object.

If the heating time, t_h, and exposed surface area, A_{surface}, are also known, the average heat flux may be estimated using

$$q''_{\text{avg}} = \frac{E}{t_h A_{\text{surface}}} \,, \tag{3.15}$$

which can be compared to the values calculated using the thermocouple plate method. Direct comparisons are possible if the object is contained within a region directly under the nozzle in which heat flux appeared to be uniform. For this reason, the test was conducted using the round nozzle and flow conditions presented in the stationary surface sample case.

3.5.2 Apparatus and Procedure

The experimental setup employed an AISI grade 304 stainless steel cylinder

embedded in an insulating plate such that one face of the cylinder was exposed. This face was coplanar with the insulation as shown in Figure 3.31.

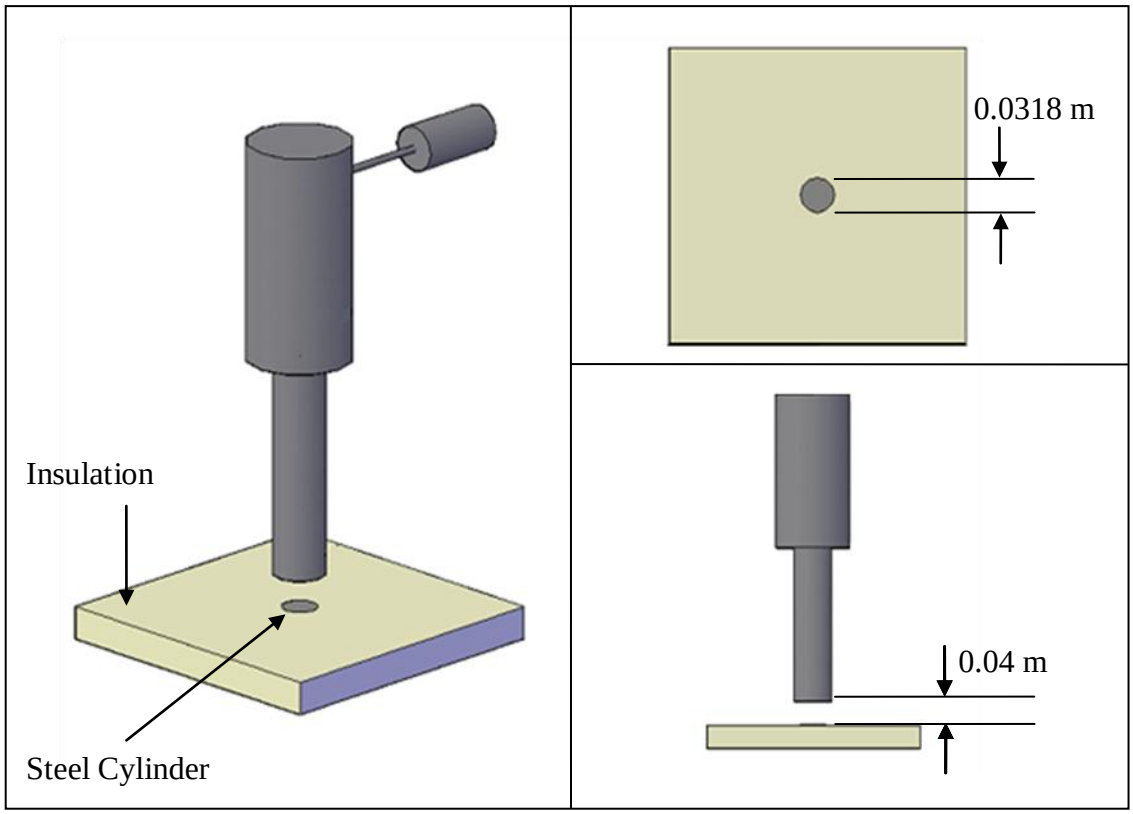

Figure 3.26: Experimental apparatus used to confirm heat flux calculations.

Once the cylinder and surrounding insulation were removed from the impingement jet, additional insulation was placed over the exposed face, preventing heat loss. Thermocouples positioned on the top and bottom faces of the cylinder allowed accurate measurement of heating time and equilibrium temperature. A flame hood was again employed around the exhaust pipe to add confinement for the hot exhaust gases. Fuel and air volumetric flow rates were recorded manually before and after the test. The

flow conditions and sample properties used in this test are given in Table 3.23.

Table 3.23: Sample properties and flow conditions for verification test.

Parameter	Value
m	0.074 kg
c_p	477 J/kg·K
A_{surface}	7.94×10^{-4} m^2
ΔT_{avg}	18.1 K
t_h	7.1 s
$\dot{\overline{m}}_{air}$	4.2×10^{-3} kg/s
$\dot{\overline{m}}_{fuel}$	2.8×10^{-4} kg/s
H	0.04 m
H/D_h	1.6
T_{exit}	900 K

3.5.3 Results

The temperature data recorded by the data acquisition system is given in Figure 3.27. The large spike in the temperature reading from the top thermocouple is due to

direct exposure to the impingement gases. The results of both heat flux experiments are compared in Table 3.24.

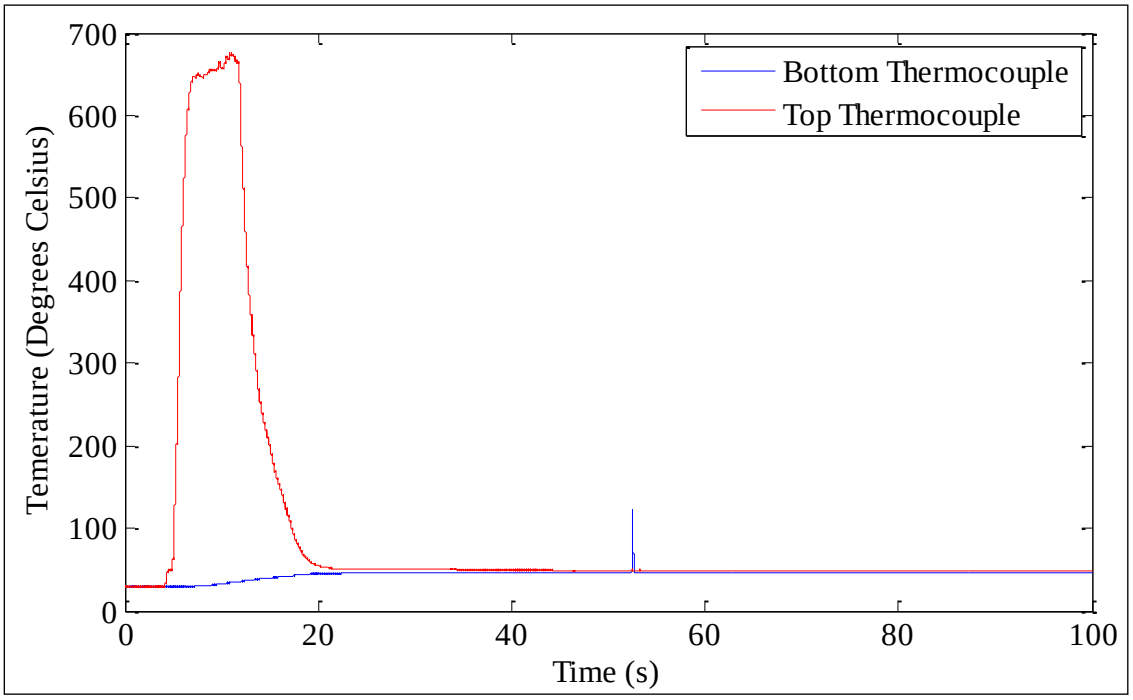

Figure 3.27: Top and bottom surface temperature of cylinder as a function of time.

Table 3.24: Results and comparison of heat flux methods.

Heat Flux		Difference	
Steel Cylinder	Thermocouple Plate	Absolute	Relative
1.13×10^{5} W/m^2	1.09×10^{5} W/m^2	4.0×10^{3} W/m^2	3.5 %

The results in Table 3.24 show excellent agreement with a relative difference of only 3.5%. One reason for this discrepancy could be a slight difference in atmospheric conditions. Nevertheless, the steel cylinder method provides an effective verification of the heat flux plate method which includes the inverse numerical technique.

3.6 Summary and Discussion

This chapter presented the results of the laboratory heat flux tests that were conducted using pulsating and steady flow conditions for both single and multiple jet configurations. The pulsating conditions were generated by pulse combustors, the design and assembly of which was presented. The development and implantation of a numerical technique used to obtain heat flux data from the surface temperature history of the impingement target was also discussed. The heat transfer characteristics of the pulse combustors and performance relative to similar steady flow jets were also analyzed. The results of stationary surface tests using a single round nozzle were given and it was found that the pulsed flow improved heat flux at the stagnation point. The moving surface tests provided more detailed information about the heat transfer characteristics. These tests employed either single or triple burner configurations that terminated in slot-shaped nozzles. The heat flux profiles from these tests were analyzed and heat transfer enhancement factors were found to be as high as 2.46. Finally, the experimental method was verified by a separate laboratory procedure. The results showed excellent agreement in the average heat flux produced by a single round nozzle impinging on a stationary surface. Thus, the heat transfer results from this chapter will be used to validate the

numerical model described in the next chapter. Those validation results are discussed in Chapter 5.

Later it will be shown that in addition to R_{amp} and H/D_h, the important dimensionless parameters also include the Strouhal number, $\overline{St}$, and the Reynolds number, $\overline{Re}$, based on the mean values at the tailpipe exit. That is,

$$\overline{St} = {\omega D_h}\Big/{\overline{U}_{exit}} \tag{3.16}$$

$$\overline{Re} = {\overline{U}_{exit}\, D_h}\Big/{\bar{\nu}_{exit}} \tag{3.17}$$

where $\bar{\nu}_{exit}$ is the average kinematic viscosity at the tailpipe exit. The values of $\overline{St}$ and $\overline{Re}$ for the single nozzle, moving impingement surface cases in this chapter are estimated to be 0.047 and 8000, respectively. Similarly, $\overline{St}$ and $\overline{Re}$ for the three nozzle cases in this chapter are estimated to be 0.043 and 5000, respectively. In subsequent numerical simulations, these values change as the oscillation frequency, hydraulic diameter, and mean exit velocity are varied. The value of $\bar{\nu}_{exit}$ will also change, but only as a consequence of the temperature and pressure conditions, rather than being a controlled variable.

CHAPTER 4

NUMERICAL MODEL

This chapter presents the development of the model used in the numerical simulations of the fluid flow in the region above the impingement surface. The general modeling approach, governing equations, and solution procedures are presented. Additionally, the simulation domain and boundary conditions are discussed. The methods used in grid refinement and time discretization are demonstrated. Finally, the resulting grid size and time step independence is verified. Validation of the numerical model is discussed in Chapter 5.

4.1 Introduction

Although extensive experimental testing was necessary in order to guide and verify numerical simulations, in some areas numerical studies offer significant advantages over experimental studies. One such advantage is the ability to vary a single parameter independently of others. For example, experimentally increasing the mean flow rate of the burner while maintaining the same pressure oscillations and exit temperatures requires extensive modification to the burner geometry. Such a task is a time intensive undertaking, especially for multiple configurations. Additionally, due to experimental limitations and the small time scales associated with 160 Hz operating

frequencies, measurement of quantities such as exhaust temperature, velocity, heat flux, and drying rate were time averaged. Numerical simulations, on the other hand, were both spatially and temporally resolved. This is especially advantageous for the details of the velocity, pressure, and temperature distributions in the flow. These features, although difficult to obtain experimentally, provide insight into the mechanisms of heat flux and drying enhancement.

4.2 Approach

The commercial software FLUENT was employed to carry out the numerical simulations of the fluid flow in the impingement zone. The main object of this work was to accurately describe the flow and resulting transport processes in a manner that was both time and computationally efficient. Thus, simplifications were made only when they offered considerable computational or time savings without introducing significant error in the quantities of interest.

4.2.1 Two-dimensional Approximation

The experimental trials and numerical simulations primarily focused on cases involving a slot shaped nozzle with a large depth to width ratio. Therefore, the flow was assumed to be symmetric in the direction of nozzle depth, the *z*-direction, in order to simplify the numerical analysis. This allowed the modeling to be conducted in only two dimensions, greatly reducing the computational domain, complexity, and cost.

In order to validate this simplification, heat flux was experimentally measured at multiple locations in the *z*-direction. A comparison of the heat flux profiles obtained at two values of *z* for the experimental trial HF25 is provided in Figure 4.1. This particular case had a single steady jet that impinged on a moving surface. However, similar agreement between $z = 0.00$ m and $z = 0.02$ m was found in all cases.

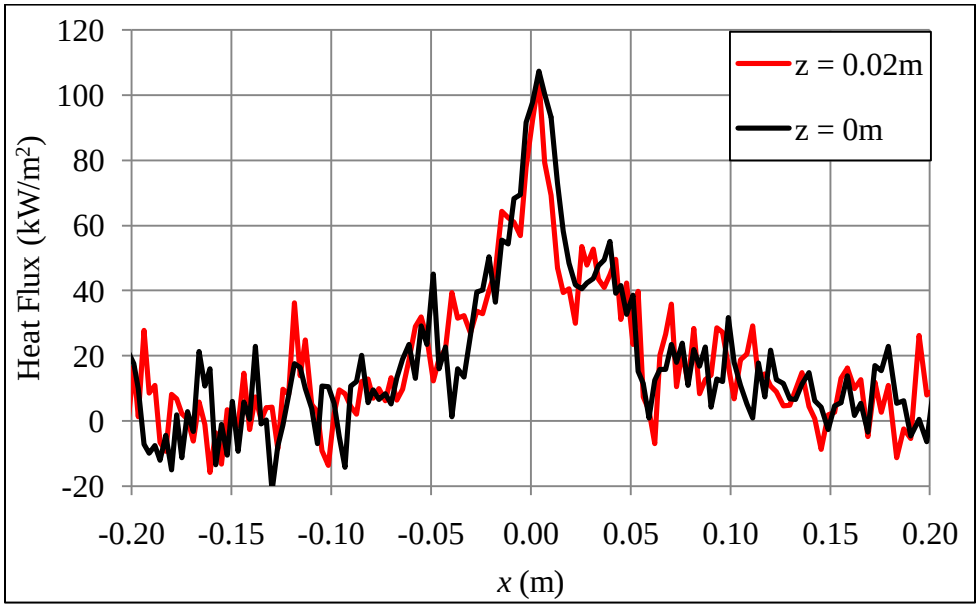

Figure 4.1: Experimental values of heat flux versus *x* for two values of *z* from case HF25.

The results show that the heat flux trends were nearly independent of *z* for the two cases considered. Although not necessarily indicative of the *z*-direction independence of the fluid flow, this does serve to bolster the assertion that the resulting conditions near the surface are similar. As a result, both the thermal and mass transport processes occurring at the sheet or impingement surface are expected to be independent of *z*, at least for the narrow region considered.

4.2.2 Tailpipe Outflow Conditions

Of primary interest were the transport processes at the impingement surface and the flow conditions in the impingement zone produced by the exhaust jet. Therefore, the modeling work in this chapter focused on the tailpipe exit and resultant flow in the impingement zone. It did not attempt to investigate or model the stochastic combustion processes in the combustion chamber that produce these flows. That is, the outflow conditions at the tailpipe exit, rather than the source of these conditions, were important to the current work. Subsequently, quantities such as the mean mass flow rate, temperature, velocity, and the amplitude and frequency of the velocity oscillations at the tailpipe exit, were central to the numerical investigations. Therefore, the boundary conditions at the inlet to the tailpipe were specified based on the objective of producing a desired flow at the tailpipe exit. This was done to either match the experimental values measured in the validation cases, or to investigate additional cases.

4.3 Implementation

4.3.1 Governing Equations

As previously stated, the commercial software FLUENT version 6.3 was employed to carry out numerical simulations for this portion of the project. FLUENT uses the Reynolds-Averaged Navier-Stokes (RANS) equations as the governing equations for turbulent flows, such as those produced by pulse combustors. The simulation utilized the V2F turbulence model, as this approach was found well suited for

use with pulse combustors in previous work (Liewkongsataporn et al., 2008). Others have also shown this model to be accurate for similar cases (Zuckerman and Lior, 2005; Scotti and Piomelli, 2002). The governing equations used by FLUENT for this two-dimensional turbulent flow are (FLUENT, 2006):

Continuity Equation

$$\frac{\partial \rho}{\partial t} + \boldsymbol{\nabla} \cdot (\rho \boldsymbol{u}) = 0 \tag{4.1}$$

Momentum Equations

$$\frac{\partial}{\partial t}(\rho \boldsymbol{u}) + \boldsymbol{\nabla} \cdot (\rho \boldsymbol{u}\boldsymbol{u}) = -\boldsymbol{\nabla} P + \boldsymbol{\nabla} \cdot (\overline{\tau} + \overline{\tau}_t) \tag{4.2}$$

$$\overline{\tau} = \mu \left[(\boldsymbol{\nabla u} + \boldsymbol{\nabla u}^T) - \frac{2}{3} \left(\boldsymbol{\nabla} \cdot \boldsymbol{u} \overline{I} \right) \right] \tag{4.3}$$

$$\overline{\tau}_t = \mu_t \left[(\boldsymbol{\nabla u} + \boldsymbol{\nabla u}^T) - \frac{2}{3} \left(\frac{\rho E_k}{\mu_t} + \boldsymbol{\nabla} \cdot \boldsymbol{u} \right) \overline{I} \right] \tag{4.4}$$

Energy Equation

$$\frac{\partial}{\partial t}(\rho E) + \boldsymbol{\nabla} \cdot [\boldsymbol{u}(\rho E + P)] = \boldsymbol{\nabla} \cdot (\lambda_{\text{eff}} \boldsymbol{\nabla} T) \tag{4.5}$$

$$E = h - \frac{P}{\rho} + \frac{u^2}{2} \tag{4.6}$$

$$h = \int_{T_{ref}}^{T} c_p dT \tag{4.7}$$

$$\lambda_{\text{eff}} = \lambda + \frac{c_p \mu_t}{Pr_t} \tag{4.8}$$

State Equation

$$p = \rho RT \tag{4.9}$$

In these equations E is the specific total energy and h, is the specific enthalpy. The additional terms in the momentum equations are due to the Reynolds stresses. These terms are modeled by the V2F turbulence model through the use of the Boussinesq hypothesis. This assumes that the so-called turbulent viscosity, μ_t, is isotropic. The Reynolds stress tensor, turbulent viscosity, turbulent kinetic energy, E_k, and effective thermal conductivity, λ_{eff}, are all calculated by the V2F turbulence model. This model solves four equations involving the turbulence parameters. These equations are (FLUENT, 2003)

$$\frac{\partial}{\partial t}(\rho E_k) + \boldsymbol{\nabla} \cdot (\rho E_k \boldsymbol{u}) = \overline{P} - \rho \varepsilon_{\text{dis}} + \boldsymbol{\nabla} \cdot \left[\left(\mu + \frac{\mu}{\sigma_k}\right) \boldsymbol{\nabla} E_k\right] \tag{4.10}$$

$$\frac{\partial}{\partial t}(\rho \varepsilon_{\text{dis}}) + \boldsymbol{\nabla} \cdot (\rho \varepsilon_{\text{dis}} \boldsymbol{u}) = \frac{C_{\varepsilon 1}^{'} \overline{P} - C_{\varepsilon 2} \rho \varepsilon_{\text{dis}}}{t_t} + \boldsymbol{\nabla} \cdot \left[\left(\mu + \frac{\mu_t}{\sigma_\varepsilon}\right) \boldsymbol{\nabla} \varepsilon_{\text{dis}}\right] \tag{4.11}$$

$$\frac{\partial}{\partial t}\left(\rho \overline{\boldsymbol{u}^2}\right) + \boldsymbol{\nabla} \cdot \left(\rho \overline{\boldsymbol{u}^2} \boldsymbol{u}\right) = \rho E_k f_e - 6\rho \overline{\boldsymbol{u}^2} \frac{\varepsilon_{\text{dis}}}{E_k} + \boldsymbol{\nabla} \cdot \left[\left(\mu + \frac{\mu_t}{\sigma_k}\right) \boldsymbol{\nabla} \overline{\boldsymbol{u}^2}\right] \tag{4.12}$$

$$f_e - L_t \nabla^2 f_e = \frac{(C_1 - 1)}{t_t}\left(\frac{2}{3} - \frac{\overline{\boldsymbol{u}^2}}{E_k}\right) + \frac{C_2 \overline{P}}{\rho E_k} + \frac{5\overline{\boldsymbol{u}^2}}{t_t E_k} \tag{4.13}$$

where

$$\overline{P} = 2\mu_t S^2, \quad S^2 = \hat{S} : \hat{S}, \quad \hat{S} = \frac{1}{2}\left(\nabla \overline{\boldsymbol{u}} + \nabla \overline{\boldsymbol{u}}^T\right). \tag{4.14}$$

The first two of these equations are from the standard "k-ε" models. The two additional equations are for the velocity valiance scale and the elliptic relaxation function, f_e. The turbulent time scale, t_t, turbulent length scale, L_t, and turbulent viscosity, μ_t, are calculated using the schemes

$$t_t = \min\left[t_t', \frac{\alpha E_k^{3/2}}{C_\mu \overline{\boldsymbol{u}^2}\sqrt{6S^2}}\right], \quad t_t' = \max\left[\frac{E_k}{\varepsilon_{\text{dis}}}, 6\sqrt{\frac{\nu}{\varepsilon_{\text{dis}}}}\right] \tag{4.15}$$

$$L_t = C_L \max\left[L_t', C_\eta \left(\frac{\nu^3}{\varepsilon_{\text{dis}}}\right)^{1/4}\right], \quad L_t' = \min\left[\frac{E_k^{3/2}}{\varepsilon_{\text{dis}}}, \frac{E_k^{3/2}}{C_\mu \overline{\boldsymbol{u}^2}\sqrt{6S^2}}\right] \tag{4.16}$$

$$\mu_t = \rho C_\mu \overline{\boldsymbol{u}^2} t_t \,. \tag{4.17}$$

The other constants and parameters employed in this model have the values given in Table 4.1.

Table 4.1: Parameters used in the V2F turbulence model.

Parameter	Value
α	0.6
C_1	1.4
C_2	0.3
$C_{\varepsilon 1}$	1.4
$C_{\varepsilon 2}$	1.9
C_η	70
C_μ	0.22
C_L	0.23
σ_k	1
σ_ε	1.3
$C'_{\varepsilon 1}$	$C_{\varepsilon 1}\left(1 + 0.45\sqrt{\frac{E_k}{\overline{\boldsymbol{u}^2}}}\right)$

4.3.2 Domain

An example of computational domain used in the single slot nozzle simulations is shown schematically in Figure 4.2. This domain consists of 32000 quadrilateral cells. Of those cells, 24000 are located in the impingement zone which is 240 cells in the *x*-direction by 100 cells in the *y*-direction. The other 8000 cells reside in the tailpipe zone which is 40 by 200 cells in the *x*-direction and *y*-direction, respectively. The distribution

of nodes followed a geometric progression so that finer grids were used near all walls. This progression most often used a common ratio of 1.1.

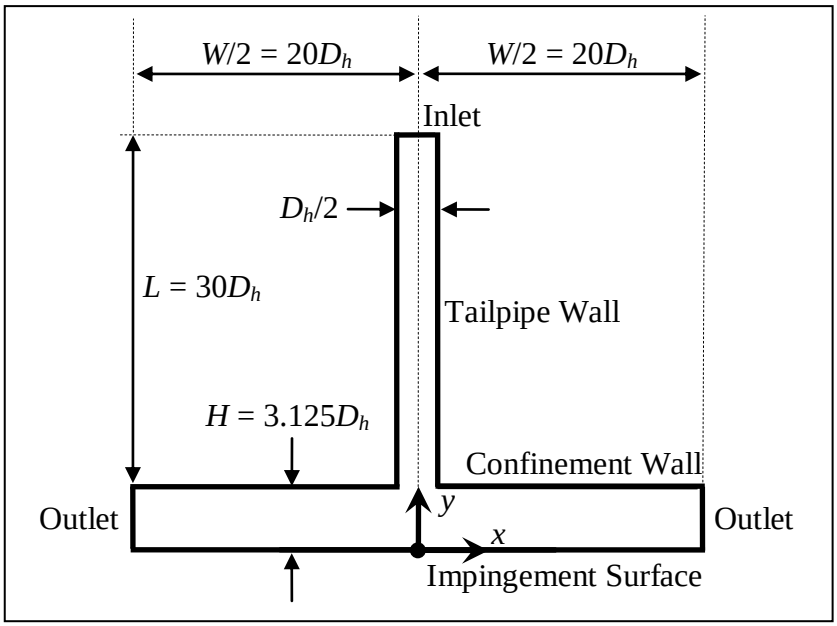

Figure 4.2: Schematic of computational domain used in single slot nozzle simulations.

The tailpipe length shown in Figure 4.2 does not correspond to the tailpipe length employed in the experimental trials. Instead, L was chosen to be sufficiently large such that the ambient fluid in the impingement zone did not reach the inlet boundary upon flow reversal.

The fluid within this domain was assumed to be air. Although slightly different than the actual combustion products from the experimental work, the properties of air are well known, simplifying the analysis. The fluid density was calculated using the ideal gas law. The specific heat capacity, thermal conductivity, and viscosity were calculated using

temperature dependent third-order, second-order, and second-order polynomial functions, respectively. These functions were derived from a least-squares curve fit to data from Incropera and DeWitt (2002).

4.3.3 Boundary Conditions

The confinement and tailpipe walls shown in Figure 4.2 were treated as stationary adiabatic surfaces. Additionally, the no-slip boundary condition was enforced as the shear condition for these walls. Although it is not physically realistic to assume zero heat flux for the tailpipe walls, this boundary condition was implemented to simplify the process of obtaining the desired outflow conditions at the exit. The impingement surface also utilized the no-slip shear condition. This boundary was either stationary or had constant velocity in the positive *x*-direction. The surface was treated as isothermal, with a constant temperature of 300 K.

For pulsating jet cases the terms "inlet" and "outlet" used in Figure 4.2 refer to the time-averaged flow condition at each boundary. Both outlets had boundary conditions of atmospheric pressure. Additionally, the backflow temperature was specified as 300 K. The turbulent viscosity ratio, μ_t/μ, was 1 and turbulence intensity, I, was 1 % for backflows at these boundaries. The inlet turbulence parameters were set to 1000 and 50 % for the turbulent viscosity ratio and turbulence intensity, respectively. These values resulted in turbulence intensity of approximately 6 % at the center of the tailpipe exit for steady flow cases. This is inline with the expected values as estimated by

$$I = 0.16 Re_{D_h}^{-1/8} , \tag{4.18}$$

an empirical relationship for fully developed internal pipe flows (FLUENT, 2006). The reference value for the turbulence intensity was the mean bulk velocity at the tailpipe exit, u_{ref}. This value also relates the turbulence intensity to the turbulence kinetic energy by

$$E_k = \frac{3}{2} (u_{\text{ref}} I)^2 . \tag{4.19}$$

The turbulent dissipation rate, ε_{dis}, is calculated as

$$\varepsilon_{\text{dis}} = \rho C_\mu \frac{E_t^2}{\mu_t} , \tag{4.20}$$

where C_μ is an empirical constant specified in the turbulence model (FLUENT, 2006). An example of the turbulent intensity at the exhaust pipe exit for a steady flow case is given in Figure 4.3.

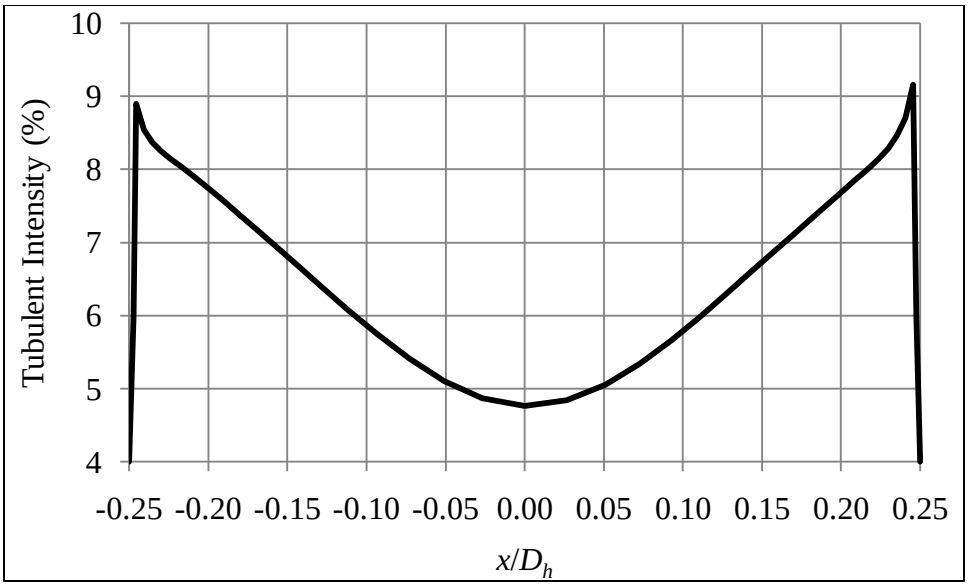

Figure 4.3: Turbulence intensity at slot tailpipe exit for a typical steady flow case.

A specified mass flux was also imposed as the inlet boundary condition. A constant mass flux was enforced for the steady flow cases and a time varying mass flux was used for the pulsed flow cases. This time dependent function can be expressed as

$$\dot{m} = \overline{\dot{m}}\left[1 + \varepsilon_{\text{amp}} \sin(\omega t)\right], \tag{4.21}$$

where $\overline{\dot{m}}$ denotes the mean mass flux. It should be noted that the amplitude of the sinusoidal oscillations, ε_{amp}, was not necessarily the same value as the amplitude of the velocity oscillations at the tailpipe exit, R_{amp}. Instead, the value of ε_{amp} was chosen to produce the desired velocity oscillations. Similarly, the inlet temperature was adjusted to obtain the desired average exit temperature.

4.3.4 Procedure

A compressible flow model was used throughout the numerical simulations. Additionally, the simulations employed a second-order upwind spatial discretization and a second-order implicit method for temporal discretization. A pressure based segregated solver was used in which the governing equations are solved for one variable at a time. The SIMPLE method of pressure-velocity coupling was employed and the default values of all under-relaxations factors were used. The scaled convergence criteria that were enforced for each time step were 1×10^{-4} for momentum and turbulence equations and 1×10^{-6} for the energy equation. For steady cases, these criteria were reduced to 1×10^{-6} for all equations.

Cases involving pulsating jets required additional criteria for classifying the flow as reaching its quasi-steady, periodic state. The simulations were run until the heat flux and tailpipe exit temperatures changed less than 1 % from one cycle to another. Simulations typically required approximately 30 cycles to reach this state.

4.4 Independence Tests

Independence tests were conducted for each domain. Sample studies demonstrating the grid and time step independence of a single nozzle domain are given below.

The time step used throughout the work was calculated by dividing an oscillation cycle into 500 equal increments. This method was employed regardless of the oscillation period encountered in each case. In order to verify that this practice produced sufficiently small time steps, quasi-steady solutions were compared using 500 and 1,000 time steps per cycle. The resultant tailpipe exit velocity in the negative *y*-direction for such a study is shown in Figure 4.4. Similarly, Figure 4.5 shows the area-averaged tailpipe exit temperature for the two different time step sizes.

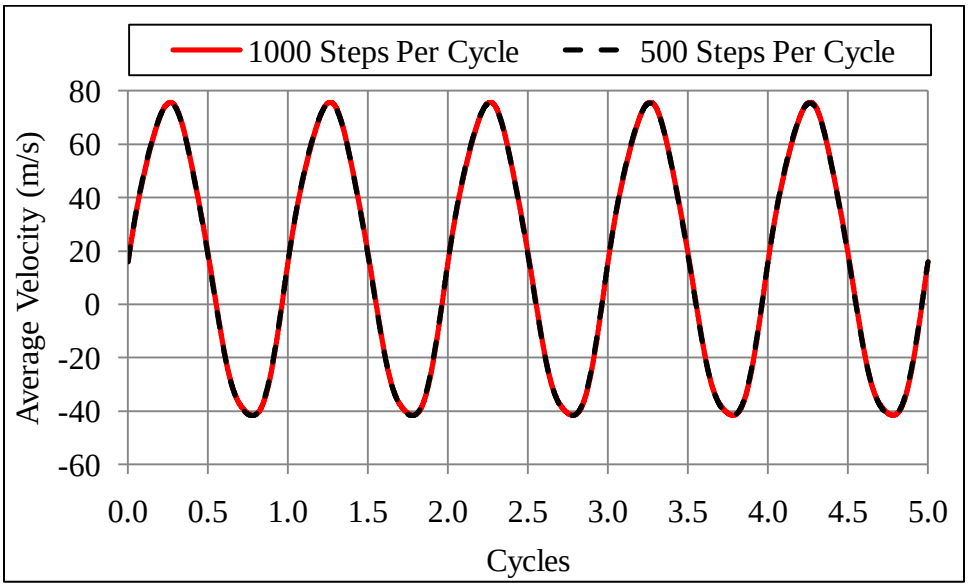

Figure 4.4: Area-averaged tailpipe exit velocity for two different time step sizes.

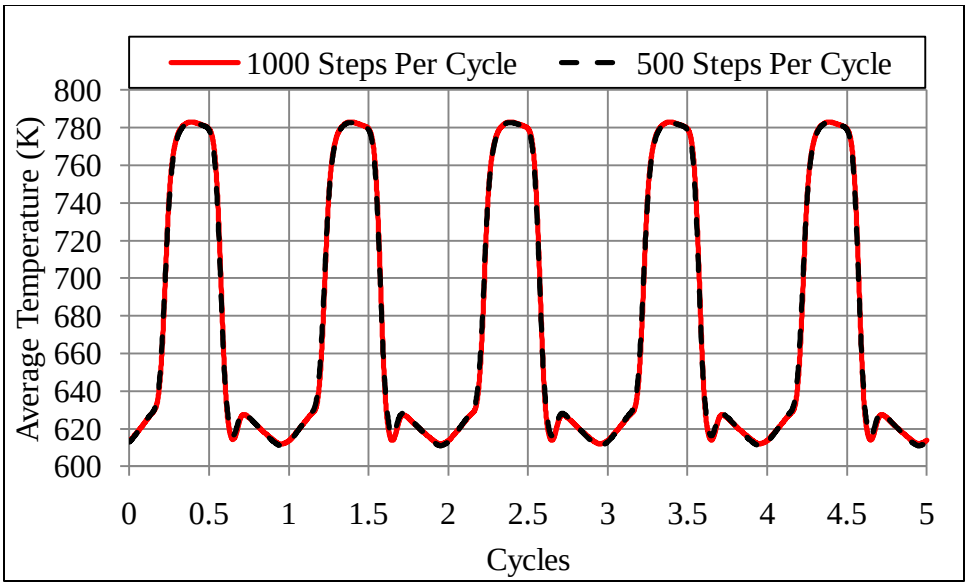

Figure 4.5: Area-averaged tailpipe exit temperature for two different time step sizes.

Figure 4.6 and Figure 4.7 show the time-averaged values of tailpipe exit velocity and impingement surface heat flux, respectively. These are presented as a function of position in the *x*-direction for the same time increments.

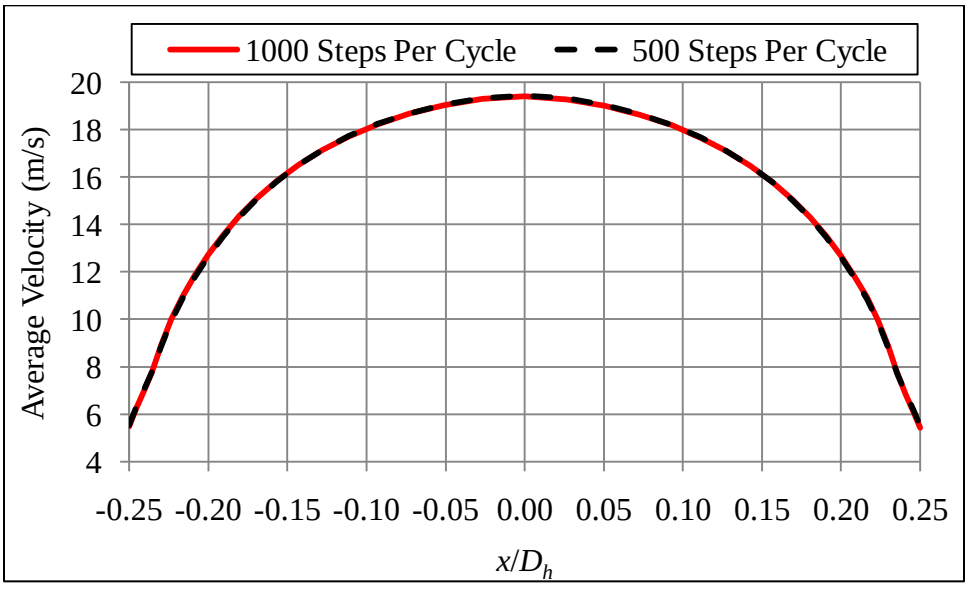

Figure 4.6: Time-averaged tailpipe exit velocity for two different time step sizes.

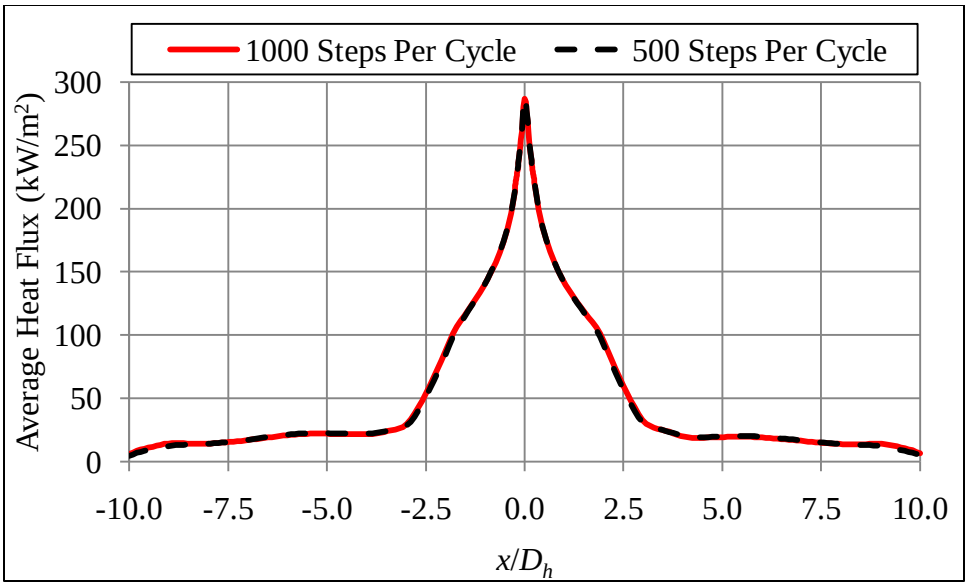

Figure 4.7: Time-averaged surface heat flux for two different time step sizes.

The results show that the reduction in time step did not alter any of the values investigated. Thus, the base time step, which was produced by dividing the oscillation into 500 increments, was deemed satisfactory. This method was employed throughout the numerical simulations of this domain.

The spatial discretization method underwent similar analyses. The domain described in section 4.3.2 was refined such that there were 50 % more elements in both the x and y directions while maintaining the same overall dimensions of the domain. Thus, there were 125 % more elements and the size of each element was decreased by approximately 66 %. Figure 4.8 shows the time-averaged heat flux on the impingement surface using both the base and refined grids.

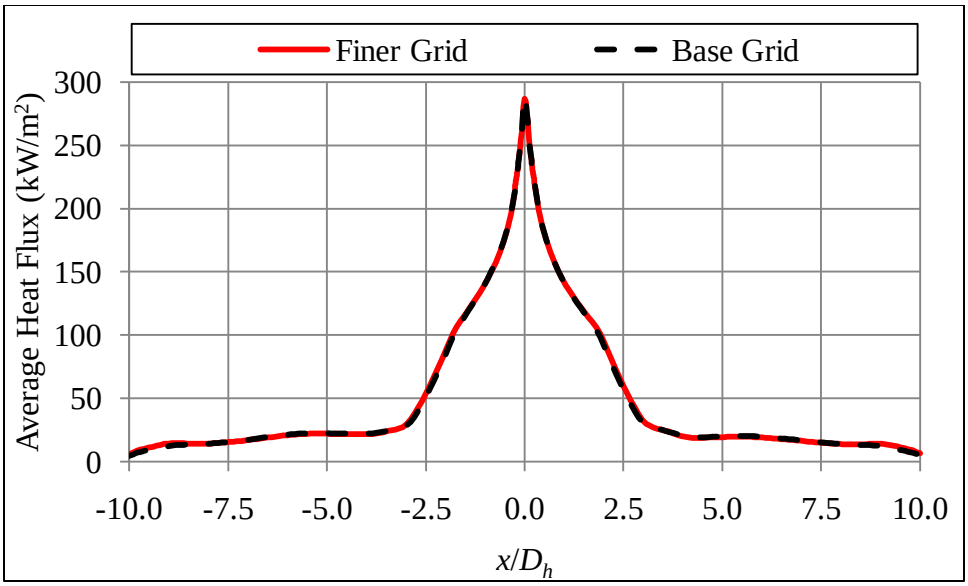

Figure 4.8: Time-averaged surface heat flux for two different grid sizes.

The decreased element size failed to yield significant changes in the solution. Therefore, the base grid was used to reduce computational costs. Although not presented, similar analyses were performed for each domain that was significantly altered from the one described in section 4.3.2. This includes both grid size and time step independence tests.

4.5 Summary and Discussion

This chapter discussed the development of the numerical model of the fluid flow in the region above the impingement surface. The governing equations employed by FUENT and the V2F turbulence model were discussed. The solution procedures presented in this chapter were followed throughout the numerical studies. Additionally, the simulation domains were similar to the one presented here. Changes in the domain

were accompanied by similar grid refinement and time discretization methods. These methods were carried out until grid size independence and time step independence were verified.

CHAPTER 5

NUMERICAL MODEL VALIDATION

5.1 Introduction

This chapter discusses the methodology used to validate the numerical model outlined in Chapter 4. The experimental results discussed in Chapter 3 were used to determine the model's performance. The pertinent simulation results, namely the impingement surface heat flux, are presented and compared with the measured values. Numerical trials corresponding to all experimental cases presented in Chapter 3 were conducted. Additionally, an empirical correlation found in literature was used to confirm the results from the model. This provided an additional method of corroboration and allowed investigation of cases other than those studied experimentally.

In order to make accurate comparisons, the simulations were conducted using the same geometry employed in the experimental tests. For multiple experimental trials that centered on a single set of conditions, the average values of these conditions were used in the simulations. For pulsed flow cases, the time-averaged heat flux from the numerical tests were used. This approach was used since the thermocouples embedded in the heat flux plate were exposed to multiple combustion cycles during any given test.

5.2 Stationary Impingement Surface

5.2.1 Approach

The experimental data from Chapter 3 was used to compare predicted and measured values of heat flux for a stationary impingement surface. Since surface temperature was only measured at a single location during these tests, the surface heat flux at the stagnation point was used to assess the performance of the model. Although this data is not as extensive as the data from the moving surface cases, cases in which heat flux profiles were obtained, it does offer a significant benefit. Specifically, the stationary surface cases lead to a more varied pool of validation cases. Not only were the trials presented in this section conducted using a different boundary condition, but they also employed different combustor geometry as well. The use of a single round nozzle produced different flow types than the slot nozzles and required the simulations to be formulated using the axisymmetric form of the governing equations. For reference, the relevant geometric parameters employed in the stationary surface cases are provided in Table 5.1.

Table 5.1: Configuration employed in experimental stationary impingement trials.

Parameter	Value
D_h	0.025 m
H	0.025 m
H/D_h	1
U_{surface}	0 m/s

5.2.2 Results

The results from the steady flow cases are reviewed first. Figure 5.1 shows a comparison of the heat flux obtained from simulations and experiments for cases HF1 through HF3. The numerical results are plotted as a function of location in order to show the predicted trend in a narrow region around the stagnation point. Although the simulation predicted $q_s^{''}|_{x/D_h=0}$ to be slightly less than the experimental values, the results are in good agreement.

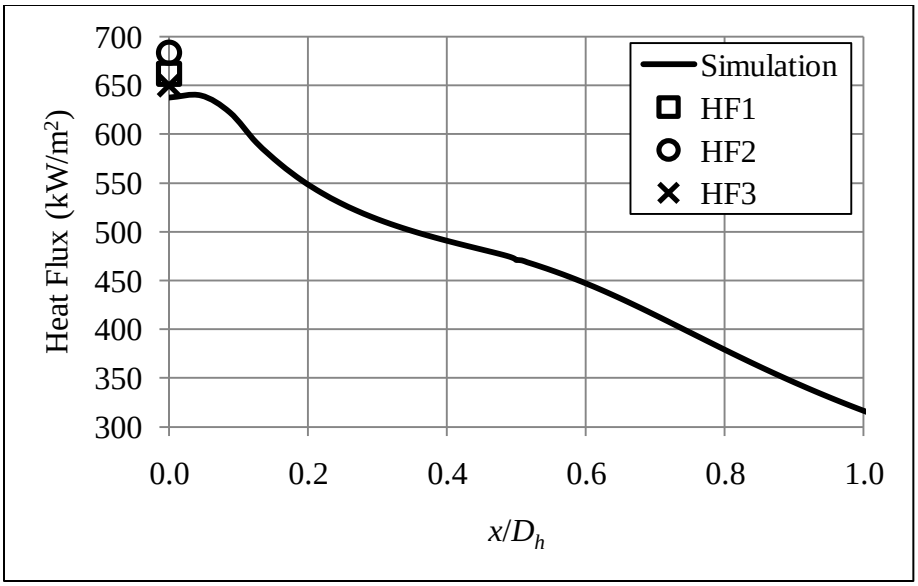

Figure 5.1: Comparison of heat flux from simulation and experiment for cases HF1-HF3.

Similar results were obtained for cases HF4 through HF7; these are shown in Figure 5.2. As with the previous comparison, the numerical results under-predicted the stagnation point heat flux.

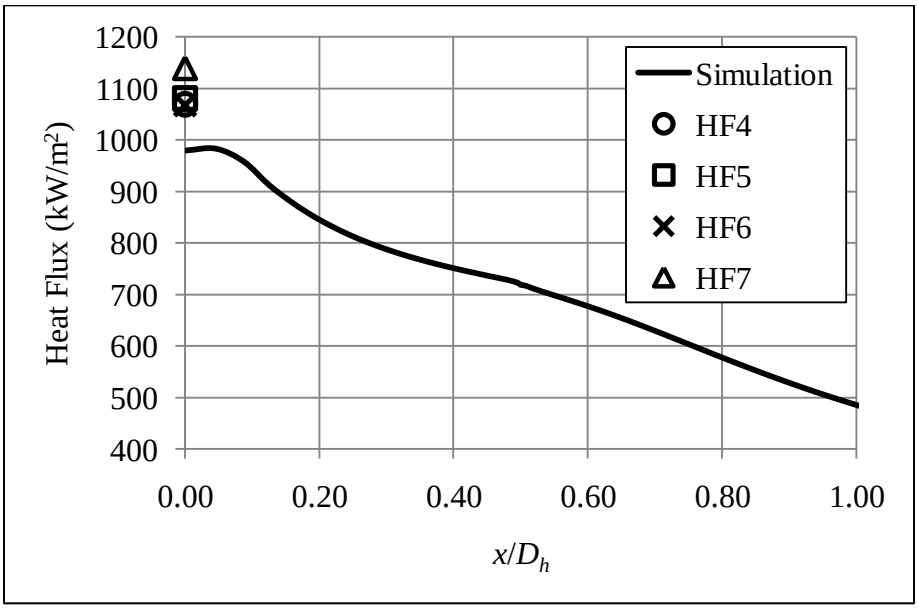

Figure 5.2: Comparison of heat flux from simulation and experiment for cases HF4-HF7.

This group of cases produced the greatest discrepancy between the predicted and measured values, the difference being 9.7 %. However, case HF7 resulted in a $q_s^{''}|_{x/D_h=0}$ value 6.3 % greater than the average of the other three experimental trials in this group. Removing HF7 from the analysis reduced the relative standard deviation of the experimental trials from 2.7 % to 0.5 %. This also reduced the average experimental value of $q_s^{''}|_{x/D_h=0}$ to only 8.3 % above the simulation results. The impact of HF7 is summarized in Table 5.2. Nevertheless, the numerical simulation produced adequate agreement for these conditions.

Table 5.2: Experimental and numerical heat flux comparison showing impact of HF7.

Case	$q_s^{''}\|_{x/D_h=0}$		Difference
	Experiment	FLUENT	
HF4	1.07×10^6 W/m^2	9.83×10^5 W/m^2	-8.0 %
HF5	1.08×10^6 W/m^2	9.83×10^5 W/m^2	-9.0 %
HF6	1.07×10^6 W/m^2	9.83×10^5 W/m^2	-7.9 %
HF7	1.14×10^6 W/m^2	9.83×10^5 W/m^2	-13.7 %
Avg. with HF7	1.09×10^6 W/m^2	9.83×10^5 W/m^2	-9.7 %
σ_{RSD} with HF7	2.7 %	-	-
Avg. without HF7	1.07×10^6 W/m^2	9.83×10^5 W/m^2	-8.3 %
σ_{RSD} without HF7	0.5 %	-	-

The results from trial HF8 are shown in Figure 5.3. In contrast to the previous cases, the simulation over-predicted $q_s^{''}|_{x/D_h=0}$ by 3.6 % when compared to the experiment. Due to such a low discrepancy the model was deemed to demonstrate good agreement with actual values.

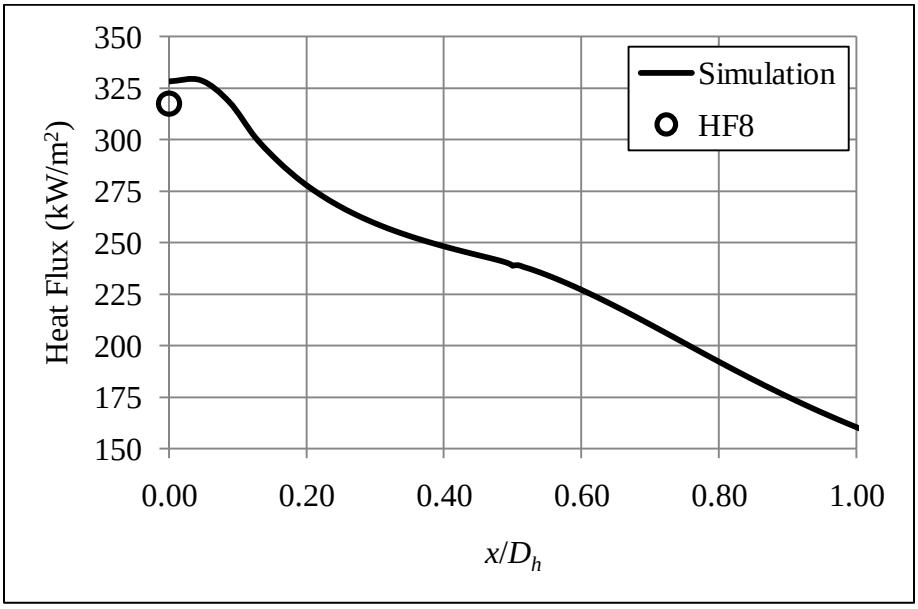

Figure 5.3: Comparison of heat flux from simulation and experiment for case HF8.

The last of the steady flow cases, HF9 through HF11, are shown in Figure 5.4. The simulation results were close to the measured values. It should be noted that Figure 5.4 presents the data for a limited range of x/D_h in order to highlight the differences between experiment and simulation. In order to provide greater context to these results, Figure 5.5 shows the surface heat flux profile for the entire simulated domain.

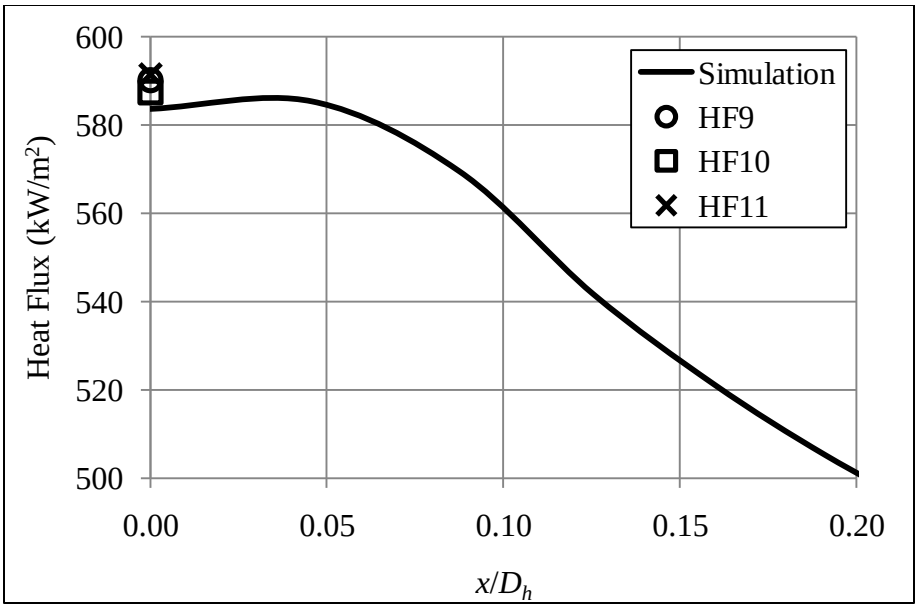

Figure 5.4: Portion of heat flux from simulation and experiment for cases HF9-HF11.

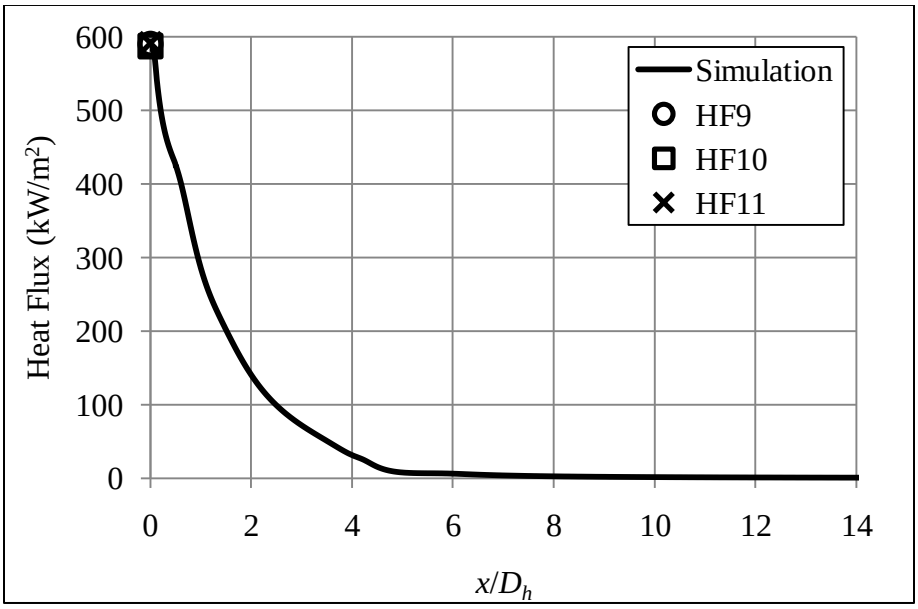

Figure 5.5: Expanded simulation and experimental results for cases HF9-HF11.

The results from the cases using a stationary surface and steady flow jet are summarized in Table 5.3. The mean mass flow rate and exhaust exit temperatures for

these cases are also presented.

Table 5.3: Summary of validation results for stationary surface and steady flow jets.

Case	$\dot{\overline{m}}$	$\overline{T}_{exit}$	$q_s^{''}\|_{x/D_h=0}$		Difference
			Experiment	FLUENT	
-	g/s	(K)	(W/m^2)	(W/m^2)	(%)
HF1	4.5	1327	6.62×10^5	6.40×10^5	-3.4
HF2	4.5	1327	6.84×10^5	6.40×10^5	-6.4
HF3	4.5	1327	6.50×10^5	6.40×10^5	-1.6
Average	-	-	6.65×10^5	6.40×10^5	-3.9
HF4	6.6	1425	1.07×10^6	9.83×10^5	-8.0
HF5	6.6	1425	1.08×10^6	9.83×10^5	-9.0
HF6	6.6	1425	1.07×10^6	9.83×10^5	-7.9
HF7	6.6	1425	1.14×10^6	9.83×10^5	-13.7
Average	-	-	1.09×10^6	9.83×10^5	-9.7
HF9	6.6	1150	5.90×10^5	5.85×10^5	-0.8
HF10	6.6	1150	5.87×10^5	5.85×10^5	-0.4
HF11	6.6	1133	5.91×10^5	5.85×10^5	-1.0
Average	-	-	5.90×10^5	5.85×10^5	-0.7
HF8	4.5	922	3.17×10^5	3.29×10^5	3.6

The results in Table 5.3 show excellent agreement throughout the trials. With the exception of HF7, all simulations were within 9 % of their corresponding experimental trials. Although the experiments only offered corroboration of stagnation point heat flux, the level of consistency presented strong evidence of the suitability of the model for these types of flows.

The results of the stationary impingement surface trials that employed pulsating impingement jets are summarized in Table 5.4. Case HF12 had an oscillation frequency of 152 Hz while that of HF13 was 177 Hz. The resulting velocity amplitude ratios were 3.67 and 3.70 for HF12 and HF13, respectively. The model over-predicted the stagnation point heat flux values for both pulsed flow cases. This still represented adequate agreement with both simulations deviating less than 10 % from the experimental values despite the disparate operating conditions of HF12 and HF13.

Table 5.4: Summary of validation results for stationary surface and pulsed flow jets.

Case	$\dot{\overline{m}}$	$\overline{T}_{exit}$	$q_s^{''}\|_{x/D_h=0}$		Difference
			Experiment	FLUENT	
-	g/s	(K)	(W/m^2)	(W/m^2)	(%)
HF12	4.5	922	4.06×10^5	4.45×10^5	9.7
HF13	6.6	1144	7.73×10^5	8.23×10^5	6.5

5.2.3 Discussion

The validation results from the stationary impingement surface cases showed excellent agreement with the experimental values. Although unable to corroborate heat flux profiles, the experimental values at the stagnation point were consistently inline with those predicted by the simulations. The heat flux enhancement factor is a key characteristic that will be used later to quantify pulsed jet. A comparison of this factor as obtained from both experiment and simulation is provided in Table 5.5.

Table 5.5: Comparison of heat flux enhancement for stationary surface tests.

Case		E_{HF}		
Steady Flow	Pulsed Flow	Experiment	Simulation	Difference
HF8	HF12	1.28	1.35	-5.9 %
HF9-HF11	HF13	1.31	1.41	-7.3 %

Table 5.5 offers additional validation of the simulation results. Despite comparing measured and predicted values for two very different exhaust flow types, the discrepancy was less than 8 %. This shows that the model not only adequately predicted the heat flux from the base cases, HF8-HF11, but also forecasted the general trends associated with introducing the exhaust oscillations.

One of the limitations of these trials is that only a limited number of trials were

conducted at each set of operating conditions. For example, only one trial was conducted for each of the outflow conditions used in trials HF8, HF11, and HF12. This allowed for a wider variety of operating conditions to be studied. The model demonstrated good agreement for two different mean mass flow rates (4.5 g/s and 6.6 g/s), three different oscillation frequencies (steady flow, 152 Hz, and 177 Hz), and a wide range of exit temperatures (922 K to 1425 K). The resulting stagnation point heat flux was accurately predicted over a range spanning an order of magnitude, from 3.17×10^5 W/m^2 to 1.14×10^6 W/m^2. In contrast, the moving surface trials focused on fewer sets of operating conditions. However, in those trials, significantly more data were compared both in terms of number of trials per condition and data points per trial.

5.3 Moving Impingement Surface – Single Nozzle

5.3.1 Approach

The results of the moving impingement surface trials afforded a more thorough assessment of the numerical model. These trials measured heat flux as a function of position. Studying the overall heat flux profiles from experiment and simulation allowed comparison between numerous data points. This also provides a more comprehensive view of the trends involved, thus producing a more rigorous evaluation of the model. In order to quantify the agreement between the predicted and measured heat flux profiles, the three characteristic quantities discussed in Chapter 3 were used. These quantities were $\overline{q}_s''\big|_{|x|\leq 0.010\text{ m}}$, $\overline{q}_s''\big|_{|x|\leq 0.030\text{ m}}$, and $\overline{q}_s''\big|_{|x|\leq 0.128\text{ m}}$.

The geometric configuration implemented in the model matched that of the laboratory trials. The pertinent dimensions are given in Table 5.6. As before, the hydraulic diameter was calculated as twice the slot width.

Table 5.6: Configuration employed in moving surface trials.

Parameter	Value
D_h	0.0128 m
H	0.020 m
H/D_h	1.56

The operational parameters employed for the trials and simulations in this section are given in Table 5.7. The oscillation frequency and velocity amplitude ratio that were employed for the pulsating impingement jet cases are also provided in this table.

Table 5.7: Operational conditions for single nozzle moving surface trials.

Parameter	Value
$\overline{\dot{m}}$	3.6×10^{-3} kg/s
$\overline{T}_{exit}$	677 K
U_{surface}	0.6 m/s
ω	135 Hz
R_{amp}	3.46

5.3.2 Sample Case

A comparison of the heat flux profiles from experiment and simulation for the steady flow case HF24 is provided in Figure 5.6. The black line in this plot is a two point moving average trend line of the experimental data, which is presented only for visual clarity. Qualitatively, the results in this plot show that the overall profiles match very well, despite the large amount of noise in the experimental data.

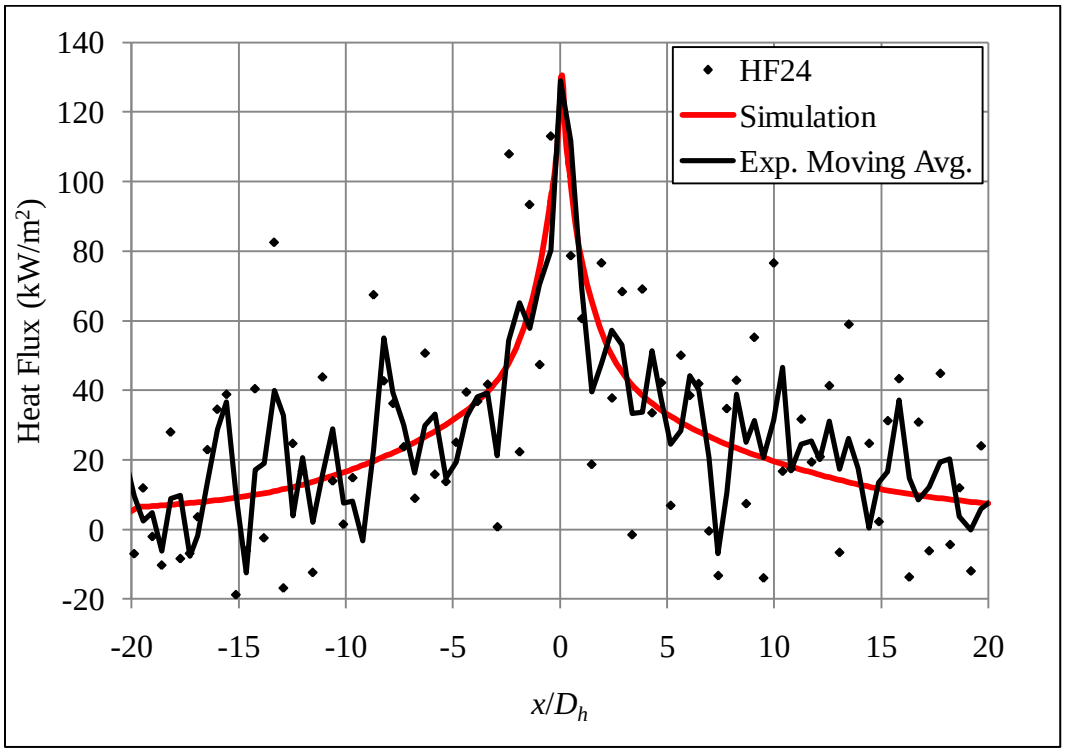

Figure 5.6: Comparison of heat flux from simulation and experiment for case HF24.

Case HF24 was chosen because it was one of the few trials in which data was collected near the stagnation point. This data sample was taken at $x/D_h = 0.0232$. As a result the peak heat flux matches well with the numerical simulations. It will be shown

later that the combination of the extremely steep heat flux profile and time based, rather than location based, sampling lead to under-represented peak heat flux values. Nevertheless, using the average heat flux over the small region surrounding the exhaust pipe centerline ($|x| \leq$ 0.01 m) allowed for appropriate comparisons to be made. Additionally, the broader ranges of $|x| \leq$ 0.03 m and $|x| \leq$ 0.128 m provide a method of quantifying the agreement in profile shape. For case HF24, these quantities are shown in Table 5.8, along with the values from the corresponding simulation.

Table 5.8: Comparison of heat flux from simulation and experiment for case HF24.

Characteristic	Experimental	Simulation	Difference
$\overline{q}_s''\big\|_{\|x\|\leq 0.010\text{ m}}$	9.24×10^4 W/m^2	9.25×10^4 W/m^2	0.2 %
$\overline{q}_s''\big\|_{\|x\|\leq 0.030\text{ m}}$	5.93×10^4 W/m^2	5.91×10^4 W/m^2	-0.3 %
$\overline{q}_s''\big\|_{\|x\|\leq 0.128\text{ m}}$	2.73×10^4 W/m^2	2.60×10^4 W/m^2	-4.8 %

Overall, the agreement with the laboratory trials was good. However, the numerical study did produce a slightly sharper heat flux profile. The peak value was over-predicted, albeit only by 0.2 %, but the average for the entire impingement zone was under-predicted by 4.8 %. Nonetheless, these values still demonstrate good agreement and bolster the validity of the model.

5.3.3 Results

The complete results for the moving surface and steady flow impingement jet trials are given in Table 5.9. Since these trials used the same set of operating conditions, the heat flux values predicted by the simulation are the ones given in Table 5.8. Namely, the model predicted $\overline{q}_s^{''}$ to be 9.25×10^4 W/m^2, 5.91×10^4 W/m^2, and 2.60×10^4 W/m^2 for the ranges $|x| \leq 0.01$ m, $|x| \leq 0.03$ m, and $|x| \leq 0.128$ m, respectively. Comparing the averages of all these cases, the model over-predicted the average heat flux for the ranges $|x| \leq 0.01$ m and $|x| \leq 0.03$ m by 3.0 % and 1.0 %, respectively. Conversely, the average value in the range $|x| \leq 0.128$ m was measured to be 2.77×10^4 W/m^2, 5.6 % higher than the 2.60×10^4 W/m^2 prediction of the model.

Table 5.9: Summary of validation results for moving surface and single, steady flow jet.

Case	$\overline{q}_s''\big\|_{\lvert x\rvert \le 0.010\ \text{m}}$		$\overline{q}_s''\big\|_{\lvert x\rvert \le 0.030\ \text{m}}$		$\overline{q}_s''\big\|_{\lvert x\rvert \le 0.128\ \text{m}}$	
	Measured	Disparity	Measured	Disparity	Measured	Disparity
-	(10^4 W/m^2)	(%)	(10^4 W/m^2)	(%)	(10^4 W/m^2)	(%)
HF14	8.54	8.3	6.19	-4.6	3.06	-15.1
HF15	8.91	3.9	5.87	0.7	2.75	-5.4
HF16	9.04	2.3	5.76	2.6	2.74	-5.2
HF17	8.94	3.5	5.87	0.7	2.80	-7.2
HF18	8.75	5.7	5.73	3.1	2.61	-0.4
HF19	8.87	4.3	5.97	-1.0	2.90	-10.3
HF20	8.79	5.2	5.74	3.0	2.61	-0.6
HF21	9.30	-0.5	5.60	5.4	2.58	0.8
HF22	9.13	1.4	6.01	-1.6	2.94	-11.7
HF23	9.56	-3.2	5.70	3.7	2.68	-3.0
HF24	9.24	0.2	5.93	-0.3	2.73	-4.8
HF25	8.88	4.2	5.86	0.9	2.66	-2.3
HF26	8.97	3.1	5.87	0.6	2.89	-10.0
Avg.	8.99	3.0	5.85	1.0	2.77	-5.8

The results for the moving surface and pulsating impingement jet trials are given in Table 5.10. The simulation resulted in time-averaged values of $\overline{q}_s''$ of 2.08×10^5 W/m^2,

1.41×10^5 W/m^2, and 4.94×10^4 W/m^2 for the ranges $|x| \leq 0.01$ m, $|x| \leq 0.03$ m, and $|x| \leq 0.128$ m, respectively. Comparing the averages of all these cases, the model over-predicted the average heat flux for the ranges $|x| \leq 0.01$ m and $|x| \leq 0.03$ m by 3.0 % and 5.0 %, respectively. As with the steady flow cases, the average value of $\overline{q}_s''$ in the range $|x| \leq 0.128$ m was under-predicted by the model. In this case, however, the disparity was 13.8 %. Although this represents a larger discrepancy, the model does agree in order of magnitude.

Table 5.10: Summary of validation results for moving surface and single, pulsed flow jet.

Case	$\overline{q}_s''\big\|_{\lvert x\rvert\leq 0.010\text{ m}}$		$\overline{q}_s''\big\|_{\lvert x\rvert\leq 0.030\text{ m}}$		$\overline{q}_s''\big\|_{\lvert x\rvert\leq 0.128\text{ m}}$	
	Measured	Disparity	Measured	Disparity	Measured	Disparity
-	(10^5 W/m^2)	(%)	(10^5 W/m^2)	(%)	(10^4 W/m^2)	(%)
HF27	1.96	6.2	1.27	11.6	5.57	-11.3
HF28	1.92	8.4	1.29	9.8	5.70	-13.2
HF29	2.01	3.4	1.40	0.8	5.83	-15.2
HF30	2.11	-1.4	1.31	8.1	5.73	-13.7
HF32	2.15	-3.5	1.41	0.0	5.79	-14.7
HF33	1.97	5.5	1.39	1.7	5.75	-14.1
HF34	2.02	2.8	1.40	0.9	5.81	-15.0
HF35	2.05	1.3	1.33	6.5	5.64	-12.4
HF36	1.98	5.2	1.32	7.1	5.77	-14.3
Avg.	2.02	3.0	1.35	5.0	5.73	-13.8

5.3.4 Discussion

The model demonstrated very good agreement with the single nozzle tests. These tests confirmed the heat flux profiles as well as the peak values. Although only two sets of operational conditions were explored in these trials, the excellent agreement in heat flux values throughout the impingement zone verifies the model's accuracy. These results also show the flexibility of the model, since the slot shaped tailpipe resulted in accurate predictions just as the round tailpipe did in the previous section.

A comparison of the heat flux enhancement factors from experiment and simulation is given in Table 5.11. These factors compare the average values for each condition. Overall the agreement is quite good. The greatest discrepancy occurred when comparing the range $|x| \leq 0.128$ m. Still, the difference of 8.3 % was deemed acceptable.

Table 5.11: Comparison of heat flux enhancement for single nozzle tests.

Criterion	E_{HF}		Difference
	Experiment	Simulation	
$\overline{q}_s''\big\|_{\|x\|\leq 0.010\text{ m}}$	2.25	2.25	-0.1 %
$\overline{q}_s''\big\|_{\|x\|\leq 0.030\text{ m}}$	2.30	2.39	-4.0 %
$\overline{q}_s''\big\|_{\|x\|\leq 0.128\text{ m}}$	2.07	1.90	8.3 %

5.4 Moving Impingement Surface – Three Nozzle

5.4.1 Approach

In order to compare the experimental and numerical results from the three nozzle trials, the average heat flux in the regions surrounding each exhaust pipe centerline were analyzed. As a departure from previous cases in which the simulation domain matched the experimental setup, a simplified domain was used. A single nozzle was modeled and the resulting heat flux was used to estimate the effect of all three nozzles. The combined heat flux of the three nozzle system was assumed to be the superposition of the heat flux produced by the individual nozzles. This is shown schematically in Figure 5.7 in which overlapping curves are simply added together to obtain the composite value. The approach greatly reduced the computational time and complexity of the domain while still providing accurate results. This approximation was only validated for the cases studied in Chapter 3. For subsequent numerical investigations in which the geometry or flow conditions diverged significantly from the multiple nozzle cases in Chapter 3, the entire domain was modeled.

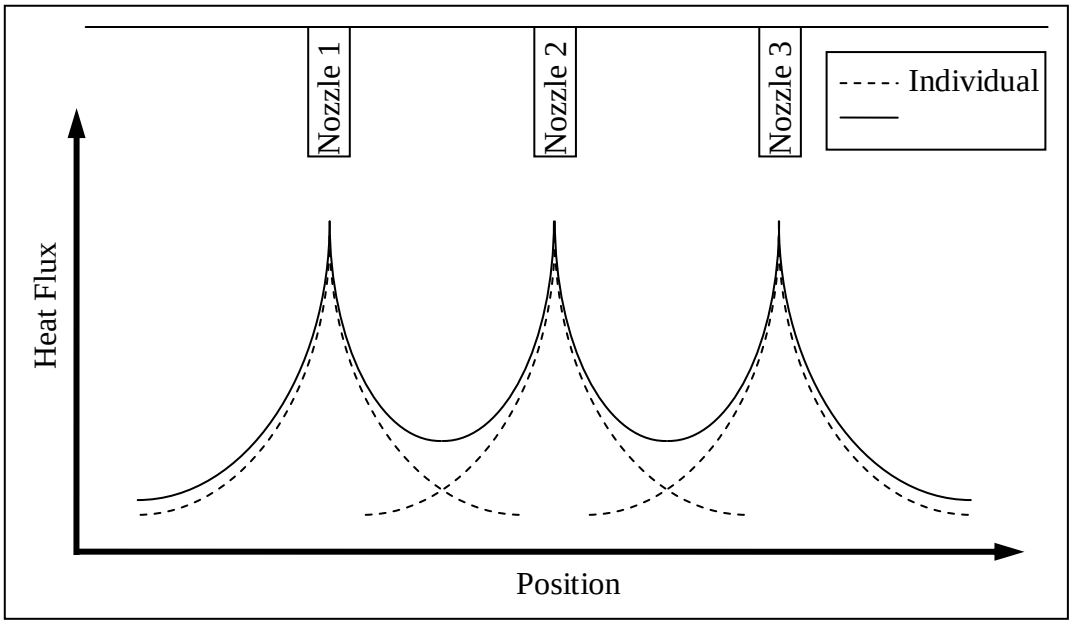

Figure 5.7: Diagram showing superposition of heat flux profiles for multiple nozzles.

Other than W_{NZ}, the geometric configuration implemented in the model matched that of the laboratory trials. These dimensions are given in Table 5.12.

Table 5.12: Configuration employed in moving surface trials.

Parameter	Value
D_h	0.0128 m
H	0.020 m
H/D_h	1.56
W_{NZ}	0.15 m

The operational parameters used in this section for both the experimental trials and simulations are given in Table 5.13. The oscillation characteristic of the pulsating jet cases are also provided in this table.

Table 5.13: Operational conditions for single nozzle moving surface trials.

Parameter	Value
$\dot{\overline{m}}$	3.6×10^{-3} kg/s
$\overline{T}_{exit}$	1005 K
U_{surface}	0.6 m/s
ω	155 Hz
R_{amp}	3.71

5.4.2 Sample Cases

Figures 5.8 through 5.10 qualitatively show the agreement between the simulations and experiment. The black lines in these plots are two point moving average trend lines. In general, the experimental and simulation heat flux results match very well in both profile shape and magnitude. However, the model did consistently produce lower heat flux in the outer regions ($|x|/D_h > 18$).

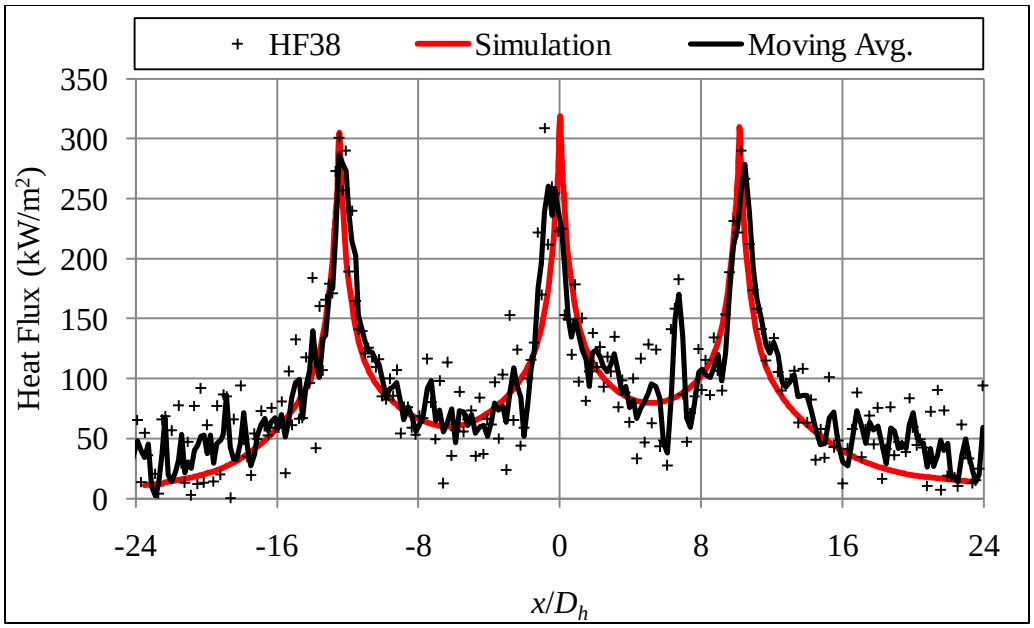

Figure 5.8: Comparison of heat flux from simulation and experiment for case HF38.

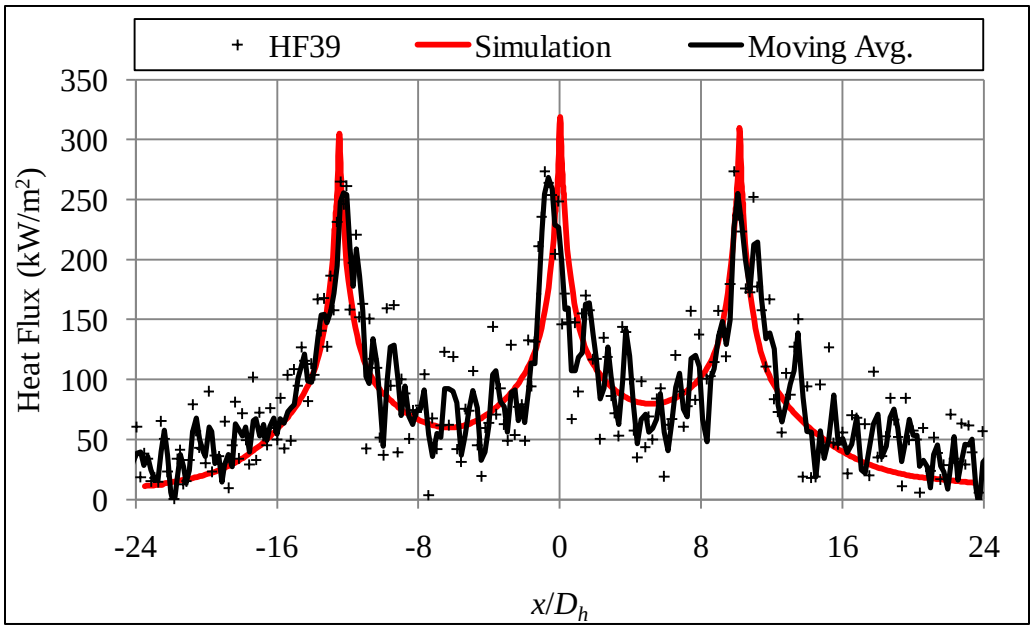

Figure 5.9: Comparison of heat flux from simulation and experiment for case HF39.

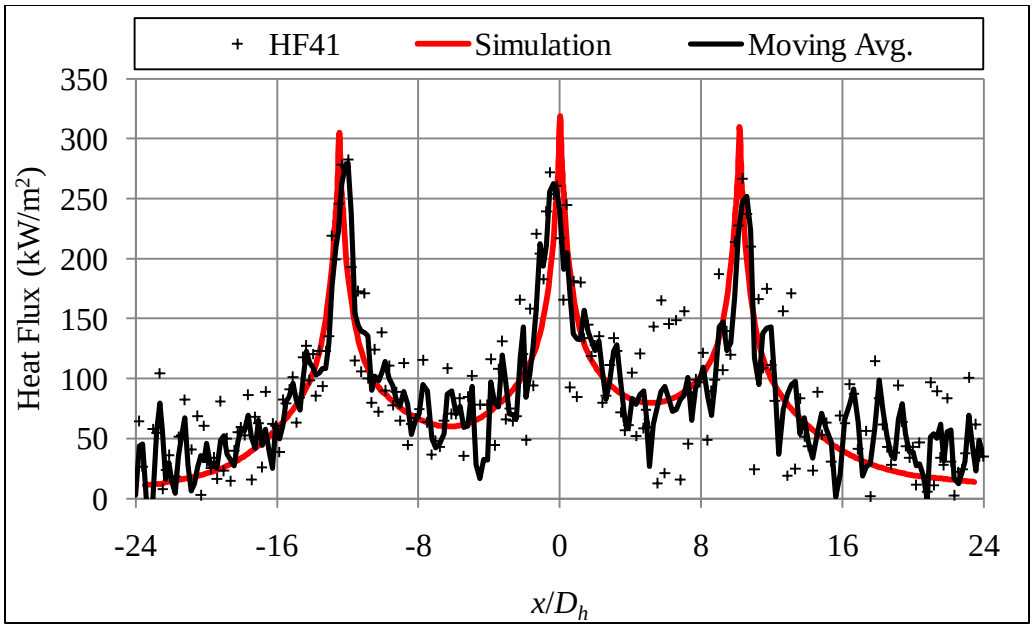

Figure 5.10: Comparison of heat flux from simulation and experiment for case HF41.

5.4.3 Results

A summary of the validation cases using steady flow is provided in Table 5.14. The heat flux values provided in this chart are the averages from cases HF37 through HF42. The model showed excellent agreement in the regions surrounding each nozzle. Nozzle 1 displayed the worst agreement, with a difference of 7.2 % in the range $|x_1| \leq 0.030$ m. As expected from Figures 5.8 through 5.10, the model did under-predict the heat flux when dealing with the range encompassing the entire impingement zone. Nevertheless, a difference of only 6.2 % still provides support for the model's validity.

Table 5.14: Summary of validation results for moving surface and steady flow jets.

Criterion	Nozzle 1			Nozzle 2			Nozzle 3		
	Exp.	Sim.	Diff.	Exp.	Sim.	Diff.	Exp.	Sim.	Diff.
-	(10^5 W/m^2)		(%)	(10^5 W/m^2)		(%)	(10^5 W/m^2)		(%)
$\overline{q}_s^{''}\big\vert_{\lvert x_n\rvert \le 0.010\text{ m}}$	2.33	2.22	-4.8	2.38	2.37	-0.6	2.28	2.23	-2.2
$\overline{q}_s^{''}\big\vert_{\lvert x_n\rvert \le 0.030\text{ m}}$	1.57	1.46	-7.2	1.65	1.60	-2.7	1.50	1.51	0.4
$\overline{q}_s^{''}\big\vert_{\lvert x_n\rvert \le 0.30\text{ m}}$	-	-	-	0.87	0.81	-6.2	-	-	-

Table 5.15 provides a similar summary of the validation cases which employed pulsed flow jets. The values here are average of cases HF43 through HF55. The agreement between experiment and simulation for thee cases, while still acceptable, was not as good as it was for the steady flow cases. The error was as high as 11.7 %, which was the disparity in average heat flux over the entire impingement zone. The other heat flux quantities from simulation were within 8.3 % of their corresponding experimental values.

Table 5.15: Summary of validation results for moving surface and pulsed flow jets.

Criterion	Nozzle 1			Nozzle 2			Nozzle 3		
	Exp.	Sim.	Diff.	Exp.	Sim.	Diff.	Exp.	Sim.	Diff.
-	(10^5 W/m^2)		(%)	(10^5 W/m^2)		(%)	(10^5 W/m^2)		(%)
$\overline{q}_s^{''}\big\vert_{\lvert x_n\rvert \le 0.010\text{ m}}$	4.93	4.92	-0.1	5.51	5.22	-5.2	4.96	4.98	0.4
$\overline{q}_s^{''}\big\vert_{\lvert x_n\rvert \le 0.030\text{ m}}$	3.26	3.39	3.9	4.05	3.74	-7.7	3.34	3.61	8.3
$\overline{q}_s^{''}\big\vert_{\lvert x_n\rvert \le 0.30\text{ m}}$	-	-	-	2.04	1.80	-11.7	-	-	-

5.4.4 Discussion

Overall, the model demonstrated good agreement with the multiple nozzle tests. The simplified method of superimposing the heat flux produced by single nozzles to form the multiple nozzle heat flux profile was shown to be adequate for these cases. This greatly reduced the computational requirements.

A comparison of the heat flux enhancement factors from the multiple nozzle experiments and simulations is given in Table 5.16. As with the previous case, these factors compare the average values for each condition. The largest discrepancy in predicted versus measured E_{HF} was obtained for nozzle 1 in the range $|x| \le 0.03$ m. This resulted from the combination of under-predicting $\overline{q}_s^{''}\big\vert_{\lvert x_n\rvert \le 0.030\text{ m}}$ for the steady flow cases and over-predicting the value for pulsed flow values. Other values of E_{HF} from

simulation were found to be within 7.8 % of the experimental values demonstrating good agreement.

Table 5.16: Comparison of heat flux enhancement for multiple nozzle tests.

Criterion	E_{HF} for Nozzle 1			E_{HF} for Nozzle 2			E_{HF} for Nozzle 3		
	Exp.	Sim.	Diff.	Exp.	Sim.	Diff.	Exp.	Sim.	Diff.
$\lvert x_n \rvert \leq 0.01$ m	2.11	2.22	-4.9 %	2.31	2.20	4.7 %	2.17	2.23	-2.6 %
$\lvert x_n \rvert \leq 0.03$ m	2.08	2.33	11.9 %	2.46	2.33	5.2 %	2.23	2.40	-7.8 %
$\lvert x_n \rvert \leq 0.30$ m	-	-	-	2.36	2.22	5.8 %	-	-	-

5.5 Single Slot Nozzle Correlation

5.5.1 Approach

In addition to the laboratory heat flux experiments, the model predictions were compared with results form an empirical correlation using steady flow jets. The correlation suggested by Martin (1977) for heat transfer due to impingement from single slot nozzle jets was used for these comparisons. This correlation can be stated as

$$\frac{\overline{Nu}}{Pr^{0.42}} = \frac{3.06}{x/W + H/W + 2.78} Re^{m} \ , \tag{5.1}$$

where the geometrical parameter m is

$$m = 0.695 - \left[\left(\frac{x}{2W}\right) + \left(\frac{H}{2W}\right)^{1.33} + 3.06\right]^{-1}. \quad (5.2)$$

The suggested range of applicability for this correlation is $3\times10^3 \leq Re \leq 9\times10^4$, where Re is based on the hydraulic diameter, D_h. The suggested geometrical restrictions are $2 \leq H/W \leq 10$ and $8 \leq x/W \leq 20$.

In order to satisfy the requirements of the correlation, the validation cases used a slot width of 6.4×10^{-3} m and $H/W = 6$. This represents a significant change in geometry from the experimental validation cases in which H/W was 1 or 3.2. Additionally, $\overline{T}_{exit}$ was chosen to be 673 K, a typical value encountered in commercial drying processes. The impingement surface temperature was a constant 373 K, roughly corresponding to surface temperatures resulting from evaporating water. These cases also employed different flow rates than those from the laboratory experiments. The four cases investigated used mean exit velocities of 8 m/s, 30 m/s, 60 m/s, and 90 m/s. The resulting Reynolds numbers ranged from 3.00×10^3 to 3.34×10^4. The Martin correlation does not take into account moving impingement surface; therefore, these cases used a stationary impingement surface.

5.5.2 Results

The results of the simulations and correlation calculations are presented in Figure 5.11, where the value U refers to the mean velocity at the tailpipe exit. The simulation results compare well with the correlation. The largest discrepancies occurred at the higher

exit velocities and at the limits of the *x*/*W* range considered. The agreement between the two methods for all four cases provides additional support for the results of the numerical model.

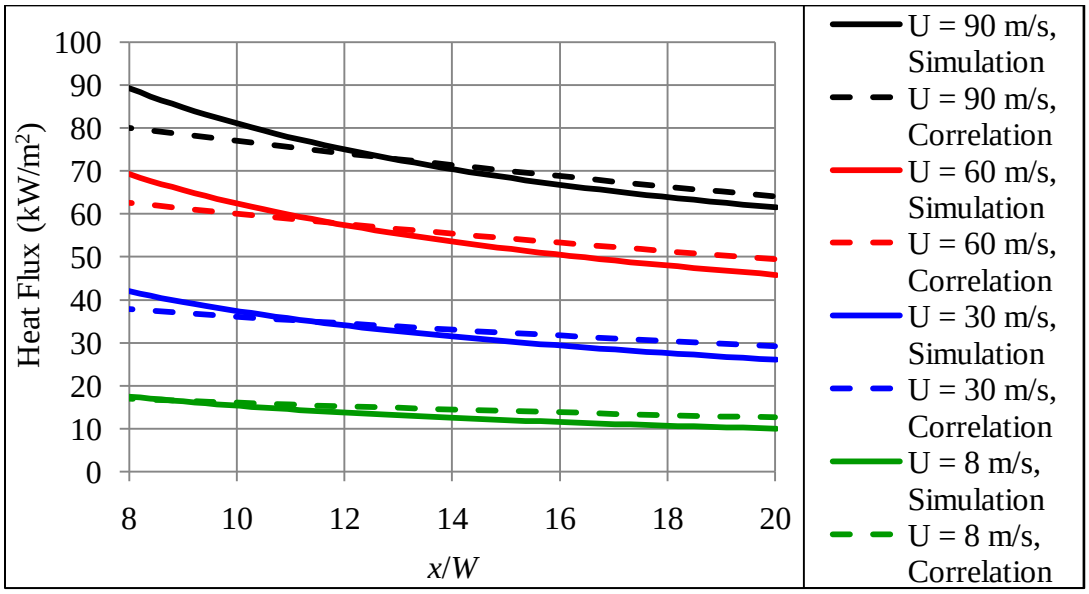

Figure 5.11: Comparison of heat flux from simulation and correlation.

5.5.3 Discussion

The correlation results offered an additional method of validating the model. This allowed comparison with cases that could not easily be reproduced in the laboratory experiments. The heat flux resulting from simulation compared well with the correlation values. The greatest disparity appeared to be at the location *x*/*W* = 8. Still, the two methods predicted values within 10 % of each other at this location for all four cases. Thus, these comparisons support the validity of the modeling results.

5.6 Summary and Discussion

The comparisons made in this chapter confirm the models findings both qualitatively and quantitatively. The simulation results consistently matched those observed in the laboratory. The peak heat flux and heat flux profiles were used to evaluate this agreement. Although the exact details of the fluid flow were not confirmed experimentally, the similarity in resultant heat flux does indicate that the fluid properties and flow conditions were likely similar near the impingement surface.

Additionally, an empirical correlation found in literature was used to assess the model's performance, providing an additional method of corroboration. This approach allowed conditions to be explored that were not easily investigated in a laboratory setting. The correlation comparisons showed good agreement using four different mean velocities at the tailpipe exit.

The model was able to accurately predict heat flux for a wide range of geometries, flow types, and operational conditions. These included round and slot shaped nozzles, stationary and moving impingement surfaces, steady and oscillating flows, and resultant heat flux values ranging from 1×10^4 to 1×10^6. Thus the model was deemed acceptable for use with the particular flows of interest to the present work.

CHAPTER 6

LABORATORY DRYING EXPERIMENTS

6.1 Introduction

This chapter describes the drying experiments that were conducted as part of the current work. These laboratory trials investigated the difference in drying rates produced by steady and pulsating impingement jets. A drying enhancement factor was used to quantify this difference. Furthermore, various porous media were used as the drying specimens in order to partially assess the effects of substrate properties. These tests utilized single and multiple nozzle configurations similar to the experiments discussed in Chapter 3. Additionally, these tests provide a means to validate the numerical drying model which is described in the next chapter.

6.2 Approach

6.2.1 Apparatus and Procedure

Experimentally determining instantaneous drying rate was not a viable research path given the goals and scope of the project. Instead, the drying tests relied on bulk drying values to quantify drying performance. The drying tests consisted of moving a wet porous sample through the impingement zone of the burners. Initial and final mass was

compared with the 378 K oven dry mass to determine the total dewatering. Additionally, total dewatering was measured for a control case in which the burners were inactive. This served as a baseline case to account for the amount of dewatering due to the experimental method itself. This dewatering included the moisture left on the sled and the evaporation that occurred during sample preparation and removal. For all cases, heat flux at the bottom of the sample was recorded using the method previously described in Chapter 3. A diagram of the experimental apparatus employed in the drying tests is given in Figure 6.1.

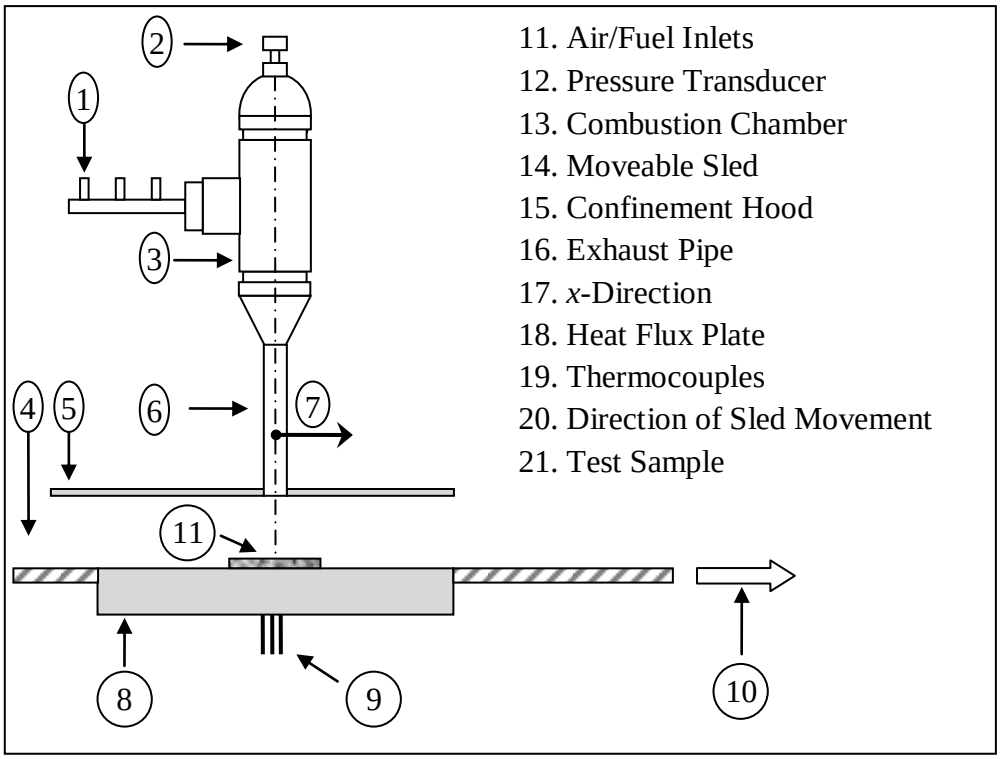

Figure 6.1: Experimental apparatus used in drying tests.

Wet samples were prepared in the manner described below. The sample was submerged in water for approximately 5 s with slight manual agitation to initially hydrate

the sample. Excess water was wiped from the sample exterior with nonabsorbent surface. The sample mass was recorded and then the sample was immediately positioned on the sled. Once the sample was in place, the sled was moved through the impingement zone while data was recorded. The sled and sample were moved through the impingement zone at constant velocity of 0.60 m/s. The sample was positioned such that it passed through the impingement zone directly under the centerline of the exhaust nozzle. Similar to the heat flux tests, the burners were placed in-line in the direction of sled movement for the multiple nozzle experiments. No tests were conducted using a stationary sled. After clearing the impingement zone, the sample was removed from the sled and stored in a sealed container of known mass. Thus, the final sample mass was calculated from the combined mass of the sample and container. The geometric parameters, such as H and D_h, matched those used in the heat flux tests. These values are given in Table 6.1.

Table 6.1: Configuration employed in drying experiments.

Parameter	Value
L	0.356 m
D_h	0.0128 m
H	0.020 m
H/D_h	1.56
U_{surface}	0.6 m/s

6.2.2 Sample Section

Sample selection was a key step in this portion of the work. Samples were chosen that covered a range of pore sizes, thermal properties, and thicknesses. A preliminary two-dimensional drying model of the porous media based on diffusion of a binary mixture, Darcy's law, and the Clausius-Clapeyron equation subject to mass, moisture, and energy conservation was used to identify key parameters and characteristics to be investigated. This also helped guide the sample choice in order to produce selections that had appropriate qualities. Although various paper samples were used, it was also desirable to perform tests on porous materials with well defined structures. Such materials are much easier to study than paper, allowing more straightforward analysis and simulations. The material that was selected, porous polytetrafluoroethylene, has a well defined pore structure and pore size distribution. Other material properties such as density, thermal conductivity, and specific heat are also well known and easy to verify. Additionally, it was desirable to employ a material that would not significantly shrink during the drying process. This eliminated the need to account for shrinkage in the numerical model, greatly simplifying the work (Karlsson and Stenström, 2005) as there was no need to predict and track material deformations. Also, it removed shrinkage as a method of dewatering, thereby simplifying the examination of the thermal and capillary forces that drive the dewatering (Katekawa and Silva, 2006). Thus, the use of a rigid material greatly reduced the complexity of the model and, therefore, the computational costs.

The samples chosen for this role were porous polytetrafluoroethylene (PFTE) sheets ranging from 6.1×10^{-4} m to 1.57×10^{-3} m in thickness. Pore sizes ranged from 1.5×10^{-5} m to 1.30×10^{-4} m and both hydrophilic and hydrophobic samples were used. A summary of the PTFE materials that were used in the drying experiments is given in Table 6.2. All test specimens were 0.025 m by 0.127 m sheets. The sheet thickness is in the direction normal to the heated surface.

Table 6.2: Properties of polytetrafluoroethylene samples used in drying experiments.

Material ID	Thickness	Pore Size	Water Interaction
-	(10^{-3} m)	(10^{-6} m)	-
PTFE-1	0.61	75-110	Hydrophilic
PTFE-2	1.57	90-130	Hydrophobic
PTFE-3	1.57	15-45	Hydrophilic
PTFE-4	2.38	50-90	Hydrophilic

The pore size ranges listed in Table 6.2 are the values given by the PTFE sheet manufacturer. In the modeling and simulations, however, experimental values from permeability tests were used. A sample of the permeability test results is given in Figure 6.2.

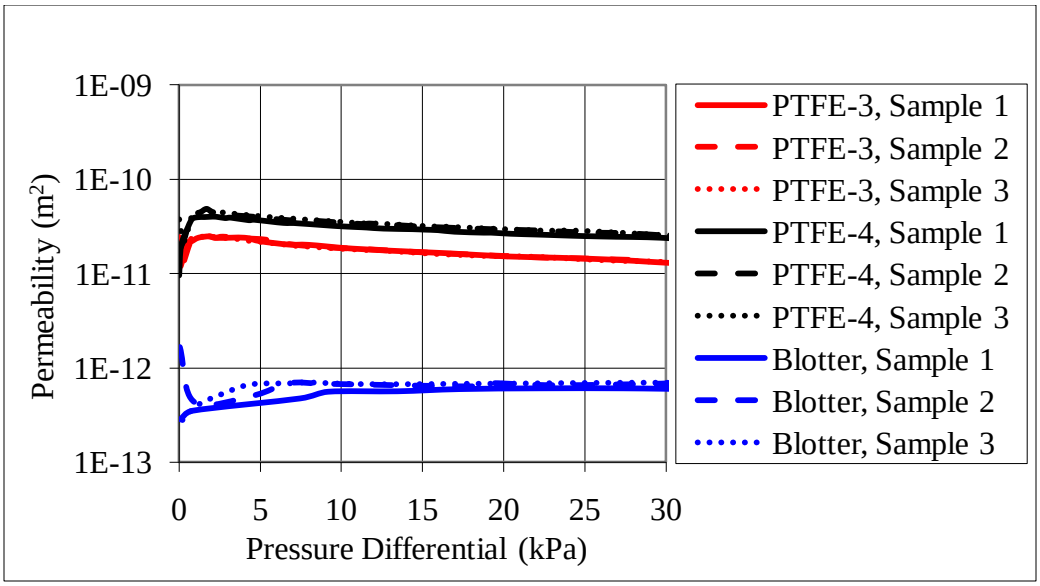

Figure 6.2: Permeability test results for PTFE-3, PTFE-4, and blotter paper.

Additionally, the results of the porosity of the materials are given in Table 6.3. These values were obtained using the volume, density, and 378 K oven dry sample weight.

Table 6.3: Calculated porosity of polytetrafluoroethylene samples.

Material ID	Average Porosity	σ_{RSD}
PTFE-1	0.783	2.6 %
PTFE-2	0.854	2.5 %
PTFE-3	0.817	2.7 %
PTFE-4	0.825	3.3 %

In addition to the polytetrafluoroethylene samples, experiments were conducted using blotter paper which had a thickness of 5.0×10^{-4} m. Therefore, the experimental matrix consisted of two flow types (pulsed and steady), single and triple nozzle configurations, and five different sample materials. In combination with the control cases, there were a total of 25 drying test configurations. For each of these configurations, 6 to 12 trials were conducted, resulting in a total of 240 individual drying tests. The variation in number of tests conducted for each configuration was simply the result of availability of sample material. For example, more blotter paper was available; thus, additional tests were permitted using this material.

6.3 Single Nozzle Tests

6.3.1 Approach

The single nozzle drying tests for the steady and pulsed flow cases were setup in such manner that the same time-averaged exhaust jet conditions existed for both cases. Each setup was used to dry all five sample materials. Other than the test specimen, the only factor that was varied was the flow type: either steady flow or pulsed flow. This allowed direct comparisons to be made between the two flow types, resulting in a better assessment of the effects due to flow pulsations. The operational parameters used in the single nozzle tests are given in Table 6.4. The relative standard deviations in $\overline{T}_{exit}$ and ω throughout all the single nozzle experiments were 1.1 % and 0.9 %, respectively.

Table 6.4: Operational characteristics for single nozzle tests.

Parameter	Value
$\dot{\overline{m}}$	3.7×10^{-3} kg/s
$\overline{T}_{exit}$	697 K
ω	135 Hz
R_{amp}	3.43

6.3.2 Sample Cases

The single nozzle drying results for material PTFE-1 are given in Table 6.5 and serve as an example of the data obtained from the drying experiments. The mass of the solid, m_s, is equal to the oven dry weight of each sample.

Table 6.5: Results of single nozzle drying tests for material PTFE-1.

Type	Case	m_s	$m_{l,i}$	$m_{l,f}$	Δm_l	$\overline{s}_i$	$\overline{s}_f$	$\Delta\overline{s}$
-	-	(10^{-4} kg)	(10^{-4} kg)	(10^{-4} kg)	(10^{-4} kg)	-	-	-
Steady	D1-1	9.26	8.55	7.84	-0.71	0.563	0.516	-0.047
	D1-2	9.35	8.52	7.80	-0.72	0.555	0.509	-0.047
	D1-3	9.40	8.90	8.27	-0.63	0.577	0.536	-0.041
	D1-4	9.11	8.83	8.01	-0.82	0.591	0.535	-0.055
	D1-5	9.15	8.55	7.84	-0.71	0.569	0.522	-0.047
	D1-6	9.38	8.90	8.14	-0.76	0.578	0.528	-0.050
	D1-7	9.03	8.49	7.75	-0.74	0.573	0.523	-0.050
	Avg.	9.24	8.68	7.95	-0.73	0.572	0.524	-0.048
Pulsed	D1-8	9.55	8.58	7.54	-1.04	0.547	0.481	-0.066
	D1-9	9.19	7.96	7.00	-0.96	0.528	0.464	-0.064
	D1-10	9.56	8.24	7.32	-0.92	0.525	0.467	-0.059
	D1-11	9.16	8.21	7.01	-1.20	0.546	0.467	-0.080
	D1-12	8.96	8.10	7.13	-0.97	0.551	0.485	-0.066
	D1-13	9.41	8.58	7.57	-1.01	0.556	0.490	-0.066
	D1-14	9.23	8.16	7.18	-0.98	0.539	0.474	-0.064
	Avg.	9.29	8.26	7.25	-1.01	0.542	0.475	-0.066

The average liquid saturation, $\overline{s}$, is defined as

$$\overline{s} = \overline{\phi}_l \Big/ \overline{\phi}\,, \tag{6.1}$$

where $\overline{\phi}_l$ is the ratio of the liquid volume to the total volume. The total volume is sometimes referred to as apparent volume and is the sum of the volumes of all species in the sample. Similarly, the porosity, $\overline{\phi}$, is the ratio of the void volume to the total volume. The use of the accent bars in these terms denotes average values. In subsequent modeling work the matrix is assumed to have uniform structure and thus constant porosity. Therefore, the accent bar will be dropped from $\overline{\phi}$ in later formulations. For reference, the saturation is related to the volumetric liquid moisture content, MC_v, mass based liquid moisture content, MC, and solids ratio by mass, S_{mass}, through

$$MC_v = \frac{V_l}{V_{total}} = \frac{V_l}{V_{void}}\phi = s\phi\,, \tag{6.2}$$

$$\frac{1}{MC} = \frac{m_{total}}{m_l} = \frac{m_l + m_s}{m_l} = 1 + \frac{m_s}{m_l} = 1 + \frac{\rho_s V_s}{\rho_l V_l} = 1 + \frac{\rho_s(1-\phi V_{total})}{\rho_l s\phi V_{total}}\,, \tag{6.3}$$

$$\frac{1}{S_{mass}} = \frac{m_{total}}{m_s} = \frac{m_s + m_l}{m_s} = 1 + \frac{m_l}{m_s} = 1 + \frac{\rho_l V_l}{\rho_s V_s} = 1 + \frac{\rho_s s\phi V_{total}}{\rho_l(1-\phi V_{total})}\,, \tag{6.4}$$

respectively.

The pulsed flow conditions produced a significantly greater change in saturation levels. This can be quantified be the drying enhancement factor, E_{DRY}. This factor is calculated as

$$E_{DRY} = \frac{\text{change in bulk saturation due to pulsed flow}}{\text{change in bulk saturation due to steady flow}} = \frac{(\Delta\overline{s})_{\text{pulsed}}}{(\Delta\overline{s})_{\text{steady}}}, \tag{6.5}$$

for the same mean exhaust exit temperature and time-averaged mass flow rate. For the single nozzle drying tests conducted with material PTFE-1 the drying enhancement factor was 1.38. While still significant, this factor was not as high as the heat flux enhancement factors encountered in Chapter 3 for similar flow conditions.

6.3.3 Results

A summary of the single nozzle drying test results for all of the materials is given in Table 6.6. The values in Table 6.6 are the average values of the 6 to 12 test runs for each condition defined by sample material and flow type. The pulsed conditions consistently resulted in greater reductions in saturation levels. For reference, the range of PTFE saturation values given in Table 6.6 corresponds to approximately 50 % to 57 % solids by mass.

Table 6.6: Results of single nozzle drying tests.

Matl.	Type	m_s	$m_{l,i}$	$m_{l,f}$	Δm_l	$\overline{s}_i$	$\overline{s}_f$	$\Delta\overline{s}$
-	-	(10^{-4} kg)	(10^{-4} kg)	(10^{-4} kg)	(10^{-4} kg)	-	-	-
PTFE-1	Steady	9.24	8.68	7.95	-0.73	0.572	0.524	-0.048
	Pulsed	9.29	8.26	7.25	-1.01	0.542	0.475	-0.066
PTFE-2	Steady	19.70	22.61	22.02	-0.59	0.432	0.421	-0.011
	Pulsed	19.45	23.03	21.71	-1.32	0.445	0.420	-0.026
PTFE-3	Steady	24.56	18.75	18.43	-0.32	0.377	0.371	-0.006
	Pulsed	24.60	19.03	18.51	-0.52	0.383	0.372	-0.011
PTFE-4	Steady	47.93	43.83	43.34	-0.49	0.427	0.422	-0.005
	Pulsed	47.32	45.02	44.21	-0.81	0.443	0.435	-0.008
Blotter	Steady	8.09	18.26	17.66	-0.60	0.624	0.604	-0.021
	Pulsed	8.14	18.07	17.28	-0.78	0.614	0.587	-0.027

6.3.4 Discussion

The drying enhancement factors for the single nozzle tests are given in Table 6.7. These results were varied, with a minimum enhancement factor of 1.29 and a maximum value of 2.28. These enhancement factors were obtained for the blotter paper and PTFE-2, respectively.

Table 6.7: Drying enhancement for single nozzle tests.

Material	E_{DRY}
PTFE-1	1.38
PTFE-2	2.28
PTFE-3	1.63
PTFE-4	1.69
Blotter	1.29

Taking into consideration the similar flow conditions, the varied enhancement factors and water removal rates indicate that material properties are a significant factor in the drying process. One such property that appears to be related to the drying enhancement is the substrate porosity. Figure 6.3 is a plot of the drying enhancement versus substrate porosity.

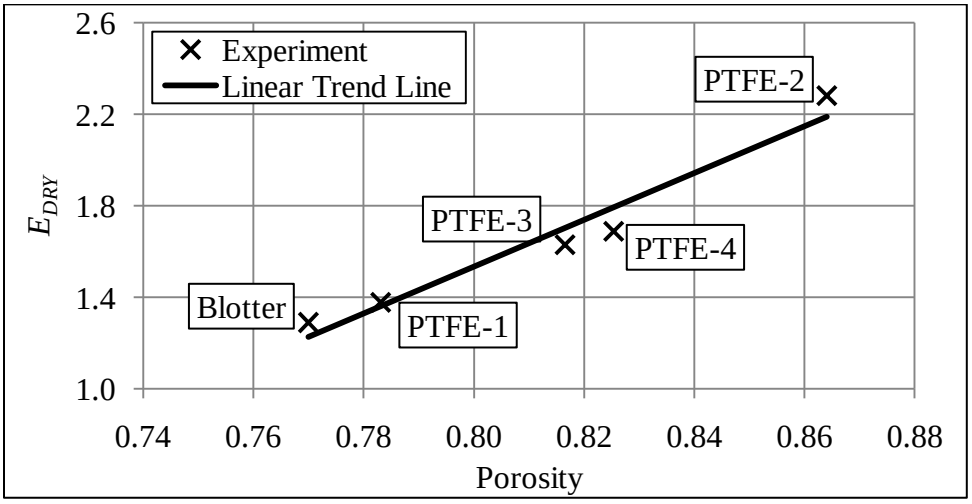

Figure 6.3: Drying enhancement versus porosity for single nozzle tests.

The solid line in Figure 6.3 is a least-squares fit linear trend line. The coefficient of determination, in this case simply the square of the sample correlation coefficient, is 0.952. The F-statistic is 59.49 with only a 0.453 % chance of a higher F-statistic occurring by chance. For the 3 degrees of freedom in this case, the critical value of the F-statistic is 10.13 using a significance level, α, of 0.05. Therefore, the linear relationship is statistically significant. For reference, the t-statistic for this case is 7.712, which is greater than the critical value of 3.182 associated with a significance level of 0.05. However, caution should be used when studying these statistics. Although they do indicate that a relationship exists, it does not necessarily mean that the porosity is a true cause of the changes in the drying enhancement. Omitted-variable bias or the presence of collinearity in the data might exist which could also account for the findings. Additionally, these findings do not assess the appropriateness of the specific regression type. However, these analyses were not intended to discern the exact relationship between the substrate properties and drying enhancement. Instead they were simply meant to show that a correlation does exist.

6.4 Three Nozzle Tests

6.4.1 Approach

The three nozzle tests also centered on one set of time averaged operational conditions. Due to the added heat from the additional burners, the mean exhaust exit temperature was higher than in the single nozzle experiments. The operational parameters used in the three nozzle tests are given in Table 6.8. The relative standard deviations in

$\overline{T}_{exit}$ and ω throughout the three nozzle experiments were 0.3 % and 0.6 %, respectively. Using these operational conditions, the flow type was the only factor that was intentionally varied, other than the test specimen.

Table 6.8: Operational characteristics for single nozzle tests.

Parameter	Value
$\overline{\dot{m}}$	3.7×10^{-3} kg/s
$\overline{T}_{exit}$	1005 K
ω	164 Hz
R_{amp}	3.61

6.4.2 Sample Case

Again, the results of the three nozzle drying tests for material PTFE-1 are given in Table 6.9 as an example of the data produced by the testing. As expected, the three nozzle system consistently produced greater water removal than the single nozzle system.

Table 6.9: Results of three nozzle drying tests for material PTFE-1.

Type	Case	m_s	$m_{l,i}$	$m_{l,f}$	Δm_l	$\overline{s}_i$	$\overline{s}_f$	$\Delta\overline{s}$
-	-	(10^{-4} kg)	(10^{-4} kg)	(10^{-4} kg)	(10^{-4} kg)	-	-	-
Steady	D1-15	9.26	8.75	7.01	-1.74	0.576	0.461	-0.115
	D1-16	9.35	8.37	6.71	-1.66	0.545	0.437	-0.108
	D1-17	9.40	8.29	6.61	-1.68	0.537	0.428	-0.109
	D1-18	9.11	8.67	7.07	-1.60	0.580	0.473	-0.107
	D1-19	9.15	8.69	7.06	-1.63	0.579	0.470	-0.109
	D1-20	9.38	8.45	6.63	-1.82	0.549	0.431	-0.118
	Avg.	9.28	8.54	6.85	-1.69	0.561	0.450	-0.111
Pulsed	D1-21	9.75	8.57	5.81	-2.77	0.536	0.363	-0.173
	D1-22	9.19	8.54	6.14	-2.40	0.566	0.407	-0.159
	D1-23	9.86	8.48	5.94	-2.54	0.524	0.367	-0.157
	D1-24	9.56	8.52	5.70	-2.82	0.543	0.363	-0.180
	D1-25	8.96	8.09	5.79	-2.30	0.550	0.394	-0.157
	D1-26	9.41	8.35	6.01	-2.34	0.541	0.389	-0.151
	Avg.	9.46	8.43	5.90	-2.53	0.543	0.380	-0.163

The drying enhancement factor for the three nozzle drying tests conducted with material PTFE-1 was found to be 1.47. This again demonstrates the mass transport advantage produced by the pulsed flow. This value was slightly higher than the enhancement factor of 1.38 encountered in the single nozzle tests for the same material.

6.4.3 Results

The three nozzle drying test results for all of the materials are given in Table 6.10. These results are the average values for each condition defined by sample material and flow type. The trends observed in the sample case continued for the other tests. The pulsed conditions resulted in greater reductions in saturation levels and the overall water removal was greater than that of the single nozzle tests.

Table 6.10: Results of three nozzle drying tests.

Matl.	Type	m_s	$m_{l,i}$	$m_{l,f}$	Δm_l	$\overline{s}_i$	$\overline{s}_f$	$\Delta\overline{s}$
-	-	(10^{-4} kg)	(10^{-4} kg)	(10^{-4} kg)	(10^{-4} kg)	-	-	-
PTFE-1	Steady	9.28	8.54	6.85	1.69	0.561	0.450	-0.111
	Pulsed	9.46	8.43	5.90	2.53	0.543	0.380	-0.163
PTFE-2	Steady	19.70	22.68	21.38	1.30	0.433	0.409	-0.025
	Pulsed	19.45	22.78	20.11	2.66	0.440	0.389	-0.051
PTFE-3	Steady	24.56	20.56	19.21	1.35	0.414	0.387	-0.027
	Pulsed	24.60	20.64	18.21	2.44	0.415	0.366	-0.049
PTFE-4	Steady	47.32	45.16	44.13	1.03	0.445	0.434	-0.010
	Pulsed	47.93	46.37	44.50	1.86	0.451	0.433	-0.018
Blotter	Steady	8.20	20.01	18.45	1.56	0.675	0.623	-0.052
	Pulsed	8.18	19.98	17.74	2.24	0.677	0.601	-0.076

6.4.4 Discussion

The drying enhancement factors for the three nozzle tests are given in Table 6.11, along with the corresponding values from the single nozzle tests. The enhancement factors from the three nozzle tests were within 12 % of those from the complimentary single nozzle experiments. As before, the blotter paper and PTFE-2 produced the minimum and maximum values of E_{DRY}, respectively.

Table 6.11: Average drying enhancement for single and three nozzle tests.

Material	E_{DRY}	
	Single Nozzle	Three Nozzles
PTFE-1	1.38	1.47
PTFE-2	2.28	2.07
PTFE-3	1.63	1.80
PTFE-4	1.69	1.78
Blotter	1.29	1.45

The three nozzle tests add further evidence of the presence of a relationship between substrate properties and drying enhancement. Figure 6.4 is a plot of the drying enhancement versus substrate porosity for the three nozzle system.

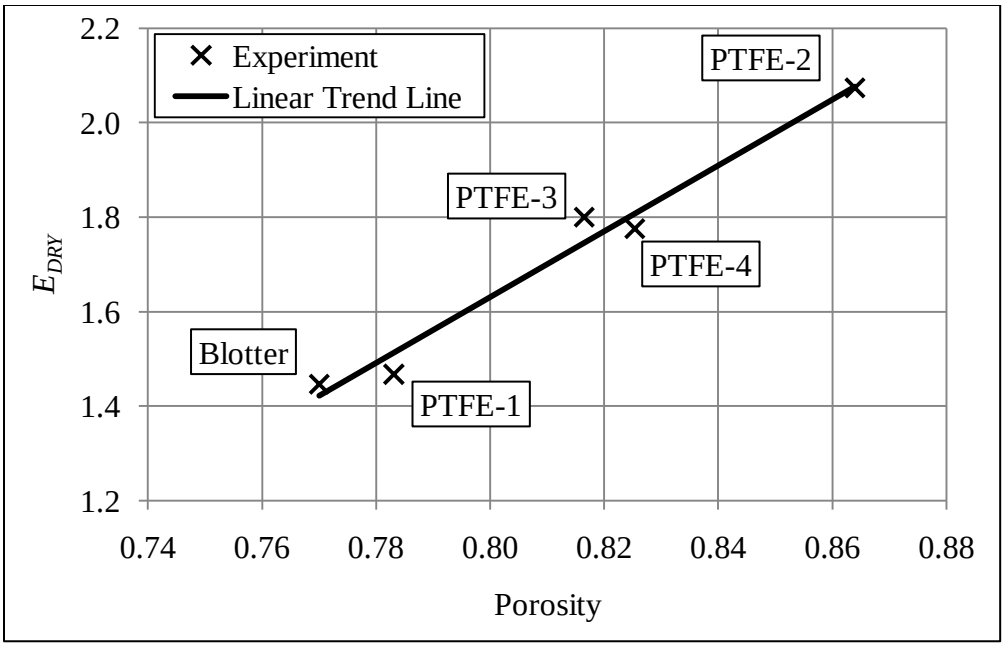

Figure 6.4: Drying enhancement versus porosity for three nozzle tests.

The solid line in Figure 6.4 is a least-squares fit linear trend line with a coefficient of determination of 0.975. The F-statistic is 119.43, with only a 0.164 % chance of a higher F-statistic occurring by chance. Similarly, the t-statistic for this case is 10.93. As before, the critical values of the F-statistic and t-statistic are 10.13 and 3.182, respectively, for a significance level of 0.05. Therefore, the linear relationship is again statistically significant.

6.5 Summary and Discussion

The pulsed flow conditions yielded greater mass transfer in all cases investigated. This drying enhancement appeared to be partially related to the substrate properties such as the porosity. Additionally, the three nozzle system produced increased drying and,

with the exception of PTFE-2, also increased the drying enhancement factor. The range of E_{DRY} spanned from 1.29 to 2.28, representing substantial increases in mass transfer.

The increase in drying performance is likely due to the same mechanism that is thought to produce increased heat flux, which is strong recirculating flow in the impingement zone (Liewkongsataporn et al., 2008). The confinement wall that was employed in these tests created an ideal situation for the pulsating jet vortices to combine to form this larger recirculating structure. Due to experimental limitations, direct evidence of the presence of these structures is not available. However, when compared with other numerical simulations, the ranges of U_{amp} and R_{amp} calculated from experimental data do indicate that recirculating flows were created (Liewkongsataporn et al., 2006). Although steady jets produce vortices due to flow instabilities, the vortices are much less organized than those from pulsating jets (Mladin and Zumbrunnen, 1997). The resulting flow structures from steady flow jets are much different than those produced by pulsating jets. Steady flow impingement is more likely to produce a wall jet that flows along the surface of the impingement target. The pulsating jet outlet flow, however, is likely to turn upward after impinging on the sample. The flow will then curl around to produce the recirculating flow previously discussed. This is diagramed in Figure 6.5.

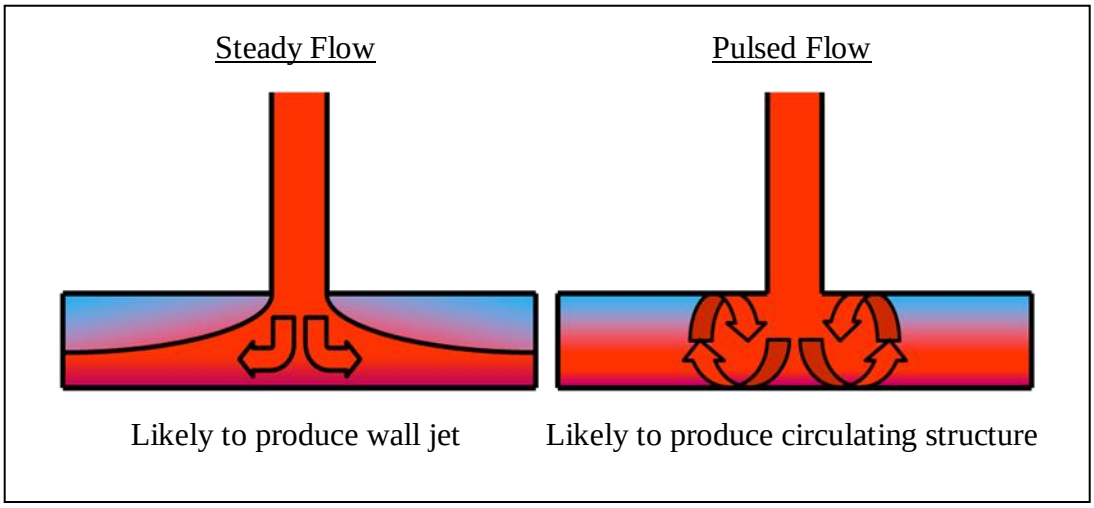

Figure 6.5: Comparison of likely flow structures due to steady and pulsed exhaust flow.

This provides an additional mechanism for heat and mass transfer during the tailpipe flow reversal portion of the combustion cycle. That is, the recirculating flow continues convective heat and mass transfer with the sample during tailpipe flow reversal. This is the behavior that is believed to be most responsible for the drying enhancement. The fact that the three burner systems yielded higher drying rates than similar single burner configurations is an expected result since there was simply more energy input and the temperature was higher. This also offers a possible explanation for the reduction in E_{DRY} from 2.28 in the single nozzle case to 2.07 for the three nozzle case. The combination of a hydrophobic material and low initial saturation could have led to slight dry out of the surface when subjected the high heat flux of the three nozzle pulsed system.

The experimental heat flux tests were used to substantiate the observed drying rates. This was done strictly as an order of magnitude comparison used to corroborate the

reasonableness of the results, not the specific values. By assuming that all the energy that was imparted to the sample was converted to sensible and latent heat only for the mass which was vaporized, one may use Δm_l to estimate said energy transfer. Since the sled velocity and impingement zone size are known, the dwell time can also be estimated, giving the average rate of energy transfer. This can then easily be expressed as a flux given that the sample sizes are known. Clearly, these assumptions only offer approximate values. In comparison with the heat flux tests conducted at similar operating conditions, the above described calculations yielded heat flux within approximately 15 % of the measured area-averaged values. Although only the order of magnitude may be accurately assessed, these comparisons did verify the range of drying rates.

CHAPTER 7

DRYING MODEL

Rather than attempting to use a single numerical model to study both the fluid flow above the sheet and the transport processes within the sheet, the problem was split into two separate domains. This chapter describes the derivation and implementation of the drying model. Just as FLUENT was used to investigate only the region above the sheet, Matlab was employed to model the processes within the substrate. This model was coupled with the FLUENT simulations through the conditions at the interface boundary. More specifically, the heat transfer coefficients, jet temperatures, and pressure profiles that were predicted by FLUENT at the impingement surface were used to specify the drying model's boundary conditions. This approach was employed because it was a time efficient yet effective method of accomplishing the large scale goals of this project. The model's design, while an important and significant undertaking, was not the primary goal but rather a means to an end. That is, the model was simply a tool used to study the pertinent phenomena, rather than being the focus of the work itself. As such, designing a single unified model of the entire process would not only be beyond the scope of this project, but would be at the expense of answering the primary research questions.

7.1 Introduction

A porous medium is a complex system consisting of a solid matrix permeated by a network of fluid filled voids. As a result, modeling the drying of this inherently multiphase system presents unique challenges. Heat and mass transfer in all phases must be considered simultaneously. The particular fluid phases and species in this work are liquid water, its vapor, and air. The basis of the numerical model is the construction of the relevant equations from a volume-averaged, macroscopic viewpoint. These macroscopic equations are formulated by averaging classical fluid mechanics and transport equations over a representative volume that is large compared to the pore size. Additionally, the primary assumptions employed in the analysis are:

1. The solid, liquid, and gaseous phases are in thermodynamic equilibrium locally
2. The solid matrix can be considered rigid with negligible shrinkage or deformation
3. The water vapor, air, and their gaseous mixture behave as ideal gases
4. The heat and mass transport within the medium are two-dimensional processes due to symmetry in the third dimension
5. Inertia and viscous dissipation effects are negligible
6. The energy transport mechanisms are conduction in all phases and convection in the fluid phases

A two-dimensional treatment is employed due to the additional complexities added by the pulsating nature of the impingement jet. Namely, the pulsating jet results in

heat and mass transfer at the impingement surface that vary not only with position, but with time as well. A diagram of this two-dimensional domain is provided in Figure 7.1. The subscript *m* applied to the coordinate system is used to differentiate it from the coordinate system used in previous chapters. In those chapters, the coordinate system was associated with the stationary nozzle, and the media moved through this reference frame. In this chapter, however, x_m and y_m form a reference frame that is fixed with the media.

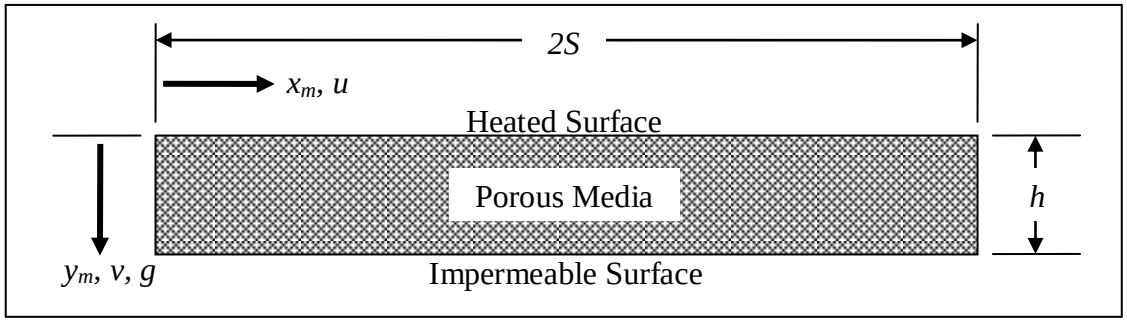

Figure 7.1: Two-dimensional domain of the porous media.

The assumption of a rigid solid matrix greatly simplifies the analysis. Under this assumption, tracking of the matrix material is not necessary and mechanical dewatering as a result of shrinkage is eliminated.

7.2 Conservation Equations

Given these assumptions, the conservation of mass may be expressed using Whitaker's volume-averaging approach (Whitaker and Chou, 1983) for the liquid phase as

$$\frac{\partial}{\partial t}(\phi_l \rho_l) + \boldsymbol{\nabla} \cdot (\phi_l \rho_l \boldsymbol{u}_l) = -\dot{m} \tag{7.1}$$

where $\dot{m}$ is the rate of liquid evaporation (Nasrallah and Perre, 1988). This liquid is converted to water vapor; therefore, it appears in the resulting mass conservation equation for the vapor phase as

$$\frac{\partial}{\partial t}(\phi_v \rho_v) + \boldsymbol{\nabla} \cdot (\phi_v \rho_v \boldsymbol{u}_v) = \dot{m} \, . \tag{7.2}$$

This also affects the gas phase conservation of mass equation which becomes

$$\frac{\partial}{\partial t}\left(\phi_g \rho_g\right) + \boldsymbol{\nabla} \cdot \left(\phi_g \rho_g \boldsymbol{u}_g\right) = \dot{m} \, . \tag{7.3}$$

The gas mixture and liquid velocities are given by Darcy's law. Darcy's equation was initially considered to be an equation of motion for a fluid moving through a homogeneous, isotropic porous medium. However, its applicability has been extended to include other flows in which inertial effects are negligible (Scheidegger, 1972). Therefore, by assuming negligible viscous and inertial effects, the liquid and gaseous momentum conservation equations can be replaced with Darcy's equations (Lu and Shen, 2007). Using relative permeability tensors, the liquid velocity is

$$\boldsymbol{u}_l = -\frac{\widehat{\boldsymbol{K}}\widehat{\boldsymbol{K}}_l}{\mu_l \phi_l}\left[\boldsymbol{\nabla}\left(P_g - P_c\right) + \rho_l \boldsymbol{g}\right] . \tag{7.4}$$

The pressure term in this equation can be restated as simply P_l by

$$P_l = P_g - P_c \ . \tag{7.5}$$

Darcy's equation for the gas phase takes the form

$$\boldsymbol{u}_g = -\frac{\hat{\boldsymbol{K}}\hat{\boldsymbol{K}}_g}{\mu_g \phi_g} \boldsymbol{\nabla} P_g \tag{7.6}$$

since gravitational effects are neglected.

Additionally, the diffusion of water vapor in this binary gas mixture results in a vapor phase velocity of (Huang, 1978)

$$\phi_v \rho_v \boldsymbol{u}_v = \phi_v \rho_v \boldsymbol{u}_g - \phi_g \rho_g D_{\text{eff}} \boldsymbol{\nabla} \left(\frac{\rho_v}{\rho_g} \right) \tag{7.7}$$

where D_{eff} is an effective isotropic diffusion coefficient which accounts for diffusion resistance variations due to tortuosity and constriction.

With the aid of the mass conservation equations, energy conservation can be stated as

$$\frac{\partial}{\partial t} \left[\overline{\phi \rho c_p} T \right] + \boldsymbol{\nabla} \cdot \left[\left(\phi_l \rho_l c_{pl} \boldsymbol{u}_l + \phi_v \rho_v c_{pv} \boldsymbol{u}_v + \phi_a \rho_a c_{pa} \boldsymbol{u}_a \right) T \right]$$

$$= \boldsymbol{\nabla} \cdot (\lambda_{\text{eff}} \boldsymbol{\nabla} T) - \Delta h^{o}_{\text{vap}}\, \dot{m} \tag{7.8}$$

by assuming constant specific heats. The quantity $\overline{\phi \rho c_p}$ in the storage term is the constant pressure heat capacity of the medium, which is given by

$$\overline{\phi \rho c_p} = \phi_l \rho_l c_{pl} + \phi_v \rho_v c_{pv} + \phi_a \rho_a c_{pa} + \phi_s \rho_s c_{ps} \ . \tag{7.9}$$

Additionally, $\Delta h^{o}_{\text{vap}}$ is related to the enthalpy of vaporization, Δh_{vap}, by the relationship (Huang, 1978)

$$\Delta h^{o}_{\text{vap}} = \Delta h_{\text{vap}} + \left(c_{pl} - c_{pv}\right) T \ . \tag{7.10}$$

7.3 Thermodynamic Relations

The gaseous phase is treated as an ideal mixture of perfect gases. As such, the water vapor and air pressures can be calculated by the Clapeyron equation

$$\rho_n = \frac{P_n M_n}{RT}; \quad n = a, v \tag{7.11}$$

where R is the universal gas constant. Additionally, the density of the mixture becomes

$$\rho_g = \rho_a + \rho_v \ , \tag{7.12}$$

and Dalton's law provides a relationship for the gas pressure as simply the sum of the partial pressures of the individual species. That is,

$$P_g = P_a + P_v \, . \tag{7.13}$$

The vapor pressure is given by the Clausius-Clapeyron equation by assuming that the media contains free water during the drying process. The resulting equation is (Whitaker and Chou, 1983)

$$P_v = P_{v,\mathrm{ref}} \exp\left[-\frac{M_a h_{a,\mathrm{vap}}}{R}\left(\frac{1}{T} - \frac{1}{T_{v,\mathrm{ref}}}\right)\right] . \tag{7.14}$$

where the reference values, $P_{v,ref}$ and $T_{v,ref}$, from Whitaker and Chou (1983) were used.

7.4 Constitutive Relations

The capillary force is calculated using Leverett J-function (Leverett, 1941)

$$P_c = \sqrt{\frac{\phi}{K}}\sigma J \tag{7.15}$$

where the quantity J may be evaluated by

$$J = \frac{0.005}{s - 0.08} + 0.22(1 - s) + 0.364\{1 - \exp[-40(1 - s)]\} \, . \tag{7.16}$$

where s is the liquid saturation. The surface tension in equation 7.15 can be represented as a linear function of temperature

$$\sigma = \sigma_0 - \beta T \tag{7.17}$$

where σ_0 and β are empirical constants (Carey, 2008).

The effective diffusivity can be found using the relationship given by Lu and Shen (2007)

$$D_{\text{eff}} = 2.175 \times 10^{-5} \left(\frac{101325}{P_g}\right)\left(\frac{T}{273.18}\right)^{1.88} . \tag{7.18}$$

This dimensional equation requires T to be specified in degrees Kelvin and P_g in Pa. The resulting units of effective diffusivity are m^2/s.

The isotropic relative permeabilities are functions of the liquid saturation, s, such that (Scheidegger, 1972)

$$K_g = 1 - 1.1s \tag{7.19}$$

$$K_l = \left(\frac{s - s_0}{1 - s_0}\right)^3 . \tag{7.20}$$

The liquid saturation is the ratio of the liquid phase volume fraction to the porosity. Therefore, the volume fractions of each of the species are given by

$$\phi_l = \phi s \tag{7.21}$$

$$\phi_s = 1 - \phi \tag{7.22}$$

$$\phi_g = \phi_a = \phi_v = \phi(1 - s)\ . \tag{7.23}$$

These volume fractions are used to calculate an effective thermal conductivity in the medium. The form of this volume-averaged relationship was proposed by Kingeny et. al. (1976) as

$$\lambda_{\text{eff}} = \left(\lambda_g^m \phi_g + \lambda_s^m \phi_s + \lambda_l^m \phi_l\right)^{\frac{1}{m}}\ . \tag{7.24}$$

7.5 Initial Conditions

The initial temperature profile is specified and the gas mixture pressure is taken as atmospheric. Therefore,

$$T|_{t=0} = T_{\text{initial}} \tag{7.25}$$

$$P_g\big|_{t=0} = P_{\text{atm}}\ . \tag{7.26}$$

The moisture content is initially distributed in hydrostatic equilibrium. That is,

$$\left.\frac{\partial P_c}{\partial y}\right|_{t=0} = \rho_l \boldsymbol{g} \, . \tag{7.27}$$

7.6 Boundary Conditions

The lower boundary located at $y_m = h$ is treated as an impermeable surface. The corresponding zero air and moisture flux conditions on this boundary can be stated as

$$\phi_l \rho_l v_l = 0 \tag{7.28}$$

$$\phi_v \rho_v v_v = 0 \tag{7.29}$$

$$\phi_g \rho_g v_g = 0 \, . \tag{7.30}$$

Additionally, this surface is assumed to be adiabatic. Therefore, the heat flux is simply

$$\lambda_{\text{eff}} \left.\frac{\partial T}{\partial y}\right|_{y_m = h} = 0 \, . \tag{7.31}$$

At the permeable heated surface $(y_m = 0)$, the moisture flux condition is

$$\phi_v \rho_v v_v + \phi_l \rho_l v_l = \frac{k_m M_v}{R}\left(\frac{P_v}{T} - \frac{\psi P_{v,\text{sat}}}{T_{\text{jet}}}\right) \tag{7.32}$$

where the jet temperature is specified. The convective mass transfer coefficient is

$$k_m = \frac{k_t}{\rho_a C_{pa}} Le^{-2/3} \tag{7.33}$$

and the Lewis number is defined as (Kaviany and Mittal, 1987)

$$Le = \frac{\alpha_{\text{jet}}}{D_{va}} . \tag{7.34}$$

The diffusion coefficient of water vapor in air, D_{va}, is calculated using a quadratic curve fit (Nellis and Klein, 2009) to data from Bolz and Tuve (1979)

$$D_{va} = -2.775 \times 10^{-6} + (4.479 \times 10^{-8})T + (1.656 \times 10^{-10})T^2 \tag{7.35}$$

using temperature units of degrees Kelvin.

The heat flux at the permeable surface is continuous, leading to

$$\lambda_{\text{eff}} \frac{\partial T}{\partial x_m} + \phi_l \rho_l u_l h_{\text{vap}} = k_t \left(T_{\text{jet}} - T\right) . \tag{7.36}$$

Finally, the pressure on this surface is specified such that

$$P_g = P_{\text{jet}} \tag{7.37}$$

where P_{jet} is the pressure of the impinging jet.

7.7 Numerical Method

A finite difference method is used to carry out the analysis. The control domain employs an offset grid configuration similar to the one proposed in Patankar (1980). In this configuration the velocity components are associated with grids that are different from the one used for all other variables. The velocity components are calculated on the faces of the control volumes. This grid configuration is shown in Figure 7.2, along with the nomenclature used in the discretization equations.

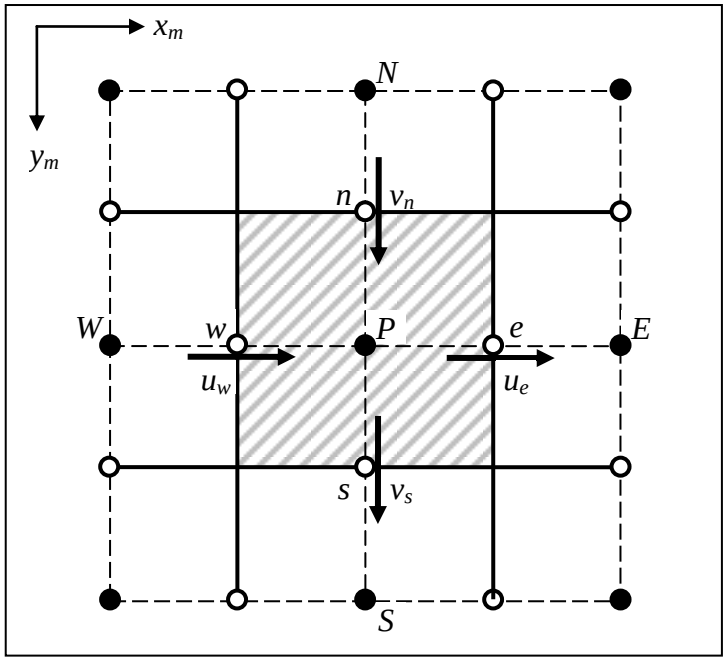

Figure 7.2: Nomenclature and grid configuration used in discretized equations.

The shaded region is the control volume associated with grid point *P*. It is separated from its neighboring main grid points (*N*, *E*, *S*, and *W*) by the control volume faces represented by solid lines. The velocity components are calculated on these faces at the points *n*, *e*, *s*, and *w*. The locations of the x_m-direction velocity components are staggered only in the x_m-direction. Similarly, the y_m-direction velocity components are staggered only in the y_m-direction. As a result, calculating the mass flow rate across a control volume face does not require interpolation of velocity components. Additionally, the pressure differential between two adjacent, rather than alternating, grid points drives the fluid flow across the control volume interface. This eliminates the masking of a wavy or alternating pressure field that might occur if all variables were calculated at the same grid points. Similar consequences of wavy velocity fields are avoided since the discretized continuity equations involve differences between adjacent velocity components. Using an implicit scheme, these equations are

$$[(\phi_l\rho_l)_P - (\phi_l\rho_l)_P^o]\frac{\Delta x_m \Delta y_m}{\Delta t} + [(\phi_l\rho_l u_l)_e - (\phi_l\rho_l u_l)_w]\Delta y_m + [(\phi_l\rho_l v_l)_s - (\phi_l\rho_l v_l)_n]\Delta x_m = -\dot{m}\Delta x_m \Delta y_m \tag{7.38}$$

$$[(\phi_v\rho_v)_P - (\phi_v\rho_v)_P^o]\frac{\Delta x_m \Delta y_m}{\Delta t} + [(\phi_v\rho_v u_v)_e - (\phi_v\rho_v u_v)_w]\Delta y_m + [(\phi_v\rho_v v_v)_s - (\phi_v\rho_v v_v)_n]\Delta x_m = \dot{m}\Delta x_m \Delta y_m \tag{7.39}$$

$$\left[(\phi_g\rho_g)_P - (\phi_g\rho_g)_P^o\right]\frac{\Delta x_m \Delta y_m}{\Delta t} + \left[(\phi_g\rho_g u_g)_e - (\phi_g\rho_g u_g)_w\right]\Delta y_m + \left[(\phi_g\rho_g v_g)_s - (\phi_g\rho_g v_g)_n\right]\Delta x_m = \dot{m}\Delta x_m \Delta y_m \tag{7.40}$$

where the superscripts indicate that the quantities $(\phi_i \rho_i)^o$ are evaluated at time t while all others are evaluated at time $t + \Delta t$. The subscripts *n*, *e*, *s*, *w*, *N*, *E*, *S*, *W* and *P* refer to the grid point location. The treatment of the momentum conservation equations leads to discretized Darcy equations of the form

$$(u_l)_e \Delta x_m = -\left(\frac{KK_l}{\mu_l \phi_l}\right)_e \left[\left(P_g - P_c\right)_E - \left(P_g - P_c\right)_P\right] \tag{7.41}$$

$$(v_l)_s \Delta y_m = -\left(\frac{KK_l}{\mu_l \phi_l}\right)_s \left[\left(P_g - P_c + \rho_l g\right)_S - \left(P_g - P_c + \rho_l g\right)_P\right] \tag{7.42}$$

for the liquid phase, and

$$\left(u_g\right)_e \Delta x_m = -\left(\frac{KK_g}{\mu_g \phi_g}\right)_e \left[\left(P_g\right)_E - \left(P_g\right)_P\right] \tag{7.43}$$

$$\left(v_g\right)_s \Delta y_m = -\left(\frac{KK_g}{\mu_g \phi_g}\right)_s \left[\left(P_g\right)_S - \left(P_l\right)_P\right] \tag{7.44}$$

for the gaseous phase.

The vapor diffusion equations take on the discretized form

$$(\phi_v \rho_v u_v)_e \Delta x_m = \left(\phi_v \rho_v u_g\right)_e \Delta x_m - \left(\phi_g \rho_g D_{\text{eff}}\right)_e \left[\left(\frac{\rho_v}{\rho_g}\right)_E - \left(\frac{\rho_v}{\rho_g}\right)_P\right] \tag{7.45}$$

$$(\phi_v \rho_v v_v)_s \Delta y_m = \left(\phi_v \rho_v v_g\right)_s \Delta y_m - \left(\phi_g \rho_g D_{\text{eff}}\right)_s \left[\left(\frac{\rho_v}{\rho_g}\right)_S - \left(\frac{\rho_v}{\rho_g}\right)_P\right]. \qquad (7.46)$$

Finally, the discretized equation of energy conservation is

$$\begin{aligned}
&\frac{1}{\Delta t}\left[\left(\overline{\phi\rho c_p}T\right)_P - \left(\overline{\phi\rho c_p}T\right)_P^o\right] \\
&+\frac{1}{\Delta x_m}\Big\{\left[\left(\phi_l\rho_l c_{pl}u_l + \phi_v\rho_v c_{pv}u_v + \phi_a\rho_a c_{pa}u_a\right)T\right]_e \\
&\qquad - \left[\left(\phi_l\rho_l c_{pl}u_l + \phi_v\rho_v c_{pv}u_v + \phi_a\rho_a c_{pa}u_a\right)T\right]_w\Big\} \\
&+\frac{1}{\Delta y_m}\Big\{\left[\left(\phi_l\rho_l c_{pl}u_l + \phi_v\rho_v c_{pv}u_v + \phi_a\rho_a c_{pa}u_a\right)T\right]_s \\
&\qquad - \left[\left(\phi_l\rho_l c_{pl}u_l + \phi_v\rho_v c_{pv}u_v + \phi_a\rho_a c_{pa}u_a\right)T\right]_n\Big\} \\
&= \frac{1}{(\Delta x_m)^2}\left[(\lambda_{\text{eff}})_e(T_E - T_P) + (\lambda_{\text{eff}})_w(T_W - T_P)\right] \\
&\quad + \frac{1}{(\Delta y_m)^2}\left[(\lambda_{\text{eff}})_s(T_S - T_P) + (\lambda_{\text{eff}})_n(T_N - T_P)\right] - \left(\Delta h_{\text{vap}}\dot{m}\right)_P . \qquad (7.47)
\end{aligned}$$

In general, properties at the control volume interfaces are calculated using an upwind scheme. That is, for a given variable, ξ, the value ξ_e is calculated as

$$\xi_e = \xi_P \max\left[\frac{u_e}{|u_e|}, 0\right] + \xi_E \max\left[-\frac{u_e}{|u_e|}, 0\right]. \qquad (7.48)$$

Although the upwind scheme is sometimes associated with so called false diffusion, the velocity vectors are expected to be largely aligned with the grid configuration thereby limiting this effect. Additionally, small values of Δx_m and Δy_m and

sufficiently large Péclet numbers further reduce the consequences of false diffusion (de Vahl Davis and Mallinson, 1972).

One of the exceptions to the use of the upwind scheme is the calculation of the effective thermal conductivity between adjacent cells. For this property, it is not the local value that was of primary concern, but rather a good representation of the heat flux at the interface. An upwind or linear interpolation (arithmetic mean) scheme would not accurately describe abrupt changes in conductivity. A better representation is obtained through the use of the harmonic mean

$$(\lambda_{\text{eff}})_e = 2\frac{(\lambda_{\text{eff}})_E(\lambda_{\text{eff}})_P}{(\lambda_{\text{eff}})_E+(\lambda_{\text{eff}})_P} \tag{7.49}$$

since the interface is located midway between adjacent grid points. Such a formulation adequately handles step changes in conductivity without requiring excessively small control volumes. As demonstrated by Patankar (1978), this approach performs much better than arithmetic mean formulations, even when source terms and continuously varying conductivities are encountered.

The solution procedure follows the semi-implicit method for pressure-linked equations, more commonly referred to as the SIMPLE algorithm. At the core of this approach is the treatment of the pressure and velocity components as the sums of a predicted value and a correction term. That is,

$$p = p^* + p' \tag{7.50}$$

$$u = u^* + u' \tag{7.51}$$

$$v = v^* + v' \tag{7.52}$$

where the starred variables are the predicted values and the terms with a prime are the corrections. An outline of the SIMPLE procedure will first be offered, followed by a more detailed discussion of the steps. However, since the SIMPLE method is well documented, this discussion will be limited to presenting the equations specific to the current work, rather than their derivation (Patankar, 1980). The main operations of the SIMPLE algorithm are:

1. Guess the initial pressure field, p^*
2. Use this pressure field in the momentum equations to calculate the predicted velocity components u^* and v^*
3. Solve the so-called pressure correction equations to get the correction term, p'
4. Calculate the new pressure field as the sum of the initial guess, p^*, and the correction p'
5. Calculate corrected values of the velocity components u and v using velocity correction formulas
6. Solve the other discretized equations, such as energy conservation, to get the values of properties that affect the flow field (e.g. ρ, T, etc.)

7. Iterate by using the corrected pressure field as the new initial guess, p^*, until convergence is obtained.

The first two of these steps are straightforward and do not require additional comment. The pressure correction equation used in step 3 takes the form

$$a_P(p_l')_P = a_E(p_l')_E + a_W(p_l')_W + a_N(p_l')_N + a_S(p_l')_S + b \tag{7.53}$$

where

$$a_E = \left(\frac{KK_l\rho_l}{\mu_l}\right)_e \frac{\Delta y_m}{\Delta x_m} \tag{7.54}$$

$$a_W = \left(\frac{KK_l\rho_l}{\mu_l}\right)_w \frac{\Delta y_m}{\Delta x_m} \tag{7.55}$$

$$a_N = \left(\frac{KK_l\rho_l}{\mu_l}\right)_n \frac{\Delta x_m}{\Delta y_m} \tag{7.56}$$

$$a_S = \left(\frac{KK_l\rho_l}{\mu_l}\right)_s \frac{\Delta x_m}{\Delta y_m} \tag{7.57}$$

$$a_P = a_E + a_W + a_N + a_S \tag{7.58}$$

$$-b = [(\phi_l\rho_l + \phi_v\rho_v)_P - (\phi_l\rho_l + \phi_v\rho_v)_P^o]\frac{\Delta x_m \Delta y_m}{\Delta t}$$
$$+[(\phi_l\rho_l u_l + \phi_v\rho_v u_v)_e - (\phi_l\rho_l u_l + \phi_v\rho_v u_v)_w]\Delta y_m$$
$$+[(\phi_l\rho_l v_l + \phi_v\rho_v u_v)_s - (\phi_l\rho_l v_l + \phi_v\rho_v u_v)_n]\Delta x_m \ . \quad (7.59)$$

The velocity correction formulas referred to in step 5 are

$$(u_l')_e = \left(\frac{KK_l}{\mu_l\phi_l}\right)_e \frac{(p_l')_P - (p_l')_E}{\Delta x_m} \quad (7.60)$$

$$(v_l')_s = \left(\frac{KK_l}{\mu_l\phi_l}\right)_s \frac{(p_l')_P - (p_l')_S}{\Delta y_m} \ . \quad (7.61)$$

The discretized energy conservation equation was solved using a recursive, line-by-line, tri-diagonal matrix algorithm. The well known tri-diagonal matrix algorithm, or TDMA, which is often used in one-dimensional systems, was applied to this two-dimensional case by solving for temperature along a given grid line. The temperatures of neighboring grid lines were taken as known values, thus reducing the equations to the familiar one-dimensional case. This practice was repeated for each grid line oriented in the y_m-direction, sweeping in the x_m-direction. Then lines oriented in the x_m-direction were analyzed. The temperature field was updated after each calculation and this process was repeated until convergence was obtained. The convergence of this method was faster than a point-by-point method since the boundary conditions at the termination of each grid line were transmitted immediately to the domain's interior along said grid line.

Hence, the practice of alternating grid line orientation brought all boundary conditions to the interior quickly.

7.8 Summary and Discussion

In summary, the drying of porous media is a complex phenomenon which involves simultaneous heat and mass transfer of a solid matrix, liquid filled voids, and a multi-species gaseous phase. Thus, modeling this inherently multiphase process produces distinctive challenges. Since shrinkage effects add complexity to the model and often require empirical fitting parameters, the solid matrix was assumed to be rigid. Conservation equations were constructed from a volume-averaged, macroscopic viewpoint. These equations were combined with thermodynamic equilibrium conditions, constitutive relations, and simplifying assumptions to create a two-dimensional model of the media. The pertinent equations and assumptions were presented. The discretization method was examined, and the governing equations were recast in discretized forms for numerical implementation. The domain, boundary conditions, and numerical solution procedure for the model were also discussed. Validation of the model is provided in Chapter 8.

CHAPTER 8

DRYING MODEL VALIDATION

8.1 Introduction

This chapter discusses the methodology used to validate the numerical drying model outlined in Chapter 7 and the results of employing said methodology. The experimental drying results discussed in Chapter 6 were used to assess the validity of the numerical procedure. Due to experimental limitations, bulk drying was used as the comparative quantity. However, using this benchmark can only confirm the average dewatering, whereas the heat flux experiments validated the results of the FLUENT simulations as a function of *x*. The agreement using that approach implied that the fluid properties and flow field near the surface were accurately predicted for the entire surface, rather than just the average values. Bulk drying, on the other hand, offers no such implications about moisture profiles or fluid velocities within the media. As such, it would be inappropriate to use the model to ascertain the exact mechanisms responsible for drying or drying enhancement. Instead, the drying model will be used exclusively for predicting average drying in subsequent work. Additionally, an empirical correlation from literature will also be used to assess the validity of the model.

8.2 Approach

The drying model required conditions to be specified at the impingement surface, conditions that were not measured experimentally. The pertinent quantities were P_{jet}, T_{jet}, k_t, and k_m. Additionally, in order to calculate k_m the Lewis number also needed to be specified. For the particular conditions of the cases studied in this work, these quantities were functions of both position, *x*, and time, *t*. Since experimentally determining these values was impractical, the FLUENT simulation results were used to provide the necessary boundary conditions. Thus, the comparisons made in this chapter serve to validate not only the drying model but also the practice of studying the media and impinging gas flow separately. Since multiple experimental trials centered on a single set of conditions, the average values of these conditions were used in the simulations. Other characteristics, such as the material properties, initial saturation, and relative humidity, were specified using the experimental values. Additionally, the simulations were conducted using the same geometry employed in the experimental tests. Table 8.1 gives the geometric configuration used throughout this chapter.

Table 8.1: Configuration employed in drying validation.

Parameter	Value
L	0.356 m
D_h	0.0128 m
H	0.020 m
H/D_h	1.56
U_{surface}	0.6 m/s

The media was modeled using 15240 quadrilateral cells. The rectangular domain consisted of 127 cells in the x_m-direction and 120 cells in the y_m-direction. Each simulation used 1×10^4 time steps. As a result, Δx_m was 1×10^{-3} m and the largest value of Δy_m was 2.65×10^{-5} m. Grid independence studies were conducted much in the manner described in Chapter 4. The values of Δx_m and Δy_m were halved to create four times as many cells as the base grid. Final saturation was not changed significantly; therefore, the base grid was used throughout the modeling work. A single number of cells in the y_m-direction was used for all substrate thicknesses, resulting in varying values of Δy_m, simply for convenience. Similarly, the time step was decreased by a factor of 2, and no significant changes were observed. Consequently, the base time step was also employed.

The thermal boundary condition for the lower, impermeable surface is stated as

$$\lambda_{\text{eff}} \frac{\partial T}{\partial y}\Big|_{y_m = h} = 0 \,. \tag{8.1}$$

since it is assumed to be adiabatic. In order to validate this assumption, the temperature of this surface was recorded during the experimental trials. The resulting heat flux is shown in Figure 8.1. For comparison, the expected heat flux at the impingement surface as calculated by FLUENT is also shown in this plot.

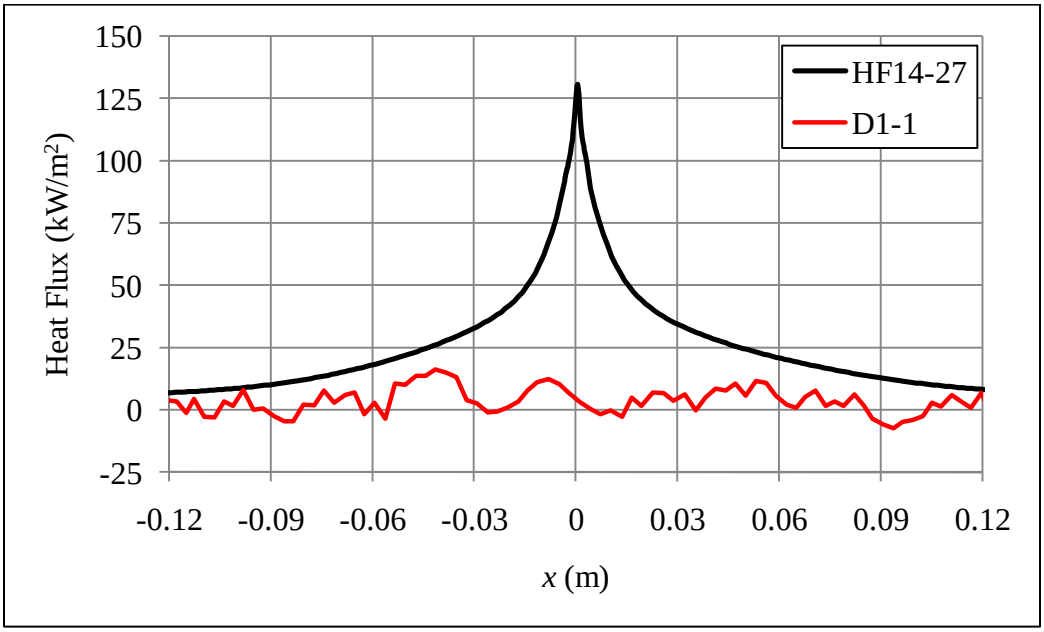

Figure 8.1: Heat flux at bottom of sample compared to expected heat flux on top surface.

Although there does appear to be a slight positive heat flux at the bottom surface, the magnitude in comparison to the heat flux at the top surface is small. Therefore, the adiabatic assumption is not expected to significantly impact the accuracy of the model.

8.3 Single Nozzle Tests

The single nozzle tests employed one set of time averaged operational conditions to dry each of the five sample materials. The operational parameters used in these tests are given in Table 8.2, along with the oscillation characteristics of the pulsed flow cases.

Table 8.2: Operational characteristics for the single nozzle tests.

Parameter	Value
$\overline{\dot{m}}$	3.7×10^{-3} kg/s
$\overline{T}_{exit}$	697 K
ω	135 Hz
R_{amp}	3.43

8.3.1 Boundary Conditions

As previously stated, the boundary conditions at the impingement surface were calculated using FLUENT. The gauge pressure along the impingement surface for the steady flow single nozzle cases is shown in Figure 8.2. Similarly, the heat and mass transfer coefficients for these cases are given in Figure 8.3. It should be noted that these results are given as a function of *x*, the coordinate system associated with the nozzle, rather than x_m, the coordinate system associated with the media. The heat transfer coefficient shown in Figure 8.3 is the so-called wall heat transfer coefficient. This

coefficient is calculated using the law-of-the-wall. The law-of-the-wall implemented in FLUENT has the form

$$T^* \equiv \frac{(T_w - T_P)\rho c_p C_\mu^{1/4} \kappa_P^{1/2}}{q_w''} \tag{8.2}$$

$$T^* = \begin{cases} \Pr y^* + \frac{1}{2}\rho \Pr \frac{C_\mu^{1/4}\kappa_P^{1/2}}{q_w''} U_P^2 & (y^* < y_T^*) \\ \Pr_t \left[\frac{1}{\kappa}\ln(Ey^*) + P\right] + \frac{1}{2}\rho \frac{C_\mu^{1/4}\kappa_P^{1/2}}{q_w''} [\Pr_t U_P^2 + (\Pr + \Pr_t)U_c^2] & (y^* < y_T^*) \end{cases} \tag{8.3}$$

where P is computed by

$$P = 9.24\left[\left(\frac{\Pr}{\Pr_t}\right)^{3/4} - 1\right]\left[1 + 0.28e^{-0.007\Pr/\Pr_t}\right], \tag{8.4}$$

and T_P is the temperature at the cell adjacent to the wall, κ is the von Kármán constant (0.4187), E is the wall function constant (9.793), and U_c is the mean velocity magnitude at $y^* = y_T^*$ (FLUENT, 2006; Jayatilleke, 1969).

The non-dimensional thermal sublayer thickness, y_T^*, in Equation 8.3 is computed as the value of y^* at which the linear and the logarithmic laws intersect, given the molecular Prandtl number of the fluid.

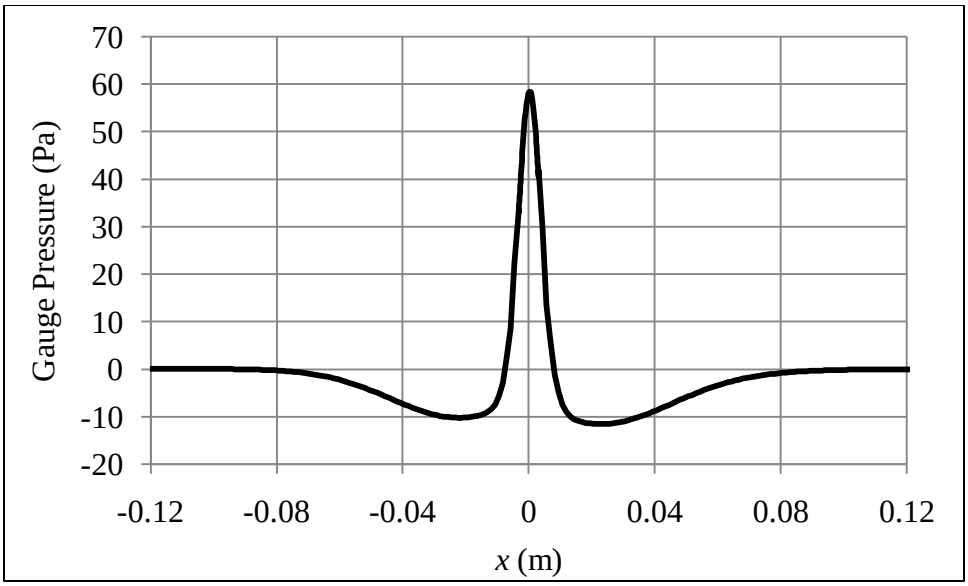

Figure 8.2: Gauge pressure at the impingement surface for the steady flow cases.

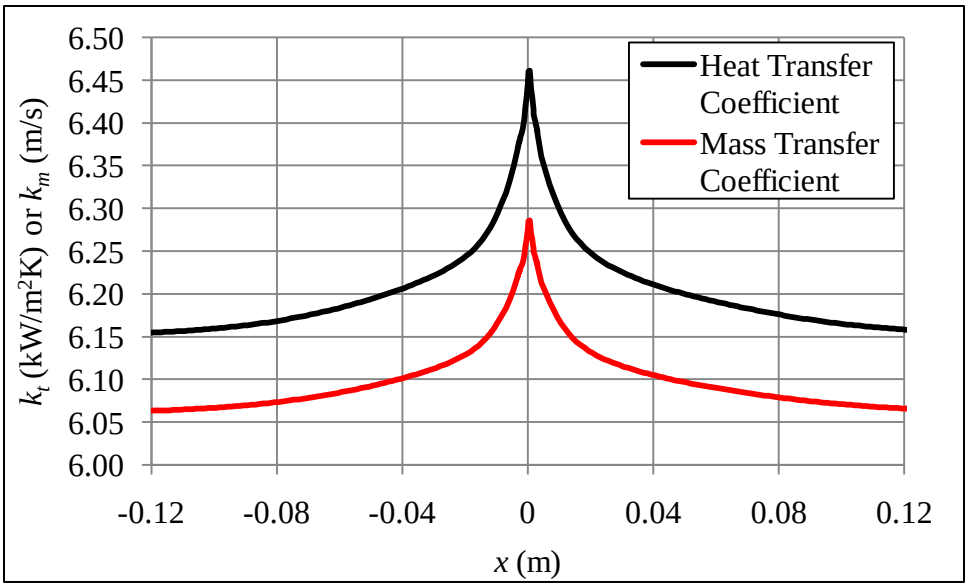

Figure 8.3: Transport coefficients at the impingement surface for the steady flow cases.

The mass transfer coefficient in Figure 8.3 is calculated using the Lewis number correlation found in equation 7.33. The Lewis number is given in Figure 8.4 as a function of position along the impingement surface.

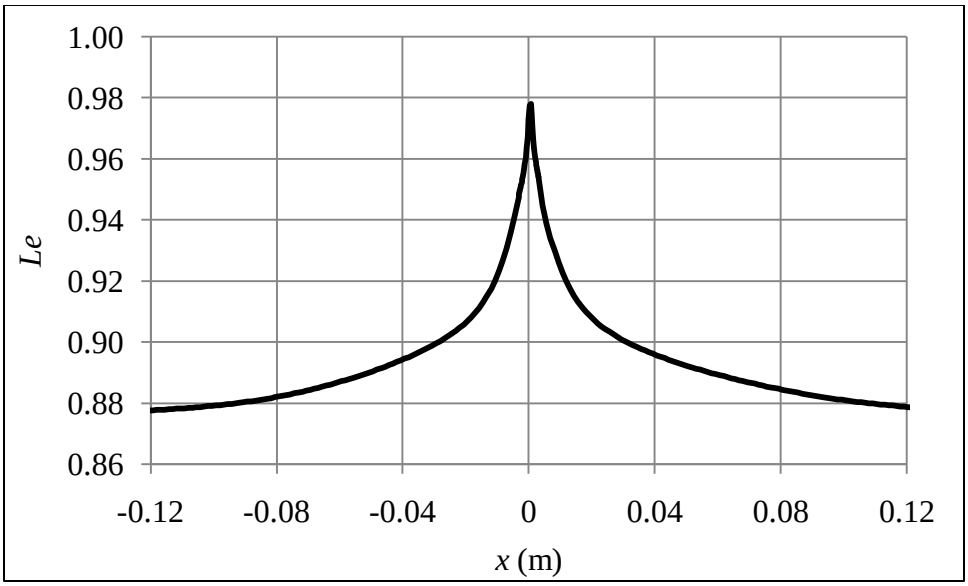

Figure 8.4: Lewis number at the impingement surface for the steady flow cases.

8.3.2 Results

The simulation results are compared with the experimental values in Table 8.3. The water removal was under-predicted by the drying model in all cases. The difference in $\Delta\overline{s}$ ranged from 7.4 % to 15.6 %. This error appears to be related to the media thickness. This is discussed in section 8.5. Still, the drying model showed adequate agreement albeit with consistently lower values of $\Delta\overline{s}$.

Table 8.3: Comparison of experiment and simulation for single nozzle configuration.

Flow	Material	$\Delta\overline{s}$		Difference
-	-	Experiment	Simulation	%
Steady	PTFE-1	-0.0480	-0.0445	-7.4
	PTFE-2	-0.0112	-0.0099	-11.6
	PTFE-3	-0.0064	-0.0057	-11.1
	PTFE-4	-0.0047	-0.0040	-15.3
	Blotter	-0.0206	-0.0190	-7.7
Pulsed	PTFE-1	-0.0663	-0.0617	-6.9
	PTFE-2	-0.0255	-0.0225	-11.9
	PTFE-3	-0.0105	-0.0093	-12.0
	PTFE-4	-0.0080	-0.0067	-15.6
	Blotter	-0.0265	-0.0241	-9.0

8.3.3 Discussion

Despite the lower predicted values of $\Delta\overline{s}$, the model provided consistent results between flow conditions for a given substrate. That is, the calculated bulk dewatering rates due to the steady and pulsed flow conditions were lower than the experimental values by similar percentages. As a result, the drying enhancement predicted by the model was similar to that observed experimentally. This is shown in Table 8.4. The predicted drying enhancement factor was within 1.6 % of the observed values for all

cases.

Table 8.4: Comparison of drying enhancement for single nozzle configuration.

Material	E_{DRY}		Difference
-	Experiment	Simulation	%
PTFE-1	1.38	1.39	0.4
PTFE-2	2.28	2.27	-0.2
PTFE-3	1.64	1.63	-0.6
PTFE-4	1.70	1.68	-1.6
Blotter	1.29	1.27	-1.4

8.4 Three Nozzle Tests

The same five sample materials were used in the three nozzle drying cases. The three nozzle tests also used the same mean mass flow rate as the single nozzle tests but had a higher mean exhaust exit temperature. The oscillation frequency and velocity amplitude ratio were also higher than those of the single nozzle tests. These operational parameters are detailed in Table 8.5.

Table 8.5: Operational characteristics for the three nozzle tests.

Parameter	Value
$\dot{\overline{m}}$	3.7×10^{-3} kg/s
$\overline{T}_{exit}$	1005 K
ω	164 Hz
R_{amp}	3.61

8.4.1 Boundary Conditions

The gauge pressure on the impingement surface calculated using FLUENT for the steady flow, three nozzle cases is shown in Figure 8.5. As expected, the peak values are higher than those from the single nozzle cases.

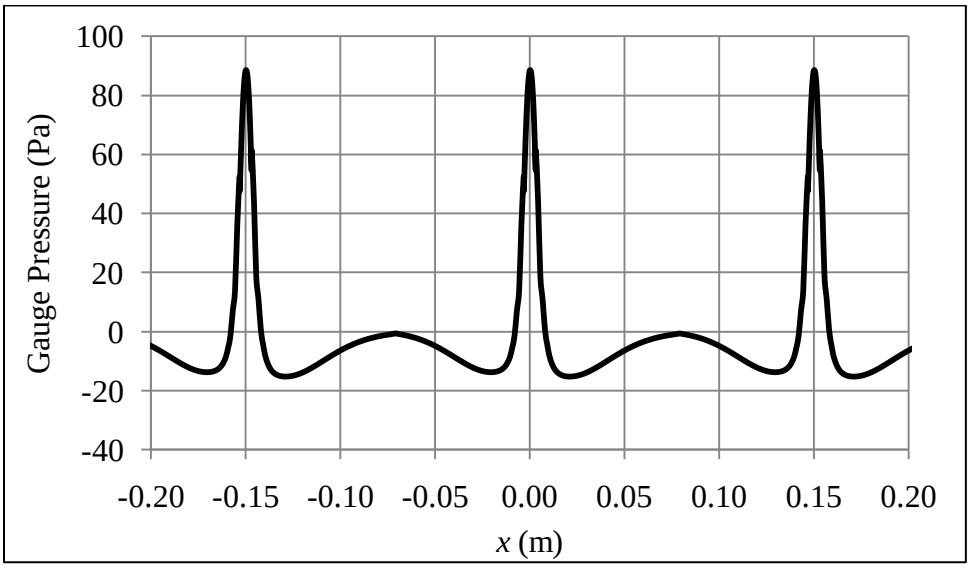

Figure 8.5: Gauge pressure at the impingement surface for the steady flow cases.

Similarly, the heat and mass transfer coefficients for the three nozzle steady flow cases are given in Figure 8.6. In comparison with the single nozzle cases, the higher exhaust exit temperature of the three nozzle system, and therefore elevated exit velocity given the similar mean mass flow rate, resulted in a higher heat transfer coefficient. As a result, the calculated value of the mass transfer coefficient, which is based on the heat transfer coefficient, was also higher than in the single nozzle cases. This is also an expected result given the differences in flow conditions. Additionally, the Lewis number was higher due to the elevated temperature, increasing k_m further. The Lewis number is given in Figure 8.7 as a function of x.

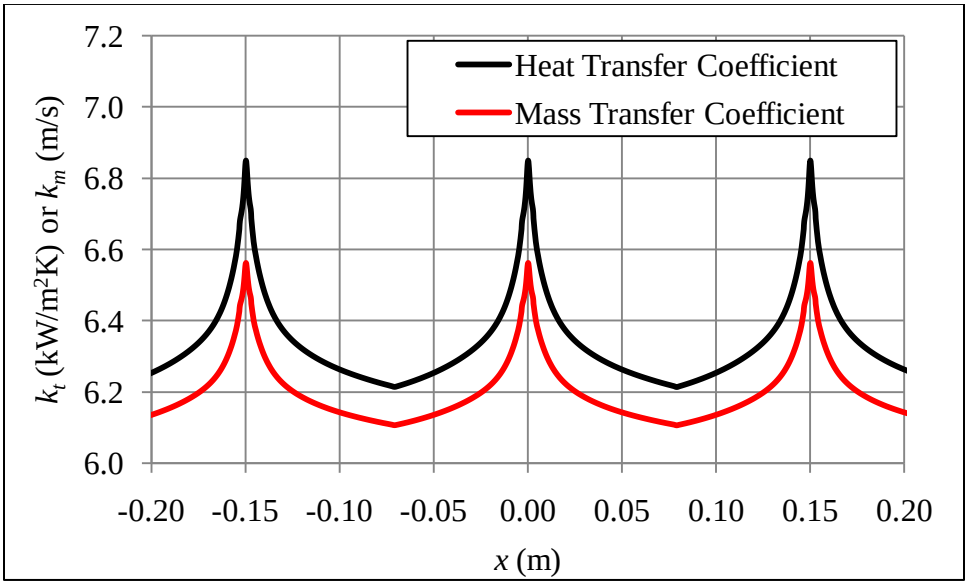

Figure 8.6: Transport coefficients at the impingement surface for the steady flow cases.

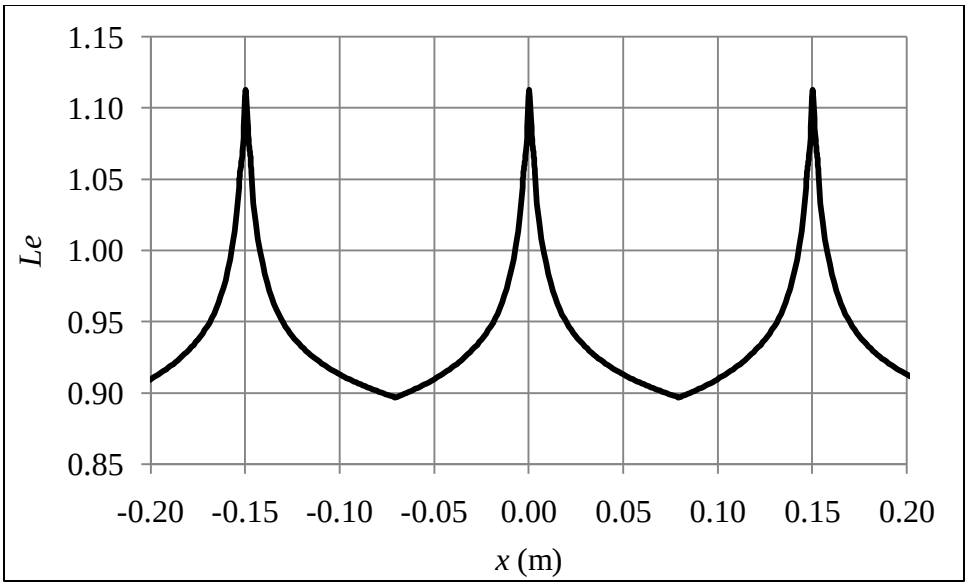

Figure 8.7: Lewis number at the impingement surface for the steady flow cases.

8.4.2 Results

The results of the three nozzle simulations and experiments are compared in Table 8.6. As with the single nozzle cases, the water removal due to the three nozzle configuration was under-predicted by the drying model. However, the difference in $\Delta\overline{s}$ was greater, ranging from 7.0 % to 18.9 %.

Table 8.6: Comparison of experiment and simulation for the three nozzle configuration.

Flow	Material	$\Delta\overline{s}$		Difference
-	-	Experiment	Simulation	%
Steady	PTFE-1	-0.1110	-0.0997	-10.2
	PTFE-2	-0.0248	-0.0213	-14.3
	PTFE-3	-0.0272	-0.0234	-13.9
	PTFE-4	-0.0102	-0.0084	-18.1
	Blotter	-0.0525	-0.0488	-7.0
Pulsed	PTFE-1	-0.1628	-0.1465	-10.0
	PTFE-2	-0.0514	-0.0435	-15.5
	PTFE-3	-0.0490	-0.0413	-15.7
	PTFE-4	-0.0181	-0.0147	-18.9
	Blotter	-0.0759	-0.0687	-9.5

8.4.3 Discussion

The simulation results were again consistent for a given substrate. The error in $\Delta\overline{s}$ for a steady flow case was similar to error encountered in the corresponding pulsed flow case. This offset resulted in an accurate prediction of the drying enhancement, as shown in Table 8.7. The difference in the simulation and experimental values of E_{DRY} was less than 3 % for all substrate materials.

Table 8.7: Comparison of drying enhancement for three nozzle configuration.

Material	E_{DRY}		Difference
-	Experiment	Simulation	%
PTFE-1	1.47	1.47	0.2
PTFE-2	2.07	2.04	-1.4
PTFE-3	1.80	1.76	-2.0
PTFE-4	1.78	1.76	-1.1
Blotter	1.45	1.41	-2.7

8.5 Summary and Discussion

The drying model used a 2-dimensional approximation based on the assumptions that the majority of heat and mass transfer occurred through the top of the media and that this transfer did not vary significantly in the direction normal to x_m and y_m. The first of these assumptions required the use of wide samples so that the sides of the sample comprised a small portion of the exposed surface area. However, the excessively wide samples were also undesirable. The second assumption required samples to be exposed to similar flow conditions at all locations in the z_m-direction. From previous laboratory work, it was determined that samples 0.0254 m in width would receive consistent heat flux in the z_m-direction from the impingement jet. Therefore, this was the sample width selected for the drying experiments. Still, edge effects such as unaccounted for heat transfer and water removal did result in errors in the drying simulations. Table 8.8 shows

the ratio of the total surface area of all the sides, A_{sides}, to the surface area of the top of the sample, A_{top}. As this ratio increases, the error attributed to edge effects are also expected to increase.

Table 8.8: Comparison of side and top surface areas.

Material	Thickness	A_{sides}	A_{top}	A_{sides}/A_{top}
-	10^{-3} m	10^{-3} m^2	10^{-3} m^2	-
PTFE-1	0.61	0.186	3.226	0.058
PTFE-2	1.57	0.479	3.226	0.148
PTFE-3	1.57	0.479	3.226	0.148
PTFE-4	2.38	0.725	3.226	0.225

The relationship between material thickness and the errors in predicting saturation change was remarkably consistent for a given flow condition. There was a nearly linear relationship between these two quantities for all four flow conditions. This is shown in Figure 8.8, a plot of error in $\Delta\overline{s}$ and the ratio A_{sides}/A_{top}. A least-squares-fit linear trend line is also shown. The slopes of these lines for a given flow type (pulsed or steady) varied by less than 3 %. Although this is not conclusive evidence, it does strongly suggest that a portion of the errors in the simulation predictions are attributable to edge effects. This is especially true since PTFE-2 and PTFE-3 had no properties or traits in common with only each other besides sample thickness, yet still had absolute difference in errors of less than 0.5 %.

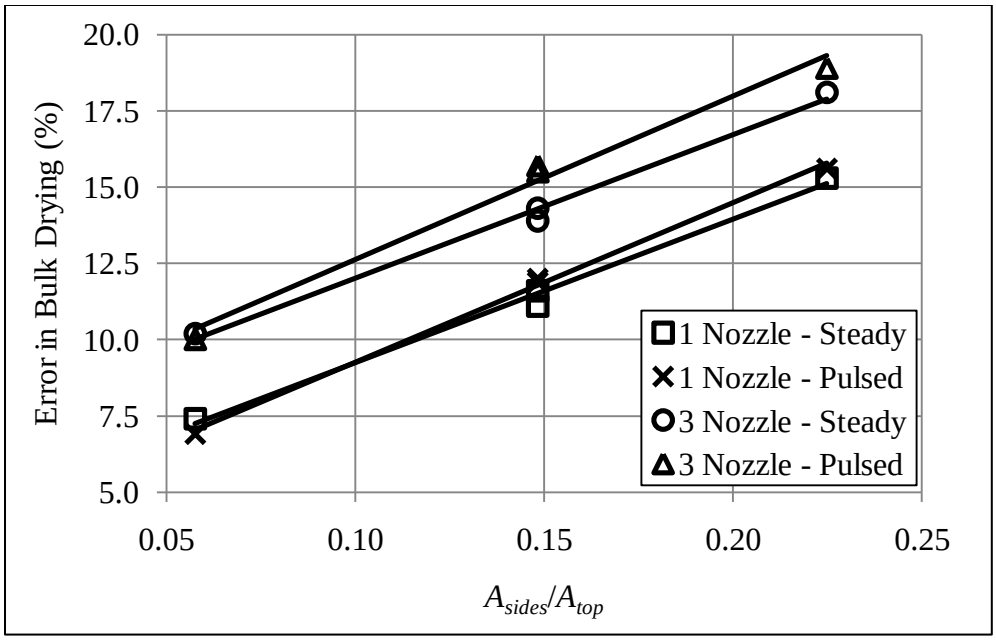

Figure 8.8: Relationship between error and sample thickness with linear trend lines.

Subsequent work, however, will focus on substrates and burners expected in an industrial setting, rather than a laboratory implementation. This involves much larger burners used to dry very wide sheets of porous media. As such, edge effects of these scenarios are expected to be much less severe than those encountered in this chapter. Furthermore, one of the primary characteristics of interest is not the exact value of $\Delta\overline{s}$, but rather the relative performance improvement generated by the pulsed flow conditions. Thus, E_{DRY} is a more important quantity to the current work. Since the results were consistent for a given condition, the predicted values of E_{DRY} were within 2.7 % of the observed experimental values for all cases. Accordingly, the model is well suited for calculating this characteristic quantity.

In order to more fully assess the performance of the model, simulations were compared with a correlation used to predict the drying rate of paper due to air impingement (Chen and Douglas, 1998). This correlation showed good agreement with experimental data in laboratory investigations of drying unbleached, unbeaten, black spruce kraft pulp handsheets (Chen and Douglas, 1998). Good agreement with drying rates obtained from a commercial setting was also shown by Chen and Douglas (1998) using data from the Trois Rivieres, Quebec, newsprint mill of the Canadian International Paper Company (Burgess and Chapman, 1972). Thus, the correlation was deemed suitable for verifying the drying rates predicted by the current model.

The semi-empirical correlation from Chen and Douglas (1998) treated the total drying rate as a combination of two different drying mechanisms: drying due to air impingement, and drying due to through-flow of the drying gases. This was a convenient separation for comparison with the current model since it assumed that no through-flow occurred. Thus, only the drying rate from steady flow air impingement was used as the relevant benchmark. The pertinent characteristics of the substrate and slot shaped nozzle that were used in the comparisons are given in Table 8.9.

Table 8.9: Parameters used for comparison with correlation.

Parameter	Value
Grammage	51 g/m^2
Thickness	1.0×10^{-4} m
D_h	4.8×10^{-3} m
H	2.4×10^{-2} m
ϕ	0.66
s_i	0.98
T_{ambient}	300 K

The properties in Table 8.9 correspond to those used in the development of the correlation for a newsprint grade paper. The operational parameters were also similar to those used by Chen and Douglas (1998). Three tailpipe exit velocities were investigated: 30 m/s, 40 m/s, and 50 m/s. For each of these flow rates three tailpipe exit temperatures were simulated: 600 K, 700K, and 800 K. Additionally, the impingement surface velocity was specified as 18 m/s. These values were chosen in order to fit the range of validity specified by Chen and Douglas (1998). The resulting drying rates are shown in Figure 8.9 using customary units of kg/m^2·h.

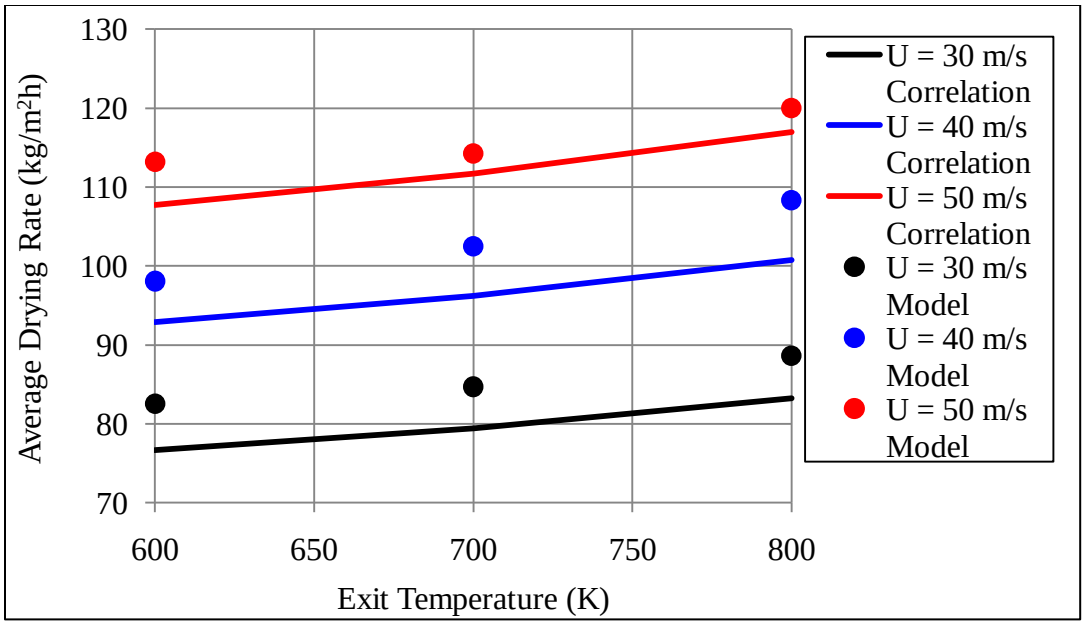

Figure 8.9: Comparison of drying rates from correlation and the numerical model.

The model consistently predicted higher drying rates than the correlation. However, the trends with exit temperature and velocity were similar using both methods. Still, the drying rates from the model were within 10 % of those from the correlation for all cases. Thus, this adds further validity to the findings using the numerical model.

CHAPTER 9

PARAMETRIC STUDY

9.1 Introduction

This chapter presents the methods and results of a numerical study designed to assess the impact of various system parameters. The mechanisms of heat transfer enhancement and the manipulation of those mechanisms through alteration of characteristic parameters were of primary interest in this chapter. Although guided by the previous experimental work, this numerical study allowed investigation of parameters that were not easily analyzed in the laboratory setting. For example, altering the velocity amplitude ratio or the hydraulic diameter of the tailpipe during experiments would necessitate design and construction of a different pulse combustor, a time consuming process. Additionally, the numerical simulations provided a means of investigating operational conditions that exceeded the capacity of the experimental apparatus, such as high speed impingement surfaces. Finally, system parameters were studied individually in order to isolate the effects of each quantity. This was not possible experimentally given the scope of the project since parameters such as the velocity ratio and oscillation frequency are linked through the geometry of the combustor.

A base case was first analyzed to provide a reference point for subsequent

changes to operational parameters and geometric configuration. Since the primary goal was to study the details of the fluid flow in the impingement zone, this chapter focuses on heat flux rather than drying. Drying and multiple nozzles will be studied in the following chapters as part of more system oriented investigations.

The effects of five parameters were studied. They were the velocity amplitude ratio (R_{amp}), oscillation frequency (ω), the time-averaged bulk fluid velocity at the tailpipe exit ($\overline{U}_{exit}$), the hydraulic diameter of the tailpipe (D_h), and the impingement surface velocity (U_{surface}). Each case used a slot-shaped nozzle since this type of configuration was the most thoroughly examined during the validation process and is likely to be used in a commercial setting. The base case had a velocity amplitude ratio of 4, as this value is often encountered in literature (Liewkongsataporn et al., 2008; Psimas et al., 2007). Similarly, the oscillation frequency for the base case was 160 Hz and the mean tailpipe exit velocity was 30 m/s. A stationary impingement surface was employed for the base case in order to isolate the effect of individual parameters on flow patterns. However, in some other investigations the constant surface velocities of up to 25 m/s were used. The nozzle to impingement surface distance, H, was selected to be 0.024 m for all cases since values from 0.02 m to 0.03 m are often employed in commercial drying applications. This also impacted the selection of the nozzle geometry. The optimal value of H/D_h for a steady flow jet is typically around 5, which loosely coincides with the length of the potential core (Martin, 1977; Incropera and DeWitt, 1977). Subsequently, D_h was chosen to be 4.8×10^{-3} m for the base case to yield a H/D_h ratio of 5. The values of the parameters that were investigated are provided in Table 9.1.

Table 9.1: Values used in the parametric study.

Parameter	Values Used
R_{amp}	2.5, 3.0, 3.5, 4.0, 4.5, 5.0
ω (Hz)	80, 125, 160, 200, 250, 320, 400
$\bar{U}_{exit}$ (m/s)	10, 15, 20, 25, 30, 35
D_h ($\times 10^{-3}$ m)	3.0, 4.0, 4.8, 6.0, 8.0, 12.0
U_{surface} (m/s)	0, 5, 10, 15, 20, 25

Each of the five parameters was studied separately, resulting in 27 individual cases. Additionally, steady flow cases with the same geometry, mean flow rate, and tailpipe entrance temperature were used for comparison. As a departure from previous chapters, the tailpipe entrance temperature was consistent throughout the study, as opposed to the time-averaged exit temperature. In previous chapters the principle goal was to assess the performance advantage provided by the pulsed conditions while having congruent time-averaged quantities. Therefore, using similar mean exhaust outflow conditions yielded the most appropriate comparisons. In this chapter, however, the purpose was to study the impact of various parameters. Since altering certain parameters, such as the velocity amplitude ratio, affects the mean exit temperature, ignoring these effects would be contrary to the current goals. Therefore, a fixed method of comparison was needed in order to assess the changes in performance. A constant tailpipe entrance temperature was selected since this is both physically realistic and ensures that enhancement factors were not overestimated due to elevated $\bar{T}_{exit}$ for the steady flow

cases. Subsequently, the entrance temperature was 1200 K for all cases.

For the cases involving a stationary impingement surface, such as the base case, the symmetry condition at the mid-plane was used to halve the computational domain. An example computational domain is shown schematically in Figure 9.1. Aside from the symmetry plane, the boundary conditions were similar to those used in previous chapters. The domain had adiabatic confinement and tailpipe walls, a 300 K constant temperature impingement surface, a sinusoidally time varying mass flux inlet, and an outlet at atmospheric pressure. The length of the domain in the x-direction was $24D_h$. The same two-dimensional governing equations, solution methods, turbulence parameters, and backflow conditions described in Chapter 4 were employed.

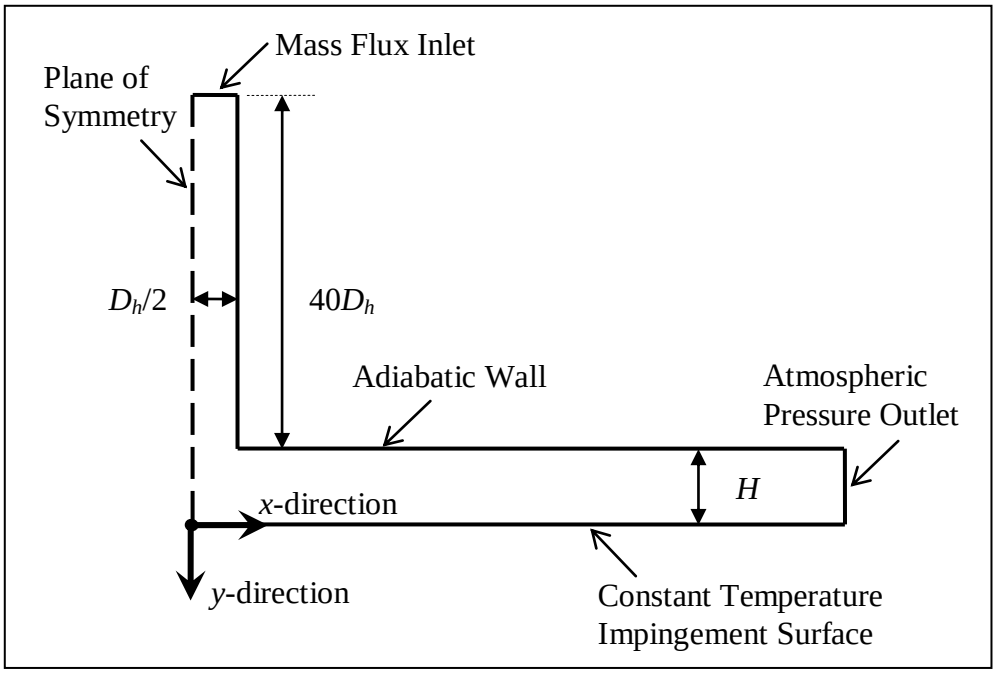

Figure 9.1: Example computational domain for stationary impingement surface cases.

9.2 Base Case

The operational parameters used in the base case are restated in Table 9.2 along with the relevant dimensionless quantities for comparison with other studies.

Table 9.2: Operational parameters used in the base case.

R_{amp}	ω	$\overline{U}_{exit}$	D_h	U_{surface}	$\overline{St}$	$\overline{Re}$	H/D_h
-	(Hz)	(m/s)	($\times 10^{-3}$ m)	(m/s)	-	-	-
4	400	30	4.8	0	0.0256	1438	5

The Strouhal and Reynolds numbers given in Table 9.2 are based on the mean values at the tailpipe exit. That is,

$$\overline{St} = {\omega D_h}\Big/{\overline{U}_{exit}} \tag{9.1}$$

$$\overline{Re} = {\overline{U}_{exit}\, D_h}\Big/{\bar{\nu}_{exit}} \tag{9.2}$$

where $\bar{\nu}_{exit}$ is the average kinematic viscosity at the tailpipe exit.

The y-direction velocity at the tailpipe exit for the base case is shown in Figure

9.2 as a function of dimensionless time, τ, which is time scaled by the period of one oscillation cycle. The convention used throughout this chapter is that $\tau = 0$ corresponds to the start of the positive portion of the *y*-velocity oscillation cycle at the tailpipe exit.

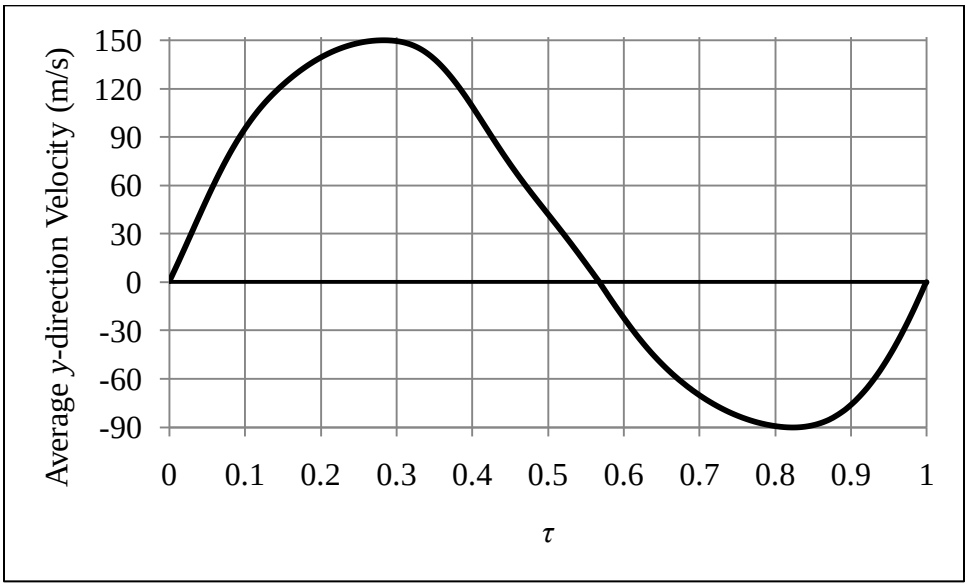

Figure 9.2: Tailpipe exit velocity for one oscillation cycle of the base case.

The *y*-velocity reached a maximum at $\tau = 0.284$ before returning to zero at approximately $\tau = 0.568$. The peak flow reversal occurred at $\tau = 0.824$ with a *y*-velocity of -90 m/s. The resulting velocity field for the base case is shown in Figure 9.3 for several different values of τ. Figure 9.3 shows a portion of the impingement zone focusing on the primary vortex.

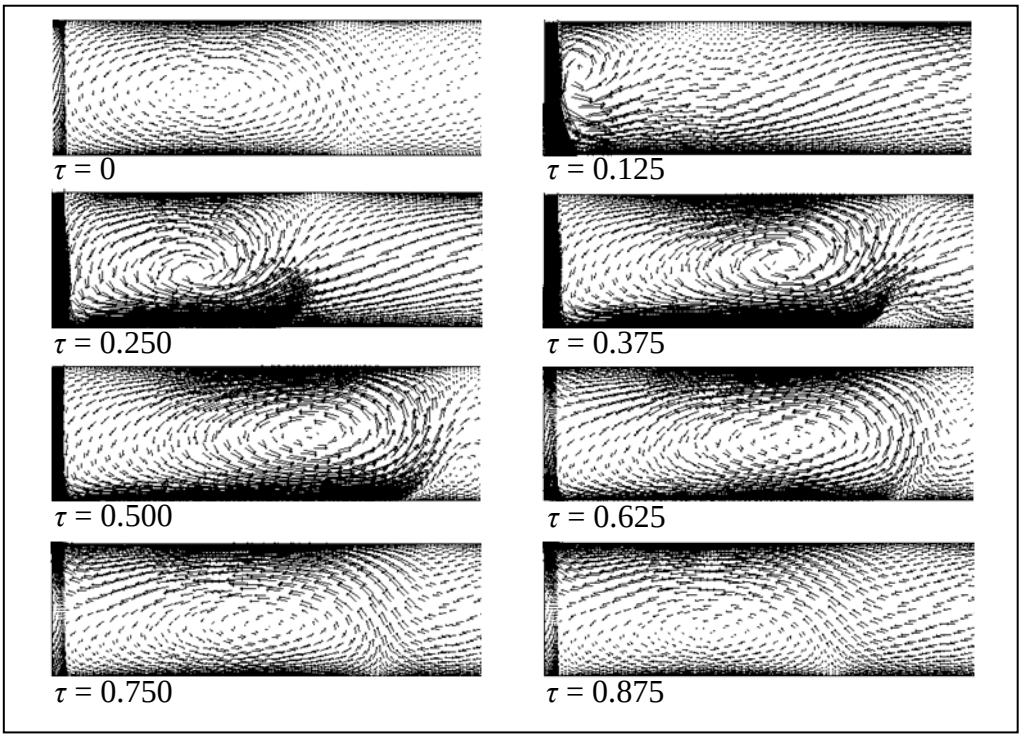

Figure 9.3: Flow field at various values of τ for one oscillation cycle of the base case.

A weak vortex can be seen at $\tau = 0$ from the previous cycle. A small but intense vortex forms as the exit velocity increases and can be seen at $\tau = 0.125$. This vortex grows as the exit velocity continues to increase. The vortex center moves in the positive x-direction for the duration of the positive velocity portion of the oscillation cycle. The vortex center then moves back in the negative x-direction after tailpipe exit velocity becomes negative. The strength of this vortex dissipates during the tailpipe flow reversal after approximately $\tau = 0.568$.

The relationship between the bulk velocity and temperature at the tailpipe exit for the base case is shown in Figure 9.4. The fluid being expelled in the initial stages of the oscillation cycle was previously drawn into the tailpipe during flow reversal. As a result,

the exit temperature did not start to increase significantly until $\tau \approx 0.18$. Additionally, mixing of this lower temperature fluid with the 1200 K inlet fluid led to increasing exit temperature until $\tau \approx 0.52$. This roughly corresponds to the start of the flow reversal portion of the cycle. The temperature declines until reaching a minimum of 732 K at τ = 0.712. The pulsed flow conditions of the base case yielded a mean tailpipe exit temperature of 901 K which was significantly lower than 1200 K value of the complimentary steady flow case.

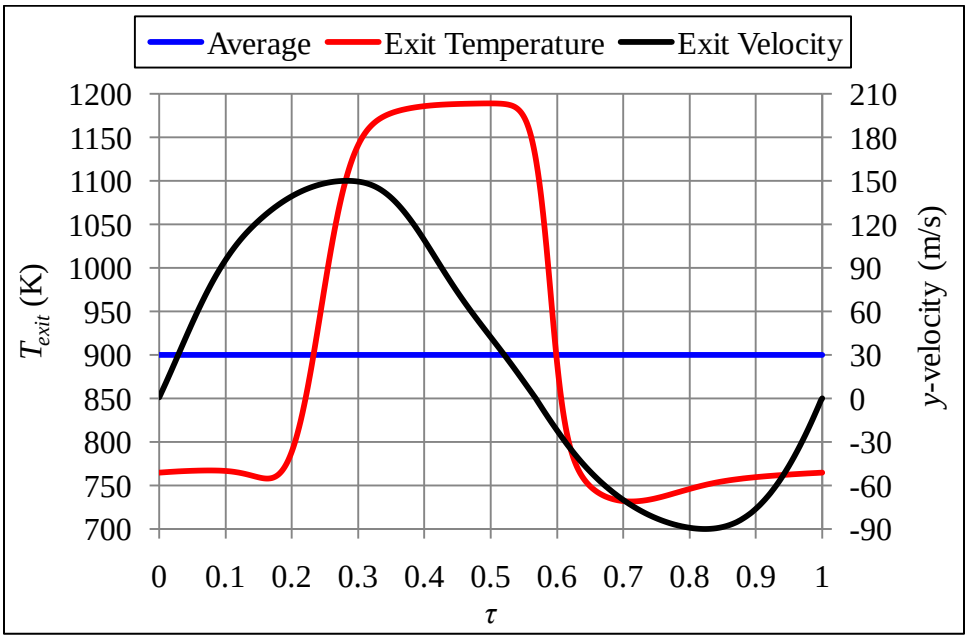

Figure 9.4: Bulk tailpipe exit temperature for one oscillation cycle of the base case.

The resulting temperature field for the base case is given in Figure 9.5 at 8 values of τ. Based on Figure 9.3 and Figure 9.5 the highest heat flux is expected to occur near τ = 0.375 due to the combination of the large, intense vortex and the high temperature near the impingement surface. The temperature field also showed abundant heat near the

impingement target at τ = 0.500, and less so at τ = 0.250 and τ = 0.625. The low temperature conditions near the right-most, or outlet, boundary were due to backflow of ambient fluid during tailpipe flow reversal. Consequently, this cool region was largest at $\tau \approx 0$, corresponding to the end of the flow reversal. Similarly, this region reaches a minimum size around $\tau \approx 0.5$ at which point the flow reversal begins again.

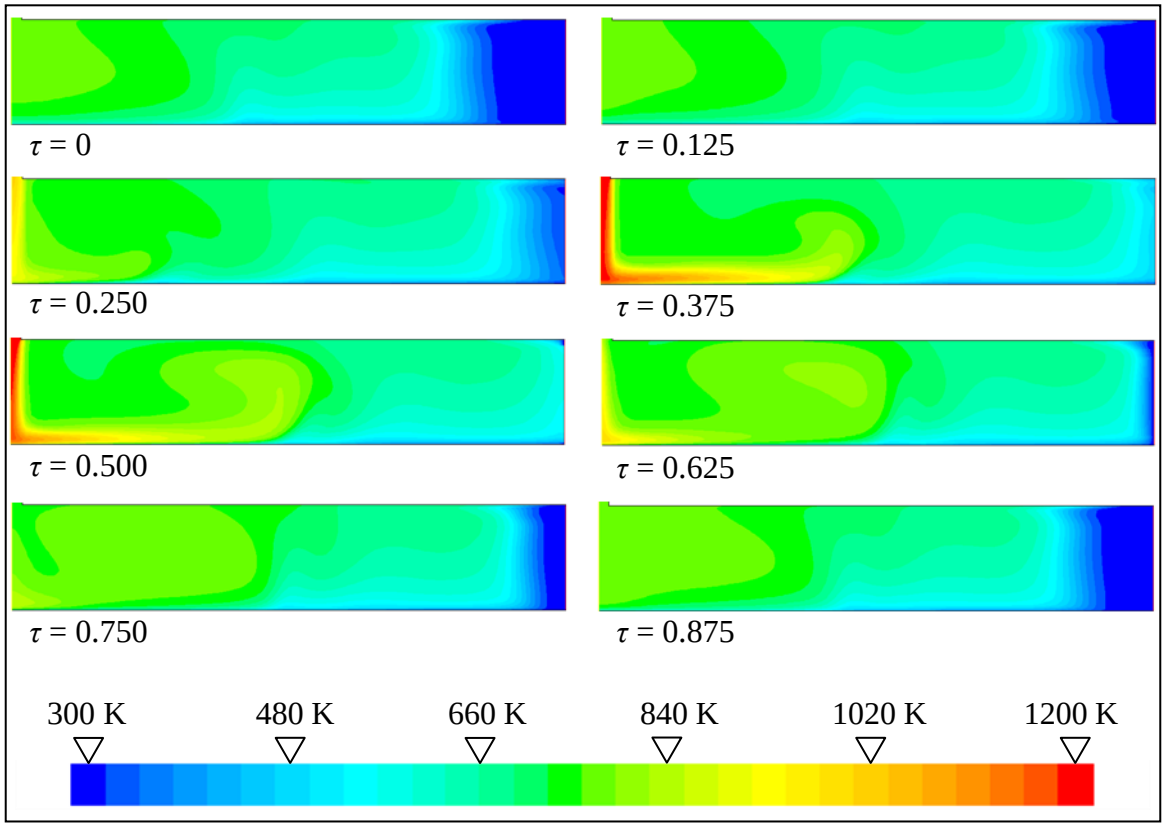

Figure 9.5: Temperature field at various τ for one oscillation cycle of the base case.

The combination of velocity and fluid properties at the tailpipe exit shown in Figure 9.4 yielded the Reynolds numbers given in Figure 9.6. Re_{exit} was calculated using the hydraulic diameter of the tailpipe, the bulk y-direction velocity magnitude, and the average kinematic viscosity at the tailpipe exit.

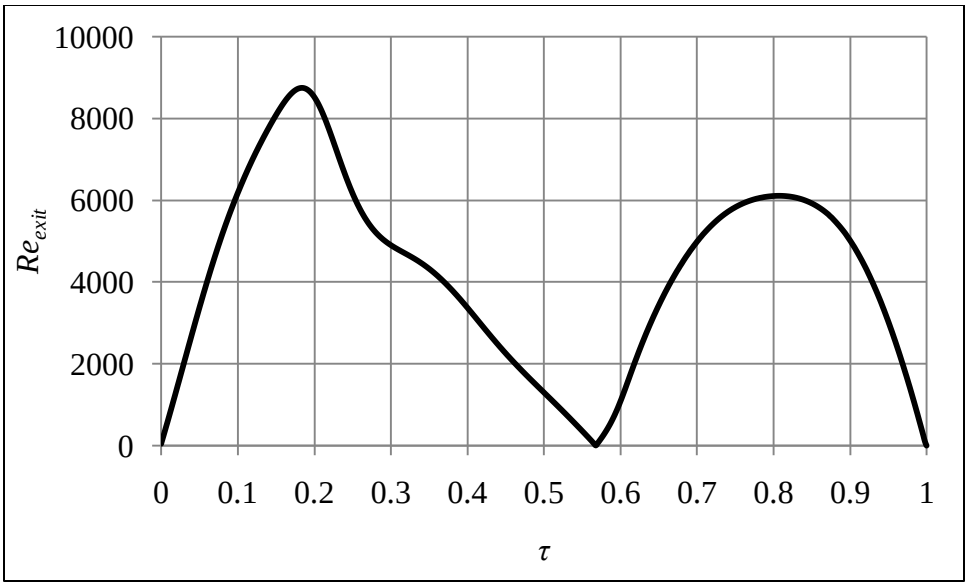

Figure 9.6: Tailpipe exit Reynolds number versus τ for the base case.

In contrast to the pulsating flow base case, the velocity field of the complimentary steady flow case is shown in Figure 9.7. This case had the same geometry, mean flow rate, and tailpipe entrance temperature as the base case. A weak vortex was formed but was of much lower intensity than the one produced by the pulsating conditions of the base case.

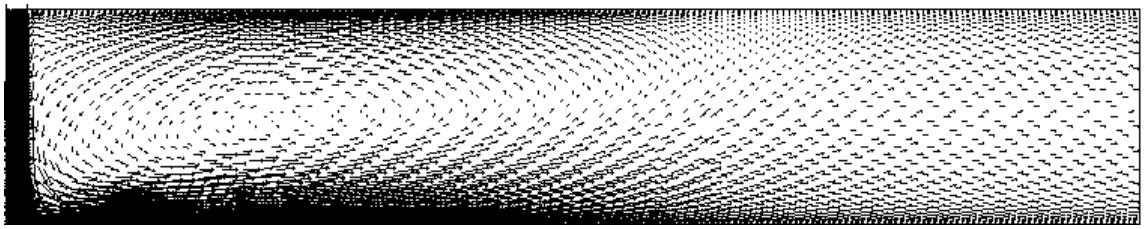

Figure 9.7: Flow field for the steady flow comparison case.

The resultant temperature field for the steady flow case is shown in Figure 9.8. The fluid temperature at the tailpipe exit was 1200 K, and there was significantly more

heat in the impingement zone for the steady flow case than there was for the base case. This was a result of the backflow of 300 K ambient air in the base case.

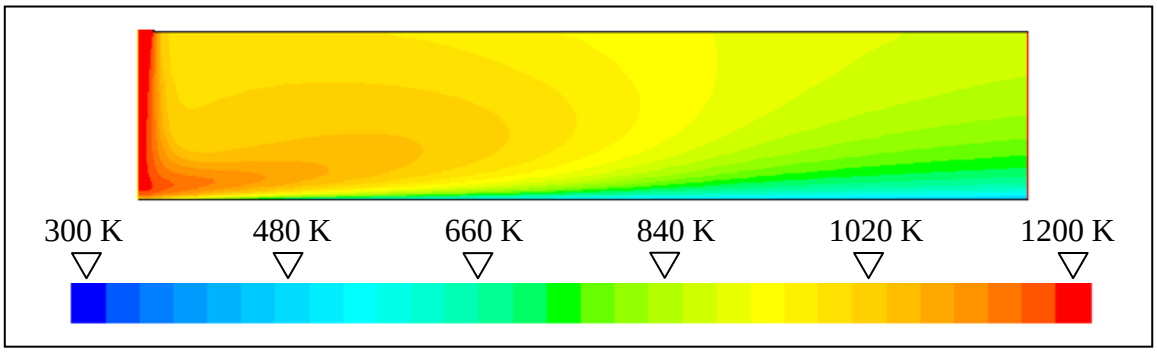

Figure 9.8: Temperature field for the steady flow comparison case.

Despite the higher average jet temperature, the steady flow produced lower time-averaged heat flux for most of the impingement surface. This is shown in Figure 9.9. The region $0 \leq x/D_h \leq 16$ shown in Figure 9.9 was the region considered during the calculation of time- and area-averaged heat flux, as well as the associated enhancement factors. This region was selected because it was deemed large enough to capture the significant effects while not being overly large so that noteworthy details were under-represented. At a distance of $x/D_h = 16$ the surface heat flux had dropped to less than 10 % of the peak value for both the pulsed and steady cases.

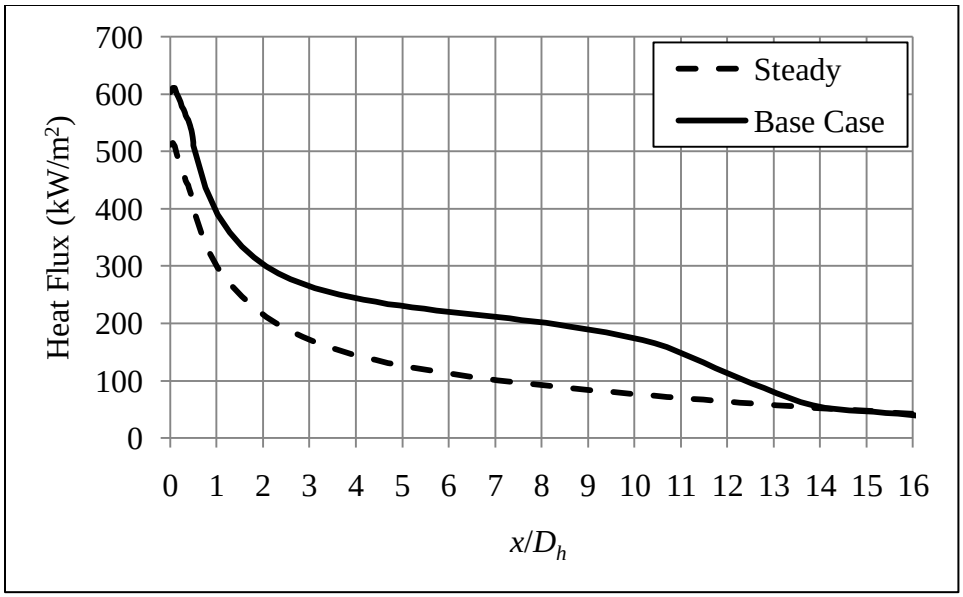

Figure 9.9: Comparison of time-averaged heat flux for the base and steady cases.

The base case produced heat flux at the stagnation point of 6.03×10^5 W/m^2 compared to 5.11×10^5 W/m^2 for the steady flow case. As x/D_h increased, the time-averaged heat flux initially increased near the stagnation point before decreasing for the rest of the domain for both the pulsed and steady flows. The maximum time-averaged heat flux was 6.11×10^5 W/m^2 for the base case at $x/D_h = 0.053$. Similarly, the peak value of the steady case was 5.11×10^5 W/m^2 which also occurred at $x/D_h = 0.053$. The increase in heat transfer performance is quantified by the heat transfer enhancement factor, E_{HF}. This factor is shown in Figure 9.10 as a function of x/D_h.

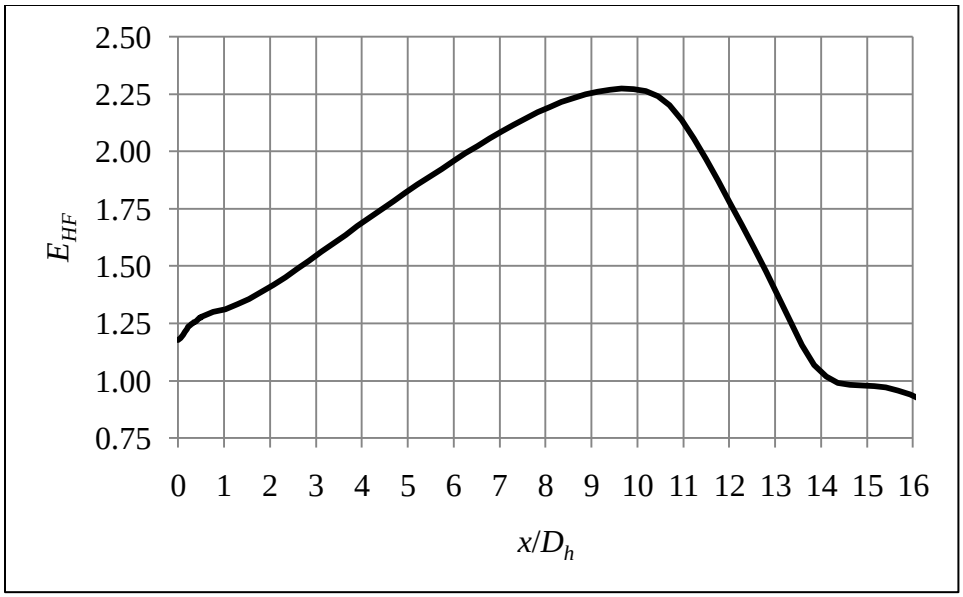

Figure 9.10: Heat flux enhancement factor versus position for the base case.

The base case produced 17.9 % higher heat flux at stagnation point. The enhancement increased to a maximum value of 2.27 at $x/D_h = 9.66$. After that point, E_{HF} decreased with increasing x/D_h. The base case failed to produce significant heat flux enhancement for $x/D_h > 14$. For the entire range $x/D_h < 16$, the time- and area-averaged heat flux, $\overline{\overline{q''}}$, was 2.01×10^5 W/m^2 compared to only 1.24×10^5 W/m^2 for the steady case. Thus, the average heat flux enhancement factor, $\bar{E}_{HF}$, was 1.61. Although this value is lower than those encountered in previous chapters, it is important to note that the steady jet in this comparison had a much higher mean temperature than the pulsating jet, as discussed previously. Still, a 61 % increase in average heat transfer is a considerable improvement.

Although the average heat flux and enhancement factors are perhaps the most important, valuable information can be gained by examining the instantaneous heat flux

profiles. Such profiles are given in Figure 9.11 for 8 values of τ.

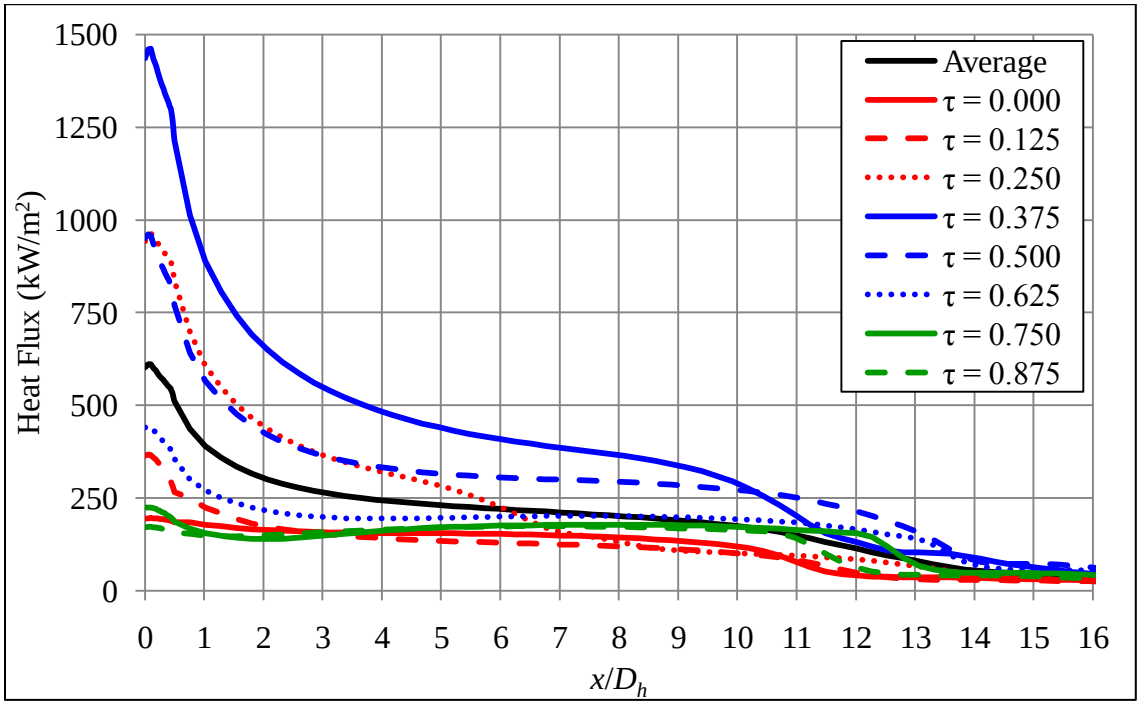

Figure 9.11: Heat flux at various values of τ for the base case.

The times shown in Figure 9.11 that resulted in the most significant heat transfer were $\tau = 0.250$, $\tau = 0.375$, and $\tau = 0.500$. Although similar heat flux values were obtained at $\tau = 0.250$ and $\tau = 0.500$ in the range $x/D_h < 5$, the profiles diverged past $x/D_h = 5$. This was the result of different jet characteristics and underlying mechanisms of heat transfer. At $\tau = 0.250$ the impingement jet was near its maximum velocity, as shown in Figure 9.4, but the jet temperature was still increasing at the tailpipe exit and had not yet supplied abundant heat to the impingement zone. Therefore, the high jet velocity produced a compact, intense vortex that was at a relatively low temperature, as shown in Figure 9.3 and Figure 9.5. The high velocity resulted in high heat flux in the range $x/D_h < 5$, despite the lower temperature. The heat flux quickly dropped off with increasing x/D_h, however,

and was lower than the time-averaged value beyond x/D_h = 6.5. Conversely, at τ = 0.500 the exit velocity was near its minimum magnitude, but the jet temperature was at its peak. Therefore, this low velocity jet resulted in heat flux similar to that at τ = 0.250 for x/D_h < 5 due to the elevated temperature. Additionally, by this time the center of the vortex had moved in the positive x-direction, and more heat was present in the impingement zone. Therefore, the heat flux remained relatively high past x/D_h = 5 and was above the time-averaged value for the remainder of the domain. As expected, the highest heat transfer rate was encountered at τ = 0.375, since this time yielded the most ideal combination of high temperature and vortex strength. The peak heat flux at this time was 2.39 times the time-averaged value. The enhancement factors associated with the instantaneous heat flux profiles are given in Figure 9.12. As expected, these factors followed similar patterns to those in Figure 9.11.

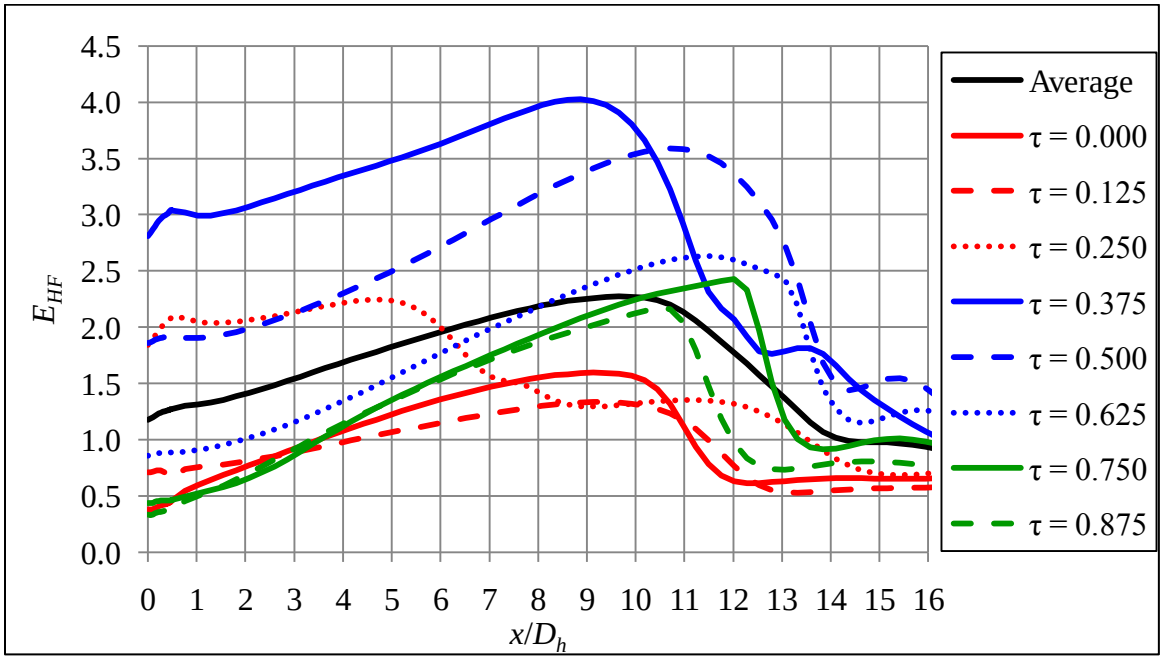

Figure 9.12: Heat flux enhancement factor at various values of τ for the base case.

In general, the x/D_h location of the peak enhancement factor at each time seemed to correspond with the size and location of the primary vortex. For example, once it reached the impingement surface, the vortex was shown to grow and move in the positive x/D_h direction from τ = 0.250 to τ = 0.625. The peak enhancement factor followed a similar pattern, shifting in the positive x/D_h direction at each time from τ = 0.250 to τ = 0.625. Similarly, the vortex and peak enhancement factors moved in the negative x/D_h direction at each time from τ = 0.750 to τ = 1.125 (τ = 0.125 of the next oscillation).

In terms of overall heat transfer performance, the pulsed flow produced good results at each time. Only τ = 0 and τ = 0.125 produced $\bar{E}_{HF} < 1$ for a large region of x/D_h. As a result, the steady flow was out performed at all other times shown. These results are summarized by the area-averaged values in Table 9.3. The highest average heat transfer enhancement was obtained at τ = 0.375 with $\overline{q''}$ more than three times that produced by the steady flow jet.

Table 9.3: Area-averaged heat flux and enhancement factors at various values of τ.

Time	$\overline{q''}$	$\bar{E}_{HF}$
-	($\times 10^5$ W/m^2)	-
τ = 0.000	1.15	0.93
τ = 0.125	1.14	0.92
τ = 0.250	2.25	1.81
τ = 0.375	3.86	3.10
τ = 0.500	2.98	2.39
τ = 0.625	1.84	1.48
τ = 0.750	1.43	1.15
τ = 0.875	1.30	1.04
Steady Case	1.24	-

As noted before, the area averaged heat flux and associated enhancement factors were calculated over the range $x/D_h \leq 16$. Although this range was considered to be optimal for representing the overall impact while still adequately describing noteworthy details, other ranges could have been selected. For reference, Figure 9.13 gives the time- and area-averaged heat flux as a function of the range used in the averaging. That is, the vertical axis is the heat flux averaged over the range $x/D_h \leq x_o$. Similarly, Figure 9.14 gives the corresponding heat flux enhancement factor using the same methodology.

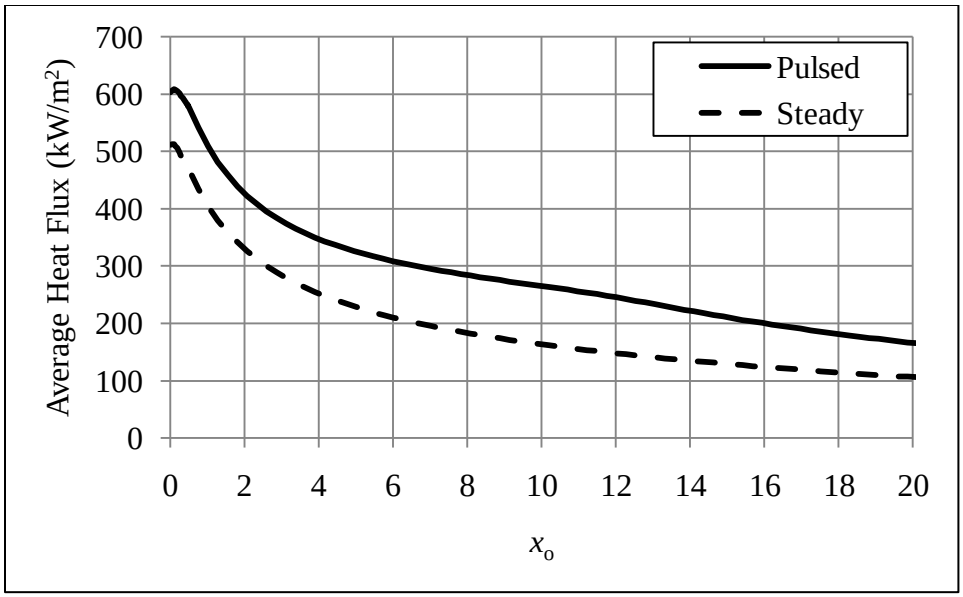

Figure 9.13: Heat flux averaged over the range $x/D_h \leq x_o$.

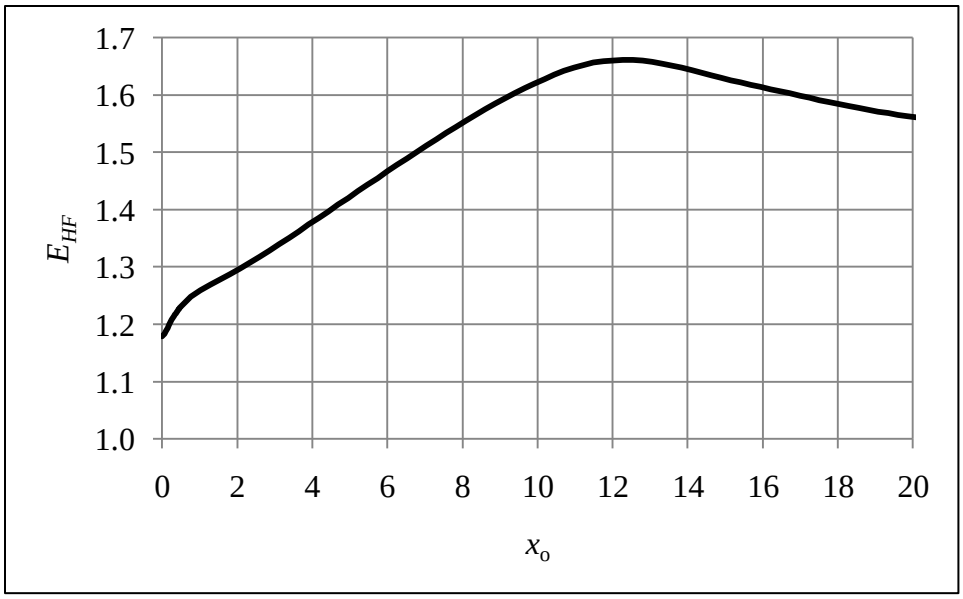

Figure 9.14: Enhancement factor based on heat flux averaged over the range $x/D_h \leq x_o$.

For example, the average heat flux over the range $x/D_h \leq 6$ was 3.09×10^5 W/m^2. Similarly, the maximum average enhancement factor was obtained using the range $x/D_h \leq 12.275$. Although this chapter deals primarily with heat flux, the total rate of heat transfer

per unit width in the *z*-direction can easily be calculated by simply integrating over the desired range. The total heat transfer rate to the impingement surface is shown in Figure 9.15 as a function of the range of integration.

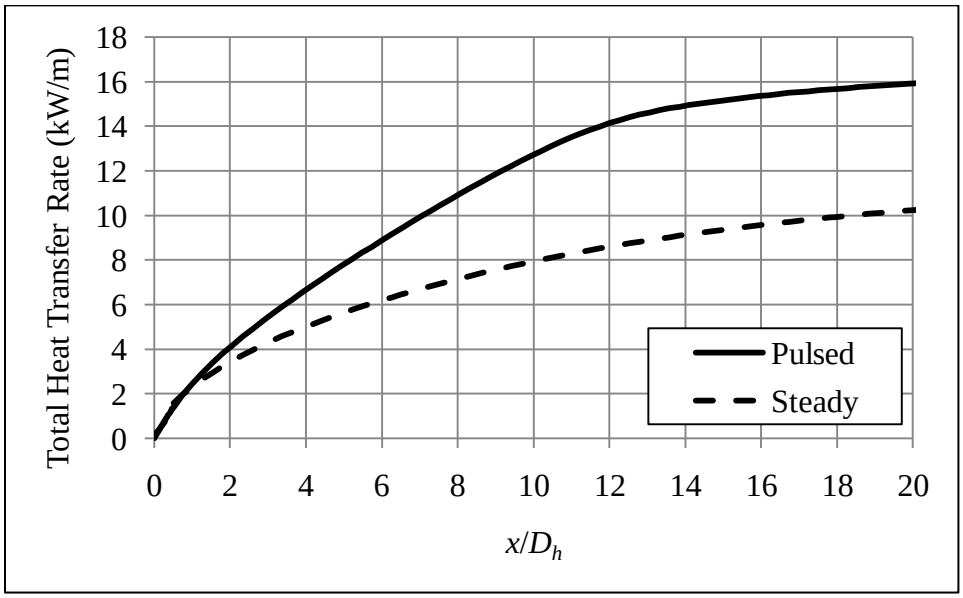

Figure 9.15: Total heat transfer rate as a function of position.

9.3 Effects of Amplitude Ratio

In this section six velocity amplitude ratios are considered: 2.5, 3.0, 3.5, 4.0, 4.5, and 5.0. R_{amp} = 4.0 corresponds to the base case and serves as a reference point. Since the details of the base case have already been discussed, only the significant changes in the other cases will be addressed. Other operational parameters remain the same as the base case; namely, ω = 160 Hz, $\overline{U}_{exit}$ = 30 m/s, D_h = 4.8×10^{-3} m, and H/D_h = 5. Since the mean values were unchanged, the dimensionless parameter $\overline{St}$ also remained 0.0256. The same numerical domain, stationary impingement surface, and 1200 K inlet temperature

were also used. The resulting bulk temperatures at the tailpipe exit are shown in Figure 9.16.

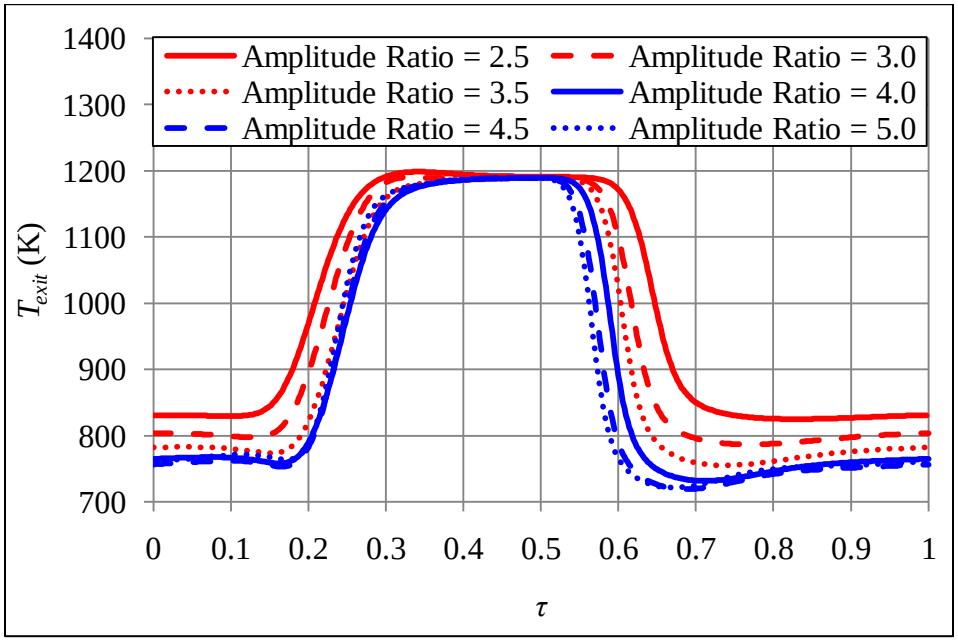

Figure 9.16: Bulk tailpipe exit temperature for one oscillation and various values of R_{amp}.

While the maximum values were similar for each case, the temperatures profiles were wider for lower amplitude ratios. The minimum temperatures encountered in each case also increased with decreasing R_{amp}. Subsequently, the mean exit temperature followed a similar pattern, increasing with decreasing R_{amp}. The resulting maximum, minimum, and average exhaust exit temperatures for each velocity amplitude ratio are shown in Figure 9.17.

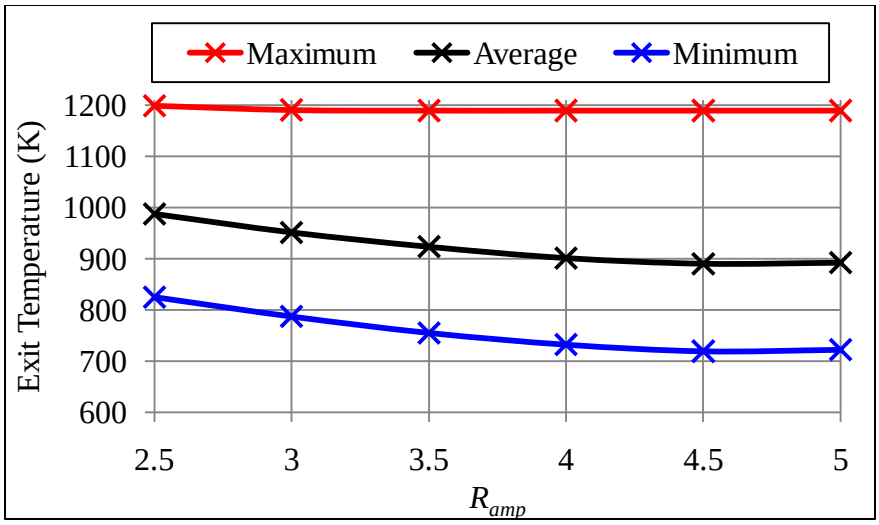

Figure 9.17: Bulk tailpipe exit temperatures for various values of R_{amp}.

In general, the average temperatures decreased with increasing amplitude ratios. This was a result of increased flow reversal leading to greater backflow of low-temperature ambient air at the outlet. The maximum tailpipe exit temperature was the least impacted by the changes in R_{amp}, deviating by only 2 K in all cases. The minimum temperature, however, ranged from 825 K for R_{amp} = 2.5 to 719 K for R_{amp} = 4.5. The amplitude ratio had the largest impact on temperatures at low values. The change in mean tailpipe exit temperature also altered the dimensionless parameter $\overline{Re}$ as shown in Table 9.4.

Table 9.4: Mean Reynolds number at the tailpipe exit.

R_{amp}	$\bar{T}_{\text{exit}}$	$\overline{Re}$
-	(K)	-
2.5	987	1239
3.0	951	1315
3.5	923	1381
4.0	901	1438
4.5	890	1468
5.0	892	1463

The instantaneous velocity fields at eight values of dimensionless time are shown in Figure 9.18 for R_{amp} = 5. The flow structures were similar to those of the base case, albeit with a slightly larger and stronger vortex. The progression and general shape of the vortex, however, paralleled those of the base case.

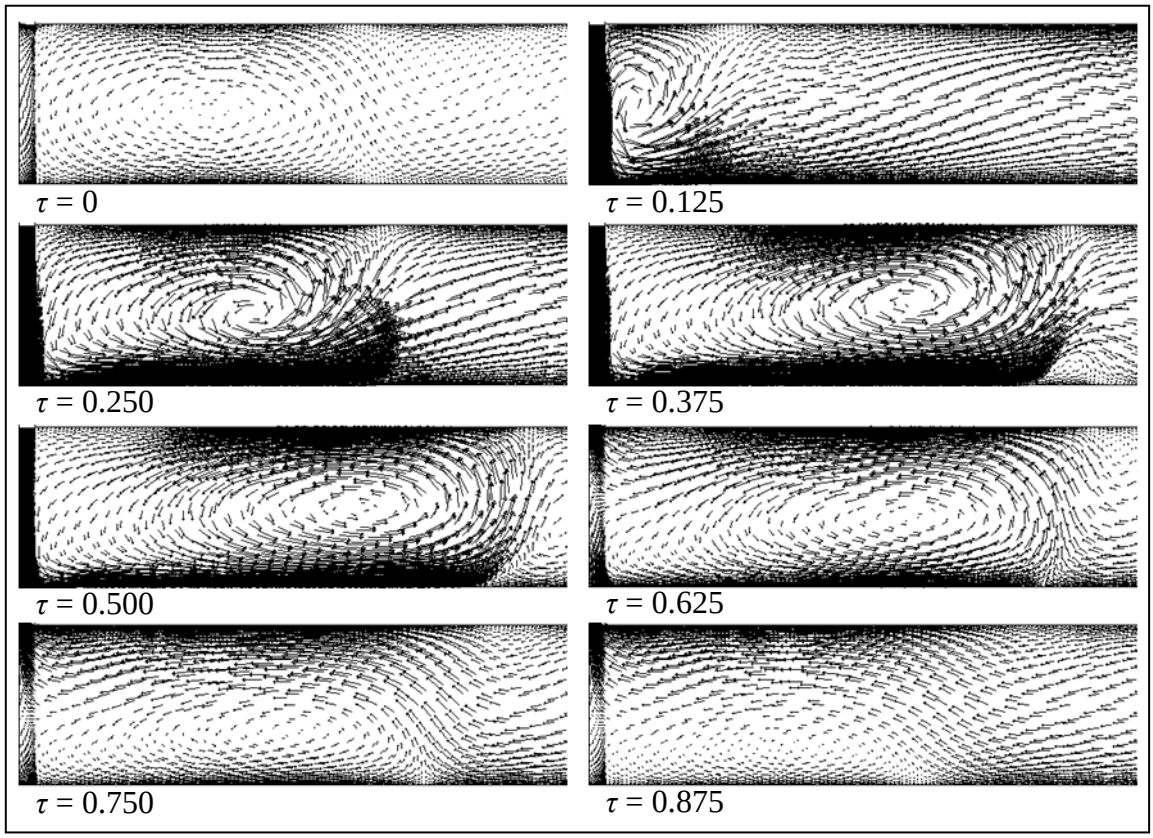

Figure 9.18: Flow field at various values of τ with R_{amp} = 5.

Additionally, the instantaneous temperature fields at 8 values of dimensionless time are shown in Figure 9.19 for R_{amp} = 5. As expected, the similar flow field also produced a temperature field comparable to the base case. The increase in backflow at the outlet is clearly visible in Figure 9.19. This was responsible for the lower minimum and average exhaust exit temperatures as discussed previously and shown in Figure 9.16 and Figure 9.17.

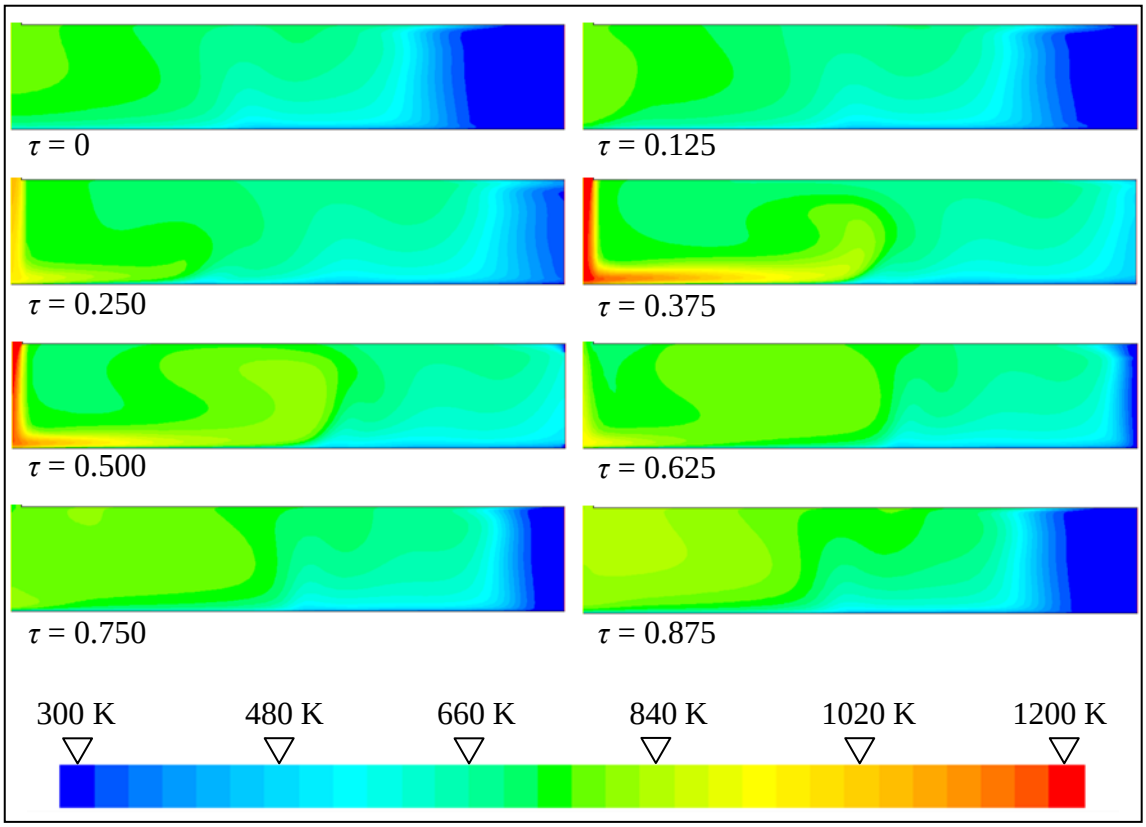

Figure 9.19: Temperature field at various values of τ with R_{amp} = 5.

The velocity and temperature fields generated by the other amplitude ratios emulated those presented for R_{amp} = 4 and R_{amp} = 5. The vortex size and strength did increase with increasing amplitude ratio, but the vortex shape and development were consistent between cases. The enlarged vortices were somewhat mitigated by slightly lower temperatures in the impingement zone. The combination of comparable, although not identical, flow fields and temperature distributions resulted in similar heat transfer characteristics. The time-averaged heat flux profiles for each amplitude ratio are shown in Figure 9.20 as a function of x/D_h.

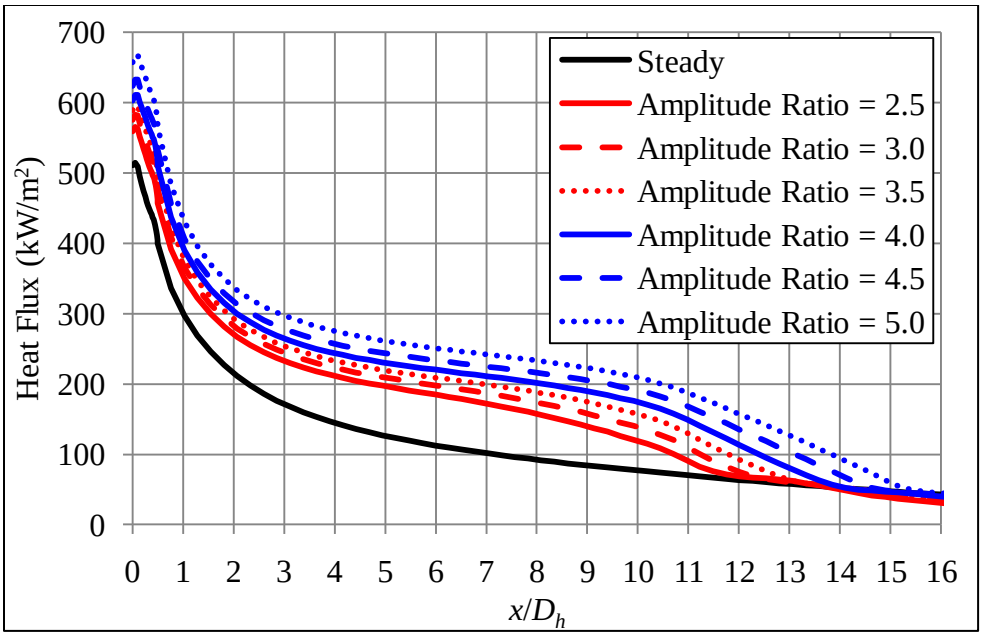

Figure 9.20: Time-averaged heat flux profiles for various velocity amplitude ratios.

As expected, the profile shapes were similar for all the pulsed cases. Higher amplitude ratios consistently produced greater heat flux throughout the region of interest, thereby shifting each curve up. In general, the heat flux improvement due to elevated R_{amp} increased as x/D_h increased. For example, R_{amp} = 5 produced heat flux at x/D_h = 2 that was 6.63×10^4 W/m^2 or 24.8 % higher than the value for R_{amp} = 2.5. At x/D_h = 10, however, the difference had grown to 9.15×10^4 W/m^2, a 79.8 % disparity. All of the profiles did converge past $x/D_h \approx 12$. Similar behavior is also demonstrated in Figure 9.21, a plot of the time-averaged heat flux enhancement factors as a function of R_{amp} and x/D_h.

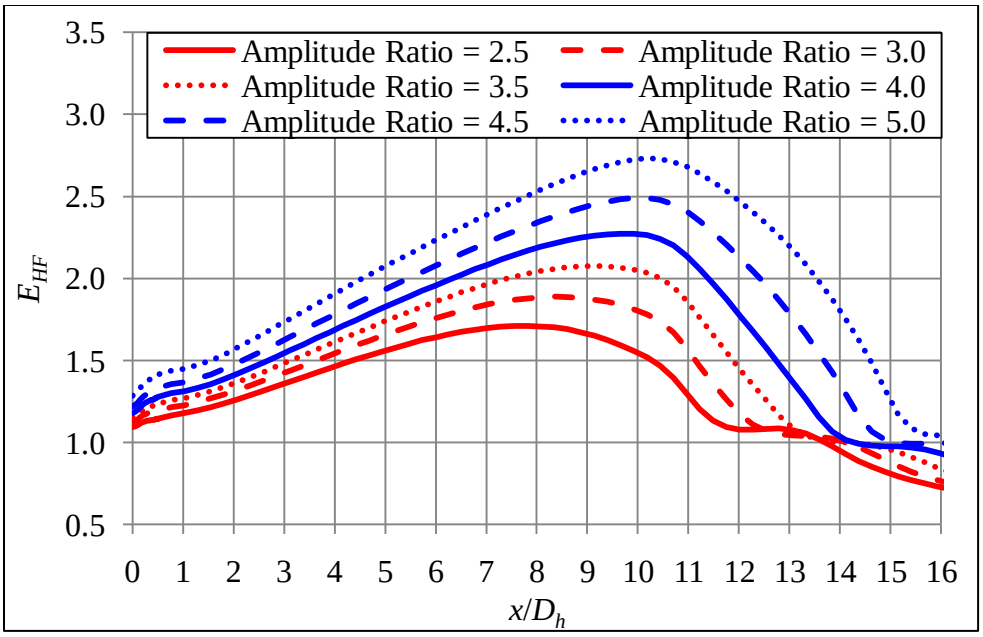

Figure 9.21: Time-averaged heat flux enhancement factors for various R_{amp}.

The heat flux enhancement for all cases increased with x/D_h until reaching a peak value somewhere in the range $7.8 < x/D_h < 10.2$. Past the peak, the enhancement decreased significantly with increasing x/D_h. By $x/D_h = 16$ the enhancement was reduced to only 4 % for $R_{amp} = 5$ and E_{HF} was less than 1 for all other cases as a result of encroachment of low temperature backflows. Higher R_{amp} resulted in greater enhancement and wider profiles. The x/D_h location of the peak enhancement values also increased with R_{amp}, again corresponding with larger vortices. The overall heat transfer performance is summarized in Table 9.5.

Table 9.5: Average heat flux and $\bar{E}_{HF}$ for various R_{amp}.

R_{amp}	$\overline{q''}$	$\bar{E}_{HF}$
-	($\times 10^5$ W/m^2)	-
0	1.24	-
2.5	1.66	1.33
3.0	1.77	1.42
3.5	1.88	1.52
4.0	2.01	1.61
4.5	2.16	1.73
5.0	2.35	1.89

All pulsating cases produced significantly higher average heat flux than the steady impingement jet. The maximum value $\overline{q''}$ was 2.35×10^5 W/m^2, corresponding to an 89 % improvement in heat transfer over the steady flow case. This value was obtained for R_{amp} = 5. The average heat flux, and thus the average enhancement, increased with velocity amplitude ratio, despite the average exit temperature decreasing. This is highlighted in Figure 9.22, a plot comparing the time- and area-averaged heat flux for each R_{amp} using the base case as the reference value. For example, R_{amp} = 2.5 yielded 17.5 % less heat transfer than the base case, while R_{amp} = 5 resulted in 17.1 % more heat transfer compared to the base case (R_{amp} = 4).

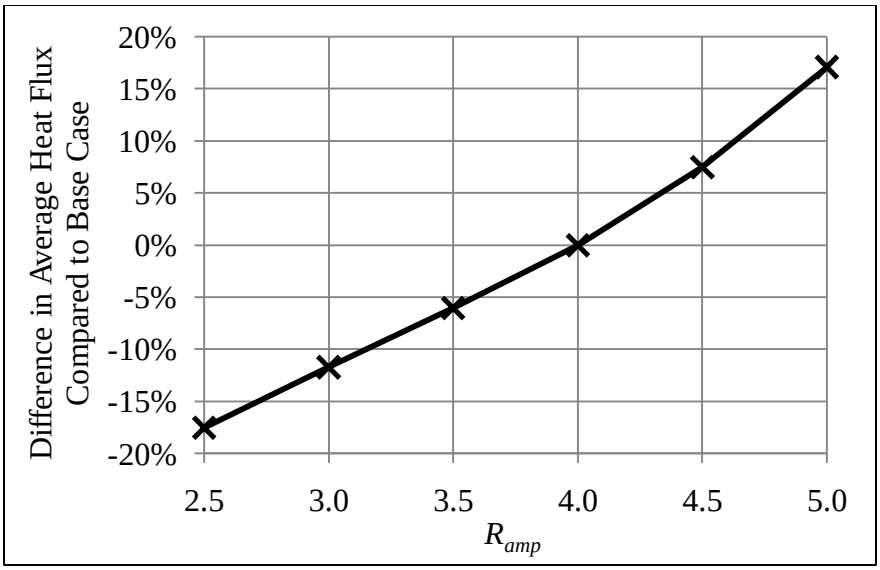

Figure 9.22: Time-averaged heat flux compared to the base case.

Increasing the velocity amplitude ratio resulted in a nearly linear increase in average heat transfer. Therefore, to achieve maximum heat transfer it is suggested to obtain the highest value of R_{amp} possible, at least for conditions and ranges similar to the ones considered in this section.

9.4 Effects of Oscillation Frequency

In this section the effects of seven oscillation frequencies are presented. The frequencies and resulting dimensionless parameters are given in Table 9.6. As before, the other operational characteristics matched those of the base case: R_{amp} = 4, $\overline{U}_{exit}$ = 30 m/s, D_h = 4.8×10^{-3} m, and H/D_h = 5. For reference, the base case corresponds to ω = 160 Hz.

Table 9.6: Oscillation frequencies and resulting dimensionless parameters.

ω	$\bar{St}$	$\overline{Re}$
(Hz)	-	-
80	0.0128	1307
125	0.0200	1417
160	0.0256	1438
200	0.0320	1467
250	0.0400	1530
320	0.0512	1678
400	0.0640	1616

The same numerical domain, stationary impingement surface, and 1200 K inlet temperature from the base case were used in these cases. The resulting bulk tailpipe exit temperatures for each oscillation frequency are shown in Figure 9.23. The difference in temperatures was partially responsible for the change in $\overline{Re}$ shown in Table 9.6.

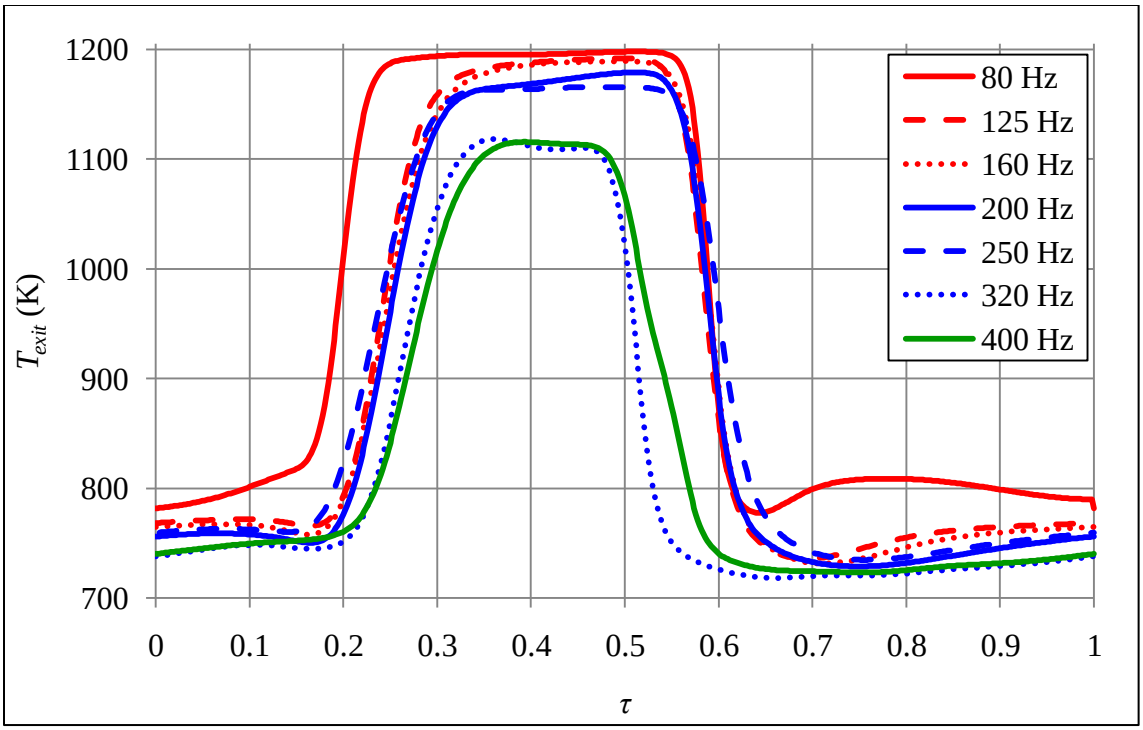

Figure 9.23: Bulk tailpipe exit temperatures for one oscillation cycle and various ω.

Each temperature profile formed one of three distinct shapes. ω = 80 Hz yielded a wide plateau, high maximum and minimum temperatures, and a pronounced rise after τ = 0.65. Oscillation frequencies from 125 Hz to 250 Hz produced narrower plateaus, slightly lower maximum temperatures, significantly lower minimum values, and only a gradual secondary rise in temperature at the end of the cycle. Finally, the shapes of the temperature profiles resulting from ω = 320 Hz and ω = 400 Hz had much narrower plateaus, considerably lower maximum temperatures, and no significant secondary local maxima. These distinct differences in exit temperatures are also reflected in the time-averaged values shown in Figure 9.24.

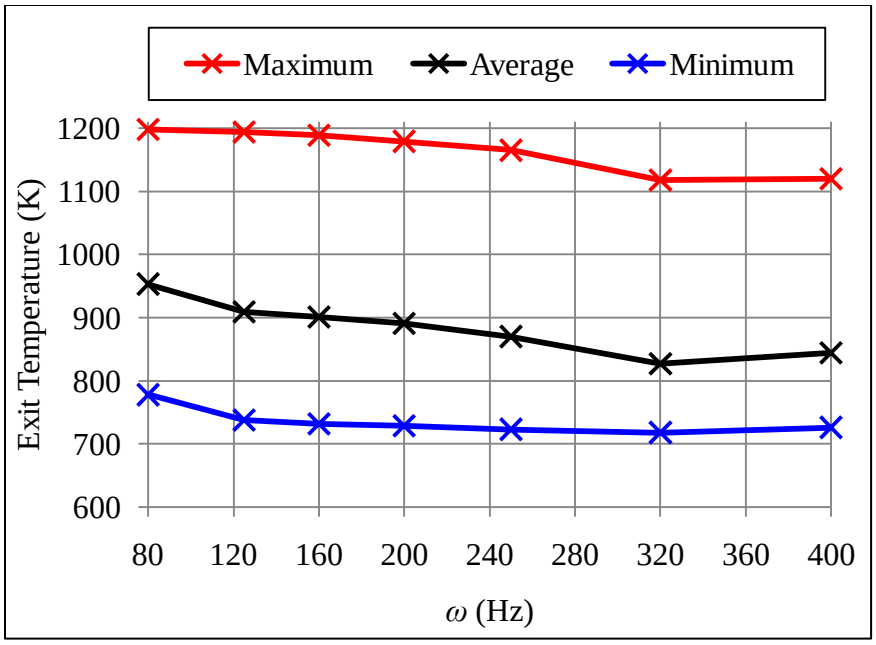

Figure 9.24: Bulk tailpipe exit temperatures for various oscillation frequencies.

The minimum exit temperatures remained relatively consistent with the exception of the elevated value for ω = 80 Hz. There was a noticeable shift in the maximum temperature, however, for ω = 320 Hz and ω = 400 Hz. These shifts in tailpipe outflow conditions are expected to yield different heat flux profiles as well. The resulting time-averaged heat flux profiles are given in Figure 9.25.

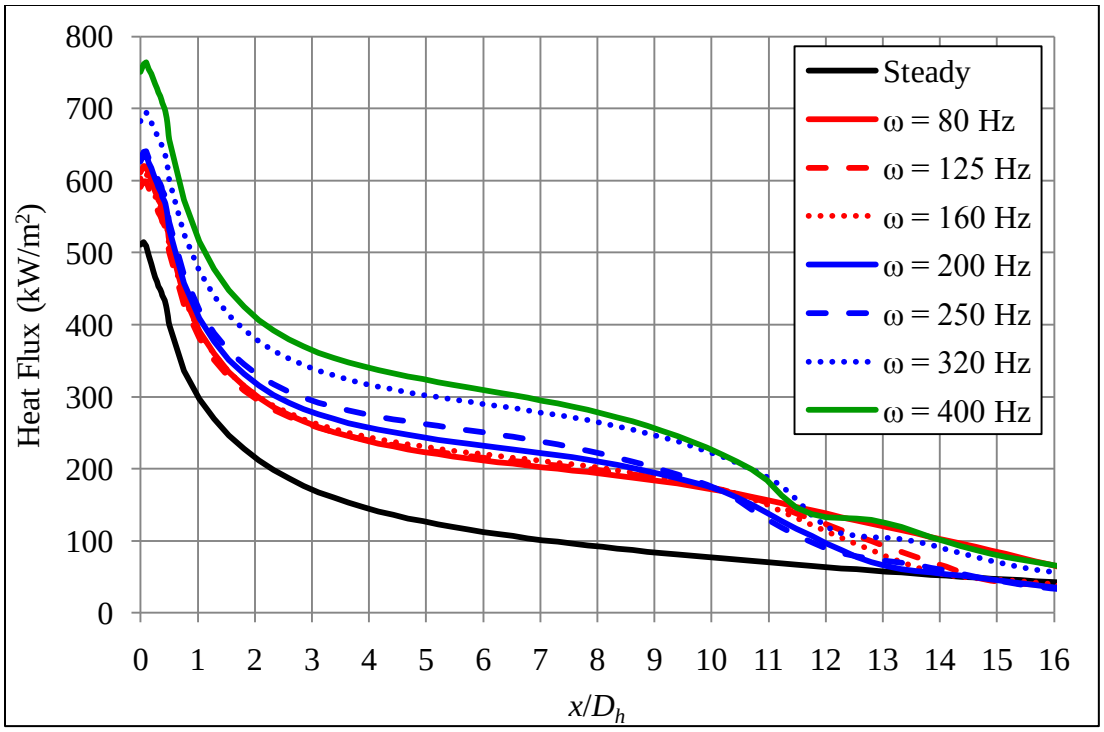

Figure 9.25: Time-averaged heat flux profiles for various oscillation frequencies.

The heat flux profiles also had three distinct shapes, and the cases were separated into the same groups as before. The shapes were relatively similar in the region $x/D_h < 10$, although the curves for $\omega = 320$ Hz and $\omega = 400$ Hz were shifted higher. In the region $x/D_h > 10$, the heat flux declined considerably for $\omega = 320$ Hz and $\omega = 400$ Hz, and less so for 125 Hz $\leq \omega \leq$ 250 Hz. Conversely, the $\omega = 80$ Hz case did not experience an abrupt change in slope in this region. The resulting heat flux enhancement factors are shown in Figure 9.26

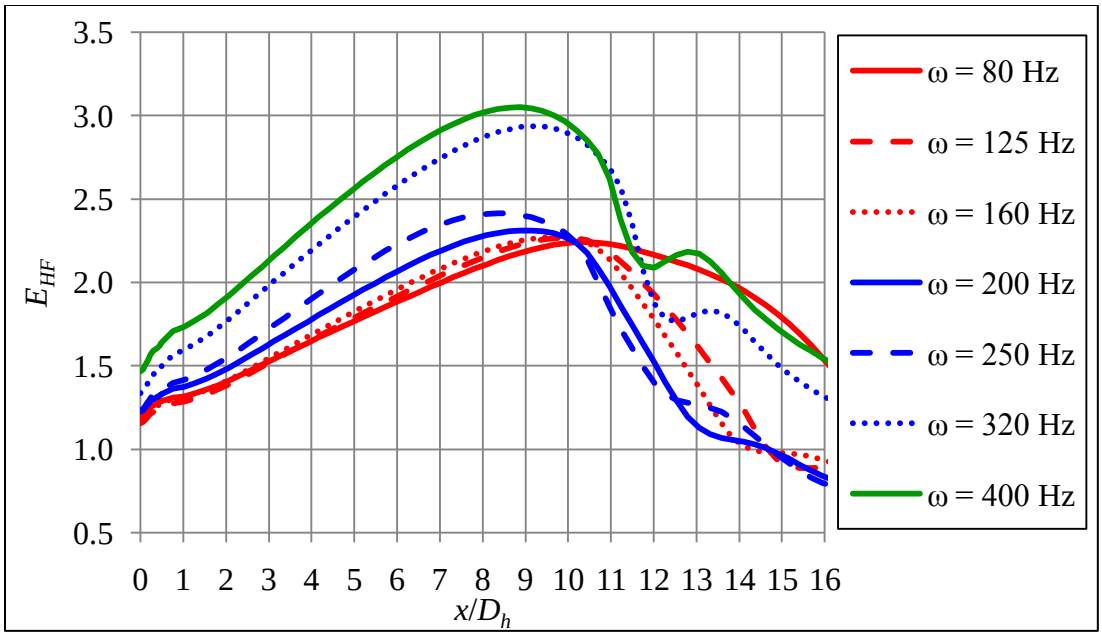

Figure 9.26: Time-averaged heat flux enhancement for various ω.

As expected from the heat flux profiles, the three familiar groupings are still evident in Figure 9.26. The ω = 80 Hz case had the lowest enhancement for $x/D_h < 10$ but retained most of its peak value throughout the entire region of interest. At x/D_h = 16 this case still maintained an enhancement factor of 1.55, 69.2 % of its maximum of 2.24. The enhancement profiles for cases with 125 Hz $\leq \omega \leq$ 250 Hz all had the same general shape as the base case (ω = 160), with a steep drop-off after x/D_h = 10. All of these cases had $\bar{E}_{HF} < 1$ at x/D_h = 16. The ω = 320 Hz and ω = 400 Hz cases had considerably higher enhancement factors than the other cases in the region $x/D_h < 11$ but experienced the same steep decline as the base case. At x/D_h = 16 the enhancement factor for ω = 400 Hz was 1.55, only 50.8 % of its maximum value of 3.05. The resultant time- and area-averaged heat flux values for each case are given in Table 9.7.

Table 9.7: Average heat flux and enhancement for various ω.

ω	$\overline{q''}$	$\bar{E}_{HF}$
(Hz)	($\times 10^5$ W/m^2)	-
80	2.09	1.68
125	2.00	1.61
160	2.01	1.61
200	2.06	1.65
250	2.14	1.72
320	2.55	2.05
400	2.73	2.20
Steady	1.24	-

With the exception of ω = 80 Hz the heat flux increased with increasing oscillation frequency. Due to the more uniform heat flux profile, however, the ω = 80 Hz case slightly outperformed the 125 Hz $\leq \omega \leq$ 200 Hz cases. By ω = 250 Hz, the higher frequency case had obtained a performance advantage. The ω = 320 Hz and ω = 400 Hz cases produced significantly higher values mainly due to the rather high values in the range $x/D_h < 11$. The maximum value of $\overline{q''}$ was 2.73×10^5 W/m^2, which was obtained in the ω = 400 Hz case. This corresponds to a 120 % increase in heat transfer compared to the steady flow case. The average heat flux values are compared in Figure 9.27 using the base case as the reference point.

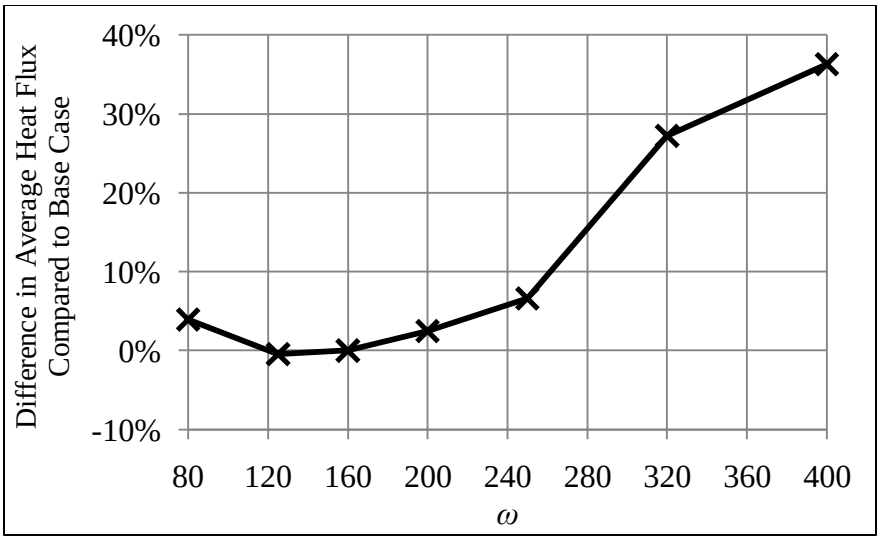

Figure 9.27: Time-averaged heat flux compared to the base case.

In general, the highest oscillation frequencies also yielded the greatest heat transfer performance. The ω = 400 Hz case resulted in 36.3 % higher average heat flux than the base case. Still, the low frequency 80 Hz case also outperformed the base case, albeit by only 4.0 %. In order to discern the mechanisms responsible for the three distinct natural groupings frequently encountered in this section, the ω = 80 Hz and ω = 400 Hz cases will be discussed more thoroughly. The base case has already been discussed so it will serve as a representative of the third group. The instantaneous flow fields of the ω = 80 Hz case is shown in Figure 9.28 for 3 values of τ.

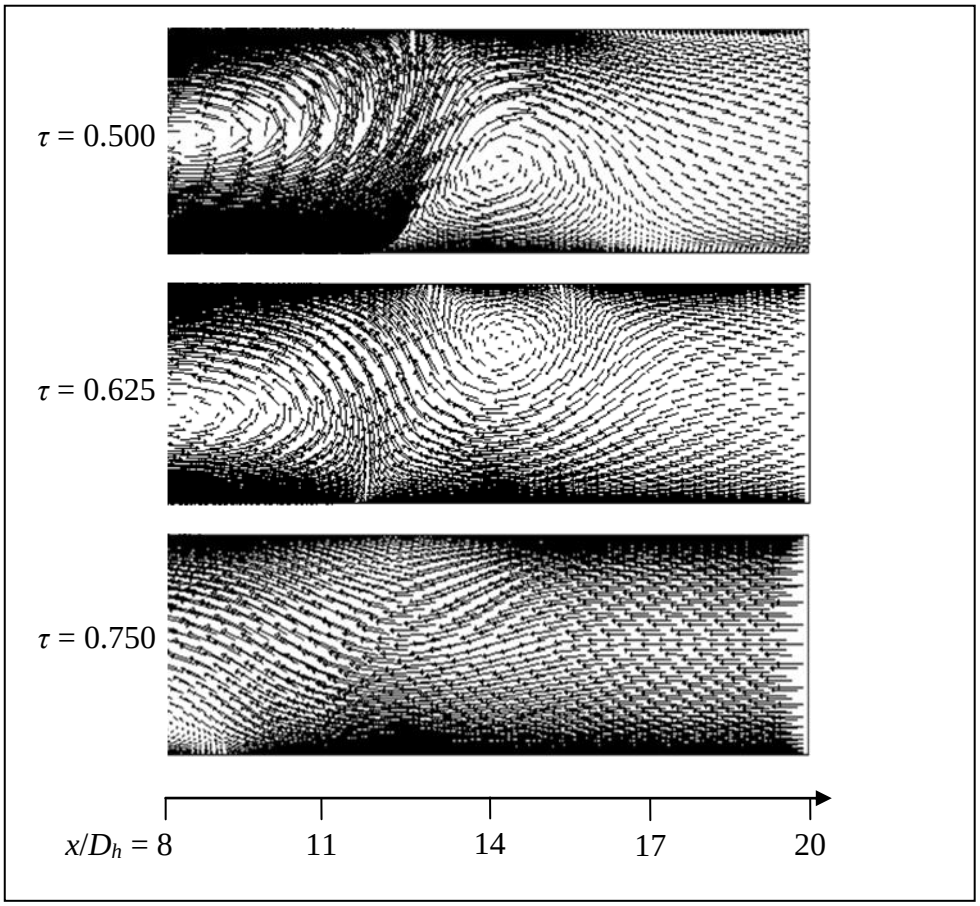

Figure 9.28: Portion of domain showing instantaneous flow fields for ω = 80 Hz.

Only a portion of the numerical domain is shown in Figure 9.28 in order to highlight an important feature that distinguishes this case from those with different oscillation frequencies. A secondary vortex was formed between τ = 0.375 and τ = 0.500 to the right of the primary vortex. This smaller, short-lived vortex can be seen at τ = 0.500 and τ = 0.625, but had dissipated by τ = 0.750. Such a vortex was not encountered in the other cases that were investigated. The presence of the secondary vortex partially accounts for the instantaneous heat flux profiles in Figure 9.29.

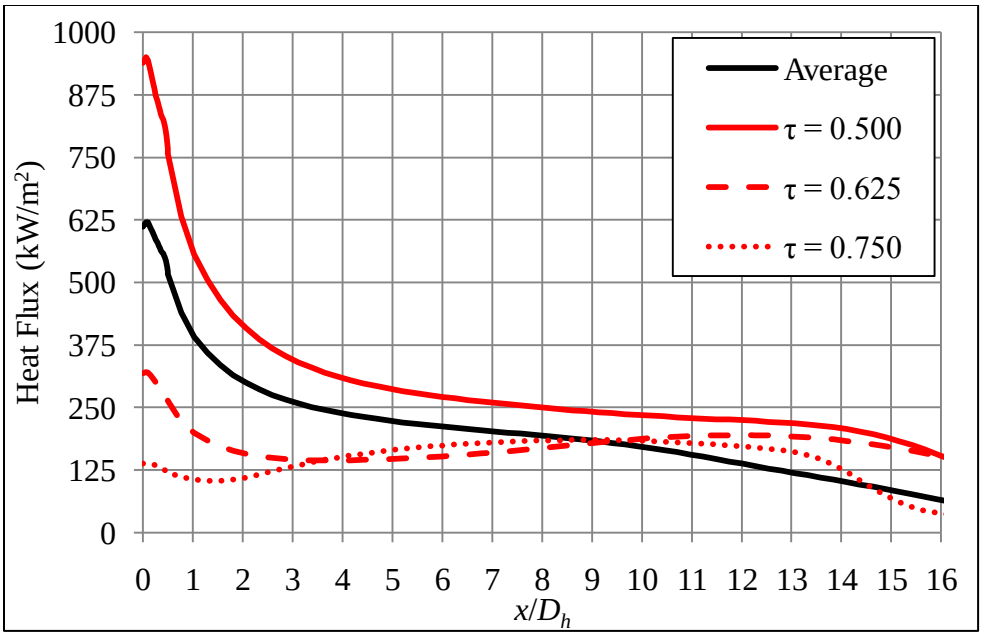

Figure 9.29: Heat flux profiles at 3 values of τ for ω = 80 Hz.

The dimensionless times presented in Figure 9.29 correspond to those shown in Figure 9.25. All three profiles were greater than the one-cycle average in the region x/D_h > 10. However, the times in which the secondary vortex was most apparent, τ = 0.500 and τ = 0.625, also produced notably greater heat flux in the region x/D_h > 13. Conversely, the profile for τ = 0.750 had a significant drop-off past x/D_h = 13. This pattern is even more apparent in the corresponding enhancement factors shown in Figure 9.30.

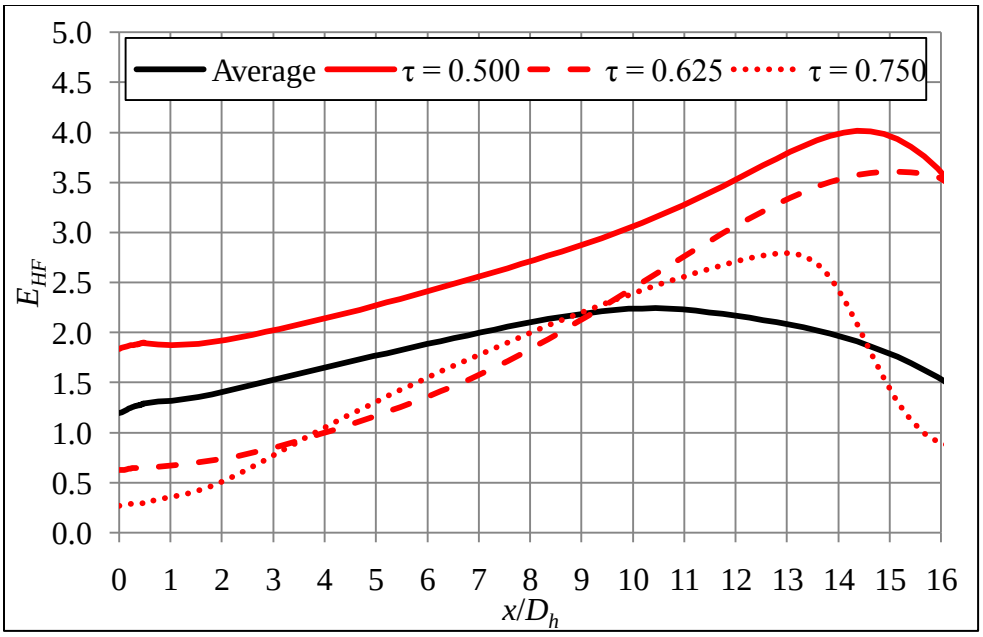

Figure 9.30: Heat flux enhancement at 3 values of τ for ω = 80 Hz.

The enhancement factors for τ = 0.500 and τ = 0.625 increased significantly with increasing x/D_h. In fact, the maximum values for these two times did not occur until x/D_h > 14. The elevated heat flux and corresponding enhancement due to the secondary vortex appear to be the explanation for the more evenly distributed heat flux when compared to the other cases. The secondary vortex aided heat transfer in the region to the right of the primary vortex during the middle of the oscillation cycle. No such mechanism was present in the cases with ω > 80 Hz; thus, the heat flux at higher values of x/D_h was significantly reduced in said cases.

The final natural grouping consisted of the ω = 320 Hz and ω = 400 Hz cases. This group also displayed flow patterns that were different than those of the other groups. The instantaneous flow fields of the ω = 400 Hz case is shown in Figure 9.31.

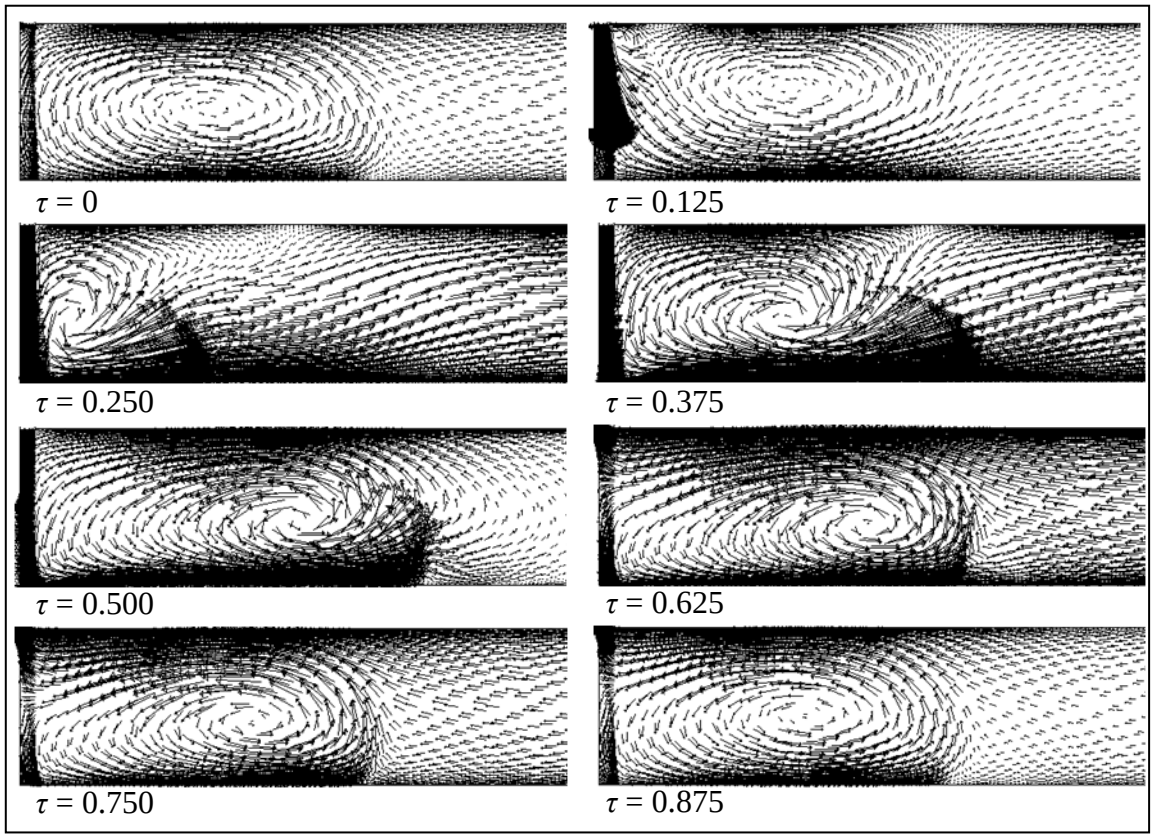

Figure 9.31: Flow fields at various values of τ for ω = 400 Hz.

The flow fields in Figure 9.31 showed two key attributes that were unique to the ω = 320 Hz and ω = 400 Hz group. First, the primary vortex was clearly present throughout the entire oscillation cycle. The vortex in the base case, for example, was severely diminished after τ = 0.625 and was only vaguely discernable from τ = 0.750 to τ = 1.000 in Figure 9.3. Conversely, Figure 9.31 shows a readily apparent vortex structure at all values of τ. The second distinguishing attribute of the flow fields for ω = 320 Hz and ω = 400 Hz group was related to the size of the vortex. With the exception of τ = 0.250 and perhaps τ = 0.750, the size of the vortex was relatively consistent across times as compared to the other cases. The short period of this case did not allow adequate time for the vortex to grow in size compared to the base case. The combination of the small

yet intense and persistent primary vortex produced the extremely high heat flux values in the range $x/D_h < 10$. This is shown in Figure 9.32, where the minimum heat flux values in that range were much higher than those of the base case.

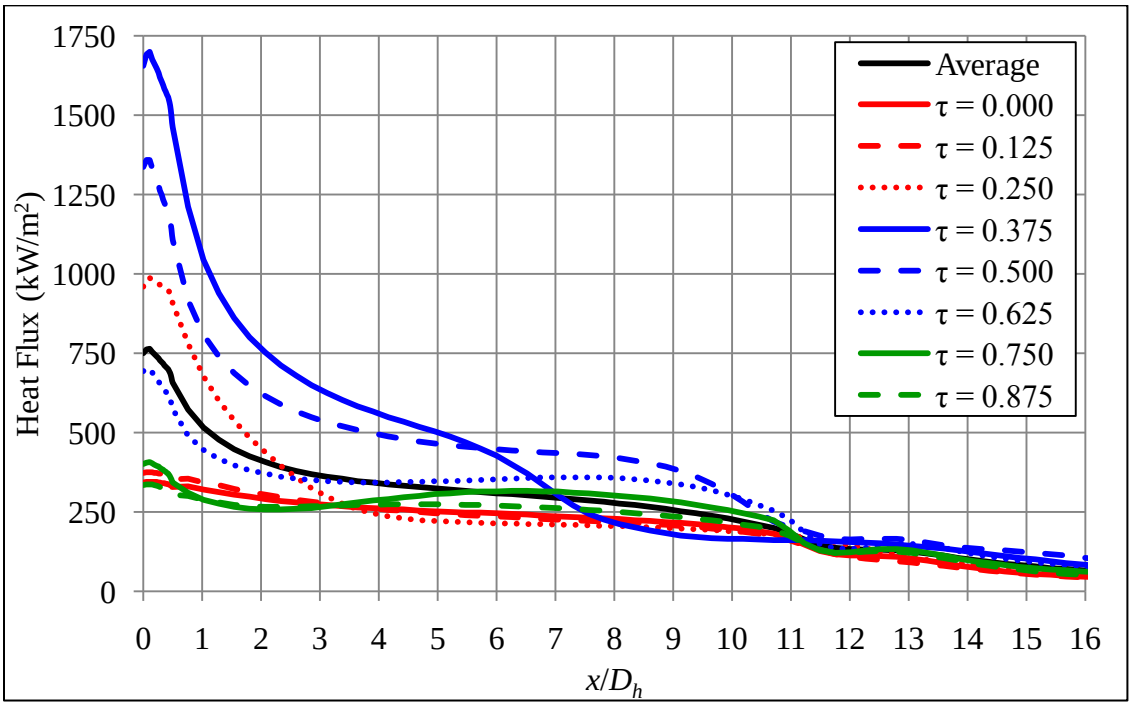

Figure 9.32: Heat flux profiles at various values of τ for ω = 400 Hz.

The correlation between heat flux and vortex size was also reflected in the enhancement factor for ω = 400 Hz shown in Figure 9.33. Past $x/D_h \approx 11$, a distance which corresponds to the outer extent of the primary vortex, the enhancement declined considerably. Thus, the unique heat flux patterns of the high oscillation frequency cases were also apparently direct effects of the distinct vortex structures.

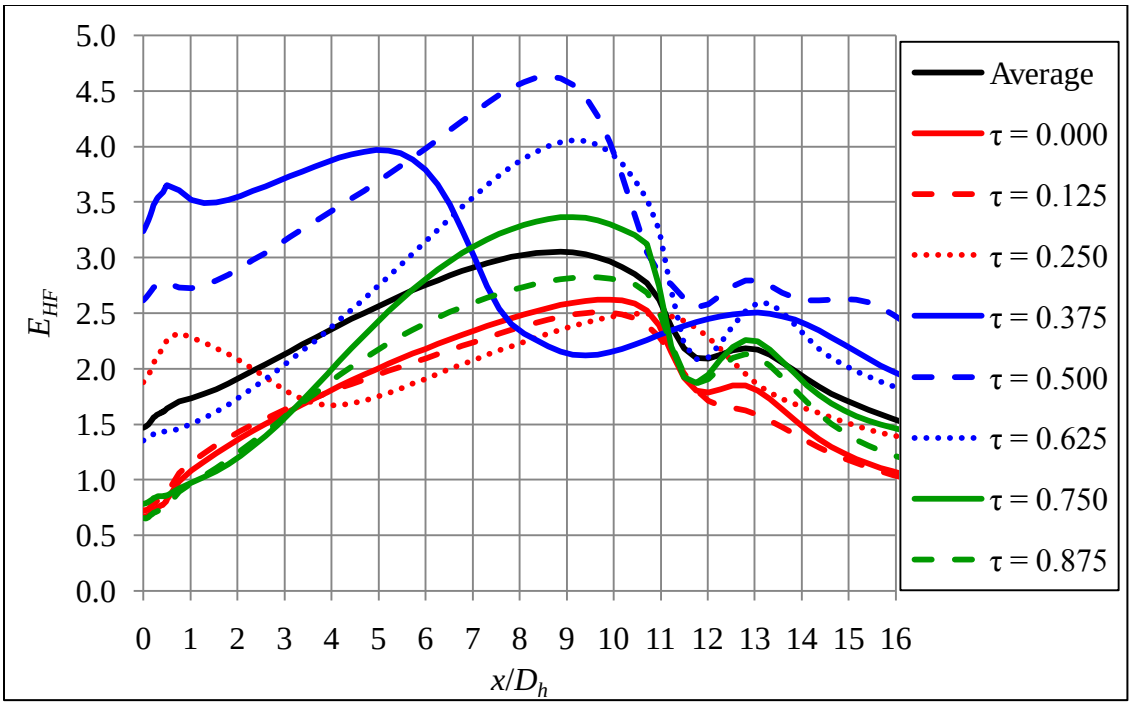

Figure 9.33: Heat flux enhancement at various τ for ω = 400 Hz.

9.5 Effects of Mean Velocity

Now that the primary time-varying characteristics have been discussed, the role of the mean velocity at the tailpipe exit will be investigated. The mean velocities and resulting dimensionless parameters employed in this section are given in Table 9.8. All other controlled parameters matched those of the base case.

Table 9.8: Mean velocities and resulting dimensionless parameters at the tailpipe exit.

$\overline{U}_{exit}$	$\overline{St}$	$\overline{Re}$
(m/s)	-	-
10	0.0768	527
15	0.0512	774
20	0.0384	1012
25	0.0307	1232
30	0.0256	1438
35	0.0219	1628

The tailpipe exit temperatures were relatively consistent throughout these cases. The maximum, minimum, and time-averaged bulk temperatures at the tailpipe exit are given in Figure 9.34.

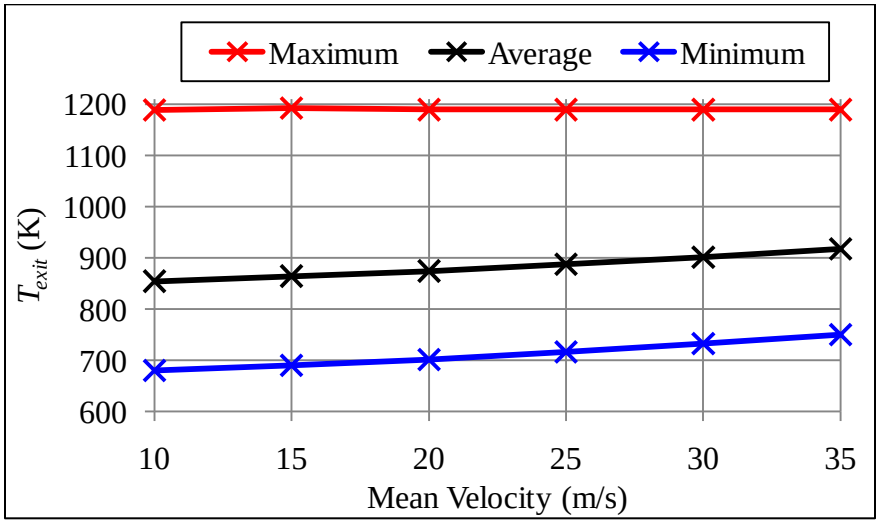

Figure 9.34: Bulk tailpipe exit temperatures for various oscillation frequencies.

The maximum temperatures varied by only 4 K. The minimum temperatures, however, increased with increasing mean velocity. Thus, the average temperatures followed a similar pattern, ranging from 854 K for $\overline{U}_{exit}$ = 10 m/s to 917 for $\overline{U}_{exit}$ = 30 m/s.

The resulting flow field for $\overline{U}_{exit}$ = 10 m/s is shown in Figure 9.35. This case was selected because it was the most different from the base case. Still, the familiar single primary vortex was observed. This vortex was much smaller and weaker than that of the base case. Additionally, the vortex took longer to develop than in the base case.

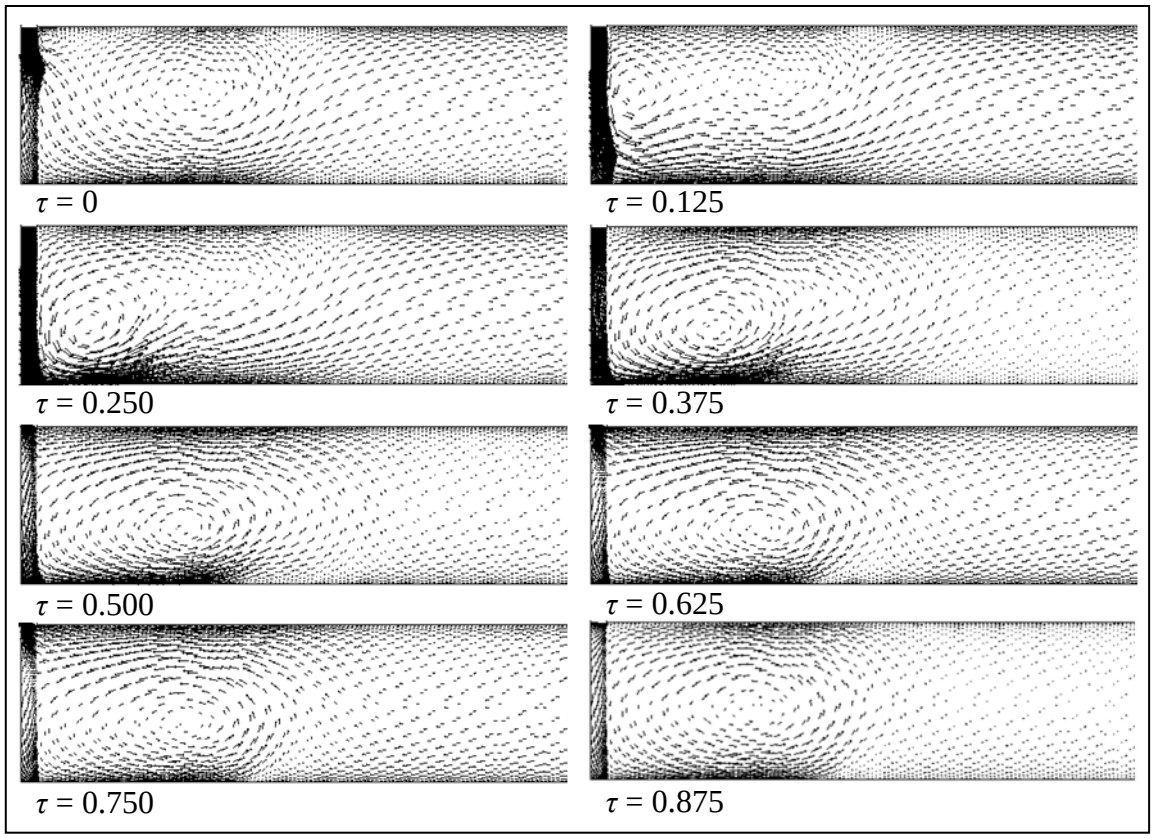

Figure 9.35: Flow field at various values of τ with $\overline{U}_{exit}$ = 10 m/s.

The smaller size and lower strength of the vortex was an expected result since the mean bulk velocity, and therefore peak bulk velocity given the same R_{amp}, was only 33 % of the base case. The reduced bulk velocity also impacted the temperature distribution in the impingement zone. The instantaneous temperature fields produced by $\overline{U}_{exit}$ = 10 m/s are shown in Figure 9.36 for various values of τ.

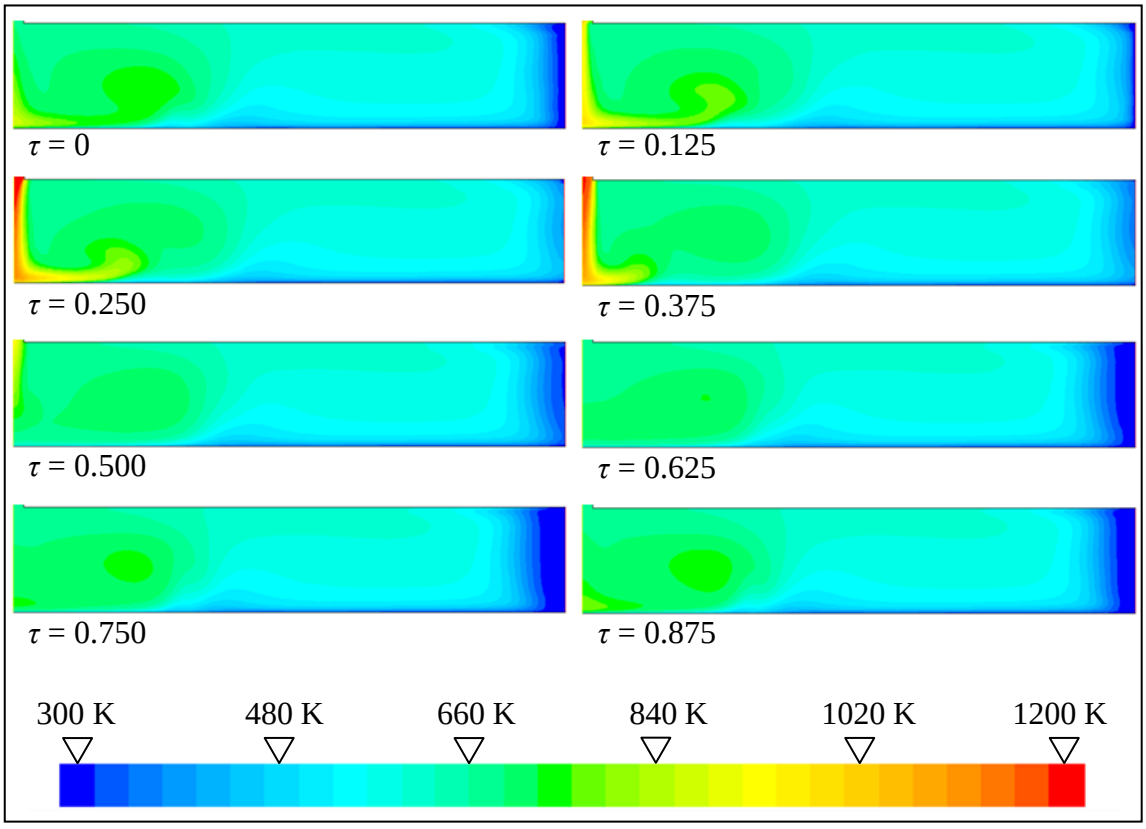

Figure 9.36: Temperature field at various values of τ with $\overline{U}_{exit}$ = 10 m/s.

Overall there was much less heat present in the impingement zone when compared to the base case. This was simply the result of a lower rate of system energy input. That is, the base case had the same 1200 K temperature at the tailpipe entrance but approximately three times the mean mass flux when compared to the $\overline{U}_{exit}$ = 10 m/s case.

Thus, the mean energy influx of the system was much larger for the base case, and temperatures in the impingement zone were correspondingly elevated. One potential advantage of the $\overline{U}_{exit}$ = 10 m/s case, however, was that the peak velocity during flow reversal was also much lower when compared to the base case. Thus, the encroachment of cool air near the outlet boundary was also reduced, as substantiated by Figure 9.36. This led to a somewhat flatter and more uniform heat flux profile, as shown in Figure 9.37.

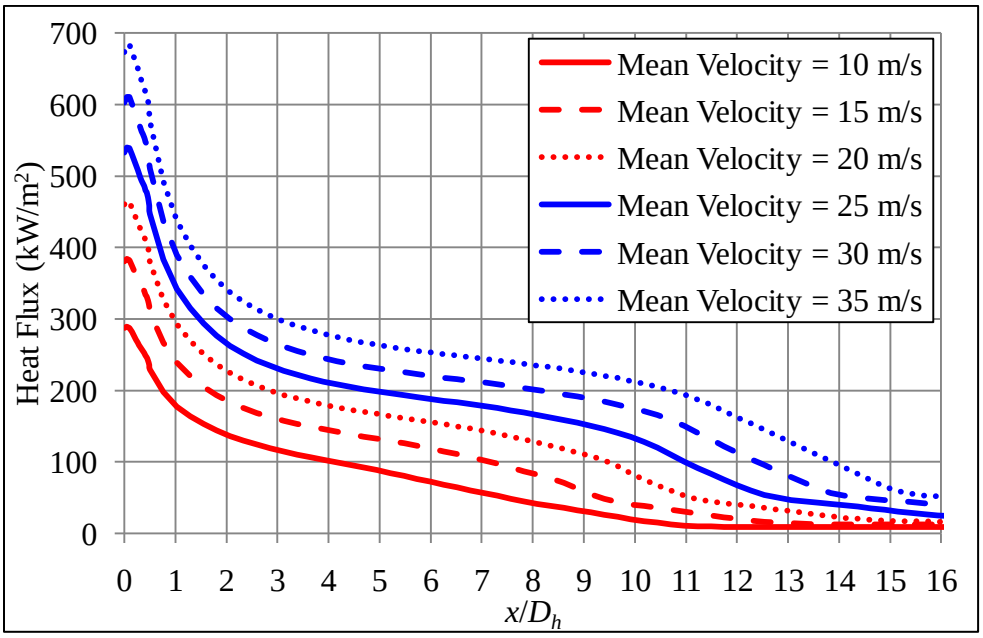

Figure 9.37: Time-averaged heat flux profiles for various values of $\overline{U}_{exit}$.

As expected, heat flux increased with mean velocity as a result of larger, higher intensity vortices and elevated energy influx. In general, the profile shapes were similar, but with somewhat flatter profiles at lower mean velocities. In the range $x/D_h \leq 8$ the local heat flux was nearly linearly correlated with mean velocity. This is shown in Figure

9.38, a plot of local heat flux as a function of $\overline{U}_{exit}$ and x/D_h.

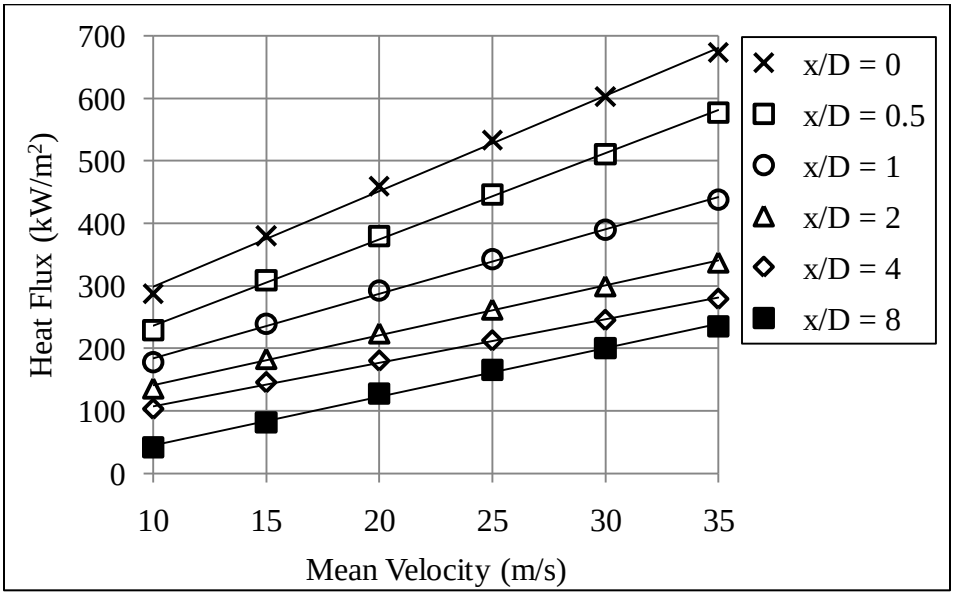

Figure 9.38: Comparison of time-averaged local heat flux for various values of $\overline{U}_{exit}$.

The solid lines in Figure 9.38 are least-squares fit linear trend lines. The minimum coefficient of determination (square of the sample correlation coefficient) was 0.997. Additionally, the lowest F-statistic for any of the trend lines was 1451, with only a 0.0003 % chance of a higher F-statistic occurring by chance. For reference, the 4 degrees of freedom in this case resulted in a critical F-statistic value of 74.13 using a significance level, α, of 0.01. Therefore, the linear relationships in this range were statistically significant.

As a slight departure from previous sections, each pulsating case in this section was compared to a different steady flow case. The steady flow cases employed the 6 mean exit velocities used in the pulsating cases. Thus, complimentary cases using the

same $\overline{U}_{exit}$ were compared for calculation of the enhancement factors. The steady flow heat flux profiles are shown in Figure 9.39.

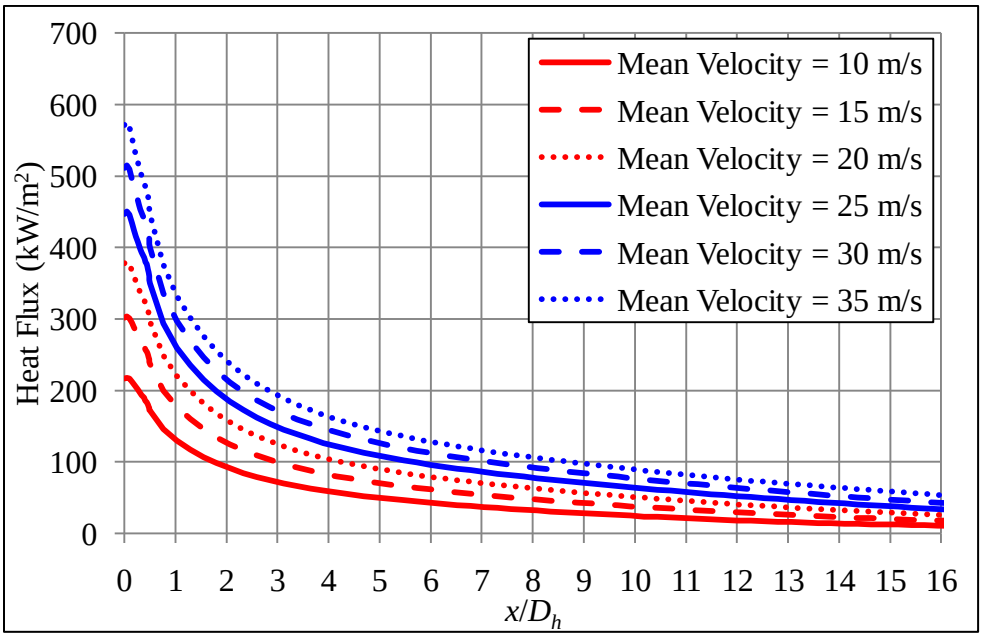

Figure 9.39: Heat flux profiles for steady flow with various $\overline{U}_{exit}$ values.

The resulting heat flux enhancement factors are shown in Figure 9.40. The profiles had similar shapes. They initially increased with x/D_h before reaching a maximum and trending downward. The values in the range $x/D_h < 4$ were nearly identical between cases. The maximum enhancement factors and the x/D_h location of said factors increased with increasing $\overline{U}_{exit}$. This was most probably the result of the stronger and larger vortices produced at high mean velocities.

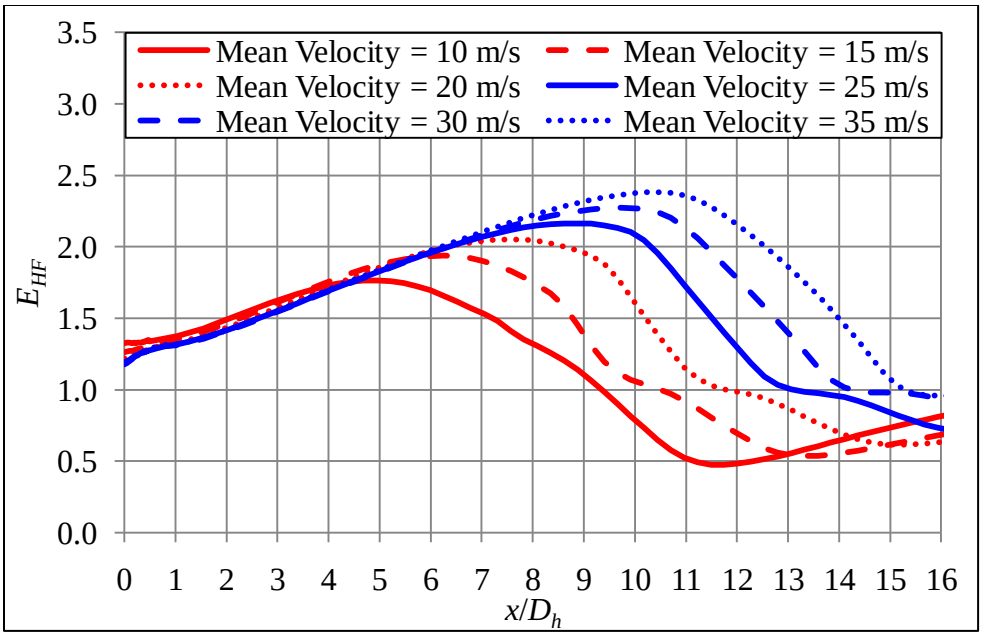

Figure 9.40: Heat flux enhancement for various values of $\overline{U}_{exit}$.

The average heat flux values of the pulsed and steady cases for the range $x/D_h \leq 16$ are shown in Table 9.9. The average enhancement factors are also shown for each pair of complimentary cases. All pulsed cases produced higher heat transfer than the corresponding steady flow case. The increase was 36 % for the lowest flow rate and increased with $\overline{U}_{exit}$ to a maximum enhancement of 68 % for $\overline{U}_{exit}$ = 35 m/s.

Table 9.9: Average heat flux and enhancement factors for various $\bar{U}_{exit}$.

$\bar{U}_{exit}$	$\overline{q''}$ (×10^5 W/m^2)		$\bar{E}_{HF}$
(m/s)	Steady	Pulsed	-
10	0.48	0.65	1.36
15	0.68	0.97	1.43
20	0.88	1.31	1.49
25	1.06	1.65	1.55
30	1.24	2.01	1.61
35	1.42	2.39	1.68

Not only did the enhancement increase with mean velocity, but the heat flux for both steady and pulsating flows did as well. In fact, the relationship between average heat flux and exit velocity was nearly linear for both cases, as shown in Figure 9.41.

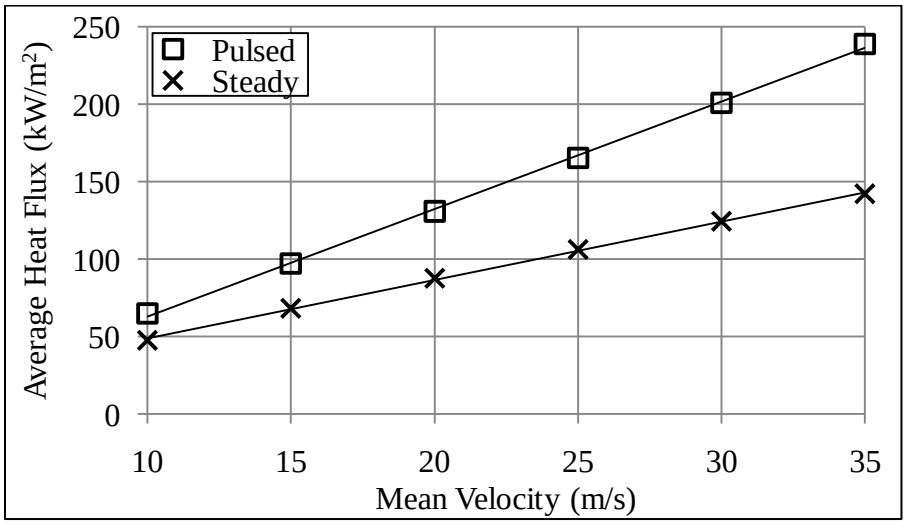

Figure 9.41: Averaged heat flux as a function of flow type and mean exit velocity.

The linear trend lines in Figure 9.41 both had coefficients of determination of 0.999 and were deemed statistically significant. The fact that the heat transfer for both flow types was so nearly linearly dependent on mean velocity allows for valid analysis of intermediate cases using a linear regression. Thus, a simple relationship can be established between the pulsed and steady flow heat transfer. The results of such an analysis are shown in Figure 9.42, a plot of the average heat flux enhancement factor versus mean velocity.

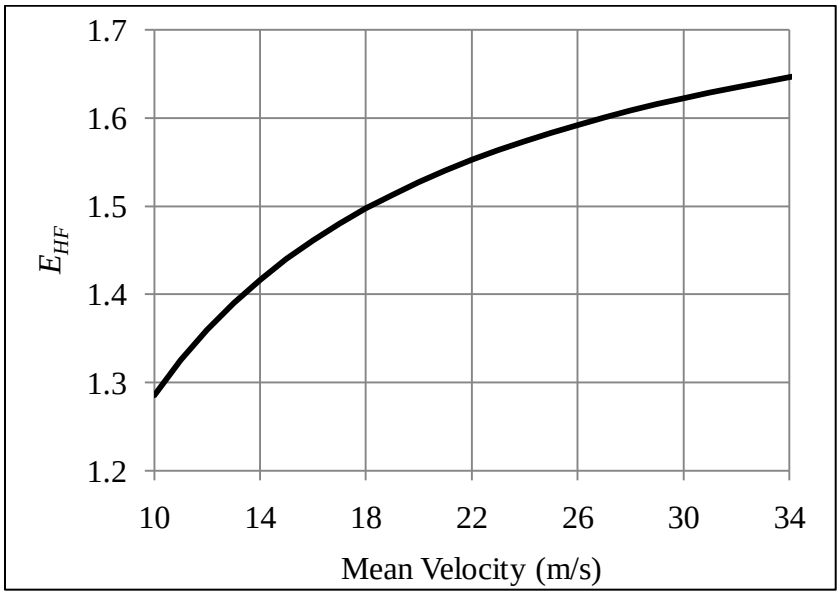

Figure 9.42: Heat flux enhancement factor versus mean velocity.

Figure 9.42 gives the projected ratio of heat flux due to the pulsating jet to that of a steady flow jet using the same mean velocity. For example, at a mean velocity of 18 m/s the pulsed flow is expected to result in 50 % more heat flux ($\bar{E}_{HF}$ = 1.5) than a steady flow case using the same velocity. Conversely, the aforementioned relationship can be used to determine the mean flow rate necessary to produce a given heat flux. First, let the

velocity equivalency factor be defined as

$$E_V = \frac{\text{Mean velocity of a pulsating jet required for a given heat flux}}{\text{Mean velocity of a steady jet required for the same heat flux}}. \quad (9.3)$$

Thus, low values of E_V are desirable since less mass flux would be required to produce the same heat flux. Figure 9.43 is a plot of the equivalency factor as a function of heat flux for the ranges investigated.

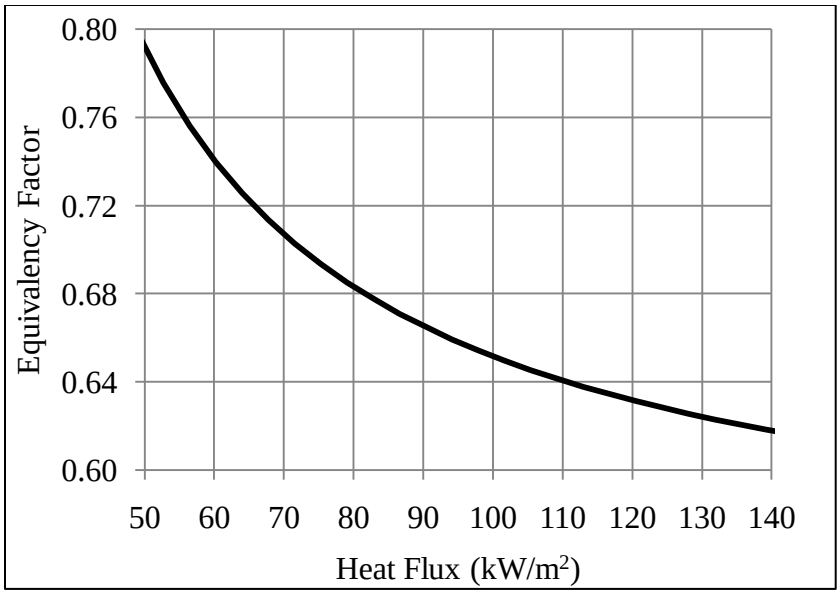

Figure 9.43: Velocity equivalency factor versus heat flux.

This plot is related to Figure 9.42, since they are both the results of the same linear regression. However, Figure 9.43 offers a different view of the results. As an example, in order to obtain a desired average heat flux of 1.10×10^5 W/m^2, the pulsating jet would require a mean exit velocity that was only 64 % of that required by a steady flow jet. This could represent a substantial decrease in energy costs. However, it is

important to note that the preceding analysis is only valid for the operational parameters employed in this section. That is, for ω = 160 Hz, R_{amp} = 4, D_h = 4.8×10^{-3} m, and H/D_h = 5.

9.6 Effects of Nozzle Diameter

This section discusses the impact that the hydraulic diameter, D_h, has on system performance. Since a slot shaped nozzle was used, the hydraulic diameter is equal to twice the slot width. The values of D_h and resulting dimensionless parameters studied in this section are given in Table 9.10. All other parameters matched those of the base case: $\overline{U}_{exit}$ = 30 m/s, ω = 160 Hz, R_{amp} = 4.

Table 9.10: Hydraulic diameters and dimensionless parameters at the tailpipe exit.

D_h ($\times 10^{-3}$ m)	H/D_h -	$\overline{St}$ -	$\overline{Re}$ -
3.0	8	0.0768	527
4.0	6	0.0512	774
4.8	5	0.0384	1012
6.0	4	0.0307	1232
8.0	3	0.0256	1438
12.0	2	0.0219	1628

The tailpipe exit temperatures were greatly affected by the hydraulic diameter. The maximum, minimum, and time-averaged bulk temperatures at the tailpipe exit are given in Figure 9.44.

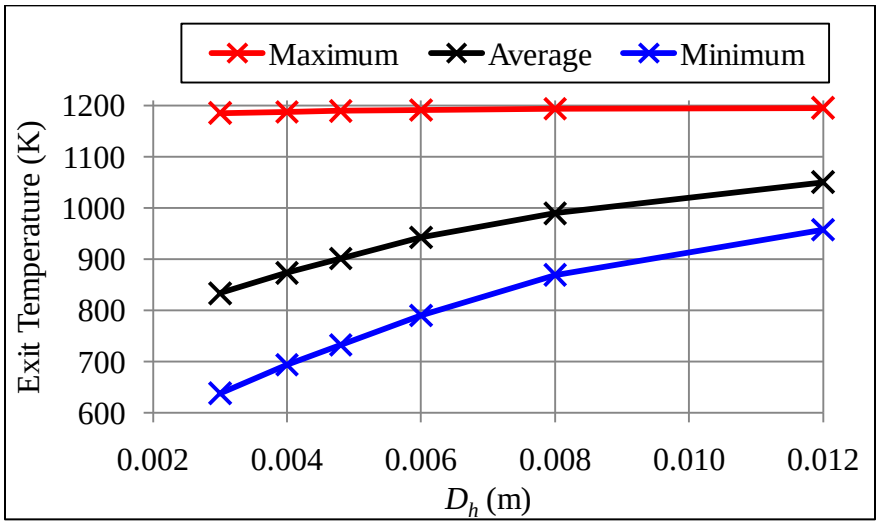

Figure 9.44: Bulk tailpipe exit temperature for various values of D_h.

Although the maximum temperatures varied little between cases, the minimum bulk temperatures spanned a 319 K range. These temperatures increased with D_h, from an initial value of 680 K for D_h = 0.003 to 750 K for D_h = 0.012. The increasing average temperatures were a result of elevated mean energy influx. The temperatures at the tailpipe entrance remained relatively constant, but the mass flux was higher for larger hydraulic diameters given the consistent mean exit velocity. Thus, systems with larger hydraulic diameters received greater mean energy flux at the inlet. The resulting time-averaged heat flux profiles are shown in Figure 9.45. As a departure from previous sections, the heat flux is shown as a function of the dimensional variable x rather than x/D_h.

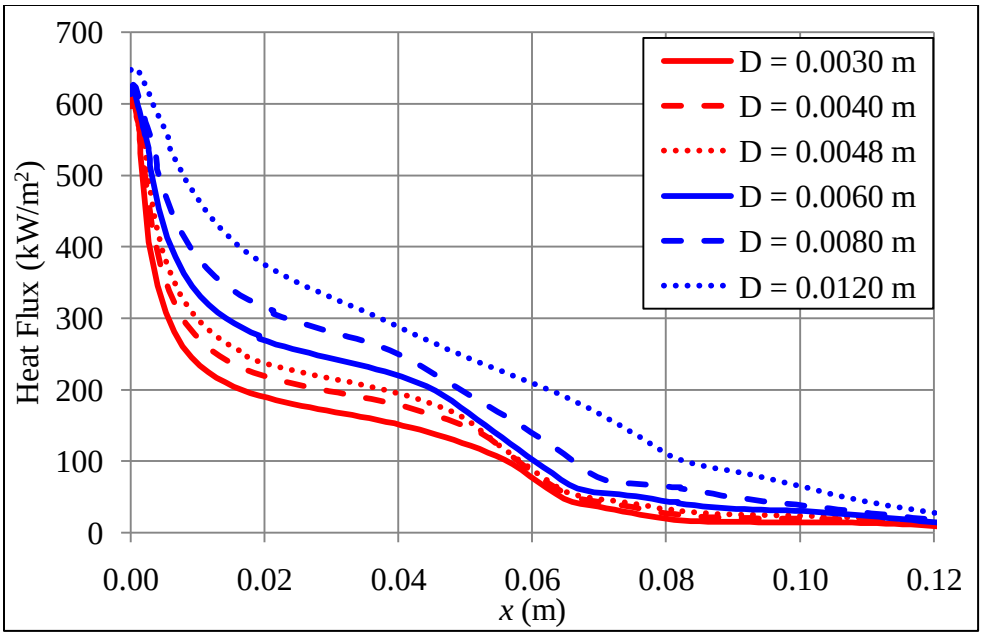

Figure 9.45: Heat flux profiles for pulsed cases with various hydraulic diameters.

In general, the profile shapes were consistent. The values at the stagnation point were similar for all cases, varying by less than 9 %. The values at x = 0.12 m also showed little variation between cases. Within those boundaries, however, the larger nozzles produced fuller heat flux profiles. Additionally, the larger hydraulic diameters yielded profiles that had slightly more consistent slopes. This was especially true for the case D_h = 0.012, which was simply the result of a larger vortex and higher temperatures in the impingement zone. Similar results were obtained for the complimentary steady flow cases. These cases used the hydraulic diameters of the pulsating cases as well as the same mean exit velocities. The heat flux profiles for the steady flow cases are given in Figure 9.46.

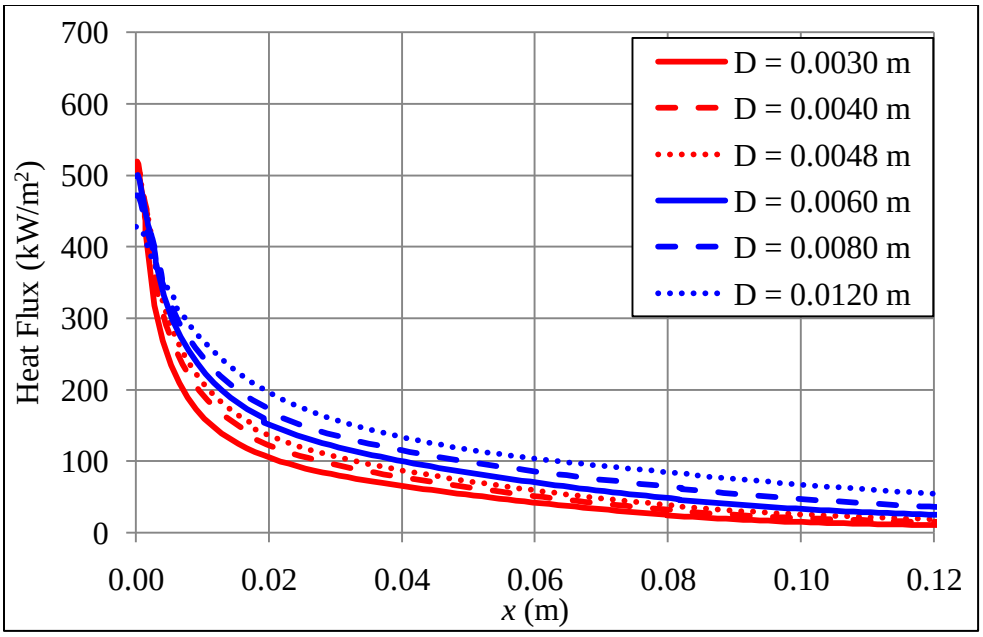

Figure 9.46: Heat flux profiles for steady flow cases with various hydraulic diameters.

The stagnation point heat flux was comparable for all steady flow cases. Farther away from x = 0.00 m, however, the larger nozzles produced higher heat flux. The profiles from the steady flow jets were used to calculate the heat flux enhancement factors shown in Figure 9.47.

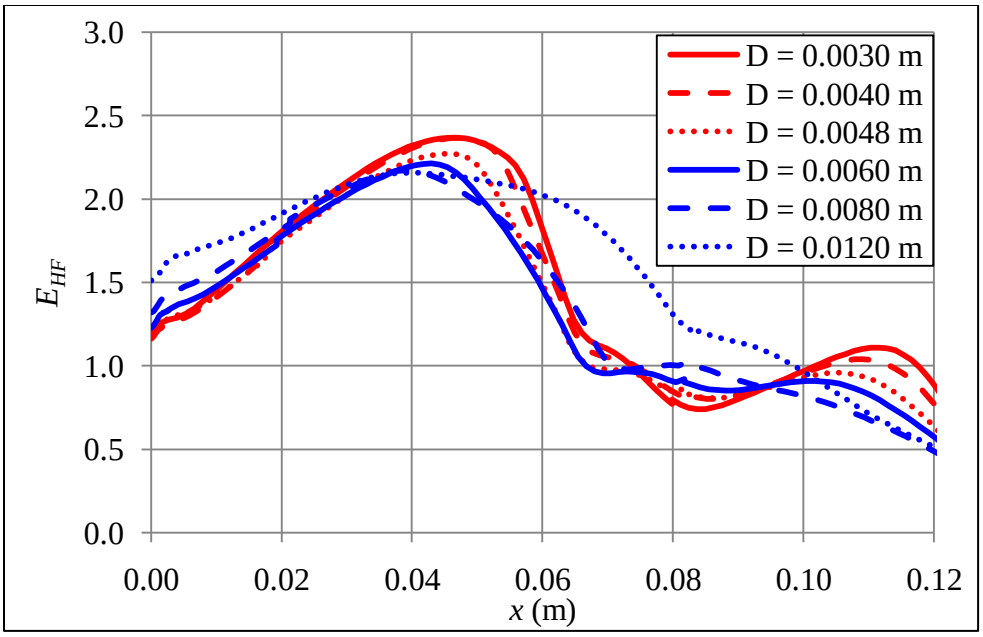

Figure 9.47: Heat flux enhancement for various hydraulic diameters.

Each pulsating case was compared with the steady flow case that had matching nozzle geometry. The enhancement curves for all cases had similar shapes. As the hydraulic diameter increased, the enhancement at the stagnation point increased, the initial slope of the curve decreased, the maximum enhancement decreased and shifted in the negative x-direction, and the slope after the maximum became less negative. In combination these effects produced more consistent enhancement factors for larger nozzles. The average enhancement factors over the range $x \leq 0.12$ m are shown in Table 9.11, along with the associated average heat flux values.

Table 9.11: Average heat flux and enhancement for various hydraulic diameters.

D_h	$\overline{q''}$ ($\times 10^5$ W/m^2)		$\bar{E}_{HF}$
($\times 10^{-3}$ m)	Pulsed	Steady	-
3.0	1.07	0.67	1.59
4.0	1.24	0.79	1.56
4.8	1.34	0.88	1.52
6.0	1.54	0.99	1.56
8.0	1.77	1.13	1.56
12.0	2.26	1.32	1.71

The pulsating jets improved heat transfer by at least 52 %. This improvement was relatively consistent with a maximum enhancement of 71 %. The average heat flux increased with D_h nearly linearly throughout the cases. The average heat flux is compared to the base case in Figure 9.48.

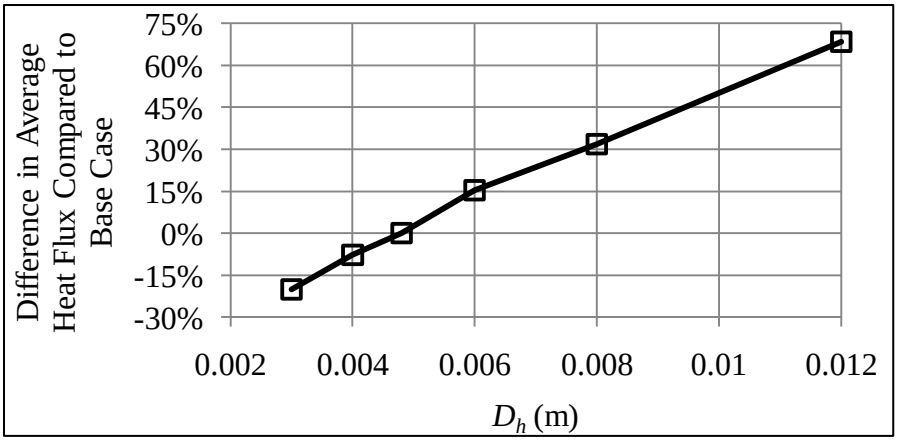

Figure 9.48: Time-averaged heat flux compared to the base case.

9.7 Effects of Surface Velocity

This section analyzes the effects resulting from the use of a moving impingement surface. This necessitated the use of a different computational domain than the previous sections since the symmetry condition was eliminated. This new domain was similar to the previously described one with the exception of being mirrored about the nozzle centerline. Additionally, it was necessary to extend the domain in the positive and negative x-directions to $\pm 30 D_h$. As a result, the case of $U_{\text{surface}} = 0$ m/s was also considered using the larger domain. The surface velocities and resulting Reynolds numbers that were implemented in this section are given in Table 9.12. All surface velocities were in the positive x-direction. Other parameters remained unchanged; thus, $\overline{U}_{exit} = 30$ m/s, $\omega = 160$ Hz, $R_{amp} = 4$, $D_h = 0.0048$, and $H/D_h = 5$.

Table 9.12: Surface velocities and Reynolds number at the tailpipe exit.

U_{surface} (m/s)	$\overline{Re}$ -
0	1736
5	1765
10	1812
15	1924
20	2034
25	2152

The Reynolds number for $U_{surface}$ = 0 m/s given in Table 9.12 was slightly different than the base case due to a change in exhaust exit temperature. This temperature difference was a direct result of the outlets being farther away from the tailpipe. Thus, backflows had a smaller effect on exit temperatures. The maximum, minimum, and time-averaged bulk temperatures at the tailpipe exit are given in Figure 9.49.

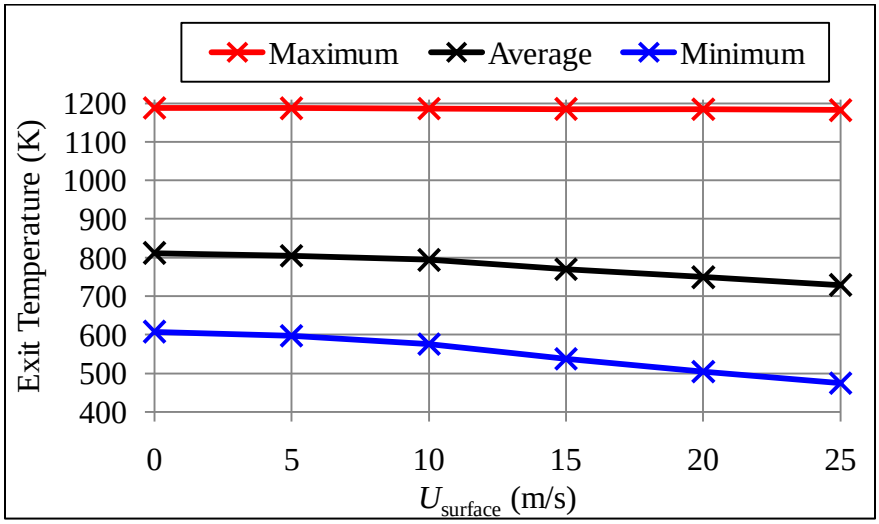

Figure 9.49: Time-averaged bulk temperatures at the tailpipe exit.

The minimum exhaust exit temperatures decreased with increasing surface velocity. This was a result of entrainment of ambient air due to the moving boundary. As the surface velocity increased, a greater amount of cool ambient fluid was dragged in from the outlet boundary due to the no-slip surface condition. This can be seen in Figure 9.50 and Figure 9.51, which show the instantaneous flow fields and temperatures fields at various values of τ for $U_{surface}$ = 25 m/s, respectively.

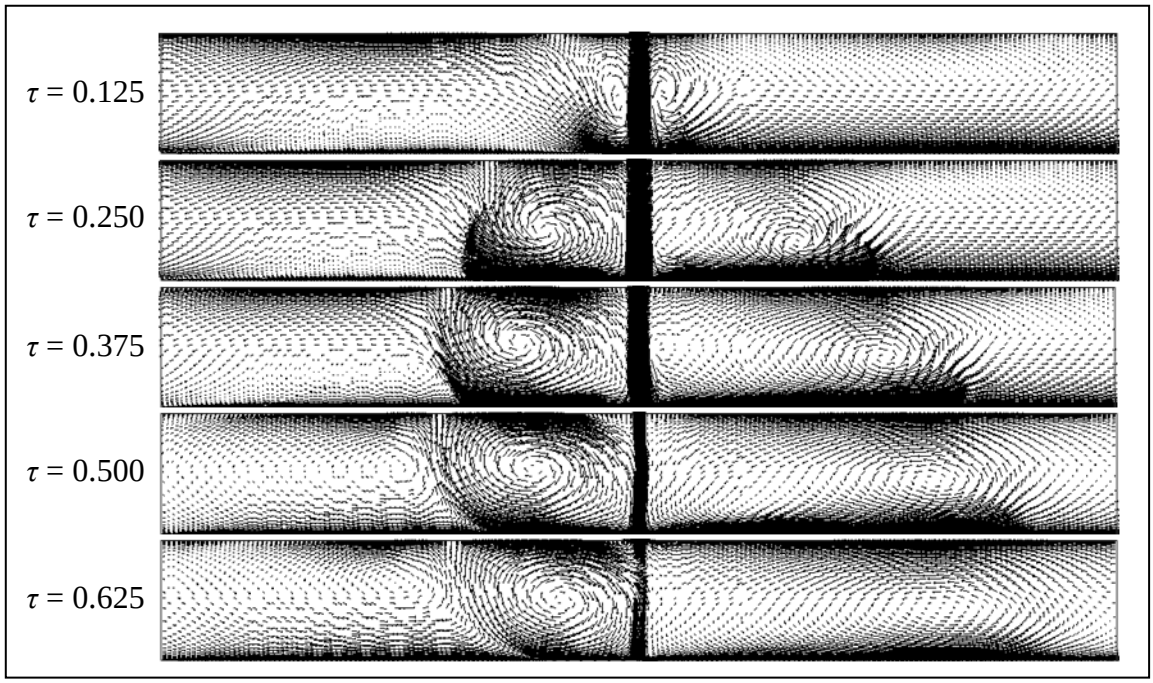

Figure 9.50: Flow field at various values of τ with $U_{surface}$ = 25 m/s left to right.

The $U_{surface}$ = 25 m/s case was chosen to demonstrate the effects of a moving boundary because it was the highest surface velocity investigated and therefore produced the most drastic results. The vortices on each side of the nozzle began to form at approximately τ = 0.125. As the exit velocity increased the vortices grew in size and strength. The rightmost vortex was carried to the right due to the rightward moving bulk flow caused by the no-slip condition at the moving impingement surface. The rightmost vortex dissipated faster than the leftmost vortex. This vortex did not proceed to move in either the positive or negative *x*-directions significantly. The primary column of fluid being expelled from the tailpipe continued to fuel the vortex while the surface somewhat counteracted the tendency of previous vortices to move outward. As a result, the average bulk temperature of the fluid was actually higher on the left half of the domain than it was on the right half. This can be seen in Figure 9.51, the temperature field at various

values of τ.

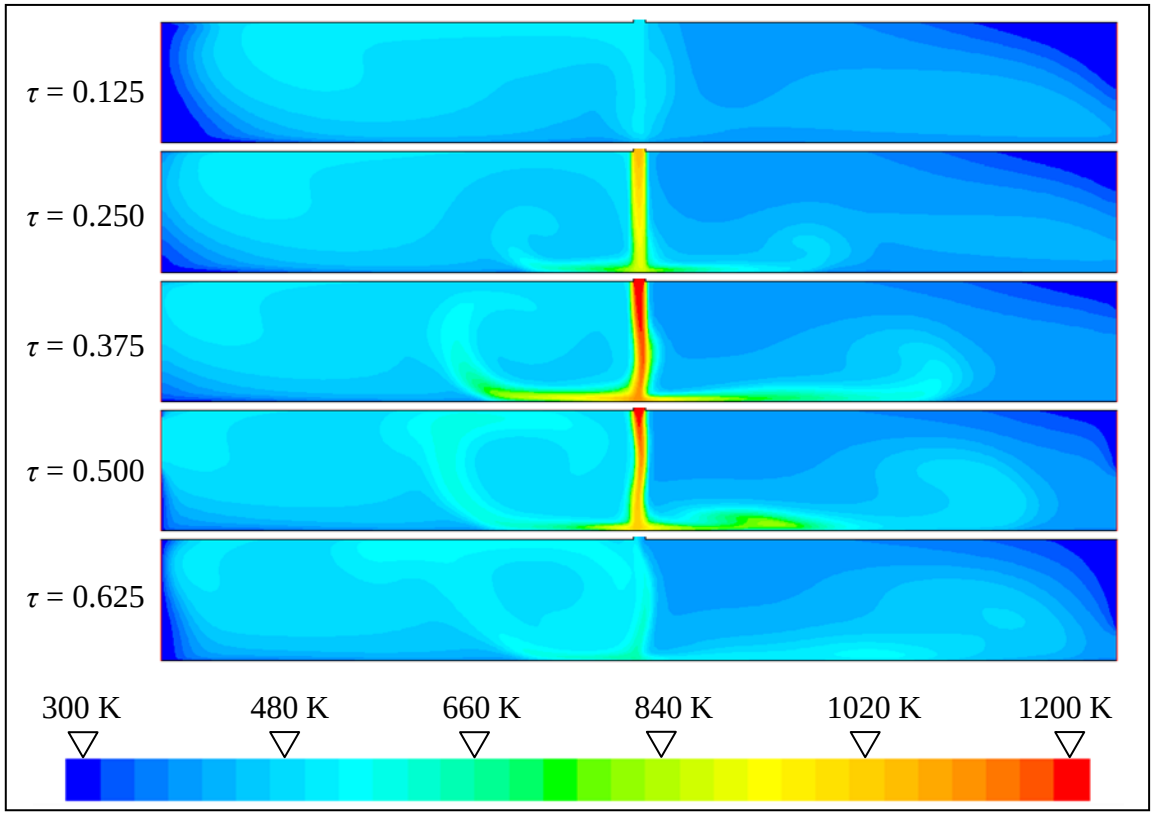

Figure 9.51: Temperature field at various values of τ with $U_{surface}$ = 25 m/s.

The resulting instantaneous heat flux profiles are shown in Figure 9.52. The most noteworthy heat transfer occurred during $0.250 \leq \tau \leq 0.500$ as a result of high vortex strength and temperature. There was considerable heat transfer in the range $x/D_h > 6$ when compared to the range $x/D_h < -6$. The rightmost vortex was able to expand and move to the right at the oscillation cycle progressed. This resulted in the elevated heat transfer in the range $x/D_h > 6$. The more concentrated vortex which formed to the left of the tailpipe did not expand as much, and, therefore, the heat flux was reduced in the range $x/D_h < -6$.

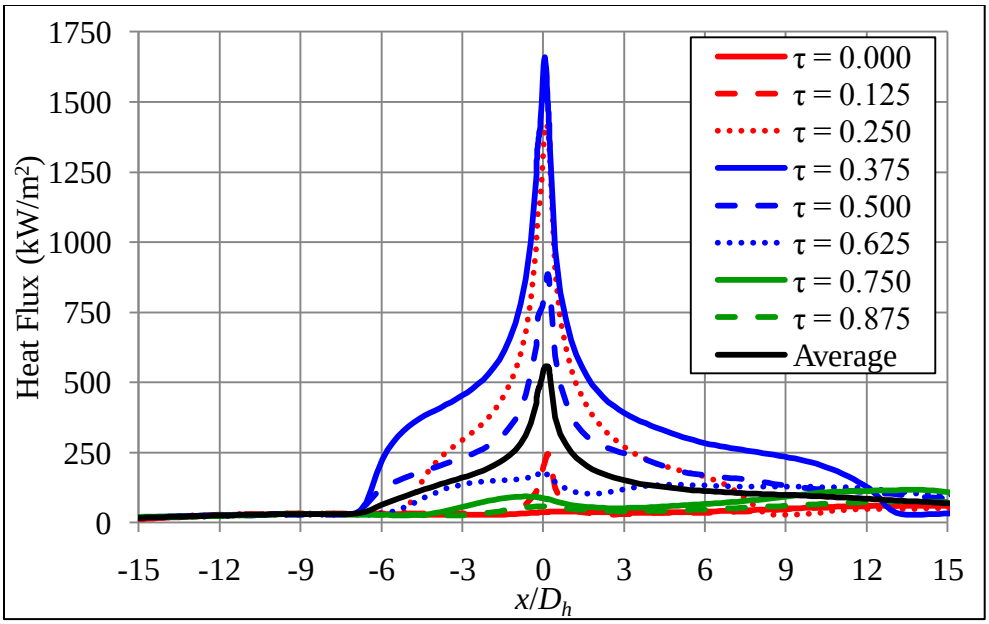

Figure 9.52: Instantaneous heat flux for various values of τ with $U_{surface}$ = 25 m/s.

The time-averaged heat flux for the pulsating jet cases are shown in Figure 9.53. The peak heat flux values were relatively unchanged by the surface velocity. However, as $U_{surface}$ increased the profile became flatter on the right due to the increased ability of the vortex to expand and move to the right. On the left side, increasing surface velocity further restrained the vortex. Thus, the profiles became steeper and similarly confined.

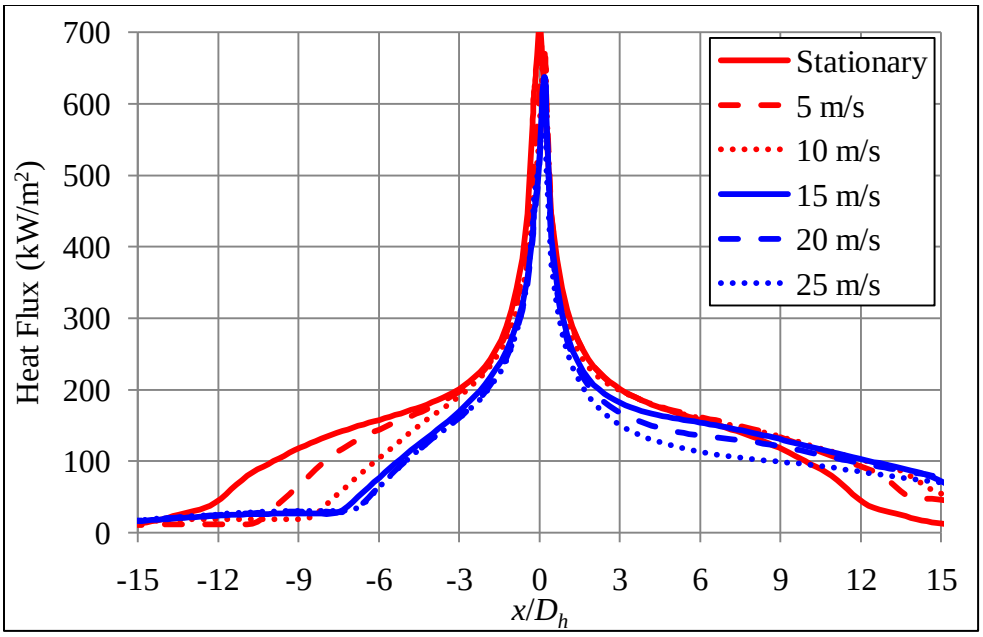

Figure 9.53: Time-averaged heat flux for pulsating jets with various values of $U_{surface}$.

In order to make adequate assessments of the heat transfer improvement afforded by the pulsating conditions, steady flow jets were investigated using the same six surface velocities of the previous cases. The resulting temperature fields of the steady flow cases are presented in Figure 9.54.

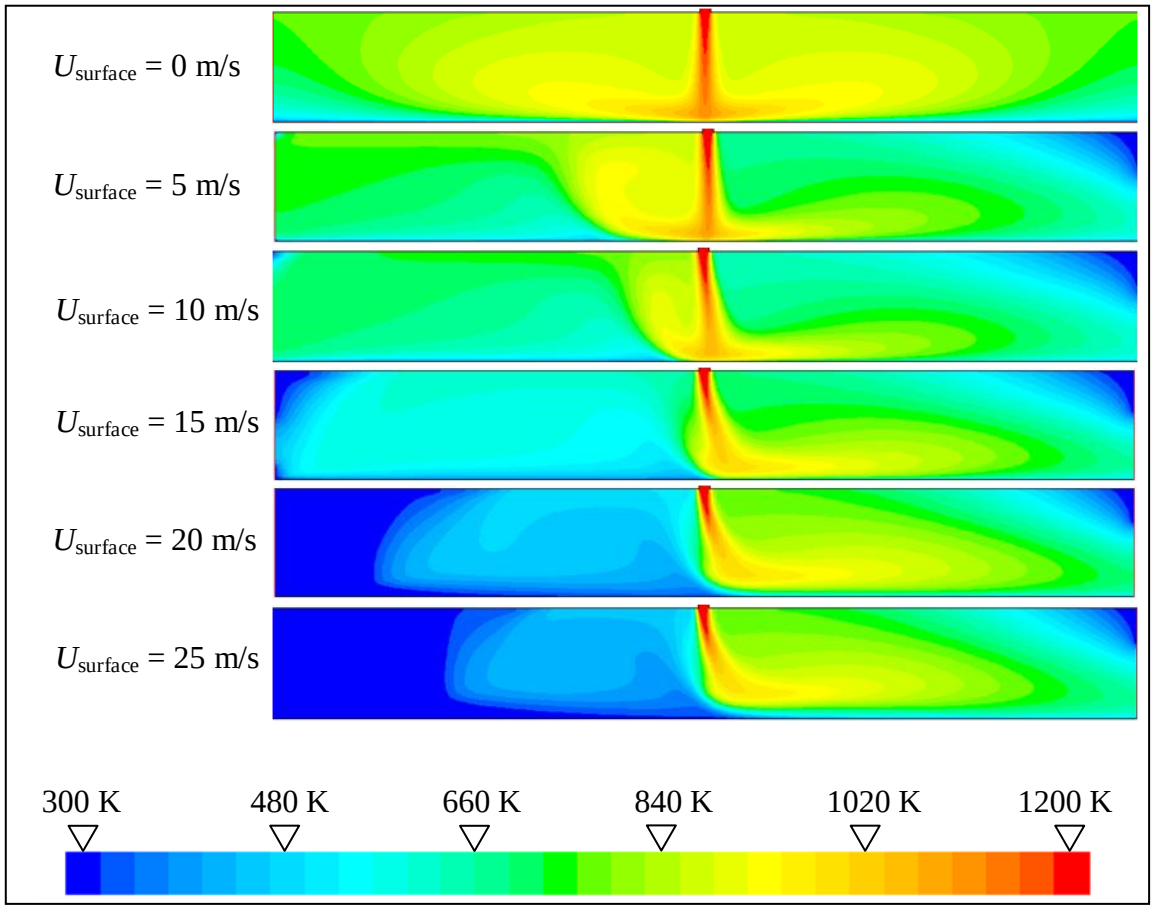

Figure 9.54: Temperature fields of steady flows with various values of $U_{surface}$.

The stationary impingement surface case had significantly more heat in the impingement zone than the pulsed flow cases and the other steady cases. As $U_{surface}$ increased the temperatures remained somewhat consistent on the right side of the domain. The left side of the domain, however, exhibited significant changes as $U_{surface}$ increased. The bulk fluid temperature for that half of the domain was drastically reduced as a stronger boundary layer of cool fluid formed near the surface. The resulting heat flux profiles for these cases are shown in Figure 9.55.

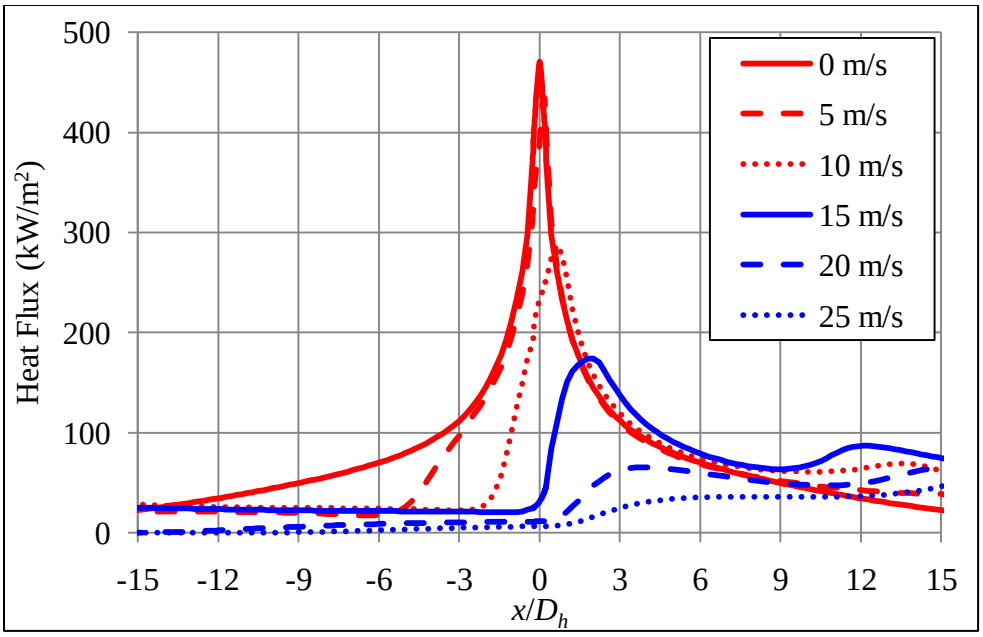

Figure 9.55: Time-averaged heat flux for steady flow jets with various values of $U_{surface}$.

The stationary impingement surface case produced the familiar symmetry profile. As $U_{surface}$ increased, the peak heat flux decreased and shifted to the right. For $U_{surface} \leq 15$ m/s there was no significant reduction in heat transfer for the range $x/D_h > 2$. However, at these velocities the heat flux was drastically reduced for $x/D_h < 2$. This was a result of the bulk flow in the positive x-direction, which prevented the hot exhaust gases from spreading to the left. This sweeping action was also apparent for the cases with $U_{surface} >$ 15 m/s. However, in these cases the impingement jet also failed to significantly penetrate the boundary layer that developed near the moving surface. This greatly reduced the effectiveness of the impinging jet, as demonstrated by the area-averaged heat flux values in Table 9.13

Table 9.13: Average heat flux and enhancement factors for various $U_{surface}$.

$U_{surface}$	$\overline{q''}$ ($\times 10^5$ W/m^2)		$\bar{E}_{HF}$
(m/s)	Pulsed	Steady	-
0	1.48	0.84	1.76
5	1.43	0.73	1.97
10	1.35	0.67	2.02
15	1.27	0.58	2.21
20	1.20	0.29	4.14
25	1.12	0.17	6.68

The pulsating jets outperformed the steady flows considerably. The minimum enhancement of 76 % was obtained for the stationary surface case. As the surface velocity increased from $U_{surface}$ = 0 m/s to $U_{surface}$ = 15 m/s, the enhancement grew considerably, but steadily. Between $U_{surface}$ = 15 m/s and $U_{surface}$ = 20 m/s the average heat flux of the steady flow case plummeted by 50 %. The inability of the steady flow to significantly disrupt the boundary layer near the surface was detrimental to heat transfer. While the pulsating flows did experience a decrease in heat flux, the drop was not as severe. This is shown in Figure 9.56, a comparison of average heat flux for each case compared to the corresponding stationary case.

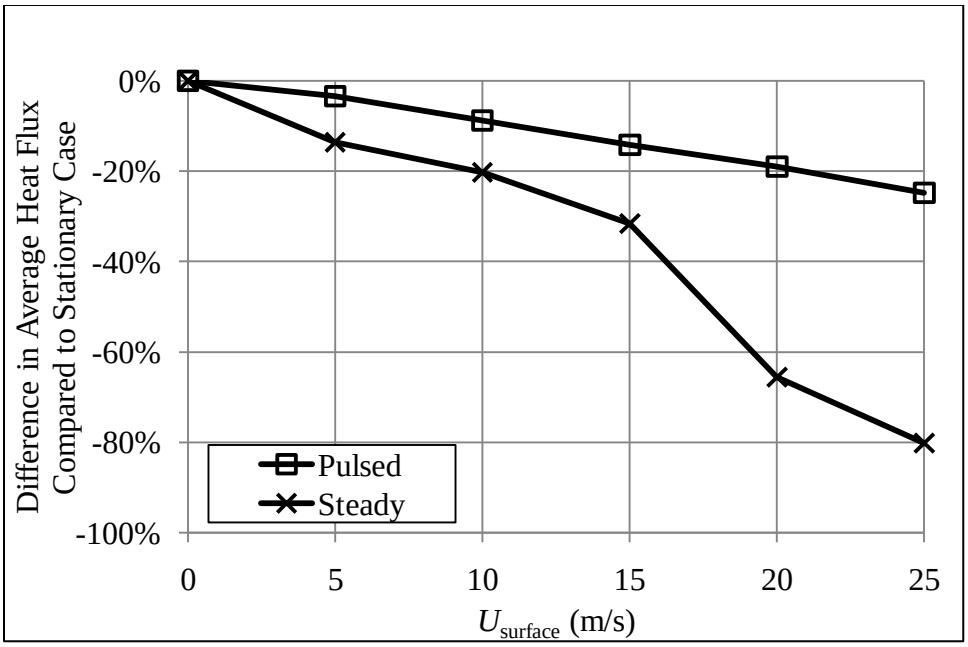

Figure 9.56: Average heat flux compared to the stationary case.

The steady flow experienced a reduction in heat flux of 14 % from the stationary case to $U_{surface}$ = 5 m/s. The largest drop, however, was encountered in the $U_{surface}$ = 20 m/s case in which the steady flow went from 32 % to 66 % below the stationary case. At the highest surface velocity, the average steady flow heat flux was only 20 % of the stationary value. The heat flux from the stationary surface case using pulsating flow, however, was only reduced by 25 % at $U_{surface}$ = 25 m/s. As a result, the pulsed conditions produced 6.68 times the heat transfer of the steady flow case at this surface velocity.

9.8 Summary and Discussion

The effects of five parameters were studied. They were the velocity amplitude ratio, oscillation frequency, the mean velocity at the tailpipe exit, the hydraulic diameter

of the slot-shaped tailpipe, and the impingement surface velocity. Each of these five parameters was studied separately and related to a base case. The base case used a stationary impingement surface and R_{amp} = 4, ω = 160 Hz, D_h = 0.0048, $\bar{U}_{exit}$ = 30 m/s, and H/D_h = 5. Each case was compared to a steady flow case with the same geometry, mean flow rate, and tailpipe entrance temperature. All pulsating jets produced significantly more heat flux than the corresponding steady flow case for the conditions studied in this chapter. The mechanism of heat flux enhancement was apparently the swirling vortices that were produced during the positive portion of the tailpipe exit velocity oscillation cycle. The extent of this improvement was related to the size, strength, and temperature of the vortices.

The heat flux increased with increasing R_{amp} was most probably due to larger and stronger vortices despite the slightly lower vortex temperature. The effects of oscillation frequency were somewhat more complex. Three distinct flow types were observed which yielded unique heat flux characteristics. At low frequencies, the velocity oscillation produced a small secondary vortex. This vortex slightly increased heat flux and made the heat flux profile more uniform. At high values of ω, persistent, concentrated vortices were observed which greatly increased heat flux near the tailpipe. The heat flux increased with $\bar{U}_{exit}$ nearly linearly due to increasing vortex size and strength as well as high energy input rate. Larger nozzles also yield greater heat flux as a result of additional energy input. Finally, increasing surface velocity led to a decrease in heat flux since entrainment of cool ambient air inhibited performance. Still, heat flux enhancement increased drastically for these cases due to the ability of pulsating jet to disrupt the

boundary layer that formed near the impingement surface. The steady flow cases were unable to significantly penetrate this layer and thus experienced large reductions in heat transfer. Therefore, pulse combustors are well suited for use with high speed impingement surfaces.

As an example of the potential cost savings, Mesto Paper, Inc. estimates that the energy usage of a steady air impingement system in a typical commercial paper machine application is 1.447×10^9 J per ton of paper (Metso Paper, Inc., 2006). Thus, for a machine producing 500 tons of paper per day and operating 350 days per year, the annual energy cost is approximately $2,530,000 per year, assuming an effective energy cost of $0.40 per 1×10^8 J. Under these assumptions and employing the conditions considered in Section 9.5, Figure 9.43 can be recast in terms of annual dollar savings for a given target heat flux as shown in Figure 9.57. Although this is a greatly simplified analysis, its purpose is to provide context for the possible financial advantages of a commercial level pulsating impingement dryer.

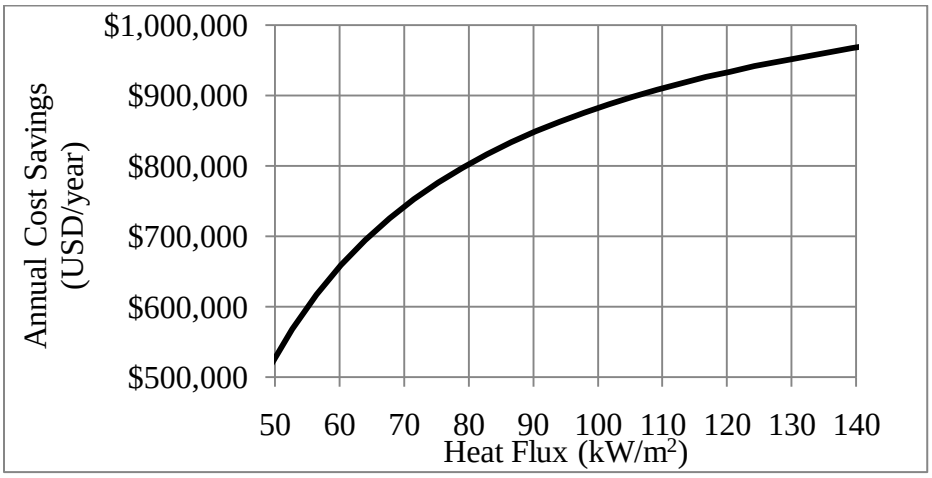

Figure 9.57: Possible annual cost savings versus target heat flux.

CHAPTER 10

FLOW REGIMES

10.1 Introduction

This chapter presents the findings of a numerical study of the combined effects of altering multiple system parameters. Whereas the previous chapter discussed the details of the heat transfer and its mechanisms, this chapter instead focuses on the overall trends and groupings of similar heat transfer mechanisms. Therefore, the time- and area-averaged heat flux is the pertinent quantity, rather than instantaneous values. The flow types observed in the numerical simulations are discussed and categorized. Furthermore, possible transition criteria are proposed to describe the shape of the corresponding flow regimes.

10.2 Approach

Whereas the preceding chapter studied the individual effects of the velocity amplitude ratio (R_{amp}), oscillation frequency (ω), time-averaged bulk fluid velocity at the tailpipe exit ($\overline{U}_{exit}$), hydraulic diameter of the tailpipe (D_h), and impingement surface velocity (U_{surface}), this chapter deals with combinations of a subset of those parameters. A factorial experimental design was implemented in order to study these parameters. Such

an experiment allowed investigation of the effect of each factor on the response variable, as well as the effects of interactions between factors. The three parameters investigated in this chapter are R_{amp}, ω, and D_h. The influence of $\overline{U}_{exit}$ and U_{surface} were not studied in this chapter as this would have greatly increased the number simulations. A fractional factorial design could have been implemented by selecting a subset of these combinations to exploit the sparsity-of-effects principle, thereby reducing the number of trials. However, the sparsity-of-effects principle assumes main effects and low order interactions dominate a system. While it is likely that the single factor effects and two-factor interactions are the most significant, there was no direct evidence of this assumption when designing the experiment. On a more fundamental level, the goal of the work presented in this chapter was not only the determination of the relationships between the three input factors and the heat flux output, but also the changes in trends and underlying flow types responsible for said changes. Thus, a full factorial experiment was used. Numerical simulations were conducted using 6 values of each of these parameters. These values mirrored those used in Chapter 9 and are presented in Table 10.1.

Table 10.1: Values used in the parametric study.

R_{amp}	ω	D_h
-	(Hz)	($\times 10^{-3}$ m)
2.5	80	3.0
3.0	125	4.0
3.5	160	4.8
4.0	200	6.0
4.5	250	8.0
5.0	320	12.0

As a full factorial experiment, all possible combinations of the values listed in Table 10.1 were investigated. Thus, this was a 6^3 (sometimes referred to as 6×6×6) factorial design and 216 simulations were conducted. The response variable in this case was the time- and area-averaged heat flux to the impingement surface, $\overline{\overline{q''}}$, for the range $x \leq 0.1$ m. This range was selected because it adequately described the heat transfer performance for a variety of nozzle diameters while still providing reasonable distinctions between cases. The parameter x is the distance from the symmetry plane shown in Figure 10.1, a diagram of the numerical domain employed throughout the simulations. As before, the temperature of the fluid entering the domain at the tailpipe inlet was specified as 1200 K. Also, the mean tailpipe exit velocity was 30 m/s for all cases since this was the most thoroughly studied exit velocity in the previous chapter.

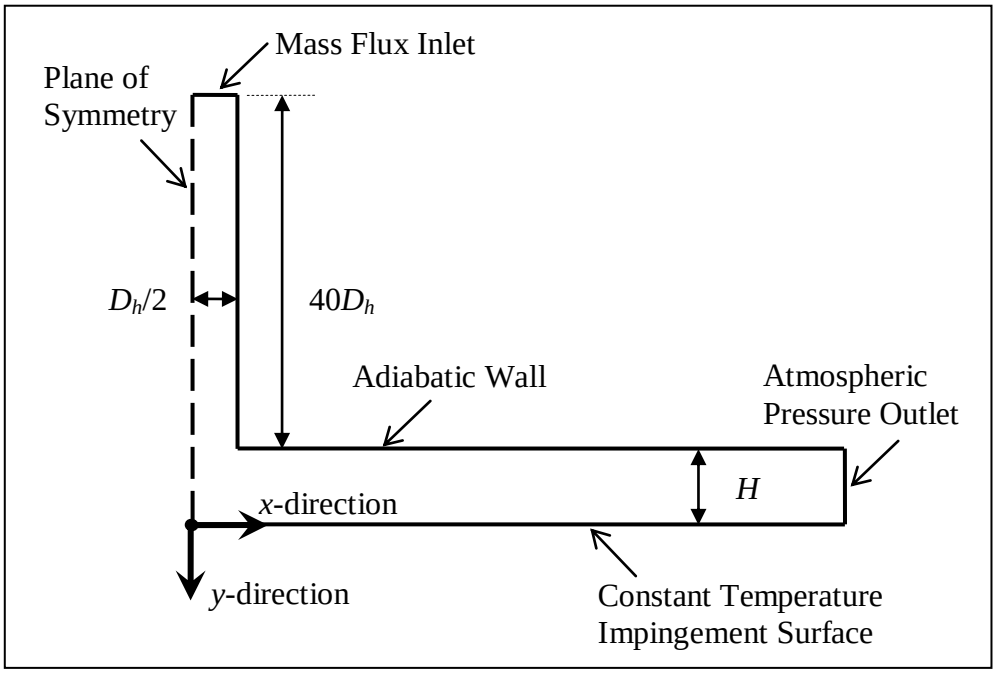

Figure 10.1: Diagram of the computational domain employed in simulations.

A stationary impingement surface was used throughout the experiments in order to reduce the domain size and corresponding computational cost. That is, the stationary surface allowed the symmetry condition to be employed throughout the simulations. Given that this domain matched that used in Chapter 9, a more detailed description of the domain itself and the associated solution procedures can be found in section 9.1 and Chapter 4, respectively.

10.3 Base Geometry

This section discusses the effects of the oscillation characteristics, R_{amp} and ω, for a given nozzle size. The hydraulic diameter of the nozzle studied in this section was 4.8×10^{-3} m, the same diameter employed in the base case of Chapter 9. With the

hydraulic diameter fixed, the number of input variables is reduced to 2.

For the range of input variables considered in this section, each case had one of three distinct flow types. These were the same flow types encountered in Chapter 9: a single strong vortex that greatly dissipated before the start of the next oscillation cycle, a single persistent vortex that remained relatively strong at the end of the cycle, and a strong primary vortex coupled with a short-lived weaker secondary vortex. The flow type encountered in each case is provided in Figure 10.2.

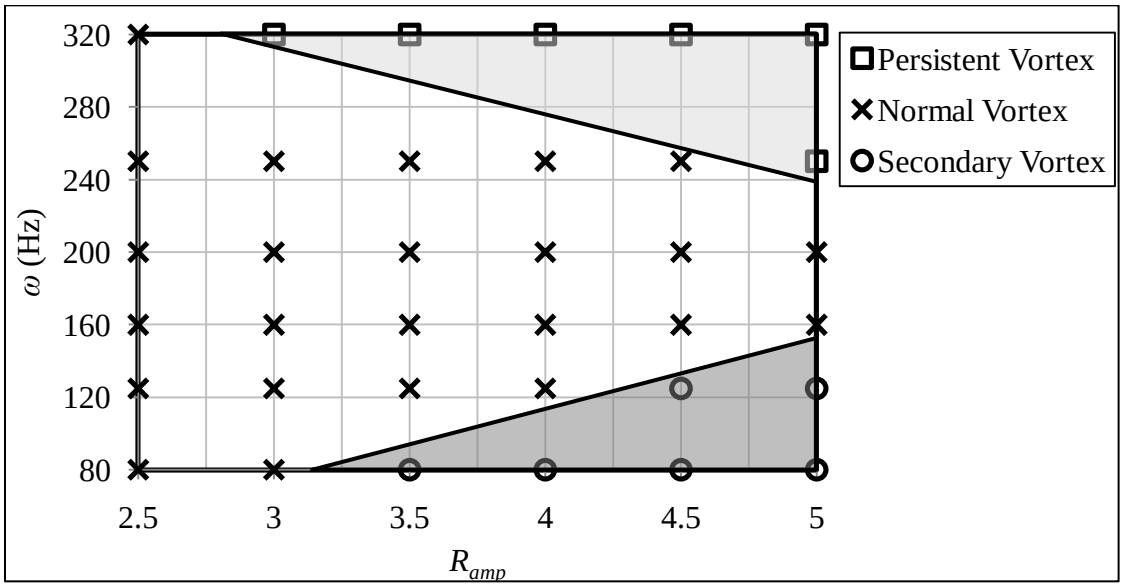

Figure 10.2: Flow type for each case with $D_h = 4.8\times10^{-3}$ m.

The axes in Figure 10.2 are the two input variables: the velocity amplitude ratio and the oscillation frequency. The markers indicate the resultant flow type for each combination of R_{amp} and ω. The shaded regions encompass all of the cases that displayed behavior different than the typical single temporary vortex. These areas are meant to

represent possible regions over which the observed behavior extends. The exact shape and threshold values of the regions are only estimates which could help guide future research. In general, the combination of low frequency, high amplitude pulsations produced a secondary vortex. Conversely, high frequency, high amplitude oscillations yielded persistent single vortices. The resultant time- and area-averaged heat flux values for these cases are shown in Table 10.2.

Table 10.2: Time- and area-averaged heat flux for $D_h = 4.8\times10^{-3}$ m and ω in Hz.

	$\overline{\overline{q''}}$ ($\times10^5$ W/m^2)					
	ω = 80	ω = 125	ω = 160	ω = 200	ω = 250	ω = 320
R_{amp} = 2.5	1.64	1.66	1.67	1.69	1.72	1.83
R_{amp} = 3.0	1.74	1.76	1.78	1.81	1.84	2.05
R_{amp} = 3.5	1.90	1.86	1.89	1.93	1.97	2.29
R_{amp} = 4.0	2.08	2.00	2.01	2.05	2.14	2.55
R_{amp} = 4.5	2.27	2.18	2.16	2.20	2.34	2.84
R_{amp} = 5.0	2.59	2.39	2.35	2.38	2.58	3.15

The heat flux values ranged from a minimum of 1.64×10^5 W/m^2 to a maximum of 3.15×10^5 W/m^2. These extrema were obtained for the lowest frequency and amplitude case and the highest frequency and amplitude case, respectively. All cases, however, produced significantly higher heat flux than the 1.24×10^5 W/m^2 value of the corresponding steady flow case. These improvements are quantified by the average heat

flux enhancement factors shown in Table 10.3.

Table 10.3: Average heat flux enhancement for $D_h = 4.8\times10^{-3}$ m and ω in Hz.

	E_{HF}					
	ω = 80	ω = 125	ω = 160	ω = 200	ω = 250	ω = 320
R_{amp} = 2.5	1.32	1.33	1.34	1.36	1.38	1.47
R_{amp} = 3.0	1.41	1.41	1.43	1.46	1.48	1.65
R_{amp} = 3.5	1.53	1.50	1.52	1.55	1.59	1.84
R_{amp} = 4.0	1.68	1.61	1.62	1.65	1.72	2.05
R_{amp} = 4.5	1.82	1.76	1.74	1.77	1.88	2.29
R_{amp} = 5.0	2.09	1.92	1.89	1.92	2.08	2.54

The same geometry and mean tailpipe exit velocities were used in all cases; therefore, only one steady flow case was necessary for comparison. As a result, the trends in the enhancement factors were identical to those of heat flux data since E_{HF} is simply $\overline{\overline{q''}}$ scaled by the steady value of 1.24×10^5 W/m^2. These trends are shown in Figure 10.3, a plot of heat flux as a function of amplitude ratio and frequency. The contours are colored by average heat flux with units of W/m^2. This surface and all subsequent 3-dimensional plots were created using Delaunay triangulation.

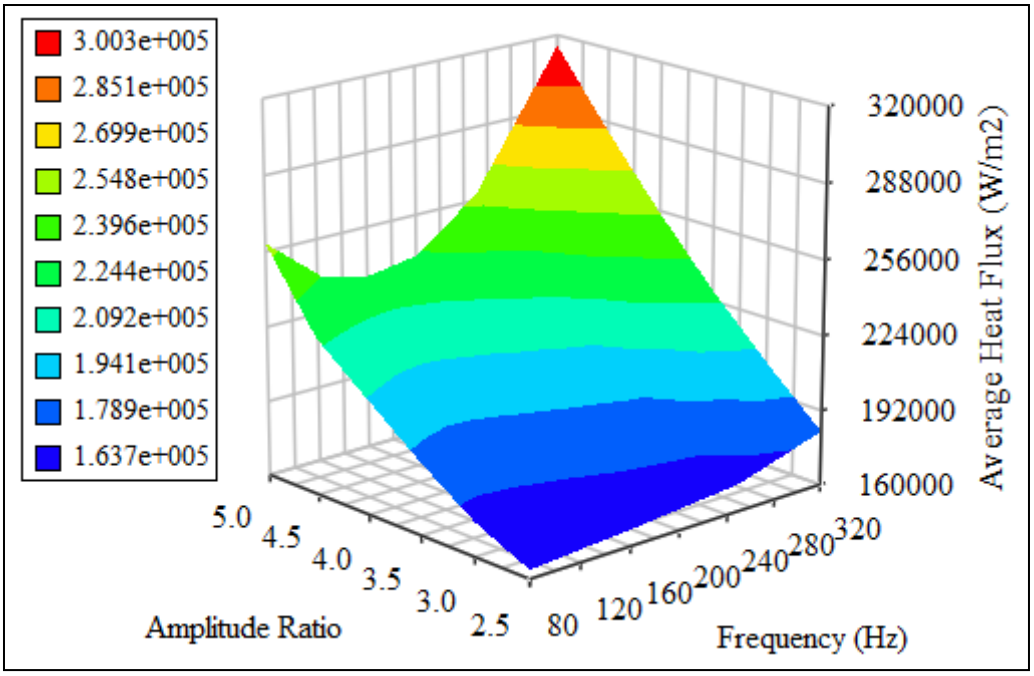

Figure 10.3: Heat flux versus amplitude ratio and frequency for $D_h = 4.8\times10^{-3}$ m.

Higher amplitude ratios always produced greater heat flux. However, the same was not true for the oscillation frequency. For most of the cases the heat flux increased with increasing oscillation frequency. Even so, for low frequency, high amplitude pulsations the heat flux decreased with increasing oscillation frequency. The exact frequency dependence of the heat flux is perhaps better shown in Figure 10.4, a plot of heat flux versus frequency with lines of constant amplitude ratio.

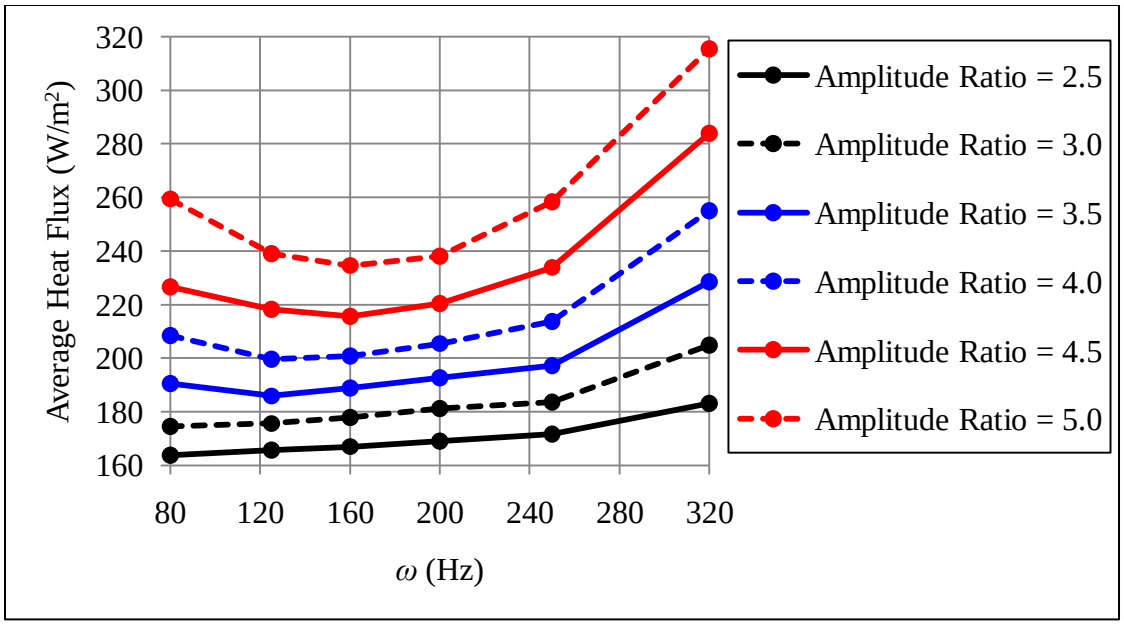

Figure 10.4: Heat flux versus frequency with lines of constant R_{amp} for $D_h = 4.8\times10^{-3}$ m.

The cases which had decreasing heat flux for increasing frequency were the same cases for which a secondary vortex was produced. The decrease in heat flux was the result of diminishing secondary vortices which were shown to enhance heat flux in Chapter 9. That is, as the frequency increased for the low frequency, high amplitude cases, the size, strength, and duration of the secondary vortices decreased, thereby reducing heat transfer. An overlay of the heat flux contours, the secondary vortex, and persistent vortex regimes is given in Figure 10.5.

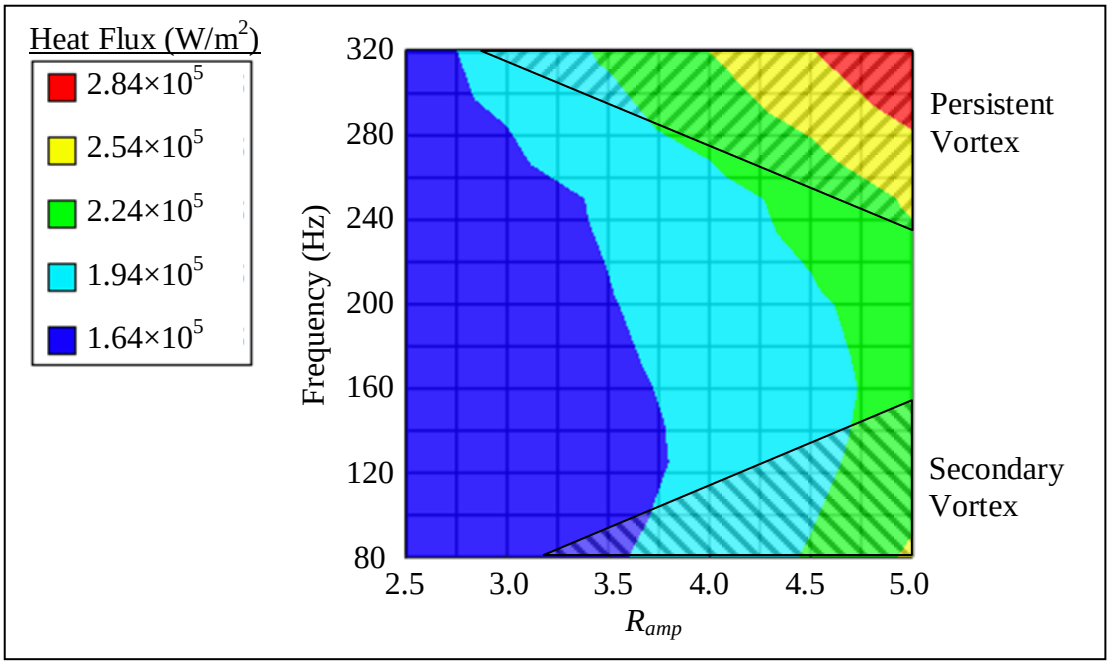

Figure 10.5: Flow regimes and heat flux contours versus amplitude ratio and frequency.

Figure 10.5 shows a change in the general trends for the region corresponding to the presence of a secondary vortex. Another attribute highlighted by Figure 10.4 is the closely-packed nature of the heat flux contours in the region corresponding to persistent vortices. This indicated relatively high heat flux gradients for that range and is corroborated by the steep slopes between data points for the high amplitude, high frequency cases in Figure 10.4. As further evidence of the influence of the flow regime, Figure 10.6 shows the frequency dependency of the heat flux. That is, Figure 10.6 shows the estimated change in heat flux with frequency for each combination of parameters.

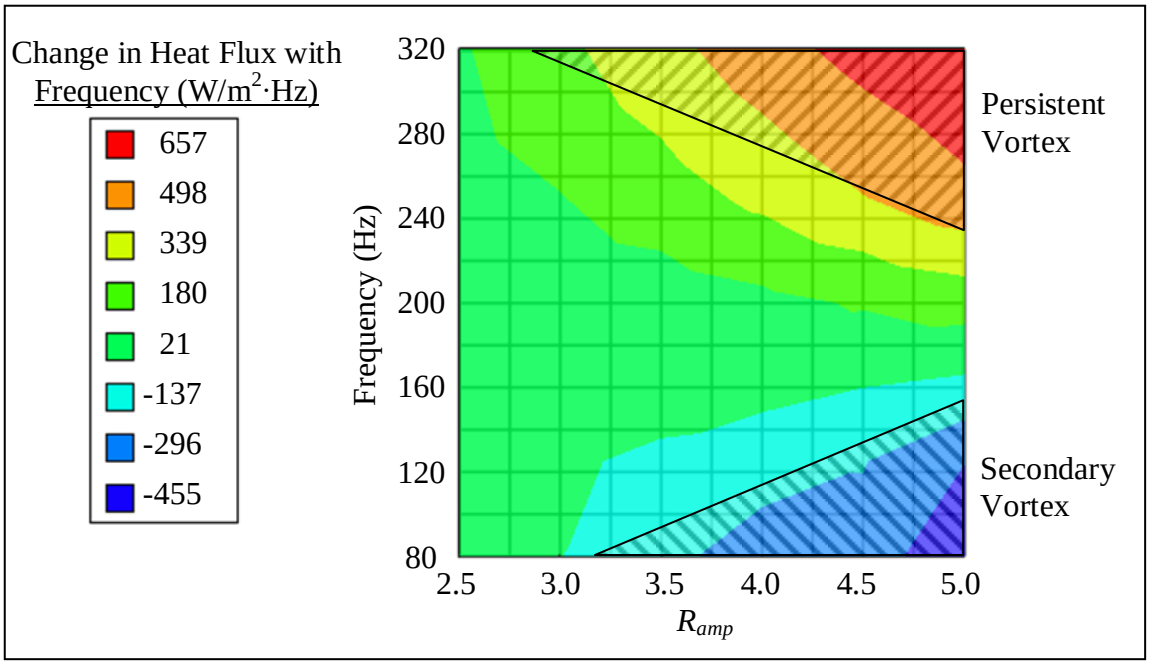

Figure 10.6: Change in heat flux with frequency for each combination of R_{amp} and ω.

The trends shown in Figure 10.6 indicate a strong relationship between the flow type, frequency, and heat flux. This also reinforces the assertion that the three distinct flow regimes not only exist, but also play critical roles in the impingement heat transfer. While the correlation between flow regime and frequency dependence is demonstrated by Figure 10.6, Figure 10.7 presents similar data for the amplitude ratio dependency of the heat flux. In Figure 10.7 the contours indicate the change in heat flux per unit change in R_{amp}.

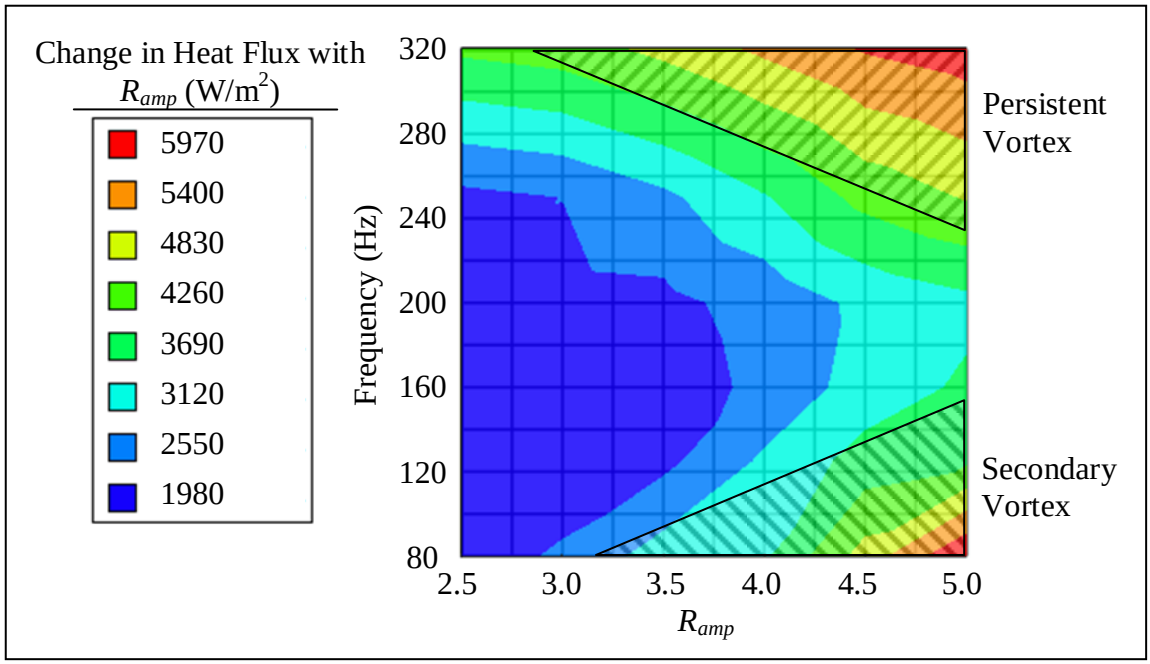

Figure 10.7: Change in heat flux with R_{amp} for each combination of R_{amp} and ω.

As before, there was a clear relationship between flow regime and amplitude ratio dependence, with the highest gradients occurring within the persistent vortex and secondary vortex regimes. The impact of these flow regimes on drying is discussed in the next section. In that section, the results of the drying simulations, which were conducted for all cases with $D_h = 4.8\times10^{-3}$ m, are presented.

10.4 Drying

The FLUENT simulations were used to study the impact on drying porous media. The porous material that was selected was a paper sheet composed of bleached, kraft pulped softwood fibers. The sheet type is commonly referred to as “blotter paper”, and is typically characterized by a rather open pore structure, due to limited applied load during

mechanical dewatering, and by a relatively high basis weight, due to it intended end use of absorbing water. The particular sheet structure that was employed in these simulations was that of a relatively high density, low thickness blotter paper. This material was selected because other numerical drying studies of such a substrate have shown good agreement with experimental data (Nasrallah and Perre, 1987; Lu and Shen, 2007). The material properties of the porous media are given in Table 10.4.

Table 10.4: Substrate properties used in drying simulation.

Parameter	Value	Source
Thickness	2.7×10^{-4} m	Lu and Shen (2007)
ϕ	0.58	Lu and Shen (2007)
s_i	0.99	Lu and Shen (2007)
λ_s	1.4 W/m·K	Lu and Shen (2007)
S_{ir}	0.01	Lu and Shen (2007)
c_{ps}	1400 J/kg·K	Nasrallah and Perre (1987)
ρ_s	1500 kg/m^3	Nasrallah and Perre (1987)
ψ	0.20	-

The operational conditions matched those used in the previous section. Thus, D_h = 4.8×10^{-3} m, H/D = 5, $\overline{U}_{exit}$ = 30 m/s, and the same combinations of R_{amp} and ω were studied. Furthermore, since a stationary surface was employed in the FLUENT simulations, the average drying rate, $\overline{\overline{m''}}$, was used to quantify the drying performance.

This quantity was the drying rate averaged over the range $x \leq 0.1$ m for the first 0.2 s of drying. This time increment was selected because it is the smallest value that is evenly divisible by the oscillation periods of all cases. Thus, full oscillation cycles were completed for each operational frequency. The resulting drying rates are given in Table 10.5

Table 10.5: Time- and area-averaged drying rate for $D_h = 4.8\times10^{-3}$ m and ω in Hz.

	$\overline{\overline{m''}}$ ($\times10^{-2}$ kg/m^2·s)					
	ω = 80	ω = 125	ω = 160	ω = 200	ω = 250	ω = 320
R_{amp} = 2.5	5.18	5.16	5.19	5.24	5.30	5.47
R_{amp} = 3.0	5.33	5.35	5.42	5.47	5.49	5.82
R_{amp} = 3.5	5.59	5.48	5.55	5.59	5.73	6.16
R_{amp} = 4.0	5.85	5.76	5.73	5.83	5.99	6.53
R_{amp} = 4.5	6.18	6.04	5.97	6.05	6.29	6.85
R_{amp} = 5.0	6.57	6.30	6.27	6.29	6.55	7.15

All cases produced significantly higher drying rates than the corresponding steady flow case, which yielded a drying rate of 3.89×10^{-2} kg/m^2·s. These improvements are quantified by the average drying rate enhancement factors, E_{DRY}, shown in Table 10.3. E_{DRY} is the ratio of the $\overline{\overline{m''}}$ of the pulsed case to that of the steady flow case.

Table 10.6: Average drying enhancement for $D_h = 4.8\times10^{-3}$ m and ω in Hz.

	E_{DRY}					
	ω = 80	ω = 125	ω = 160	ω = 200	ω = 250	ω = 320
R_{amp} = 2.5	1.33	1.33	1.33	1.35	1.36	1.41
R_{amp} = 3.0	1.37	1.38	1.39	1.41	1.41	1.50
R_{amp} = 3.5	1.44	1.41	1.43	1.44	1.47	1.58
R_{amp} = 4.0	1.50	1.48	1.47	1.50	1.54	1.68
R_{amp} = 4.5	1.59	1.55	1.53	1.56	1.62	1.76
R_{amp} = 5.0	1.69	1.62	1.61	1.62	1.68	1.84

As expected, the pulsed flow produced higher drying rates than the comparable steady flow. However, this increase was not as high as the improvement in heat flux for the highest flux cases. For example, the ω = 320 Hz and R_{amp} = 5.0 case yielded a heat flux enhancement of 154 % but a drying enhancement of 84 %. This was most likely a result of slightly decreased transport properties for the lower surface saturations of the high moisture flux cases. This is reflected in Figure 10.8, a comparison of the surface heat flux and drying rate for each case.

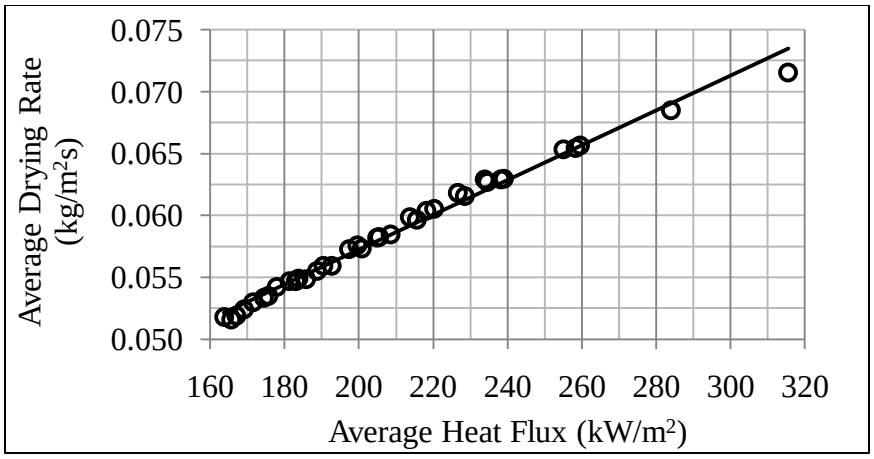

Figure 10.8: Surface heat flux and resultant drying rate for $D_h = 4.8\times10^{-3}$ m.

The trend line in Figure 10.8 is a least squares linear fit to the data. There was a nearly linear fit, with a coefficient of determination of 0.989. The higher flux cases, however, did decrease the slope of the trend line. As a result, the trends in drying rate were similar to those of the heat flux data. This is reflected in Figure 10.9, a plot of average drying rate versus oscillation frequency with lines of constant amplitude ratio.

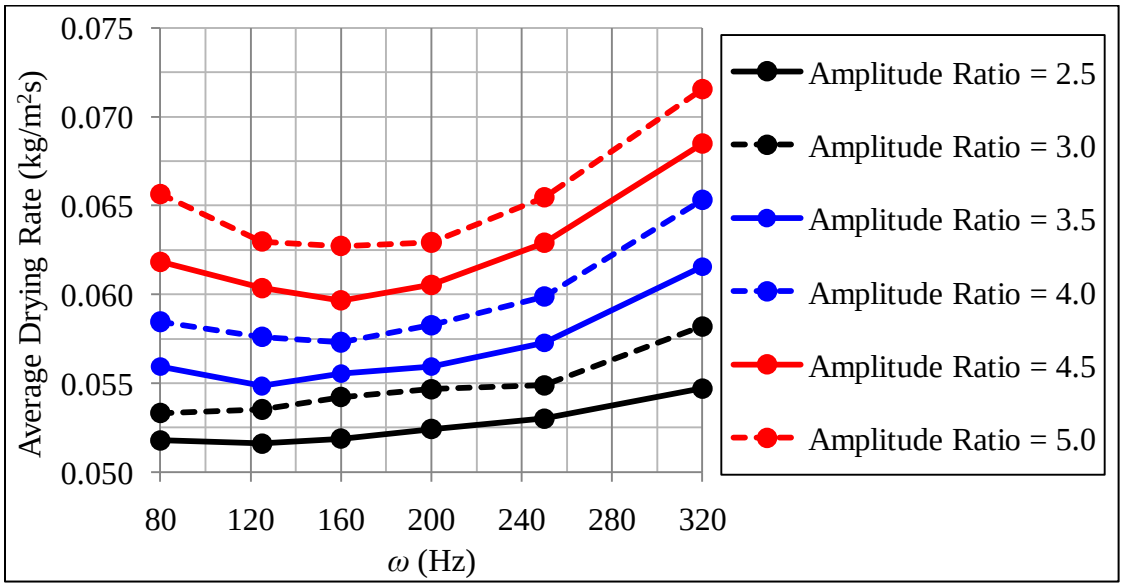

Figure 10.9: Drying rate versus ω with lines of constant R_{amp} for $D_h = 4.8\times10^{-3}$ m.

These trends were similar to the heat flux trends shown in Figure 10.4. Higher amplitude ratios produced higher drying rates for a given frequency. With the exception of the low frequency, high amplitude cases, the drying rate increased with increasing oscillation frequency. The results shown in Figure 10.8 and Figure 10.9 demonstrate that trends in the surface heat flux are a good predictor of the drying rate trends.

10.5 Other Geometries

This section presents the results of the cases that employed the nozzle diameters and resulting H/D_h ratios given in Table 10.7. The $D_h = 4.8\times10^{-3}$ m cases that were discussed in the previous section are also included in this section in order to show trends and make comparisons.

Table 10.7: Hydraulic diameters and H/D_h ratios used in this section.

D_h ($\times10^{-3}$ m)	H/D_h -
3.0	8
4.0	6
4.8	5
6.0	4
8.0	3
12.0	2

As before, the mean tailpipe exit velocity was 30 m/s for all cases. Each of the 216 cases was categorized as producing one of the 3 distinct flow types discussed in the previous section. The resulting flow regimes for each nozzle diameter are shown in Figure 10.10 as a function of oscillation frequency and velocity amplitude ratio.

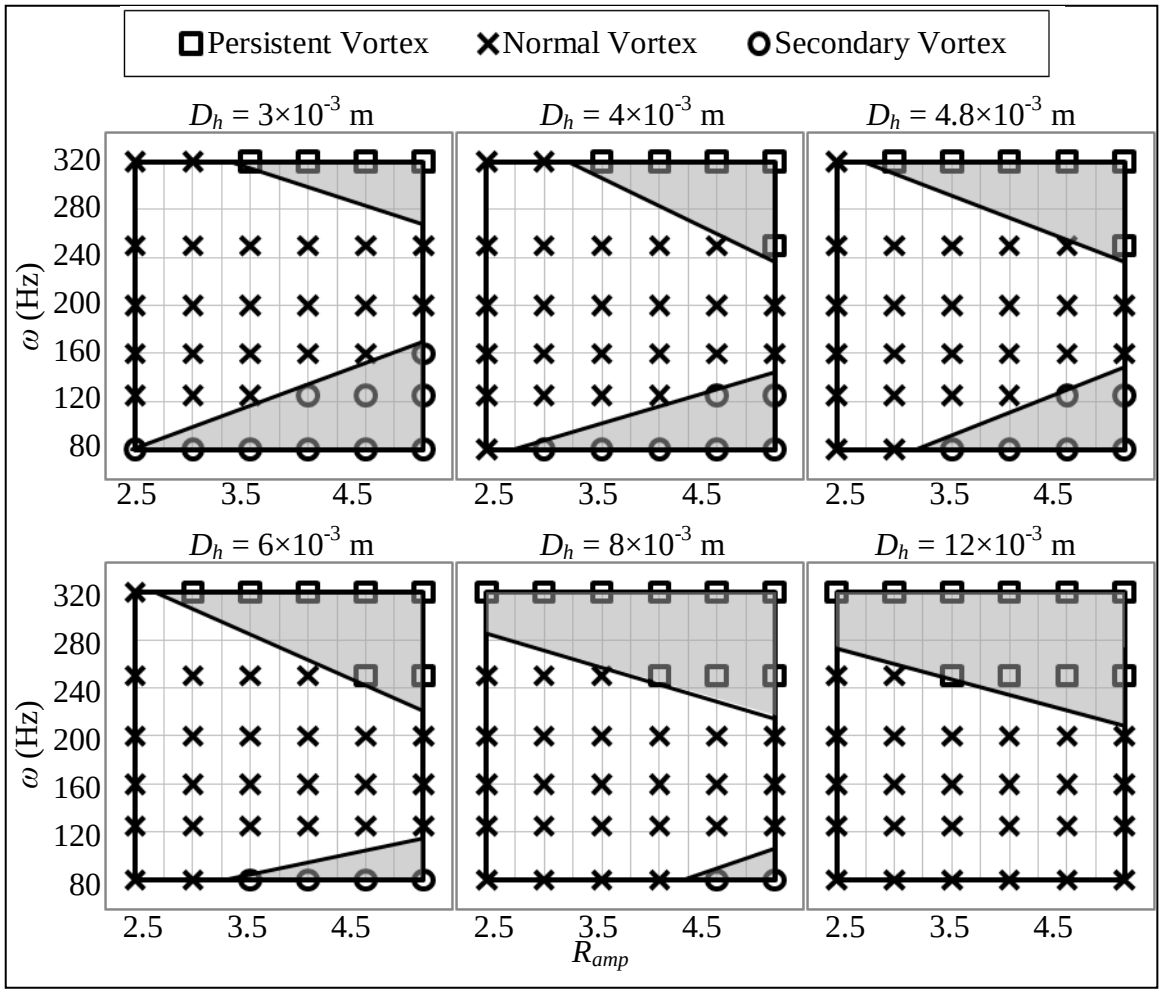

Figure 10.10: Flow type for each case with various hydraulic diameters.

The oscillation parameters that produced persistent vortices were high operational frequencies and high velocity amplitude ratios. These relationships were the expected results. High ω values simply afforded less time for the vortices to dissipate.

Additionally, high velocity amplitude ratios produced stronger initial vortices; thus, dissipation in the shortened time scale was less likely. Furthermore, the size of the persistent vortex regime always increased with increasing nozzle diameter as a result of higher flow rates and larger, stronger vortices. Conversely, the size of the secondary vortex regime decreased at larger nozzle diameters due to dominant primary vortices.

Based on the parameters studied, the cases which yielded a secondary vortex met the criterion

$$\frac{\omega D_h^{0.6}}{U_{amp}} < C_1 \tag{10.1}$$

where the critical value of the dimensional parameter C_1 was 0.028 $m^{-0.4}$. All cases which did not meet this criterion failed to produce a secondary vortex. Thus, this relationship can be used as the transition criteria for the secondary vortex regime for the parameters investigated. The characteristic quantity on the left hand side can be interpreted as the ratio of the peak local inertial forces to the peak convective inertial forces. Thus, the dimensional grouping in this inequality is similar in form to the Strouhal number. In fact, by defining a Strouhal number based on the velocity amplitude, rather than the mean velocity, the transition criterion can be written as

$$\frac{St'}{\overline{Re}^{0.4}} < \Psi_1 \tag{10.2}$$

where

$$St' = \frac{\omega D_h}{U_{amp}}, \qquad \overline{Re} = \frac{\overline{U}_{exit}\, D_h}{\overline{\nu}}. \tag{10.3}$$

The critical value of the dimensionless parameter Ψ_1 was found to be 2.3×10^{-4}.

Similarly, the dimensional form of the criterion describing the persistent vortex regime was found to be

$$\omega^2 D_h^{0.4} U_{amp} > C_2 \tag{10.4}$$

with a critical value of C_2 of 1.025×10^6 $m^{1.4}/s^3$. That is, all cases for which the above inequality was true produced persistent vortices, and these were the only cases that did so. This criterion can be stated in the dimensionless form

$$\overline{St}^2 \left(\frac{H}{D_h}\right)^{1.6} R_{amp} > \Psi_2 \tag{10.5}$$

where the critical value of the dimensionless parameter Ψ_2 was found to be 0.0975.

It is important to note that these transition criteria were obtained by fitting the resultant surface to the numerical data; thus, these results are observational. The relationships were not derived separately from fundamental arguments. As such, the criteria do not necessarily provide insight into the underlying mechanisms for the regime changes nor are they guaranteed to be applicable beyond the parameters studied in this chapter. Rather, they are intended only to describe the observed behavior and provide

information about combinations of parameters that were not investigated but still fall within the ranges considered. The relationships also allow visualization of a possible transition surface by equating the relevant grouping to the critical value. These transition surfaces are shown in Figure 10.11 along with the regime type observed in each simulation case.

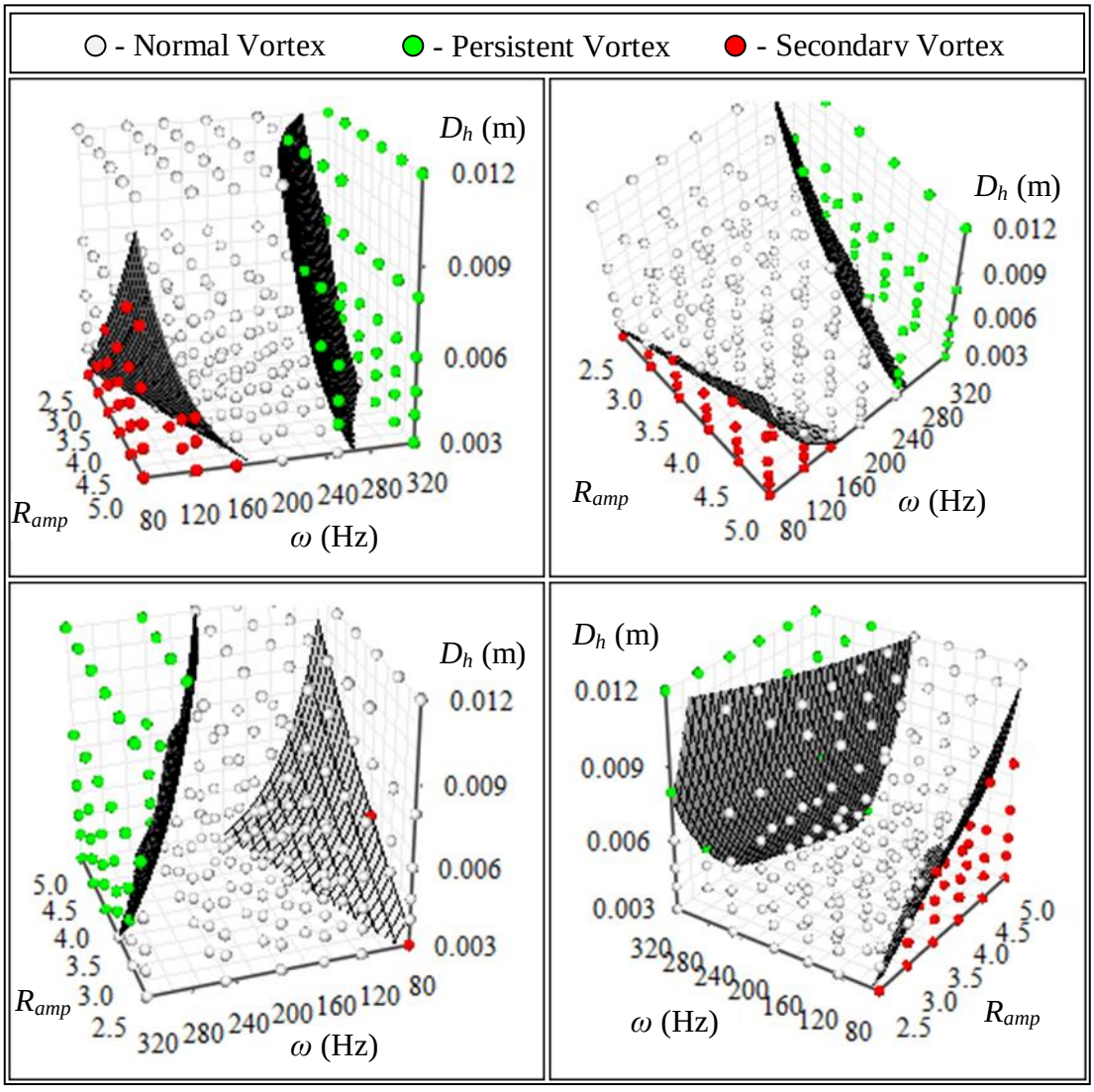

Figure 10.11: Flow type and transition surfaces based on R_{amp}, D_h, and ω.

The heat flux resulting from these flow types were in line with the findings of the D_h = 4.8×10^{-3} m cases. In general, the trends with increasing nozzle diameter were consistent, as shown in Figure 10.12. The trends with D_h were similar for all cases, with the exception of the smaller nozzle diameters for the ω = 80 Hz and R_{amp} = 5 combinations. These cases produced the strongest secondary vortices, resulting in elevated heat flux. For all cases, larger hydraulic diameters yielded greater heat flux as a result of higher energy input. The overall heat flux trends are shown in Figure 10.13, a plot of heat flux as a function of amplitude ratio and frequency. As before, the contours are colored by average heat flux, and the vertical axis has units of 10^5 W/m^2. The surfaces were created through Delaunay triangulation. Higher amplitude ratios produced greater heat flux. For regions that correspond to the secondary vortex regime, the heat flux decreased with increasing oscillation frequency. This is shown in Figure 10.14, the frequency dependency of the heat flux.

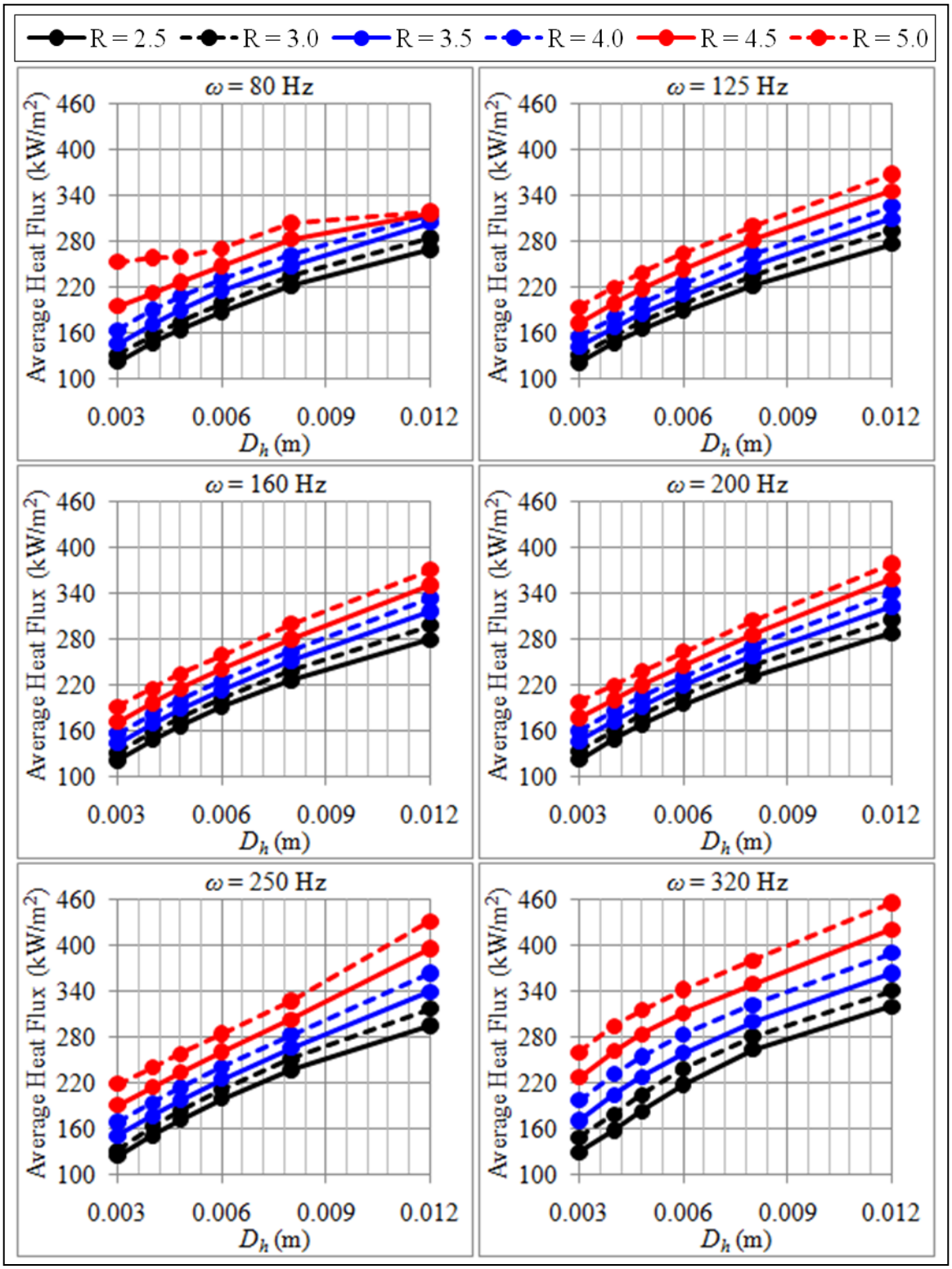

Figure 10.12: Heat flux trends with D_h for each ω with lines of constant R_{amp}.

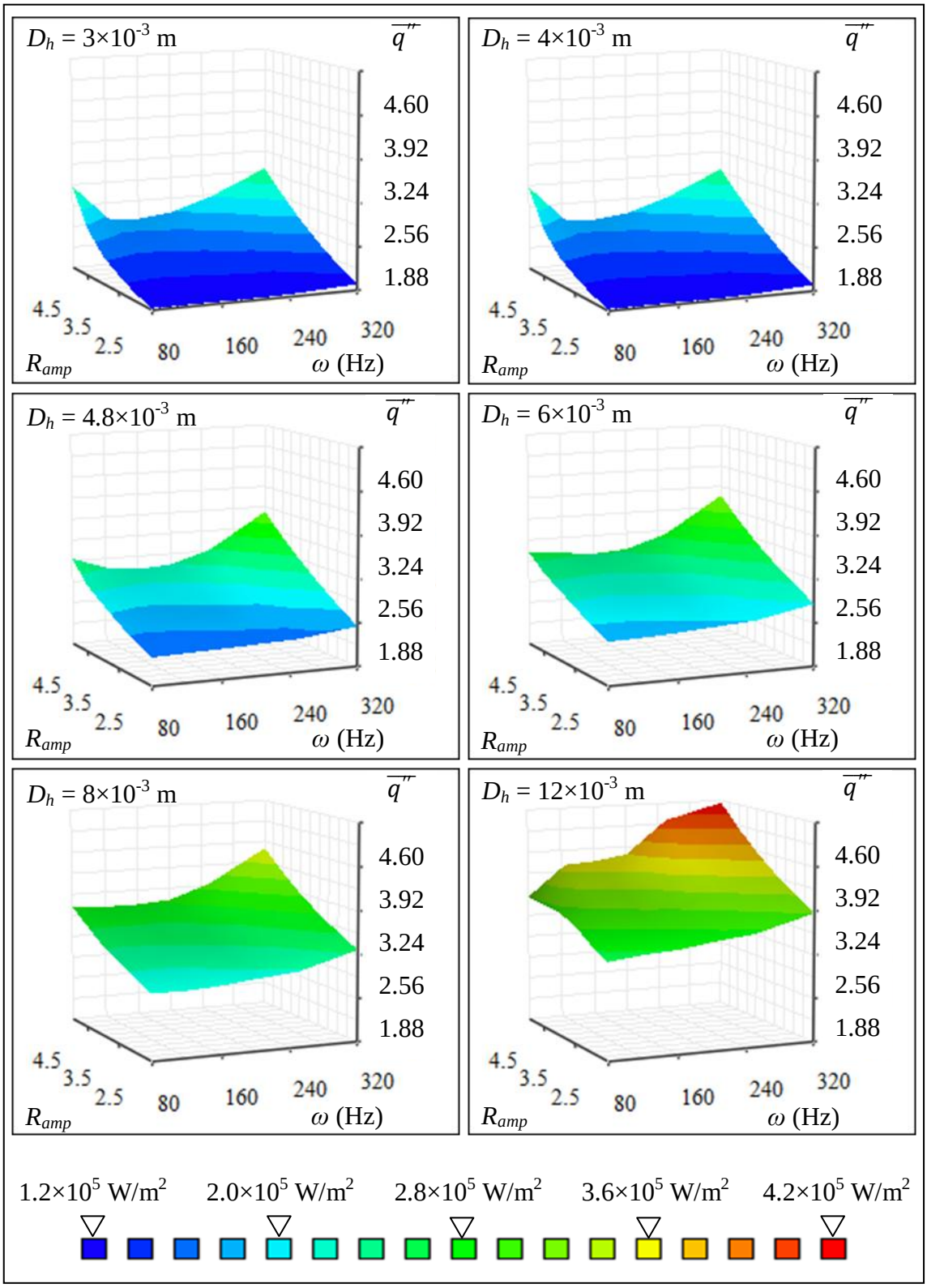

Figure 10.13: Heat flux for each D_h as a function of ω and R_{amp}.

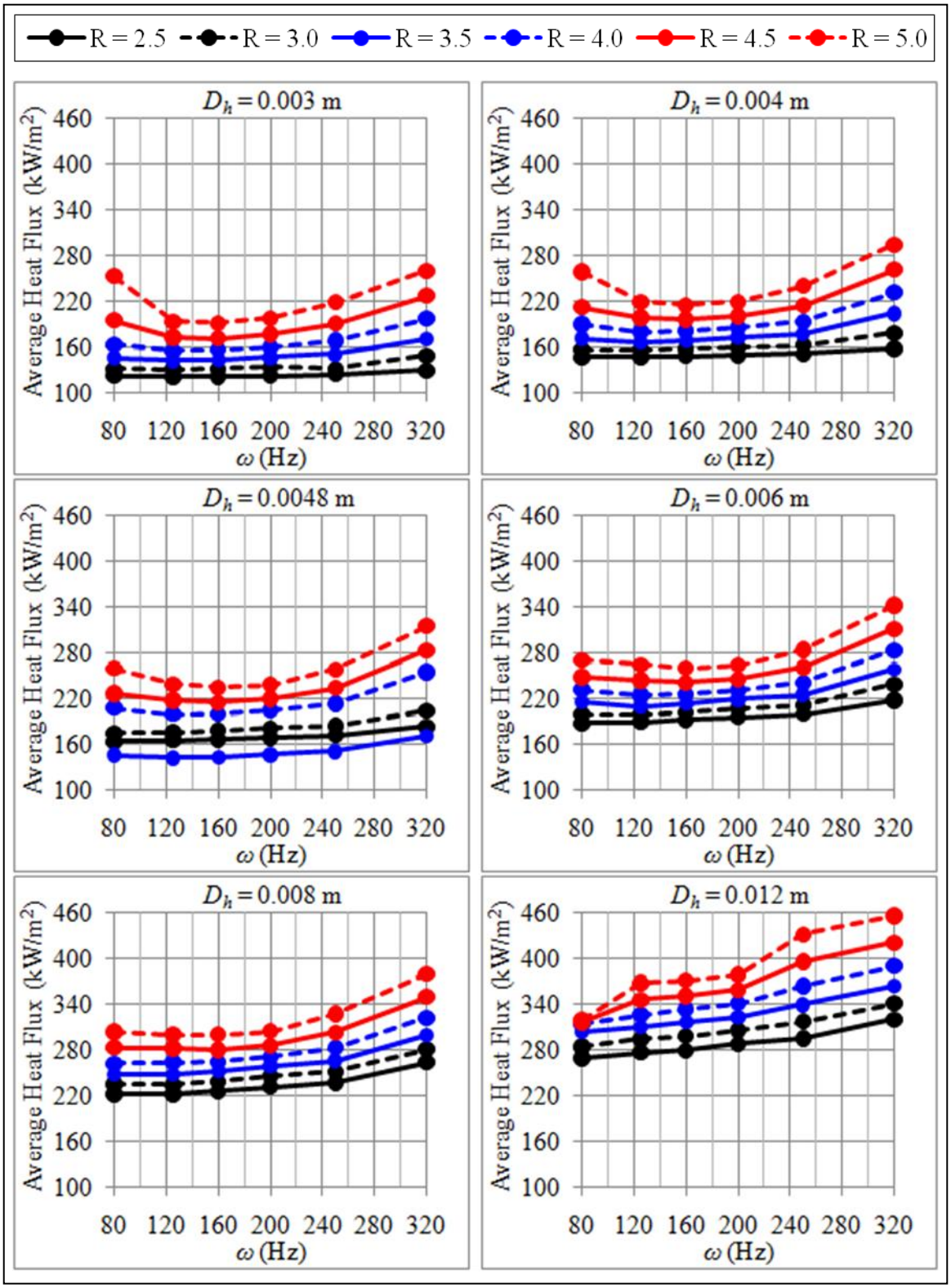

Figure 10.14: Heat flux trends with ω for each D_h with lines of constant R_{amp}.

10.6 Summary and Discussion

For a given nozzle size, and thus, mean mass flux, higher amplitude ratios produced greater heat flux. Furthermore, drying rates were found to follow similar trends since they changed nearly linearly with heat flux. The increase in heat flux was intensified if accompanied by a transition to a different flow regime. The secondary vortex and persistent vortex regimes were found to significantly enhance heat transfer. The secondary vortex regime occurred at low frequencies, while the persistent vortex regime was encountered at high oscillation frequencies. However, larger nozzle sizes also led to higher heat flux for the complimentary steady flow cases, as shown in Figure 10.15. Thus, heat flux enhancement did not always increase with nozzle size. This is shown in Figure 10.16, plots of heat flux enhancement versus D_h with lines of constant amplitude ratio. The cases corresponding to the secondary vortex and persistent vortex regimes produced the highest enhancement factors.

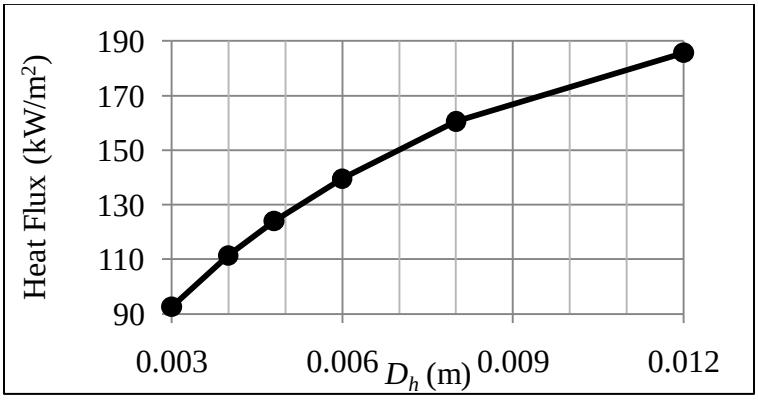

Figure 10.15: Average heat flux versus D_h for the steady flow cases.

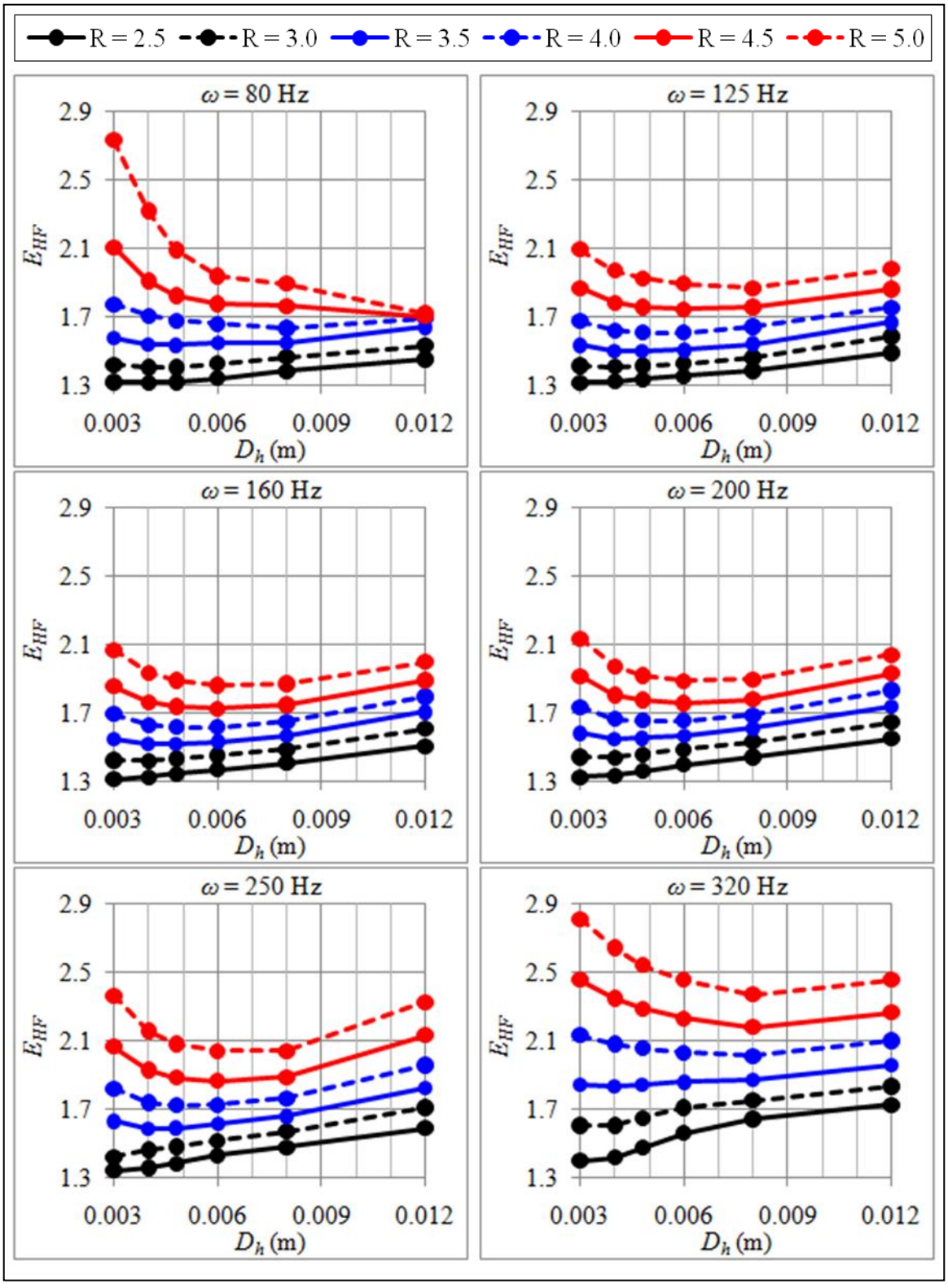

Figure 10.16: Heat flux enhancement versus D_h with lines of constant R_{amp}.

CHAPTER 11

MULTIPLE IMPINGEMENT JETS

11.1 Introduction

This chapter presents the findings of a numerical study of multiple impingement jets. FLUENT was used to investigate the fluid flow, temperature field, and heat flux of a two nozzle system. Of primary interest were jet-to-jet interactions from oscillating jets and the impact of phase difference on said interactions. Various values of phase difference were investigated including a base case in which the jet oscillations from the two nozzles were in-phase. The heat transfer to the impingement surface was also compared to a similar steady flow case.

11.2 Approach

In order to study jet-to-jet interactions, a domain consisting of two tailpipes was employed. These slot shaped tailpipes had the same hydraulic diameters and lengths. The resulting two-dimensional domain is shown schematically in Figure 11.1.

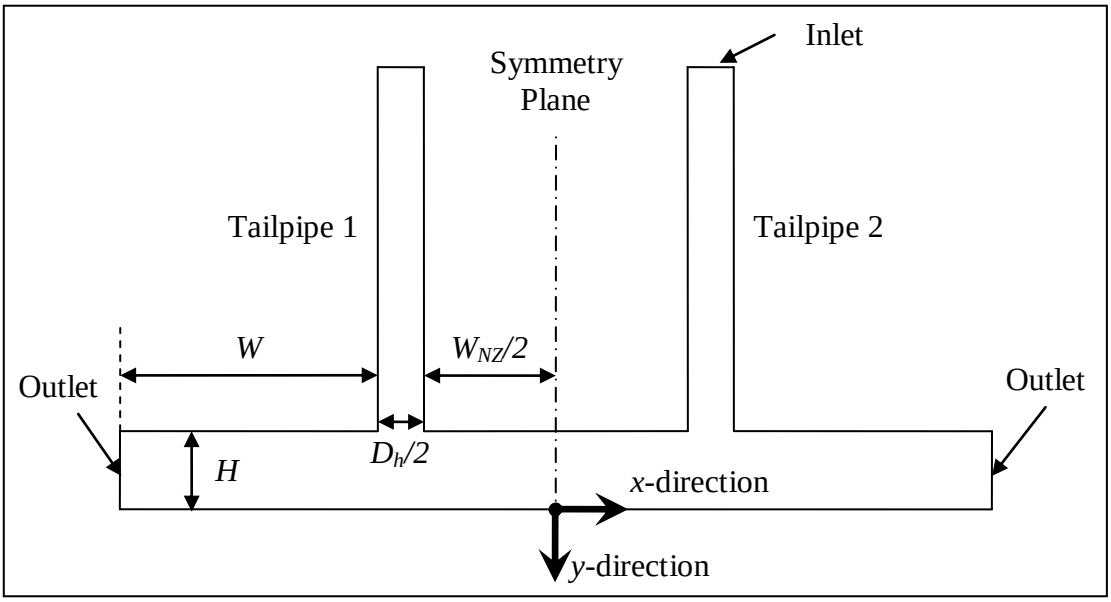

Figure 11.1: Diagram of numerical domain used in the multiple jet simulations.

The boundary conditions correspond to those employed throughout the current work. Thus, the confinement walls were specified as adiabatic surfaces, as were the tailpipe sidewalls. The outlet boundary conditions were atmospheric pressure with specified backflow turbulence parameters and 300 K backflow temperature. More information on the boundary conditions and associated solution procedures can be found in Chapter 4. In order to isolate the effects of the jet-to-jet interactions, a stationary impingement surface was employed. This is given in Table 11.1, along with the relevant geometric and operational parameters.

Table 11.1: Parameters used in the multiple nozzle simulations.

Parameter	Value
D_h	4.8×10^{-3} m
H	2.4×10^{-2} m
W	0.10 m
W_{NZ}	8.4×10^{-2} m
$\overline{U}_{exit}$	30 m/s
ω	160 Hz
R_{amp}	4
U_{surface}	0

The values given in Table 11.1 are consistent with those used in previous chapters. Thus, the H/D_h ratio was 5 in accordance with the optimal conditions given by Martin (1977). The oscillation frequency, velocity amplitude ratio, and mean velocity were values which could be obtained in a commercial application based on laboratory observations. The nozzle-to-nozzle spacing was selected based on the size of the vortices observed in previous chapters for similar boundary conditions, nozzle diameters, and nozzle-to-surface spacing. $W_{NZ}/2$ was chosen to be slightly smaller than those vortices in order to obtain significant interaction between jets yet still allow comparisons to previous study of single impingement jets.

The symmetry plane in Figure 11.1 refers only to the geometry of the domain.

Only in certain cases were the boundary conditions and resulting flows symmetric. Although both tailpipes had the same inlet temperatures of 1200 K, the oscillations were not always in-phase. The mass flux at the inlet of Tailpipe 1 was specified such that the resultant bulk velocity at the tailpipe exit, U_1, was of the form

$$U_1 = \overline{U}_{exit}\left[1 + R_{amp}\,\sin(\omega t)\right], \tag{11.1}$$

with ω in radians per second and t in seconds. Although the velocity at the exit of Tailpipe 2 followed a similar pattern, it was shifted in time by θ radians

$$U_2 = \overline{U}_{exit}\left[1 + R_{amp}\,\sin(\omega t + \theta)\right]; \tag{11.2}$$

thus, U_1 and U_1 were θ radians out of phase. For example, the desired mean exit velocity in the positive y-direction is shown in Figure 11.2 for $\theta = \pi/2$ rad and $\overline{U}_{exit}$ = 30 m/s.

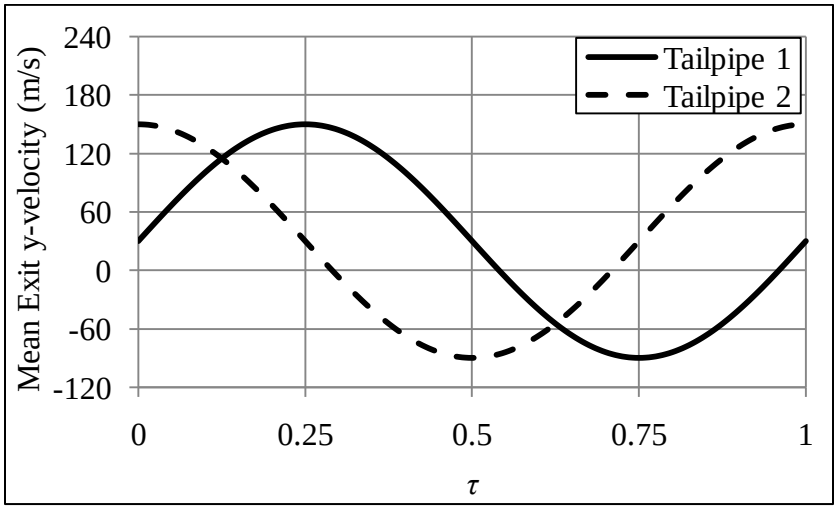

Figure 11.2: Example tailpipe exit velocities for a phase shift of $\theta = \pi/2$ rad.

Five values of θ were investigated: 0, $\pi/4$, $\pi/2$, $3\pi/4$, and π rad. All other parameters were the same for each case in order to isolate and assess the impact of the phase shift. Additionally, a steady flow case with the same mean flow rate and tailpipe entrance temperature as the pulsed flow cases was studied. This was done to facilitate analysis of the heat flux enhancement and the mechanisms of said enhancement. The case in which the jets were in-phase is discussed first.

11.3 Base Case

This section discusses the results from the base case in which both impingement jets were in-phase ($\theta = 0$). The steady flow case is also discussed in order to compare heat transfer rates and mechanisms. The instantaneous flow field and temperature field of the pulsed flow case at $\tau = 0.5$ are shown in Figure 11.3.

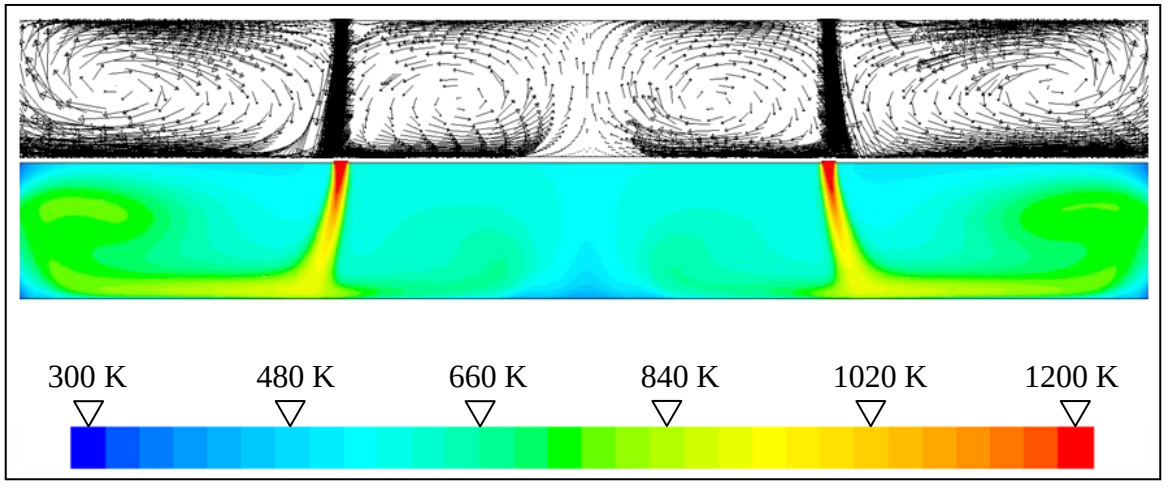

Figure 11.3: Instantaneous flow field and temperature field $\tau = 0.5$ for $\theta = 0$.

As expected, the flow field and temperature field were symmetric about the *y*-axis. The flow structures around each nozzle were similar to those observed in the single nozzle cases in which large vortices formed on both sides of the impingement jet. There were two main differences found in the multiple nozzle configuration. The first was the slight outward curve of the main fluid column, a result of the flow symmetry. That is, the mass flux across the *y*-axis was zero; thus, the mean bulk fluid flow was away from this plane. The second major difference was the shape and size of the vortices. The inner vortices were confined by the symmetry plane and were, therefore, smaller than the outer vortices. Furthermore, the outer vortices were not only allowed to grow but were also transported away from the nozzles due to the bulk fluid flow. The resulting temperature field shows significantly more heat in the outer regions of the domain than in the region between the nozzles. This was the result of a larger portion of the entering hot impingement gases diverting away from the mid-plane. This was not the case for the steady flow case as shown in Figure 11.4.

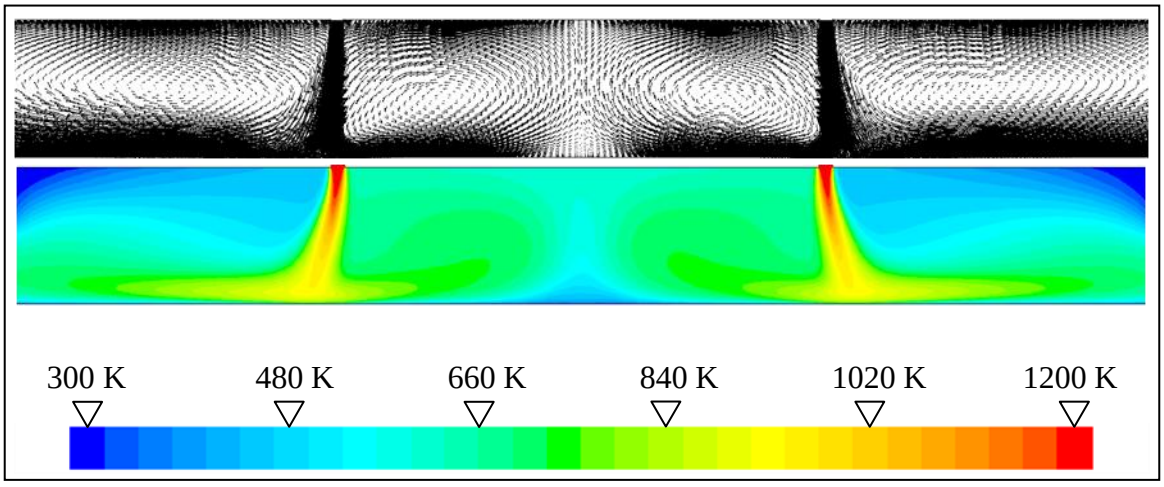

Figure 11.4: Flow field and temperature field for the steady flow case.

Higher average temperatures were encountered in the region between the two jets than in the outer regions. Vortices were formed in the inner regions but were much less intense than those of the pulsed flow case. The resulting time-averaged heat flux profiles for these two cases are shown in Figure 11.5.

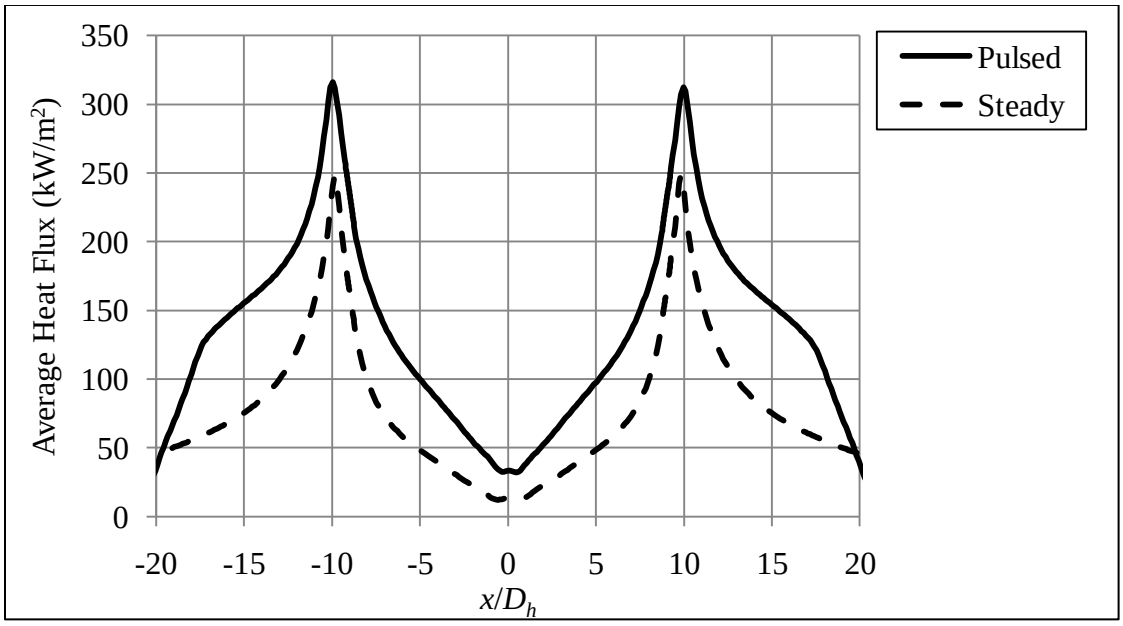

Figure 11.5: Comparison of average heat flux for the base ($\theta = 0$) and steady flow cases.

The pulsed flow produced significantly more heat flux than the steady flow case. However, both cases had somewhat similar profile shapes. The peak values occurred at approximately $x/D_h = \pm 10$ due to the aforementioned outward curve of the main fluid column. For reference, the nozzle mid-planes were located at $x/D_h = \pm 9$. The heat flux for both cases decreased as $|x|/D_h$ became larger than 10. However, the large, high temperature vortices of the pulsed flow case maintained relatively high heat flux in these outer regions. This continued until approximately $x/D_h = \pm 17$, at which point the pulsed flow heat flux began to decrease significantly. At $x/D_h = \pm 20$, the average local heat flux

of the pulsed flow case was 1.01×10^4 W/m^2 lower than that of the steady flow case. A more direct comparison of these two cases is provided in Figure 11.6, a plot of the heat flux enhancement factor. Since the heat flux profiles were shown to be symmetric, Figure 11.6 shows only the results from the positive *x*-axis.

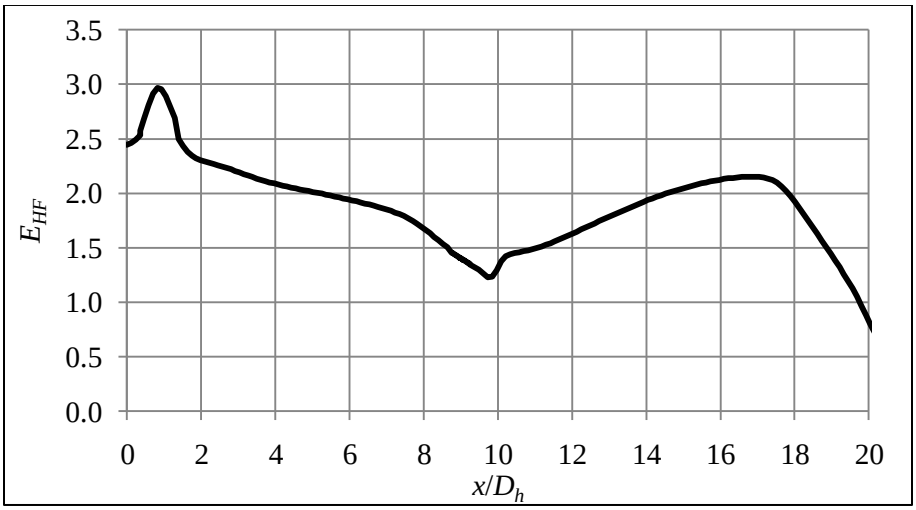

Figure 11.6: Time-averaged heat flux enhancement for the base case ($\theta = 0$).

Although the peak heat flux of the pulsed flow was only 27 % higher than that of the steady flow, the enhancement factor was significantly higher farther away from the stagnation point. Over the range $|x|/D_h \leq 20$, the time- and area-averaged heat flux of the pulsed flow was 1.29×10^5 W/m^2 while the steady flow yielded 0.77×10^5 W/m^2. As a result, the average enhancement factor was 1.68. The instantaneous heat flux and enhancement factors are given in Figure 11.7 and Figure 11.8, respectively. These plots show that the majority of the heat transfer occurred from $\tau = 0.25$ to $\tau = 0.625$. However, local heat flux was greater than that produced by the steady jet at all values of τ in the ranges $|x|/D_h \leq 8$ and $14 \leq |x|/D_h \leq 17$.

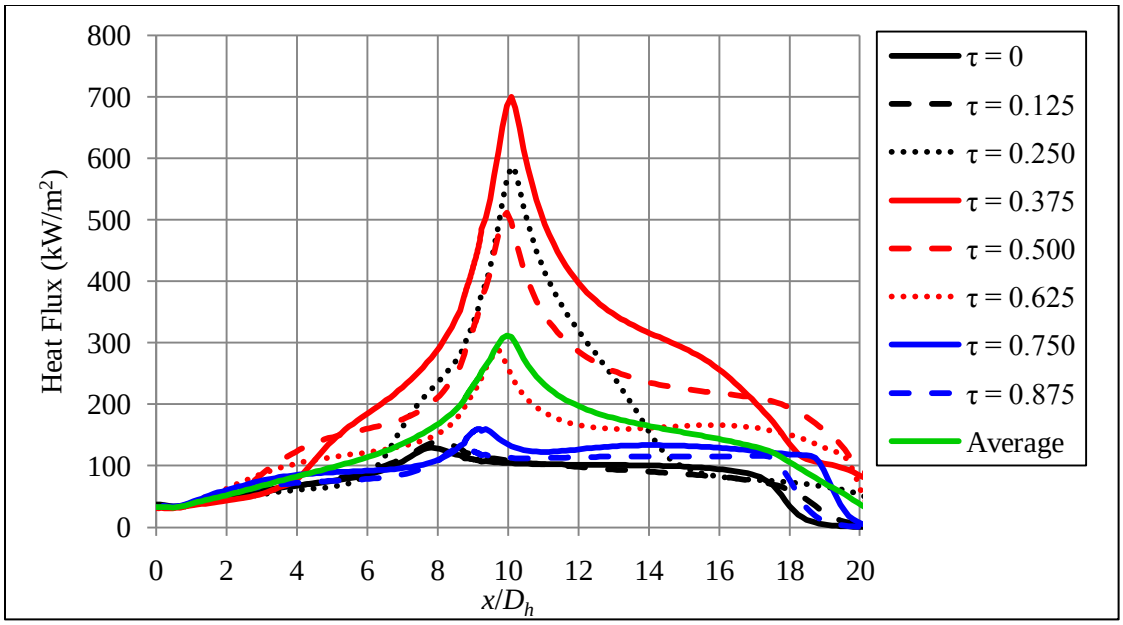

Figure 11.7: Instantaneous heat flux profiles at various values of τ for $\theta = 0$.

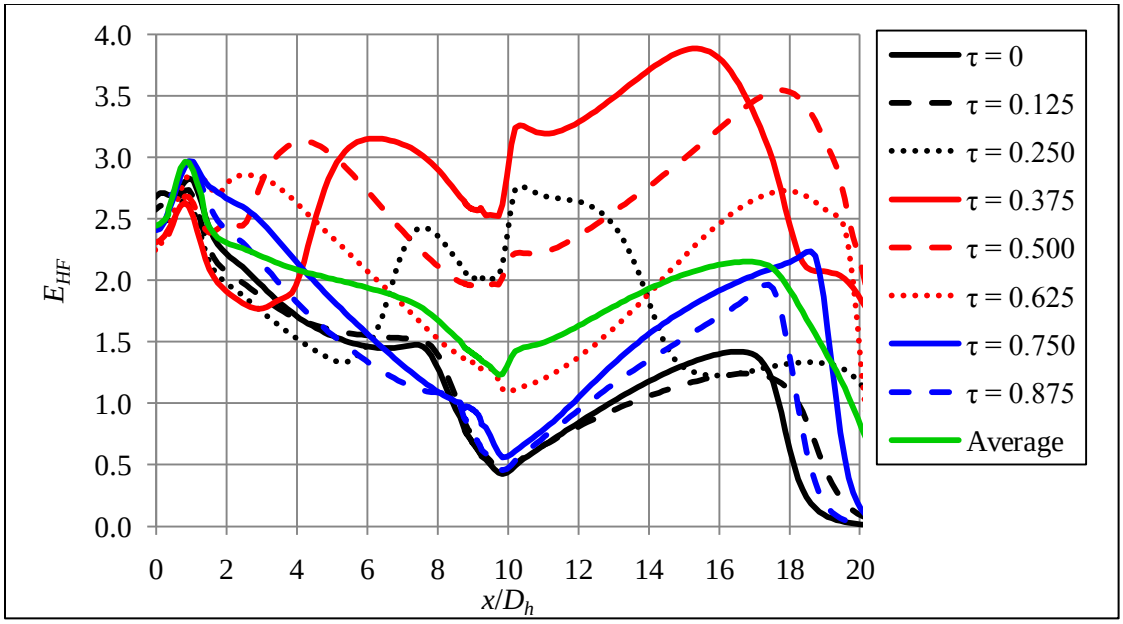

Figure 11.8: Instantaneous heat flux enhancement factors at various values of τ for $\theta = 0$.

11.4 Effects of Phase Shift

This section discusses the results of cases which were similar to the base case with the exception of the value of θ. The changes in heat flux are presented and the resulting trends are offered. A comparison of the heat flux profiles for the pulsed flow cases is provided in Figure 11.9.

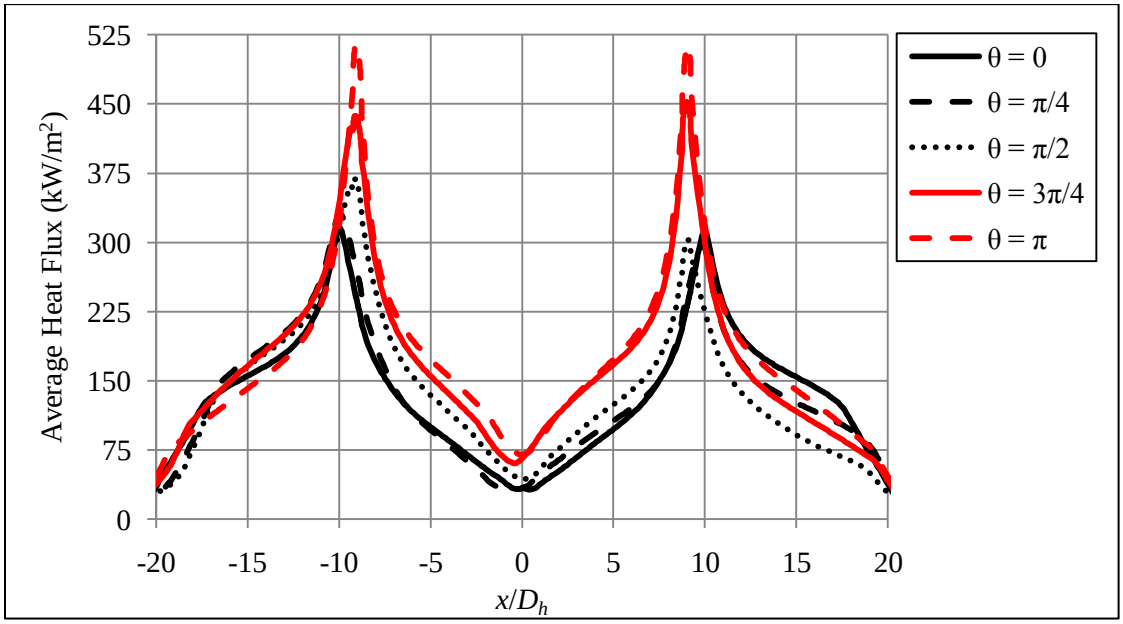

Figure 11.9: Comparison of time-averaged heat flux for various phase shifts.

As expected, only the $\theta = 0$ and $\theta = \pi$ rad cases were symmetric. In general, as the phase shift increased, the location of the peak heat flux shifted inward. This was a result of the discharge from one nozzle experiencing less opposition to inward flow from the other jet. In fact, for $\theta \neq 0$ there were portions of the oscillation cycle in which the flow reversal in one tailpipe acted in concert with the positive exit velocity of the other. Thus, the stagnation point shifted farther inward. As a result, the more direct impingement also

helped elevate the value of the peak heat flux. Furthermore, these changes in flow conditions in the region between the two jets increased the intermediate heat flux values in addition to the peak ones. In comparison to the steady flow, this region produced the greatest heat flux enhancement, as shown in Figure 11.10. Since the mean exit velocities were the same in all cases, the steady flow case in the preceding section was the appropriate complimentary case for all simulations and was used to calculate the enhancement factors.

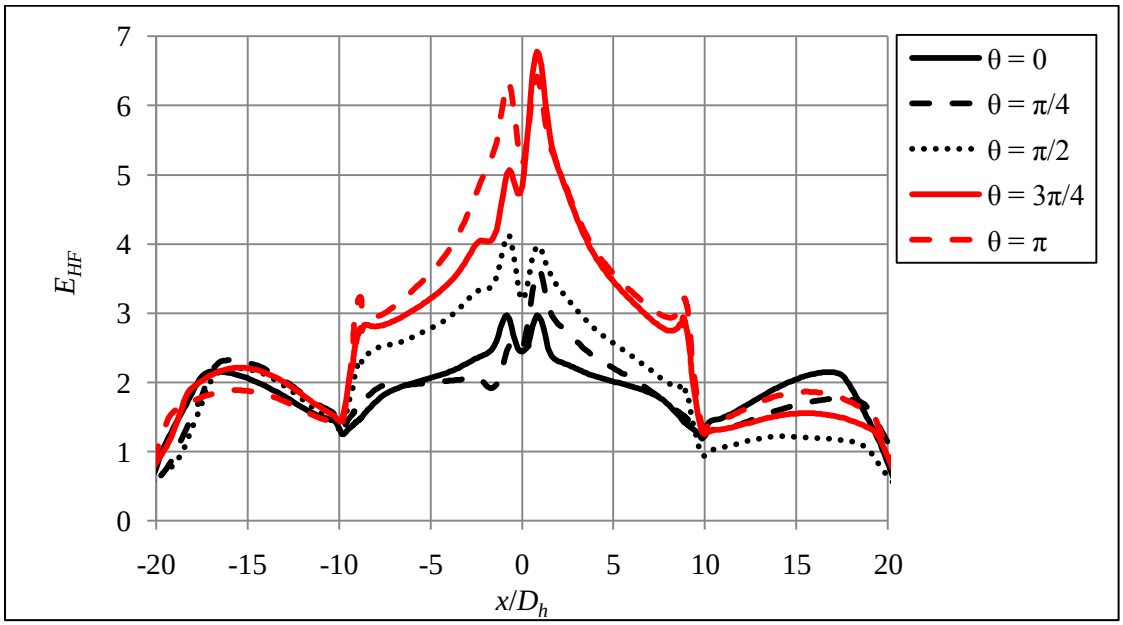

Figure 11.10: Comparison of heat flux enhancement for various phase shifts.

As expected, the largest differences among the pulsed flow cases occurred in the region between the two jets. This indicates that the jet-to-jet interactions were significant factors in determining the overall heat transfer. This overall impact is quantified in Table 11.2, which gives the time- and area-averaged heat flux and corresponding enhancement factor for each case.

Table 11.2: Average heat flux and enhancement factors for various phase shifts.

θ	$\overline{\overline{q''}}$	$\bar{E}_{HF}$
(Rad)	($\times 10^5$ W/m^2)	-
0	1.29	1.68
π/4	1.29	1.68
π/2	1.32	1.71
3π/4	1.61	2.09
π	1.68	2.19

All pulsed cases produced more heat transfer than the steady flow case. In general, the heat transfer increased with increasing phase shift. However, the phase shift had relatively little effect on overall heat flux for the $\theta = 0$, $\theta = \pi/4$ rad, and $\theta = \pi/2$ rad cases. The difference in average heat flux for these cases was less than 2.0 %. Conversely, the $\theta = 3\pi/4$ rad and $\theta = \pi$ rad cases yield much greater heat flux values than the base case. This is shown in Figure 11.11, a comparison of the average heat flux from each case to that of the base case.

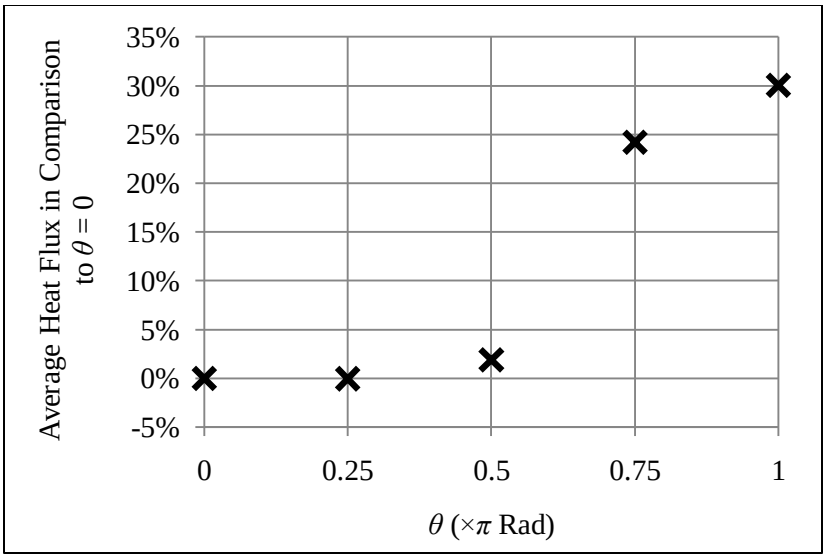

Figure 11.11: Comparison of the average heat flux to the base case for each phase shift.

The high phase shift cases produced significantly elevated heat transfer in comparison to the base case. This increase was the result of three main factors: straighter main fluid columns, enlarged inner vortices, and elevated temperatures in the region between the jets. In order to demonstrate these phenomena, instantaneous flow field for the $\theta = \pi$ rad case is given in Figure 11.12 at 8 values of τ.

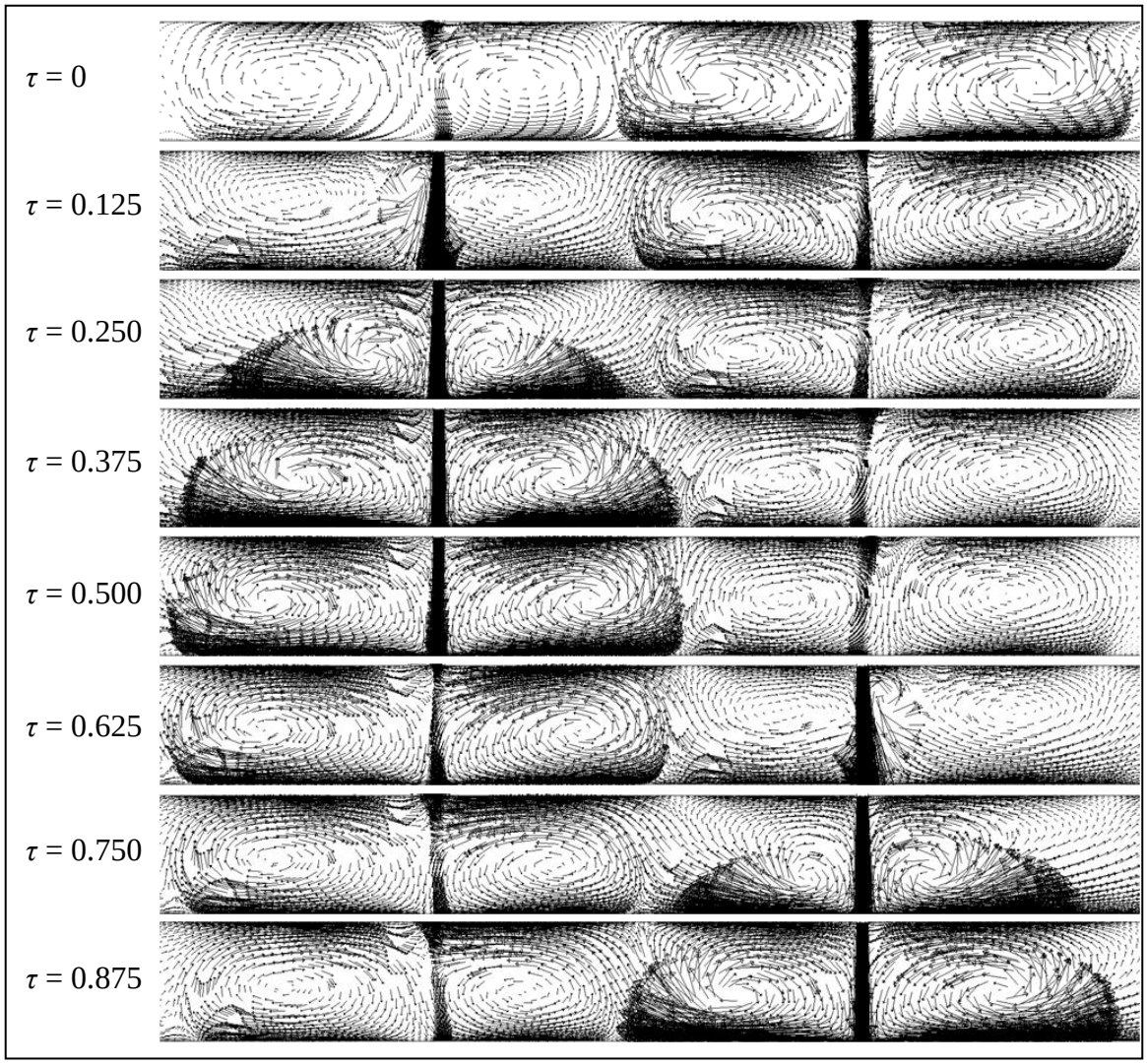

Figure 11.12: Instantaneous flow fields for $\theta = \pi$ at various values of τ.

Since the two jets were at the maximum phase difference, they produced the least amount of resistance to vortex growth and bulk flow towards the *y*-axis from the opposing jet. As a result, the main fluid column did not curve outward as severely as it did for the $\theta = 0$ case. Additionally, the inner vortices were allowed to expand and were similar in size to the outer vortices, thereby aiding in heat transfer in the inner region. The temperature in this region was also affected significantly, as shown in Figure 11.13.

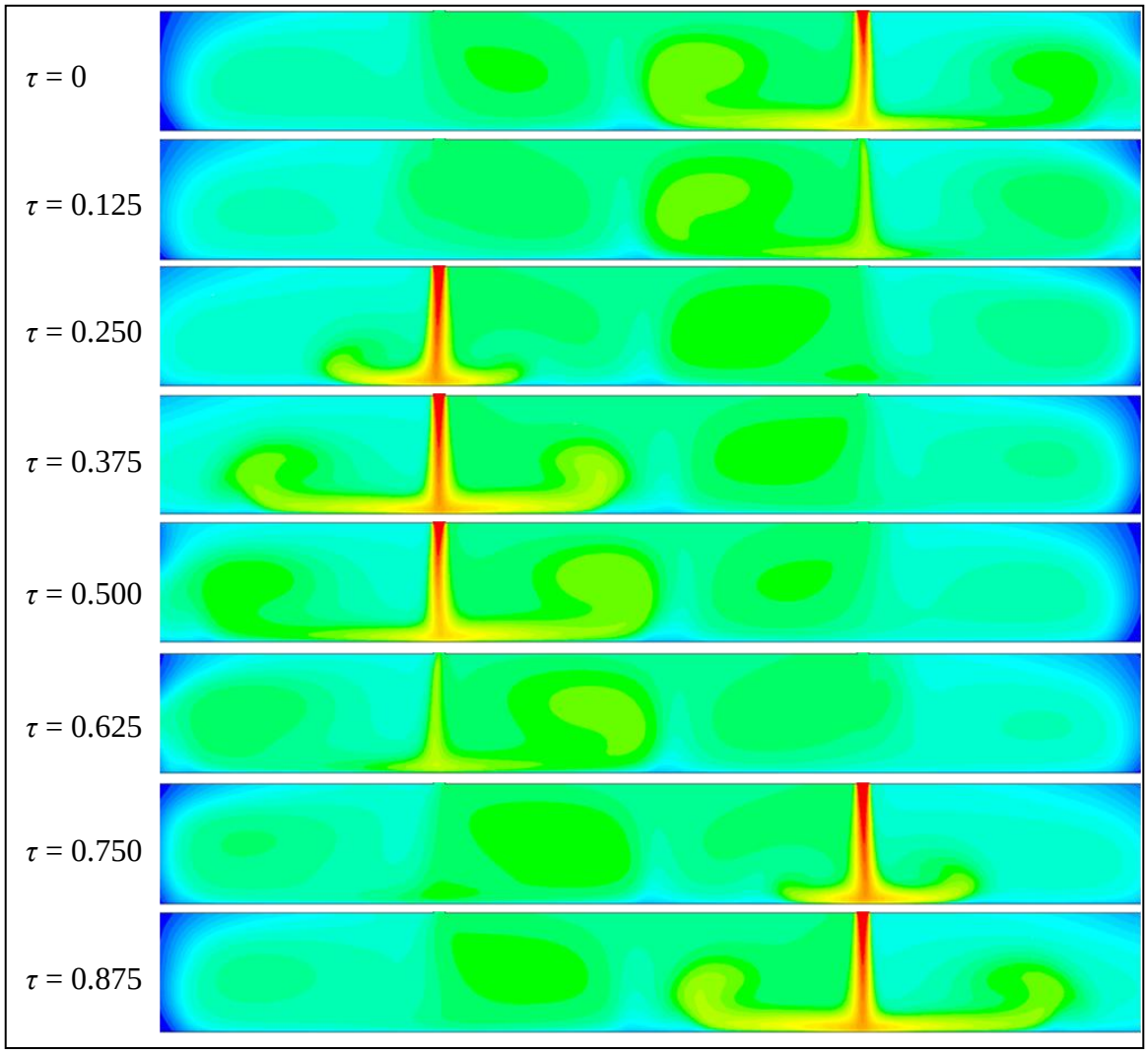

Figure 11.13: Instantaneous temperature fields for $\theta = \pi$ at various values of τ.

The average temperature in the inner region was much higher for the $\theta = \pi$ case than it was for the base case. As before, this was a consequence of a more even distribution of the tailpipe discharge. The resultant instantaneous heat flux profiles are shown in Figure 11.14.

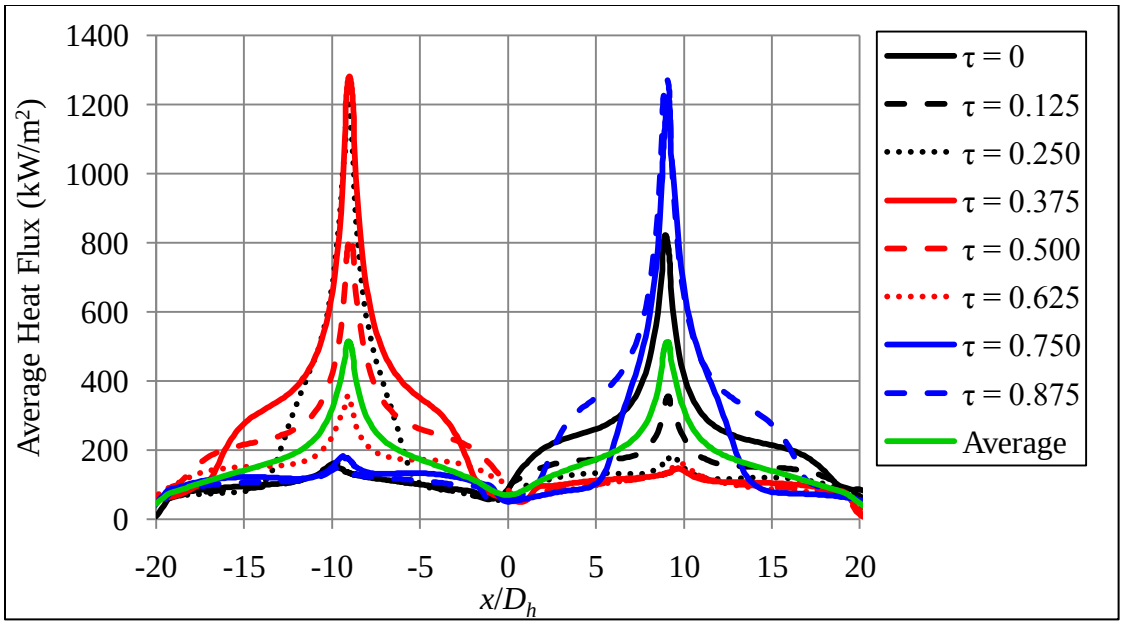

Figure 11.14: Instantaneous heat flux profiles at various values of τ for $\theta = \pi$.

The $\theta = \pi$ case produced a 62.9 % higher peak heat flux than the $\theta = 0$ case. This was the result of the main fluid columns of each jet impinging at angles closer to $\pi/2$ rad combined with higher inner region temperatures. Furthermore, the larger, hotter inner vortices greatly increased the heat flux in this region. The outer regions, however, did not experience significantly altered heat flux compared to the base case.

11.5 Summary and Discussion

Jet-to-jet interactions were found to greatly affect the heat transfer performance of a two nozzle pulsating impingement jet system. The presence of multiple jets decreased the effective impingement angle of the main jet column, altered the bulk fluid flow, decreased the temperature in the inner region, and constrained the inner vortices, thereby reducing their size. These factors combined to lower heat flux when compared to similar

jets that had a high phase difference, especially in the inner region. Thus, the performance of future systems could possibly be improved through manipulation of the phase difference, perhaps through the use of a computer controlled fuel injection coupled with feedback from the combustion chamber pressure. Still, all pulsed cases significantly improved heat transfer compared to the steady flow case.

CHAPTER 12

CONCLUSIONS

This work signifies a significant advancement of the PAD project. One of the most important features of this work was the thoroughness of the validation process. The numerical methods were extensively validated using experimental data from pulsating and steady flow jets, stationary and moving impingement surfaces, round and slot shaped nozzles, single and multiple burner systems, and surface heat flux and bulk drying of paper and various porous PTFE samples. Additionally, simulations results were compared with correlations from literature to add further validity to the numerical methods. Thus, the numerical techniques and methods that were developed and employed in this work were found to be well suited for the current application.

Still, the numerical study provided significant contributions to the knowledge of these types of impingement jets. The approach that was employed was to analyze not just the heat flux or drying, but also the details of the fluid flow that resulted in said heat and mass transport. It was found that the key mechanisms of the enhanced transfer were the vortices produced by the oscillating flow. The characteristics of these vortices such as the size, strength, location, duration, and temperature, determined the extent of the improvement. In general, high amplitude ratios produced greater heat flux by producing larger and stronger vortices despite slightly lower vortex temperature. The effects of

oscillation frequency were somewhat more complex. For low frequencies, small secondary vortices were formed which yielded a more uniform heat flux profile and slightly increased average heat transfer. At high values of ω, persistent, concentrated vortices were formed which greatly increased average heat transfer, especially near the tailpipe. The heat flux increased with $\overline{U}_{exit}$ in a nearly linear fashion due to increased vortex size, vortex strength, and energy input rate. Similarly, additional energy input also yield greater heat flux when using larger nozzles. For moving impingement surfaces, higher surface velocities led to lower heat flux due to entrainment of cool ambient air which inhibited performance. Still, heat flux enhancement compared to steady flow jets increased drastically for these cases due to the ability of vortices produced by the pulsating jet to disrupt the boundary layer that formed near the impingement surface. The steady flow cases were unable to significantly penetrate this layer and, thus, experienced large reductions in heat transfer. Finally, for multiple impingement jets, jet-to-jet interactions were found to greatly affect heat transfer performance. The presence of multiple jets decreased the impingement angle of the main jet column, altered the bulk fluid flow, decreased the temperature in the inner region, and constrained the vortices in the region between the jets, thereby reducing their size. These factors combined to lower heat flux when compared to similar jets that had a high phase difference.

Analysis of the fluid flow revealed three distinct flow types, each with unique heat transfer characteristics. These flow types were characterized by the vortices in the impingement zone. They were: a single strong vortex that greatly dissipated before the start of the next oscillation cycle, a single persistent vortex that remained relatively strong

at the end of the cycle, and a strong primary vortex coupled with a short-lived, weaker secondary vortex. A full factorial numerical experiment was implemented to study the combinations of parameters which produced each flow type and the associated impact on heat transfer. It was found that the range over which each flow type was observed could be classified into distinct flow regimes. The trends in heat flux were greatly affected if coupled with a transition from one flow regime to another, since the secondary vortex and persistent vortex regimes were found to significantly enhance heat transfer. Subsequently, transition criteria dividing these regimes were formed based on dimensionless parameters. The critical dimensionless parameters appeared to be the Strouhal number, a modified Strouhal number, the Reynolds number, the velocity amplitude ratio, and the H/D_h ratio. Thus, the oscillatory, mean flow, and geometrical characteristics were all important factors. These factors were combined to form two dimensionless groups. These groups, Ψ_1 and Ψ_2, respectively defined the transition surfaces which separated the secondary vortex and persistent vortex flow regimes from the transient vortex regime. Further study would be required to determine if these parameters offer similar significance for other configurations.

REFERENCES

Ahrens, F. W. (1979). Prediction of heat transfer in pulse-combustion burners. In *Proceedings of the Symposium on Pulse Combustion Technology for Heating Applications*, Argonne, Illinois, pp. 46 - 66.

Ahrens, F. (1983). Heat transfer aspects of hot surface drying at high temperature and mechanical loading. *Journal of Pulp and Paper Science*, Vol. 9, Issue 3, pp. 79-82.

Ahrens, F. and Åström, A. (1986). High-Intensity Drying Of Paper. *Drying Technology*, Vol. 4, Issue 2, pp. 245-270.

Angioletti, M., Di Tommaso, R.M., Nino, E., and Ruocco, G. (2003). Simultaneous visualization of flow field and evaluation of local heat transfer by transitional impinging jets. *International Journal of Heat and Mass Transfer*, Vol. 46, pp. 1703-1713.

Bolz, R. E. and Tuve, G. L. (1976). *CRC Handbook of Tables for Applied Engineering Science*, 2nd Edition. CRC Press, Inc., Boca Raton.

Burgess, B. W. and Chapman, S. M. (1972). The Papridryer Process Part II - Mill Trials, *Pulp and Paper Magazine of Canada*, Vol. 73, No. 11, pp. 73-81.

Carey, Van P. (2008). *Liquid Vapor Phase Change Phenomena*, 2nd Edition. Taylor and Francis, New York.

Çengel, Yunus A. and Robert H. Turner. (2005). Fundamentals of Thermal-Fluid Sciences, 2nd Edition, McGraw Hill Higher Education, New York.

Chaniotis, A. K., Poulikakos, D., and Ventikos, Y. (2003). Dual pulsating or steady slot jet cooling of a constant heat flux surface. *Journal of Heat Transfer*, Vol. 125, pp. 575-586.

Chen, Guohua and Douglas, W. J. Murray. (1998). Combined impingement and through air drying of paper: a comprehensive model. *TAPPI Journal*, Vol. 81(1), pp. 244-253.

Dec, J. E. and Keller J. O. (1986). The effect of fuel burn rate on pulse combustor tail pipe velocities. *International Gas Research Conference*, pp. 498-507.

Dec, J. E., Keller, J. O., and Hongo, I. (1991). Time-resolved velocities and turbulence in the oscillating flow of a pulse combustor tail pipe. Combustion and Flame, Vol. 83, pp. 271-292.

Diller, T.E. (1993). Advances in heat flux measurements. *Advances in Heat Transfer*, Vol. 23, pp. 279-368.

Fluent Inc. (2003). FLUENT 6.1 v2f *Turbulence Model Manual*.

Fluent Inc. (2006). FLUENT 6.3 *User's Guide*.

Holmberg, D. G., and Diller, T. E. (1995). High-frequency heat flux sensor calibration and modeling. *Journal of Fluids Engineering*, Vol. 117, pp. 659-664.

Huang, C. L. D. (1979). Multi-phase moisture transfer in porous media subjected to temperature gradient. *International Journal of Heat and Mass Transfer*, Vol. 22, pp. 1295–1307.

Incropera, F. P. and DeWitt, D. P. (2002). Fundamentals of Heat and Mass Transfer, 5th Edition, Wiley, New York.

Islam, M. R., Ho, J. C., and Majumdar, A. S. (2003). Convective drying with time-varying heat input: Simulation results. *Drying Technology*, Vol. 21, pp. 1333-1356.

Jayatilleke, C. (1969). The Influence of Prandtl Number and Surface Roughness on the Resistance of the Laminar Sublayer to Momentum and Heat Transfer. Prog. Heat Mass Transfer, Vol. 23, No. 6, pp. 193-321.

Karlsson, M., and Stenstrom, S. (2005). Static and dynamic modeling of cardboard drying part 1: Theoretical model. *Drying Technology*, Vol. 23, pp. 143-163.

Karlsson, M., and Stenstrom, S. (2005). Static and dynamic modeling of cardboard drying part 2: Simulations and experimental results. *Drying Technology*, Vol. 23, pp. 165-186.

Kataoka, K., Sahara, R., Ase, H., and Harada, T. (1987a). Role of large-scale coherent structures in impinging jet heat transfer. *Journal of Chemical Engineering of Japan*, Vol. 20, No. 1, pp. 71-76.

Kataoka, K., Suguro, M., Degawa, H., Maruo, K., and Mihata, I. (1987b). The effect of surface renewal due to large-scale eddies on jet impingement heat transfer. *International Journal of Heat and Mass Transfer*, Vol. 30, No. 3, pp. 559-567.

Katekawa, M. E., and Silva, M. A. (2006). A review of drying models including shrinkage effects. *Drying Technology*, Vol. 24, pp. 5-20.

Kaviany, M. and Mittal, M. (1987). Funicular in drying of porous slab. *International of Heat and Mass Transfer*, Vol. 30, No. 7, pp. 1407-1418.

Keller, J.O., Gemmen, R.S., and Barr, P.K. (1990). Premixed combustion in an oscillating/resonant flow field part I: experimental investigation. *ASME Advanced Energy System Division*, Vol. 16, Thermal-Physical Aspects of Energy Conversion, pp. 1-22.

Keller, J. O., Eibeck, P. A., Bramlette, T. T., and Barr, P. K. (1993). Pulse combustion: tailpipe exit jet characteristics. *Combustion Science and Technology*, Vol. 94, pp. 167-192.

Kokko, T., Lautala, P., and Huhtelin, T. (2003). Advanced control strategy for impingement drying. *Drying Technology*, Vol. 21, pp. 1969-1990.

Kudra, T., Benali, M., and Zbicinski, I. (2003). Pulse combustion drying: Aerodynamics, heat transfer, and drying kinetics. *Drying Technology*, Vol. 21, pp. 629-655.

Kudra, T. and Mujumdar, A. S. (2002). Advanced Drying Technologies, Marcel Dekker, New York.

Leverett, M. C. (1941). Capillary behaviour in porous solids. *Transactions of the AIME*, Vol. 142, pp. 159–172.

Liewkongsataporn, W., Patterson, T., Ahrens, F., and Loughran, J. (2006). Impingement drying enhancement using a pulsating jet. *15th Internationl Drying Symposioum*, Budapest, Hungary.

Liewkongsataporn, W., Patterson, T., and Ahrens, F. (2008). Pulsating jet impingement heat transfer enhancement. *Drying Technology*, Vol. 26, pp. 433-442.

Lu, T. and Shen, S. Q. (2007). Numerical and experimental investigation of paper drying: Heat and mass transfer with phase change in porous media. *Applied Thermal Engineering*, Vol. 27, pp. 1248-1258.

Martin, H. (1977). Heat and mass transfer between impinging gas jets and solid surfaces. In *Advances in Heat Transfer, 13*. Hartnett, J. P., and Irvine Jr., T. F., Eds., Academic Press, New York, pp. 1-60.

Majumdar, A. S. (2004). Research and development in drying: Recent trends and future prospects. *Drying Technology*, Vol. 22, pp. 1-26.

Meola, C., de Luca , L., and Carlomagno, G. M. (1996). Influence of shear layer dynamics on impingement heat transfer. *Experimental Thermal and Fluid Science,* Vol. 13, pp. 29-37.

Metso Paper, Inc. (2006). OptiDry Twin: Impingement drying technology for improved runnability, draw management and drying capacity. Retrieved from: www.metso.com on March 15, 2010.

Mladin, E. C., and Zumbrunnen, D. A. (1995). Dependence of heat transfer to a pulsating stagnation flow on pulse characteristics. *Journal of Thermophysics and Heat Transfer,* Vol. 9, pp. 181-192.

Mladin, E. C. and Zumbrunnen, D. A. (1997). Local convective heat transfer to submerged pulsating jets. *International Journal of Heat and Mass Transfer*, Vol. 40, pp. 3305-3321.

Mladin, E. C. and Zumbrunnen, D. A. (2000). Alterations to coherent flow structures and heat transfer due to pulsations in an impinging air-jet. *International Journal of Thermal Science,* Vol. 39, pp. 236-248.

Narumanchi, S. V. J., Amon, C. H., and Murthey, J. Y. (2003). Influence of pulsating submerged liquid jets on chip-level thermal phenomena. *Journal of Electronic Packaging*, Vol. 125, pp. 354-361.

Nasrallah, S. Ben and Perre, P. (1988). Detailed study of a model of heat and mass transfer during convective drying of porous media. *International Journal of Heat and Mass Transfer,* Vol. 31, No. 5, pp. 957-967.

Nellis, G. and Klein, S. A. (2009). *Heat Transfer*. Cambridge University Press, New York.

Nilsson, J., and Stenstrom, S. (2001). Modeling of heat transfer in hot pressing and impulse drying of paper. *Drying Technology,* Vol. 19, pp. 2469-2485.

Patankar, S. V. (1978). A Numerical Method for Conduction in Composite Materials, Flow in Irregular Geometries and Conjugate Heat Transfer. *Proceedings of the 6th International Heat Transfer Conference, Toronto,* Vol. 3, pp. 297.

Patankar, S. V. (1980). *Numerical Heat Transfer and Fluid Flow*. Hemisphere/McGraw Hill, New York.

Poh, H. J., Kumar, K., and Mujumdar, A. S. (2005). Heat transfer from a pulsed laminar impinging jet. *International Communications in Heat and Mass Transfer*, Vol. 32, pp. 1317-1324.

Popie l, C. O. and Trass, O. (1991). Visualization of a free and impinging round jet. *Experimental Thermal and Fluid Science*, Vol. 4, pp. 253-264.

Psimas, M. J., Patterson, T., Ahrens, F., and Loughran, J. (2007). Heat transfer comparison of pulsating and steady flow jets. In *Proceedings of the 5th Asia-Pacific Drying Conference*, Vol. 2, Hong Kong, China, pp. 1243-1248.

Ramarao, B. V., Massoquete, A., Lavrykov, S., and Ramaswamy, S. (2003). Moisture diffusion inside paper materials in the hygroscopic range and characteristics of diffusivity parameters. *Drying Technology*, Vol. 21, pp. 2007-2056.

Lord Rayleigh, J. W. S. (1945). Theory of resonators. In *The Theory of Sound*, Volume II, 2nd Edition (1st American Edition), Dover, New York.

Reuter, D., Daniel, B. R., Jagoda, J., and Zinn, B. T. (1986). Periodic mixing and combustion processes in gas fired pulsating combustors. *Combustion and Flame*, Vol. 65, pp. 281-290.

Sailor, D. J., Rohli, D. J., and Fu Q. (1999). Effect of variable duty cycle flow pulsations on heat transfer enhancement for an impinging air jet. *International Journal of Heat and Fluid Flow*, Vol. 20, pp. 574-580.

Sanderson, S. R., and Sturtevant, B. (2002). Transient heat flux measurement using a surface junction thermocouple. *Review of Science Instruments*, Vol. 73, pp. 2781-2787.

Scheidegger, A. E. (1972). *The Physics of Flow through Porous Media*, 3rd Edition. University of Toronto Press, Toronto.

Scotti, A. and Piomelli, U. (2002). Turbulence models in pulsating flows. *AIAA Journal*, Vol. 40, pp. 537-544.

Sheriff, H. S., and Zumbrunnen, D. A. (1999). Local and instantaneous heat transfer characteristics of arrays of pulsating jets. *Journal of Heat Transfer*, Vol. 121, pp. 341-348.

Smook, G. A. (1992). *Handbook for Pulp & Paper Technologies*, 2nd Ed. Angus Wilde Publications: Bellingham, WA.

Tang, Y. M., Waldherr, G., Jagoda, J. I., and Zinn, B. T. (1995). Heat release timing in a nonpremixed Helmholtz pulse combustor. *Combustion and Flame*, Vol. 100, pp. 251-261.

Thyageswaran, S. (2004). Numerical modeling of pulse combustor tail pipe heat transfer. *International Journal of Heat and Mass Transfer*, Vol. 47, pp. 2637-2651.

de Vahl Davis, G. and Mallinson, G. D. (1972). False diffusion in Numerical Fluid Mechanics. *University of New South Wales, School of Mechanical and Industrial Engineering Report*, 1972.

Viskanta, R. (1993). Heat transfer to impinging isothermal gas and flame jets. *Experimental Thermal and Fluid Science*, Vol. 6, pp. 111-134.

Weineisen, H. and Stenstrom, S. (2005). Modeling through drying of tissue - Effect of port size distribution on drying characteristics. *Drying Technology*, Vol. 23, pp. 1909-1923.

Whitaker, S. and Chou, W. (1983). Drying Granular Porous Media - Theory and Experiment. *Drying Technology*, Vol. 1, Issue 1, pp. 3-33.

Yang, H., Sakai, N., and Watanabe, M. (2001). Drying model with non-isotropic shrinkage deformation undergoing simultaneous heat and mass transfer. *Drying Technology*, Vol. 19, pp. 1441-1460.

Zbicinski, I. (2002). Equipment, technology, perspectives and modeling of pulse combustion drying. *Chemical Engineering Journal*, Vol. 86, pp. 33-46.

Zinn, B. T. (1996). Pulse combustors applications: past, present and future. In *Unsteady Combustion*, Editors, Culick, F., Heitor, M. V., and Whitelaw, J. H., Kluwer Academic Publishers, the Netherlands.

Zuckerman, N., and Lior, N. (2005). Impingement heat transfer: Correlations and numerical modeling. *Journal of Heat Transfer*, Vol. 127, pp. 544-552.